# JOURNAL OF CAVE AND KARST STUDIES

April 2009
Volume 71, Number 1
ISSN 1090-6924
A Publication of the National Speleological Society

## IN THIS ISSUE:

- SCUTTLE FLIES IN INDIA
- ROBBER FROG IN MEXICO
- SEAL BONES IN SARDINIA
- STALAGMITE RECORDS IN SPAIN
- SEDIMENT FACIES IN CAVES OF MALLORCA ISLAND
- TROGLOBITIC SPIDER IN EASTERN NORTH AMERICA
- FLANK MARGIN CAVES OF KANGAROO ISLAND, SOUTH AUSTRALIA

*AND MORE...*

**Published By**
**The National Speleological Society**



The *Journal of Cave and Karst Studies* (ISSN 1090-6924, CPM Number 40065056) is a multi-disciplinary, refereed journal published three times a year by the National Speleological Society, 2813 Cave Avenue, Huntsville, Alabama 35810-4431 USA; Phone (256) 852-1300; Fax (256) 851-9241, email: nss@caves.org, World Wide Web: http://www.caves.org/pub/journal/.
Check the *Journal* website for subscription rates. Back issues and cumulative indexes are available from the NSS office.

POSTMASTER: send address changes to the *Journal of Cave and Karst Studies*, 2813 Cave Avenue, Huntsville, Alabama 35810-4431 USA.

The *Journal of Cave and Karst Studies* is covered by the following: ISI Thomson Services Science Citation Index Expanded, ISI Alerting Services, and Current Contents/Physical, Chemical, and Earth Sciences.



Front cover: Snake Lagoon on Kangaroo Island, South Australia, see Mylroie and Mylroie in this volume. Photo by J. Mylroie.

# EDITORIAL
## *Journal of Cave and Karst Studies* Use of FSC-Certified and Recycled Paper

MALCOLM S. FIELD

Beginning with this issue, the *Journal of Cave and Karst Studies* now includes the Forest Stewardship Council (FSC) logo on the inside cover. According to the FSC web site (http://www.fsc.org/about-fsc.html) ''FSC is an independent, non-governmental, not for profit organization that was established to promote the responsible management of the world's forests. It provides standard setting, trademark assurance and accreditation services for companies and organizations interested in responsible forestry. Products carrying the FSC label are independently certified to assure consumers that they come from forests that are managed to meet the social, economic and ecological needs of present and future generations.''

FSC certification allows consumers to identify products that provide assurance of social and environmental responsibility on the part of the producer. This is accomplished by requiring that all materials be tracked from the certified source. The path taken by the raw materials harvested from an FSC-certified source are tracked using a chain-of-custody through processing, manufacturing, distribution, and printing until it is an end product and ready for distribution.

The FSC logo is applicable and allowed only for FSC-Certified and Recycled Paper use. By having selected an FSC-certified paper for printing the *Journal*, we are provided the right to use the FSC logo. Approved use of the seal ensures that the paper and processes that we use for the *Journal* are being produced in compliance with strict guidelines protecting the environment, wildlife, workers and local communities.

Interestingly, the *Journal* has actually been conforming to FSC standards for more than a year, which reflects the conservation mindset of the members of the National Speleological Society. As is known to many of you, conservation is a major part of the National Speleological Society, although we are more focused on the more limited concept of cave and karst conservation (http://www.caves.org/committee/conservation/). However, by using FSC-certified paper we are directly supporting forest conservation and may be indirectly supporting cave and karst conservation, depending on where the paper is being harvested. This is something that the National Speleological Society can be proud of and it reflects well on our members' commitment to being conservation minded.

P. Paquin, N. Dupérré, D.J. Buckle, and J.J. Lewis – *Oreonetides beattyi*, a new troglobitic spider (Araneae: Linyphiidae) from eastern North America, and re-description of *Oreonetides flavus*. *Journal of Cave and Karst Studies,* v. 71, no. 1, p. 2–15.

# *OREONETIDES BEATTYI*, A NEW TROGLOBITIC SPIDER (ARANEAE: LINYPHIIDAE) FROM EASTERN NORTH AMERICA, AND RE-DESCRIPTION OF *OREONETIDES FLAVUS*

P. Paquin[1,5], N. Dupérré[2], D.J. Buckle[3], and J.J. Lewis[4]

**Abstract:** A new troglobitic Linyphiidae, *Oreonetides beattyi* n.sp., is described from caves of eastern North America. The species is morphologically close to *Oreonetides flavus* Emerton and proposed as sister-species. Both species are described, illustrated and their distribution is documented. The intra-specific variation of *O. beattyi* is detailed: female genitalia display unusual variability, but males provided stable species level diagnosis. A male from Bull Cave (Tennessee) that shows significant genitalic variation is problematic, however. With limited sampling, the genetic bar-coding approach did not provide helpful insights to determine if this specimen belongs to a different species, is morphologically aberrant, or simply belongs to a population geographically distant enough to explain genetic variability. We propose the cryophilic affinities/relict population hypothesis to explain the ecological affinities of some Linyphiidae that are restricted to caves in most of their ranges, but occur on the surface at the northern edge of their distribution. We suggest an evolutionary scenario for the disjunct distribution of *Oreonetides beattyi* n.sp. in eastern caves and *O. flavus* in more northern latitudes on the west coast of North America.

## Introduction

In taxonomy, species boundaries are determined by the examination of series of closely related species in order to identify distinctive characters or gaps in gradation of shapes, length, counts, etc. of variable morphological features. Characters retained to delimit species are detailed and used as diagnostic. Intra-specific variability is rarely reported and remains a neglected aspect of most taxonomic papers, and consequently, there is a widespread perception that variation within a species is highly unusual. In spider taxonomy, intra-specific variability has been documented for color patterns [e.g. *Araneus* (Levi, 1971; Court and Forster, 1988), *Theridion frondeum* Hentz, 1850 (Emerton, 1882, plate 3, fig. 1), *Latrodectus katipo* Powell, 1870 (Vink et al., 2008), *Sitticus fasciger* (Simon, 1880) (Proszynski, 1968)], but coloration is rather volatile, easily altered in preserved specimens, and rarely used to delimit species. Genitalic characters, however, are reputed to be stable within a species, while providing the needed information to distinguish species (Eberhard, 1986), which makes these features ideal for taxonomic purposes. Intra-specific variability of genitalia is therefore much more problematic. Nonetheless, several cases are known. For instance, Roberts (1987, p. 180), provided examples of intra-specific variability of the male palp of *Araneus diadematus* Clerck (1757) (Araneidae), Levi (1971) illustrated genitalic variation of male and female *Araneus*, Gertsch (1984) illustrated the variation he admitted for the male genitalia of *Eidmanella pallida* (Emerton, 1875) (Nesticidae) and Blest and Vink (2000) documented the variability of the retrolateral tibial apophysis (RTA) for a few species of Stiphidiidae. Important intra-specific variations of female genitalia have been shown for *Cicurina* (Dictynidae) (Paquin and Hedin, 2004; Paquin et al., 2008), and supported by genetic data (Paquin and Hedin, 2004, 2007). These examples are troubling as many species are based on the examination of few specimens, where species are differentiated only by minor genitalic details and are found in sympatry.

A sound evaluation of intra-specific variability is largely dependent on the number of specimens available, but in the case of rare species, often known only from one or two specimens, it is impossible to assess. Misevaluation of this variation can lead to the erroneous interpretation of species limits because characters that are randomly variable within a species must not be used to establish taxa. In such cases, a re-assessment of the taxonomy based on longer series of specimens results in synonymies. Synonyms usually have relatively minor significance because species names are scientific hypotheses to be refuted, modified, redefined, or improved. However, synonymies have deep impacts when involving species that are legally protected (threatened,

[1] Cave and Endangered Invertebrate Research Laboratory, SWCA Environmental Consultants, 4407 Monterey Oaks Boulevard, Building 1, Suite 110, Austin, Texas, 78749, U.S.A. ppaquin@swca.com
[2] Division of Invertebrate Zoology, American Museum of Natural History, Central Park West at 79th Street, New York NY 10024, U.S.A. nduperre@amnh.org
[3] 620 Albert Avenue, Saskatoon, SK, S7N 1G7, Canada, djbuckle@shaw.ca
[4] Lewis & Associates LLC, Cave, Karst & Groundwater Biological Consulting, 17903 State Road 60, Borden, IN 47106-8608, U.S.A. lewisbioconsult@aol.com
[5] This is publication no. 10 of the Karst Biosciences and Environmental Geophysics Research Laboratories, SWCA Environmental Consultants

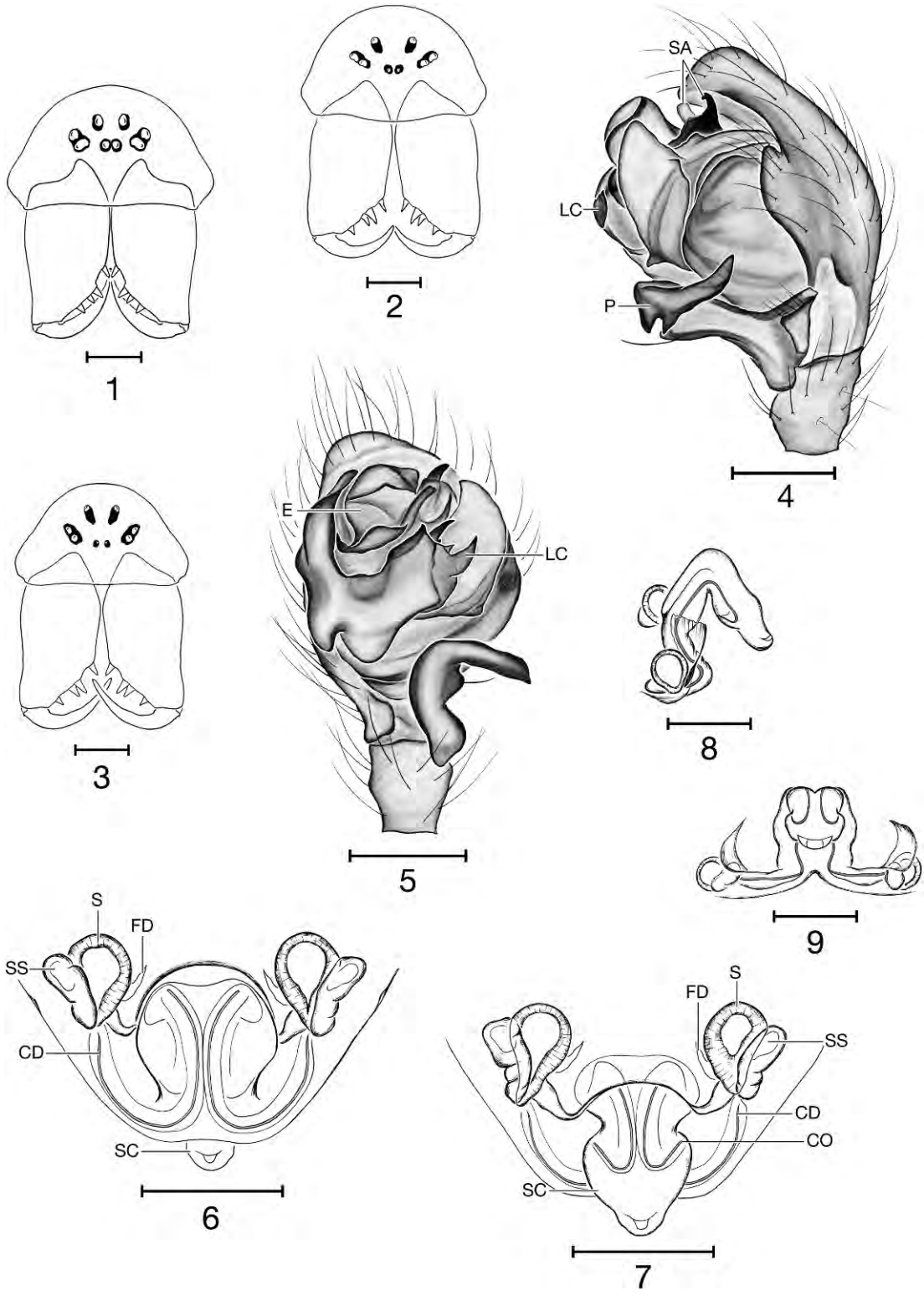


**Figures 1–9.** ***Oreonetides beattyi*** **n.sp. 1, face of male, frontal view (Calf Cave, Tennessee); 2, face of female, frontal view (Smith's Folly Cave, Indiana); 3, face of female, frontal view (JJ's Sister Cave, Indiana); 4, palpus of male, retrolateral view; 5, palpus of male, ventral view; 6, cleared epigynum, ventral view; 7, cleared epigynum, dorsal view, 8, cleared epigynum, lateral view; 9 cleared epigynum, posterior view. Abbreviations used: CD copulatory ducts, CO copulatory openings, E embolus, FD fertilization ducts, LC lamella characteristica, P paracymbium, SA suprategular apophysis, SC scape, S spermatheca, SS secondary spermatheca. Scale bars for Figures 1–3, 5–9 = 0.1 mm; Figure 4 = 0.05 mm.**

listed, or species considered for listing) (see Longacre, 2000; Bender et al., 2005). Legal protection is ultimately funneled into a species name, a system that does not harmonize well with a discipline that progresses by proposing revised hypotheses. For instance, Paquin et al. (2008) synonymized two names of eyeless troglobitic *Cicurina* that were the focal point of a legal debate around the taxonomic soundness of cave spiders that are species of concern in Texas (United States). This synonymy was a direct consequence of an initial misevaluation of intra-specific variability due to the rarity of identifiable material. Such synonymy suggests that caution should be used in the description of cave-restricted taxa, because the rarity, narrow distributions, and high dependence on sensitive habitats make troglobites ideal candidates for enhanced conservation measures.

Recent cave surveys carried out in Indiana (Lewis and Rafail, 2002; Lewis et al., 2004; Lewis and Lewis, 2008a, b) and Tennessee (Reeves, 2000; Lewis, 2005) revealed the existence of a new troglobitic spider belonging in *Oreonetides* Strand 1901. Further research led to the discovery of additional specimens from other eastern caves in museum collections. Based on this information, we conducted additional sampling in 2004 in order to increase the number of specimens available for study, particularly the males. The collection of fresh material allowed the use of a DNA bar-coding approach (Hebert et al., 2003) for an independent assessment of species limits and variability. In the present paper, we describe this new troglobitic spider and document its intra-specific variability. We re-describe the epigean species *Oreonetides flavus* (Emerton, 1915) which is hypothesized as sister-species. The distribution of the two species is discussed in the light of a possible evolutionary scenario behind the speciation of the troglobitic species. The limitation of the bar-coding approach is also briefly addressed.

## Methods

### Specimen Examination

Specimens were examined in 70% ethanol under a SMZ-U Nikon dissection microscope. A Nikon Coolpix 950 digital camera attached to the microscope was used to take a photograph of the structures to be illustrated. The digital photo was then used to trace proportions, the illustration was detailed and then shaded by referring to the structure under the microscope. Female genitalia were excised using a sharp entomological needle and transferred to lactic acid to clear non-chitinous tissues. A temporary lactic acid mount was used to examine the genitalia under an AmScope XSG Series T-500 compound microscope, where genitalia were photographed and illustrated as explained above. For the study of the embolic division, the male palps were placed for ~10 minutes in warm KOH and washed in 80% alcohol.

All measurements are in millimeters and were made using an optical micrometer on the microscope. When possible, five specimens of each sex were measured for the descriptions. Calculation for the location of Tm I follows Denis (1949). Palpal and epigynal terminology follows Saaristo (1972), van Heldsingen (1981) and Hormiga (1994). Color description was done under halogen lighting, using traditional color names. Subsequently, we matched the color of the specimen to a reference Pantone chart (Pantone Formula Guide, solid matte) and added the color code to the description. Latitude and longitude data are given in decimals and should be considered an approximation, and in the case of cave locations, they are not given in order to preserve the confidentiality of the information.

### Molecular Analysis

Specimens recently collected were preserved in the field in 100% ethanol and preserved on ice to avoid DNA degradation (Vink et al., 2005). DNA extraction was done using a DNEasy® kit following the manufacturer's indications. Using PCR (polymerase chain reaction), we amplified a ~1 kb fragment of the Cytochrome Oxidase I (CO1) mtDNA gene using primers C1-J-1751-SPID, C1-J-2309, C1-N-2568, and C1-N-2776-SPID (Hedin and Maddison, 2001, Vink et al., 2005) and PCR protocols similar to those detailed in Paquin and Hedin (2004). PCR products were purified using the Wizard® SV Gel and PCR Clean-up System of Promega following the manufacturer's indications and sequenced at the core facilities (Portland State University and Berkeley University). Templates were sequenced in both directions for each fragment, using PCR primers and except for the shorter fragment, only sequenced from the 5-foot-end using C1-N-2776-SPID. The sequences read were assembled into sequence contigs and edited using Sequencer 4.5 and MacClade 4.0 (Maddison and Maddison, 2003). MrModeltest version 2.2 (Posada and Crandall, 1998; Nylander, 2004) and PAUP* 4.0b10 (Swofford, 2002) were used to select a best-fit model of molecular evolution using the Akaike Information Criterion (AIC) (see Posada and Buckley, 2004). Phylogenetic analyses were conducted using MrBayes version 3.1.2 (Ronquist and Huelsenbeck, 2003) software. We used a GTR+I+G model with fixed substitution and rate parameters (obtained in MrModeltest) to conduct an un-partitioned Bayesian analysis using this best-fit model of molecular evolution. All analyses were run for ten million generations, sampling every 1000th tree (all other parameters set to program defaults (Ronquist and Huelsenbeck, 2003)). Majority rule consensus trees were constructed, discarding the first 2000 trees as burn-in. The analysis includes two other surface *Oreonetides* species, *Pithyohyphantes* sp., a basal Linyphiidae and *Pimoa* sp. (Pimoidae), a sister group to Linyphiidae (Hormiga 1994, 2000) used as outgroup.

The bulk of specimens were collected by JJL, and by PP, ND and Jeremy Miller (curated in the Collection

Paquin-Dupérré; CPAD, Shefford, Québec). Voucher specimens are also deposited in the collection of Donald J. Buckle (DBC, Saskatoon, Saskatchewan, Canada). Specimens from the following collections were also examined: American Museum of Natural History (AMNH, New York, USA); Canadian National Collection (CNC, Ottawa, Ontario Canada), Museum of Comparative Zoology (MCZ, Harvard, Cambridge, Massachusetts, USA); Lyman Entomological Museum (LEM, McGill University, Ste-Anne-de-Bellevue, Canada) and the Burke Museum University of Washington (UWBM, Seattle, Washington, United States).

## Taxonomy

**Family:** Linyphiidae Blackwall, 1859

**Genus:** *Oreonetides* Strand, 1901

**Type Species:** *Oreonetides vaginatus* (Thorell, 1872).

**Diagnosis:** See van Heldsingen (1981).

**Composition:** Includes 15 described species, 6 of which are found in North America. Several North American species remain undescribed.

**Distribution:** Russia, China, Mongolia, Europe, Japan and North America (Platnick, 2008).

### New Species

*Oreonetides beattyi* (Figs. 1–19 and 27–28)

*Oreonetides flavus* (Emerton, 1915) (Reeves, 2000). Misidentification.

*Oreonetides* sp. (Peck, 1998; Gertsch, 1992).

**Type Material:** HOLOTYPE: United States: Lawrence Co., Smith's Folly Cave, Tincher Hollow Special Area, Hoosier National Forest, 26.viii.2004, in cave, 1♂, P. Paquin and J. Miller (AMNH).

**Material Examined:** United States: *Indiana*: Jefferson Co., Grays Cave, on Middle Fork Creek, Big Oaks National Wildlife Refuge, 03.ii.2001, in cave on rotting wood, hand collected, 1♀, J. Lewis, (CPAD); 25.viii.2004, in cave, hand collected, 2♀, P. Paquin, (CPAD); Lawrence Co., Sullivan Cave, 2 mi. W. Springville, 29.xii.2007 1♀, J. Lewis and S. Lewis (CPAD); JJ's Sister Cave, 1 mi. SW Bryantsville, 29.ix.2000, in cave, hand collected, 3♀, J. Lewis and R. Burns (CPAD); 29.ix.2000, in cave, hand collected, 1♀, J. Lewis and R. Burns (CPAD); 26.viii.2004, in cave, hand collected, 1♂, J. Miller (CPAD); Smith's Folly Cave, Tincher Hollow Special Area, Hoosier National Forest, 29.vii.2001, in cave, hand collected, 1♀, J. Lewis and S. Rafail (CPAD); 29.ix.2000, Berlese extraction of leaf litter from cave, 1♀, J. Lewis and R. Burns (CPAD); 25.vii.2002, 2♂ 1♀, J. Lewis (DBC); 26.viii.2004, in cave, 1♂ 8♀, P. Paquin and J. Miller (CPAD); 27.x.2001, in cave, 1♀, J. Lewis and R. Burns (CPAD); Ripley Co., Louis Neill Cave, Big Oaks National Wildlife Refuge, 16.iv.2001, in cave, hand collected, 1♀, J. Lewis, S. Miller and T. Vanosdol-Lewis (CPAD); *Maryland*: Washington Co., Snivley's Cave, near Keedysville, 12.ix.1968, 1♀ [no collector] (AMNH); Snivley's Cave No.2, near Eakles Mill, 04.viii.1973, between rocks and litter, 1♀, A. Norden and B. Ball (AMNH); 03.v.1969, 1♀ (AMNH); *Pennsylvania*: Armstrong Co., Hineman Cave, 2 mi. W. Buffalo Mills, 11.vii.1957, 1♂, C. Krekeler and J.R. Himann (AMNH); Dauphin Co., Indian Echo Cave, 16.i.1937, in cave, hand collected, 1♀, K. Dearwolf (AMNH); Brownstone Cave, 16.i.1937, in cave, hand collected, 6♀, K. Dearwolf (AMNH); *Tennessee*: Blount Co., Bull Cave, Great Smoky Mountains National Park, 02.viii.2000, in cave, hand collected, 1♀, M. Hedin (CPAD); Calf Cave #1, Great Smoky Mountains National Park, 28.vii.2004, in cave, hand collected, 1♂, P. Paquin (CPAD); Marion Co. Speegle Cove Cave, 7 mi. N.W. Jasper, 28.x.2004, inside cave, 1♀, J. Lewis and C. Holliday (CPAD); *Virginia*: Tazewell Co., Rosenbaum's Water Cave, 02.ix.1962, 1♀, J. Holsinger (AMNH); Montgomery Co., Vickers Road Cave, 16.x.1971, 1♀, L.M., T.B.L. Ferguson and J.R. Holsinger (AMNH).

**Diagnosis:** Males and females of *O. beattyi* n.sp. differ from all other members of the genus by the presence of noticeably reduced eyes which vary from approximately one third the size of the eyes of *O. flavus* to tiny, pale white spots. Males are diagnosed by the bidentate ridge of distal arm of paracymbium, their short terminal apophysis and lamella characteristica. Females are characterized by their oval spermathecae, and their elongated secondary spermathecae positioned ventrally.

**Description:** Male (n = 4): Total length: 1.54 ± 0.18; carapace length: 0.72 ± 0.04; carapace width: 0.56 ± 0.04; carapace off-white to light yellow-orange (142M), smooth, shiny, with 4–5 erect setae along midline. Eyes of irregular form, reduced in particular the anterior median (AME) and the posterior median eyes (PME) (Figs. 1–3), to almost completely absent, with presence of white pale spots. Chelicerae light yellow (134M) to yellow-orange (142M), promargin with 4 teeth, retromargin with 4–5 denticles (Figs. 1–3). Cheliceral stridulatory organ visible, with ~35–40 ridges. Abdomen off-white to light gray (Warm gray 1M), densely covered with long semi-erect setae, venter of abdomen with oval striated epigastric plates. Legs light yellow (134M) to light yellow-orange (142M); leg formula 4-1-2-3; tibia I-III with two long dorsal macrosetae, tibia IV with one such setae; metatarsus I with dorsal trichobothrium, TmI situated at 0.35-0.41; metatarsus IV lacking dorsal trichobothrium, coxa IV with small stridulatory pick. Total length leg I: 2.26 ± 0.4; leg II: 2.16 ± 0.12; leg III: 1.89 ± 0.08; leg IV: 2.40 ± 0.13. Palpal femur with small, basal stridulatory pick. Palpus length: 0.33 ± 0.05. Male palp: cymbium with lateral lobe (Fig. 4); paracymbium (P) with one basal protrusion cup-shaped, tip covered with minuscule papillae, second protuberance bearing 5 setae (Fig. 4), trunk of paracymbium bearing an isolated seta distally and a longitudinal ridge basally, distal arm of paracymbium with sclerotized bidentate ridge (Fig. 4); embolus (E) tri-partate, middle part bearing the

sperm duct (Figs. 10 and 11); radix (R) with a small pointed, mesal projection (Figs. 10 and 11); terminal apophysis (TA) short, basally enlarged and pointed apically (Figs. 10 and 11) lamella characteristica (LC), short, large, translucent and curved (Figs. 10 and 11), distal end slightly variable, either rounded and rugose (Figs. 10–12) or pointed and smooth (Figs. 11 and 13).

Female (n = 5): Total length: 1.85 ± 0.2; carapace length: 0.80 ± 0.04; carapace width: 0.58 ± 0.06; overall coloration as in male. Carapace smooth and shiny, with 4–5 erect setae along midline. Eyes as in male, with (AME) and (PME) reduced, to almost completely absent, with presence of white pale spots. Cheliceral promargin with 4 teeth, retromargin with 4–5 denticles. Cheliceral stridulatory organ with ~30 ridges. Abdomen densely covered with long semi-erect setae; venter with oval striated epigastric plates. Leg formula 4-1-2-3; tibia I-III with two dorsal macrosetae, and tibia IV with one such setae; metatarsus I with dorsal trichobothrium situated at 0.36–0.39; metatarsus IV lacking dorsal trichobothrium; coxa IV with small stridulatory pick. Total length leg I: 2.66 ± 0.4; leg II: 2.57 ± 0.24; leg III: 2.32 ± 0.23; leg IV: 2.86 ± 0.31. Palpal femur with small basal stridulatory pick; palpal tarsus without claws. Epigynum width 0.24 ± 0.03. Epigynum consists of a tightly folded scape (Fig. 8), distal part of scape protruding basally (Figs. 6 and 7), primary spermathecae ovale (S), secondary spermathecae (SS) elongated, situated either ventro-laterally, ventro-mesally, or ventro-internally in relation to primary spermathecae (Figs. 14–19), copulatory ducts (CD) long and sinuous (Figs. 14–19), copulatory openings (CO) located midway on ventral surface of scape (S) (Fig. 7), fertilization ducts (FD) rather short and straight (Figs. 6 and 7).

**Distribution:** Known only from caves from the Appalachian Valley in Virginia, the Appalachian Plateau from Pennsylvania south to Tennessee and west to the Interior Low Plateaus in Indiana (Figs. 27–28).

**Habitat:** All known specimens were collected in caves.

**Etymology:** Named in honor of Joseph A. Beatty, professor emeritus, Department of Zoology, Southern Illinois University-Carbondale.

Species

*Oreonetides flavus* (Emerton, 1915), (Figs. 20–25 and 28)

*Microneta flava* (Emerton, 1915, plate III, fig. 2).

*Aigola flava* (Crosby, 1937, plate I, figs. 5–6).

*Oreonetides flavus* (van Helsdingen, 1981, figs 7–12; Crawford, 1988; Buckle et al., 2001).

**Type Material:** *Microneta flava* Emerton, MCZ, EXAMINED.

Label: "*Microneta flava* Emerton, Canada: Alberta: Louggan, Lake Louise, in moss, Aug. 10, 1905 J. H. Emerton Collection" [51.4252′N, 116.1805′W] MCZ #21313 holotype: male, syntype: female.

**Material Examined:** Canada: *Alberta*: 36 km NW Hinton, 3.75 W of Rock Lake Rd. [53.9333′N, 118.0833′W] 03.-17.vi.2004, 1♂, pitfall, H. Williams (LEM); Cameron Lake, Waterton Lakes National Park [49.0166′N, 114.0667′W] 04.vii.1980, interception trap, 1♀, H.J. Teskey (CNC); Bow Pass, 64 mi NW of Banff [53.7167′N, 116.5002′W] 12.x.1953, Berlese sample in spruce duff, 5♀, O. Peck (CNC). United States: *Washington*, Okanagan Co. Tiffany Sping Camp, 6700′ [2042 m] [48.699′N, 119.955′W], 31.vii.1985, 2♀, R. Crawford (UWBM).

**Diagnosis:** Males and females of *O. flavus* are distinguished from *O. beattyi* by the presence of well developed eyes. Males are further diagnosed by their long and spine-like terminal apophysis (TA) and their significantly longer lamella characteristica (LC). Females are diagnosed by their rounded spermathecae (S) and the dorso-mesally positioned secondary spermathecae (SS).

**Description:** Male (n = 2): Total length: 1.59 ± 0.11; carapace length: 0.75 ± 0.07; carapace width: 0.61 ± 0.01; carapace smooth, shiny, light orange (135M), 4–5 erect setae along midline. Eyes well-developed, rounded and ringed with black pigment (Fig. 20). Sternum light yellow-orange (134M). Chelicerae light orange (135M), promargin with 5–6 teeth (Fig. 20), retromargin with 5–6 denticles. Cheliceral stridulatory organ visible with ~30 striae. Abdomen light gray (warm gray 1M) densely covered with long semi-erect setae; venter of abdomen with oval striated epigastric plates. Legs light yellow (1205M) to light orange (134M), leg formula 4-1-2-3; tibia I-IV with two long dorsal macrosetae, metatarsus I with dorsal trichobothrium, TmI located at 0.33, metatarsus IV lacking dorsal trichobothrium, coxa IV with small stridulatory pick. Total length leg I: 2.15 ± 0.04; leg II: 2.00 ± 0.08; leg III: 1.79 ± 0.13; leg IV: 2.40 ± 0.02. Palpal femur of with small, basal stridulatory pick. Palpus length: 0.35 ± 0.02. Male palp: cymbium with lateral lobe (Fig. 21); paracymbium (P) with one basal cup-shape protrusion, covered with minuscule papillae, second basal protuberance bearing 4 setae (Fig. 21), trunk of paracymbium bearing an isolated seta distally and a longitudinal ridge basally, distal arm of paracymbium with sclerotized ridge (Fig. 21); embolus (E) tri-partate (Figs 22–23), middle part bearing the sperm duct; radix (R) with a small rounded, mesal projection (Fig. 23); terminal apophysis (TA) long, smoothly tapering apically (Fig. 23); lamella characteristica (LC) transparent, long, curved, with rugose tip (Figs 22–23).

Female (n = 6): Total length: 1.84 ± 0.16; carapace length: 0.80 ± 0.06, carapace width 0.61 ± 0.01; overall coloration as in male. Carapace smooth and shiny, with 4-5 erect setae along midline. Eyes normal, rounded, ringed with black pigment. Cheliceral promargin with 5–6 large teeth, retromargin margin with 5–6 small denticles. Cheliceral stridulatory organ with ~25 striae.

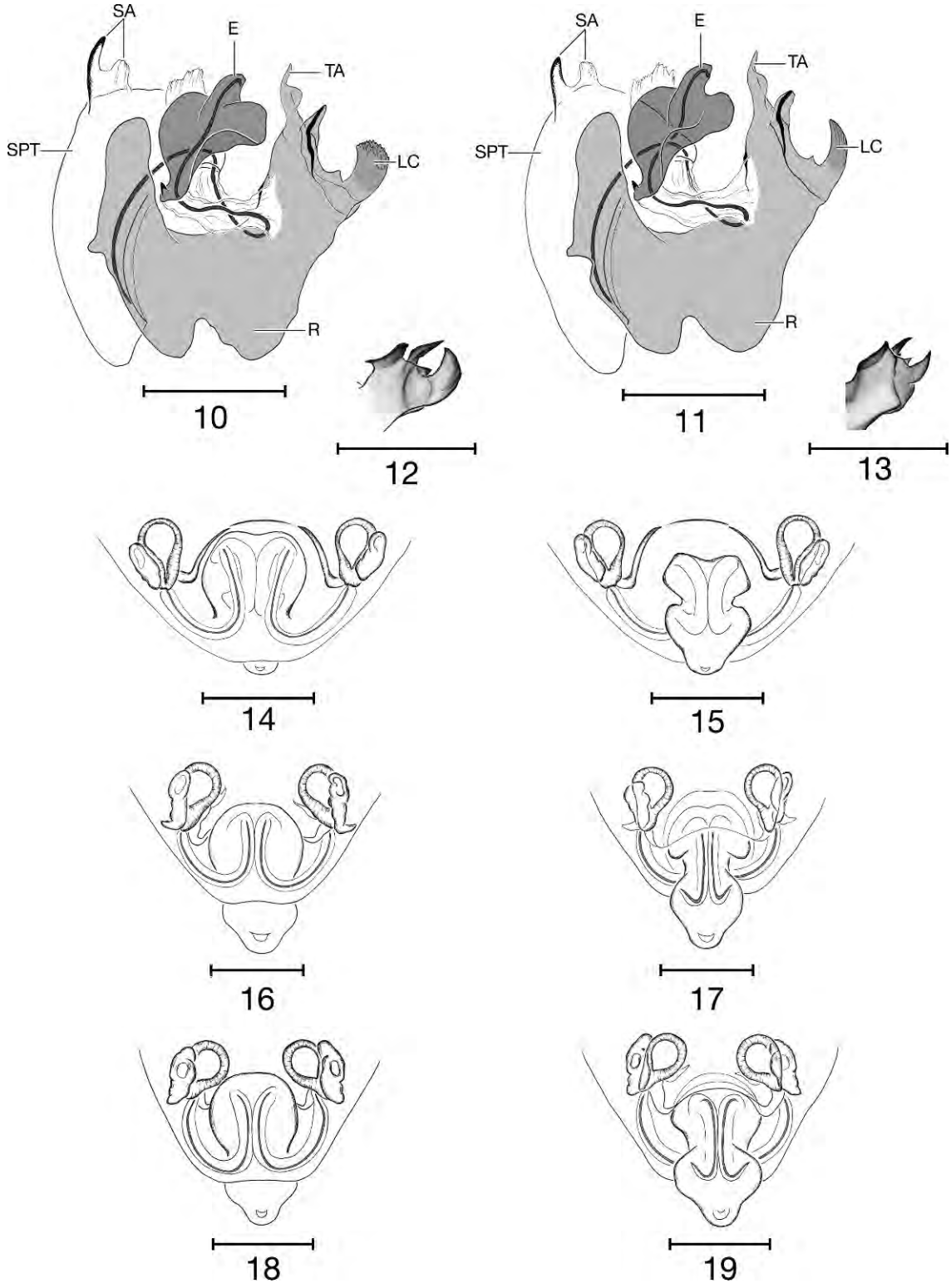


**Figures 10–19.** ***Oreonetides beattyi*** **n.sp. 10, embolic division of male palpus, schematic view (Calf Cave, Tennessee); 11, embolic division of male palpus, schematic view (Smith's Folly Cave, Indiana); 12, lamella characteristica of male palpus (Calf Cave, Tennessee); 13, lamella characteristica of male palpus (Smith's Folly Cave, Indiana); 14, cleared epigynum, ventral view (Bull Cave, Tennessee); 15, cleared epigynum, dorsal view (Bull Cave, Tennessee); 16, cleared epigynum, ventral view (Snivley's Cave, Maryland); 17, cleared epigynum, dorsal view (Snivley's Cave, Maryland); 18, cleared epigynum, ventral view (Rosenbaum's Cave, Virginia); 19, cleared epigynum, dorsal view (Rosenbaum's Cave, Virginia). Abbreviations used: E embolus, LC lamella characteristica, R radix, SA suprategular apophysis, SPT suprategulum, TA terminal apophysis. Scale bars for Figures 10–19 = 0.05 mm.**

Abdomen covered with long semi-erect setae; venter with oval striated epigastric plates. Leg formula 4-1-2-3; tibia I-IV with two long dorsal macrosetae, metatarsus I with dorsal trichobothrium, TmI located at 0.33–0.36, metatarsus IV lacking dorsal trichobothrium, coxa IV with small stridulatory pick. Total length leg I: 2.50 ± 0.11; leg II: 2.32 ± 0.12; leg III: 2.13 ± 0.09; leg IV: 2.81 ± 0.02. Palpal femur with small stridulatory pick set basally; palpal tarsus with no claws. Epigynum width: 0.29 ± 0.01. Epigynum consists of a tightly folded scape (S), distal part of scape protruding basally (Figs. 24–25); primary spermathecae rounded (S) (Figs. 24–25); secondary spermathecae (SS) elongated, situated dorso-mesally (Figs. 24–25); copulatory duct (CD) long and sinuous (Figs. 24–25); copulatory openings (CO) located midway on ventral surface of scape (S) (Figs. 24–25); fertilization ducts (FD) rather short and curved (Fig. 25).

**Distribution:** Canada: Alberta; United States: Washington (Fig. 28).

**Habitat:** Epigean species, apparently associated with forest litter.

**Note:** The specimen from Sea Cliff, New York, reported by van Helsdingen (1981) could not be located for examination despite numerous efforts at the Museum of Comparative Zoology (Harvard), and its identity remains uncertain. This surface record is indicated on the distribution map by a star (Fig. 28, see also discussion).

## Results

### Morphological Variability

The examination of available material clearly allows the distinction of *O. flavus* from *O. beattyi* n.sp. and shows similarities that suggest a close relationship between the two species. The amount of eye reduction observed in *O. beattyi* ranges from significantly reduced to almost completely absent with only pale spots remaining, which leaves no doubt about troglobitic adaptations. *Oreonetides flavus* displayed no variability of genitalic features. Examination of the epigynum of *O. beattyi*, however, showed surprising variability, particularly in the distance between the primary spermathecae and the position of the secondary spermathecae in relation to the primary spermathecae (Figs. 14–19). Such variation was observed between females collected in the same cave and sometimes within a single female as some epigynums were not symmetrical. Males of *O. beattyi* showed no variation in palpal morphology, except for the one collected from Bull Cave, Tennessee (Figs. 10 and 12), which differed in the shape and texture of the lamella characteristica and could not be comfortably assigned to the species.

### Molecular Analysis

Seven individuals belonging to *O. beattyi* were sequenced in order to test if morphological variability could reveal multiple species. The phylogenetic tree (Fig. 26) shows a strongly supported tip clade (0.92) of five individuals from three caves in Indiana that display little genetic variability. As expected, specimens collected in the same cave share more similar haplotypes. However, the specimen from Calf Cave #1 in Tennessee (*Oreonetides*-7) is distinct from the tip clade with a strongly supported (value 1.00) relatively short branch length.

### Distribution

Given the proposed relationship as sister species, the disjunct distribution is remarkable with *O. flavus* occurring in the western part of the continent and comparatively more to the north. *O. beattyi* n.sp. is confined to the east and found exclusively in caves (Fig. 28).

## Discussion

### Species Variability of *Oreonetides beattyi* n.sp.

The series of specimens studied provides insights into the understanding of genitalic variability of the species, particularly for females. Variation of the spermathecae is rarely reported in Linyphiidae, a set of characters otherwise perceived as stable. However, based on a number of specimens that allowed a robust assessment of morphological variation, Schikora (1995) reported significant intraspecific variability of male and female genitalic structures. In a troglobitic linyphiid, comparable intra-specific variability has been reported for females of *Porrhomma cavernicola* (Keyserling, 1886) by Miller (2005). In the present case, the collection of several specimens of *O. beattyi* n.sp. from the same cave displaying variability of the epigynum is convincing evidence that the variation is intra-specific. There is no doubt that female characters cannot be used reliably to recognize more than one species. Comparatively, an important radiation of troglobitic spiders found in Texas (*Cicurina*, subgenus *Cicurella*) (see Gertsch, 1992; Cokendolpher, 2004; Paquin and Dupérré, 2009) did not benefit from a long series of specimens, and many species were described on the basis of a single female, which led to taxonomic confusion (Paquin et al., 2008).

The information provided by the males however, may suggest a different interpretation. The genitalia of all known males are similar, even between localities that are distant from each other, suggesting a single species. However, the male collected from Bull Cave (Tennessee) displayed noticeable variability, with a broader lamella characteristica and a different configuration of the rugose tip (Figs. 10 and 12). Considering the stability of this structure in all other known males, this could be interpreted as a species-level character, although slight variability of the lamella characteristica has been shown in genera such as *Agyneta* Hull, 1911 (Saaristo and Koponen, 1998; Dupérré and Paquin, 2007) and *Maro* O. Pickard-Cambridge, 1906 (Dondale and Buckle, 2001).

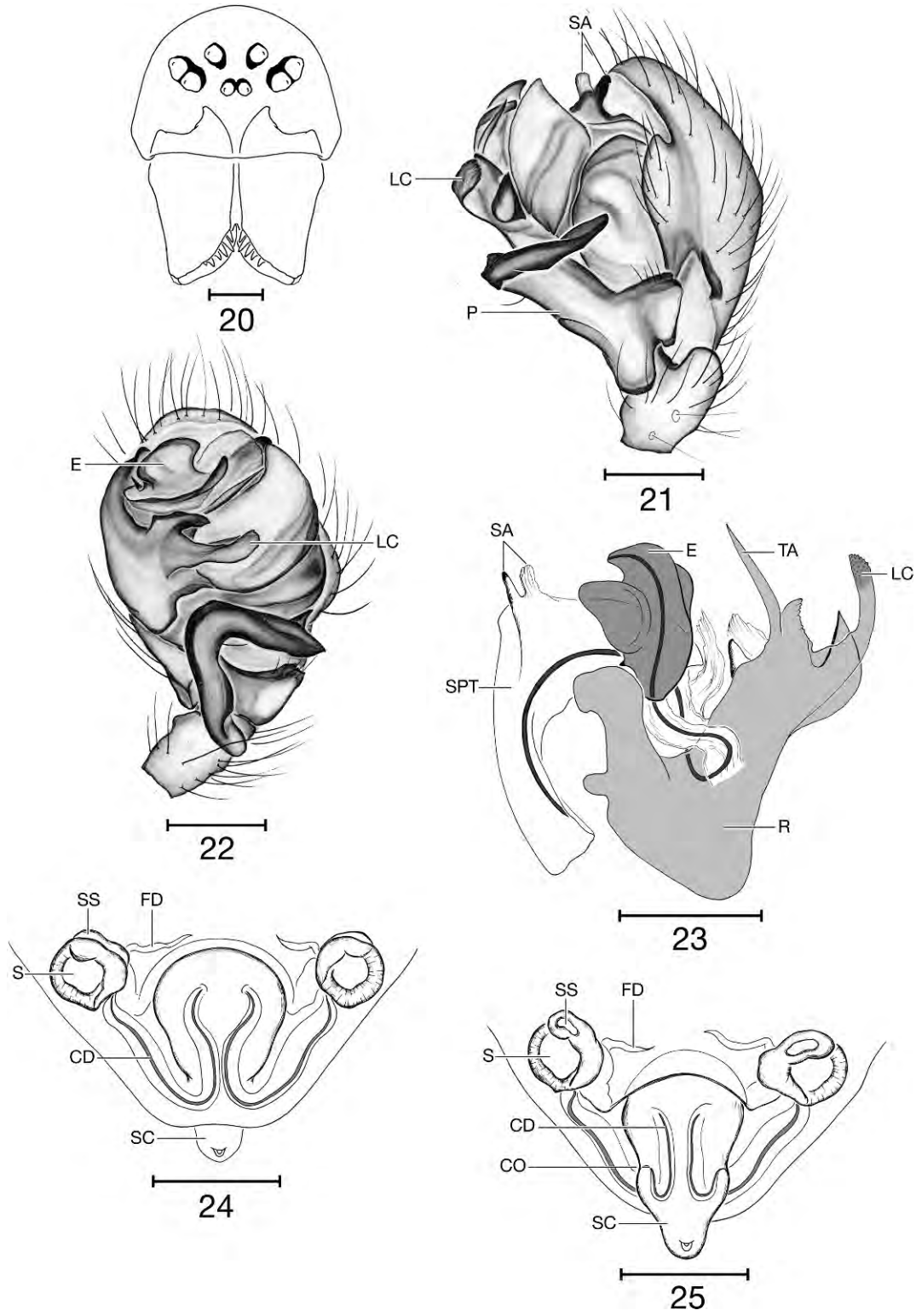


**Figures 20–25.** ***Oreonetides flavus*****. 20, face of male, frontal view; 21, palpus of male, retrolateral view; 22, palpus of male, ventral view; 23, embolic division of male palpus, schematic view; 24, cleared epigynum, ventral view; 25, cleared epigynum, dorsal view. Abbreviations used: CD copulatory ducts, CO copulatory openings, E embolus, FD fertilization ducts, LC lamella characteristica, P paracymbium, R radix, SA suprategular apophysis, SC scape, S spermatheca, SPT suprategulum, SS secondary spermatheca, TA terminal apophysis. Scale bars for Figures 20–25 = 0.1 mm.**

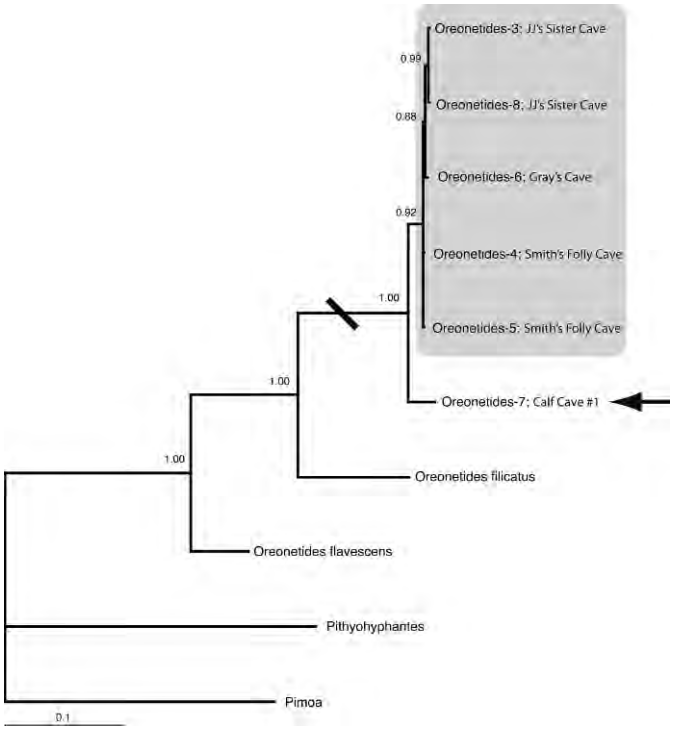


**Figure 26. Bayesian consensus phylogram based on COI sequence data. Values above branches are posterior probabilities.**

The molecular data provide support for the identification of the variability of female genitalia as intra-specific (grey box, Fig. 26). For the male from Bull Cave, the phylogenetic tree does not support or reject that the species found in that cave differs from *O. beattyi*. A female (*Oreonetides*-7, arrows in Fig. 26) from Calf Cave #1, which is located only a few meters from Bull Cave within the same sinkhole and likely harbors the same *Oreonetides* species, was included for DNA analysis. The genetic distinctiveness of *Oreonetides*-7 does not allow us to determine whether this is due to its being a different species, part of an isolated population, restricted gene flow as expected between cave populations, or geographic distance between Bull Cave and Calf Cave #1 and the cluster from Indiana (see Fig. 27). Such a result clearly exemplifies one of the numerous limitations in the application of the genetic bar-code approach for species level identification as advocated by Hebert et al. (2003). A tree with *Oreonetides*-7 nested within the tip clade, or *Oreonetides*-7 as distinct as *O. filicatus* or *O. flavescens* would have provided interpretable insights, but the tree obtained here is inconclusive in that regard. The physical barriers to dispersal and gene flow inherent to cave life result in additional difficulties for accurate interpretations, especially with a limited number of specimens, as is often the case for troglobites. Paquin and Hedin (2007) showed genetic divergences within a single troglobitic spider in an area of ~30 × 15 km, that are greater than for all North America for mobile species of Lepidoptera (Nice et al., 2005). Such discrepancies are still poorly understood and suggest the cautious use of the bar-code approach.

As with the morphological and molecular data, geography and distribution do not provide insights that favor either a distinct species or intra-specific variability. The cluster from Tennessee (that includes Bull Cave and Calf Cave #1) could either harbor a different species or a distinct population of the same species, and both scenarios would be geographically cohesive. Based on available data, it seems best to consider the male from Bull Cave to belong to *O. beattyi* n.sp. and represent variation within the same species. A single specimen does not provide enough certitude to discard the possibility of an aberrant specimen and propose a robust species hypothesis. However, this interpretation may be easily refuted by future collections of additional males displaying morphology similar to that specimen.

## Troglobitic Linyphiidae and the Cryophilic Affinities/Relict Population Hypothesis

Affinities for caves have been previously reported in the genus: *Oreonetides shimizui* (Yaginuma, 1972) is found in Japanese caves, although the species does not display obvious morphological adaptations to cave life such as noticeable eye reduction (Yaniguma, 1972; Eskov, 1992). In eastern North America, several linyphiid species display different degrees of troglobitic adaptations. *Anthrobia mammouthia* Tellkampf, 1844 shows pronounced adaptations with leg elongation and a total lack of eyes, *Porrhomma cavernicola* (Keyserling, 1886) and *Islandiana* spp. still have eye remnants, while *Phanetta subterranea* (Emerton, 1875) known from at least eleven U.S. states and more than a thousand localities, does not show striking morphological adaptations to cave life such as pronounced eye reduction. None of these species are known from surface records, even *P. subterranea,* with its absence of pronounced troglomorphic characters. In other cases, however, the dependence to cave habitats is not as clear. *Bathyphantes weyeri* (Emerton, 1875), *Centromerus latidens* (Emerton, 1882), *Taranucnus ornithes* (Barrows, 1940) are widespread in caves of the eastern North America; almost all records are known from caves, but some specimens have been found on the surface at the northern edge of their distributions. A similar pattern is observed for *Oaphantes* n.sp. on the west coast. We propose the cryophilic affinities/relict population hypothesis to explain this troublesome restriction to caves in southern locations and surface records at the northern edge, within the same species. The implications of this hypothesis have been referred to, at least indirectly, by some authors (see Barr, 1967; Peck, 1973; Peck and Lewis, 1978; Barr and Holsinger, 1985), but not formally proposed as such. Affinity for colder conditions, or avoidance of warm climate, is a driving force behind the dynamic of distribution ranges (Parmesan and Yohe, 2003) and invasion of caves (Barr, 1967). Facing conditions tending

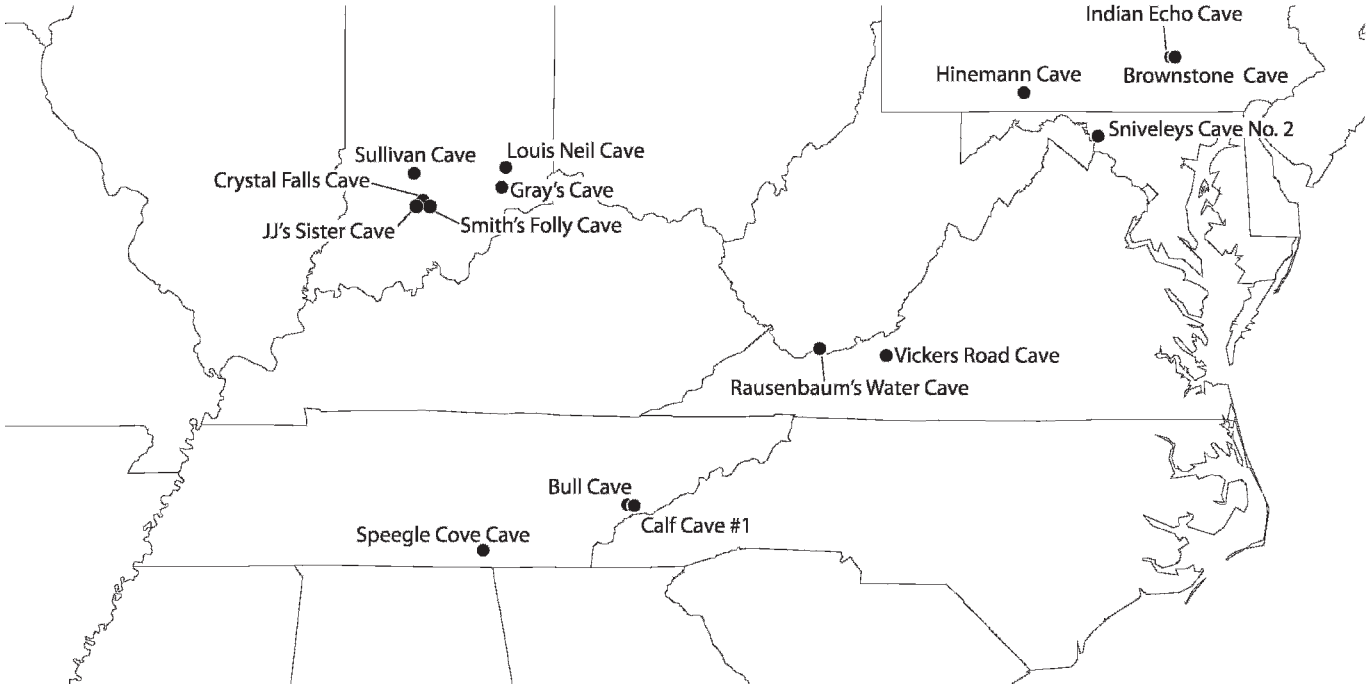


**Figure 27. Distribution map of *Oreonetides beattyi* n.sp. in eastern North America.**

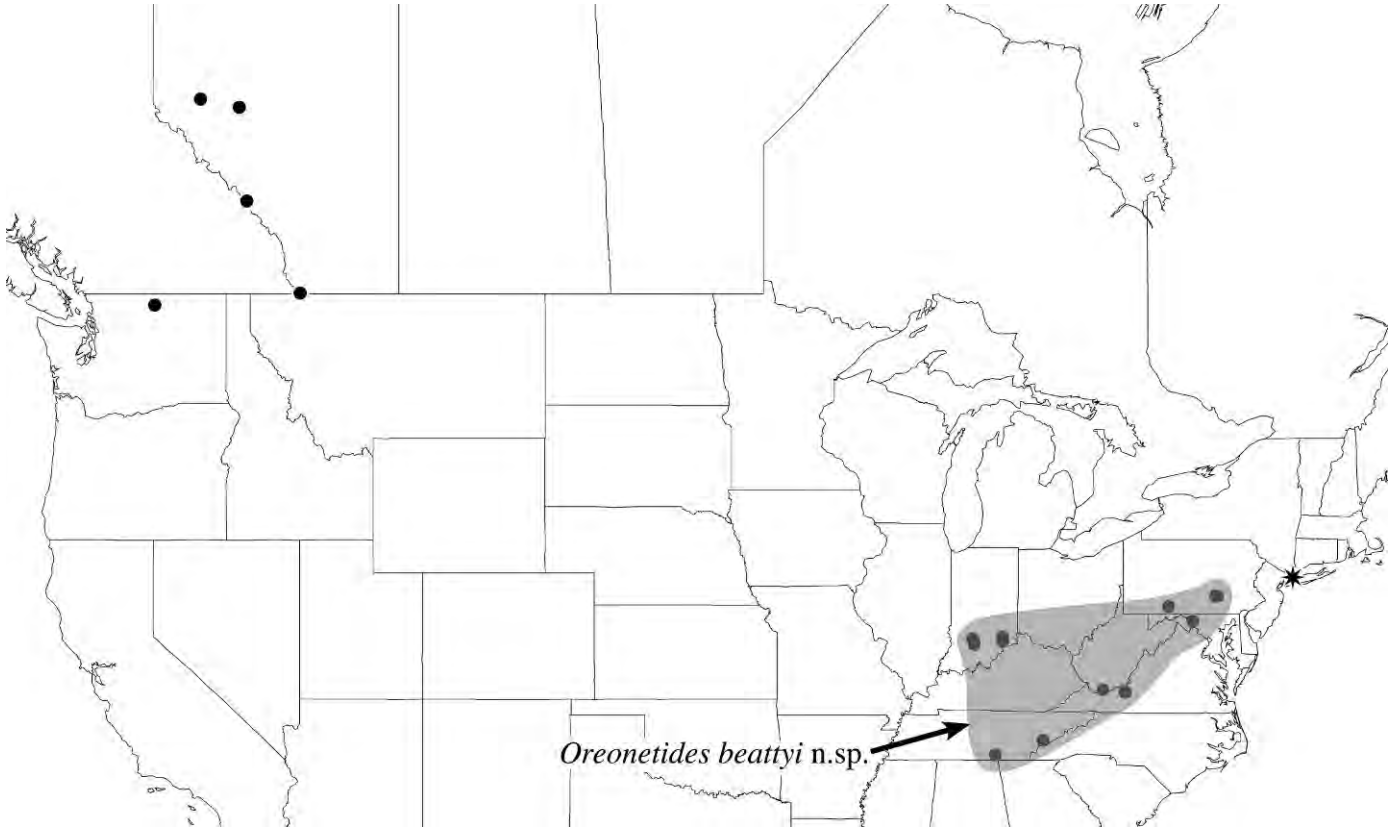


**Figure 28. Distribution map *Oreonetides flavus* in North America. The star symbol represents an older record of *O. flavus* that could not be verified. The distribution of *O. beattyi* n.sp. is provided (shaded area) for comparative purposes.**

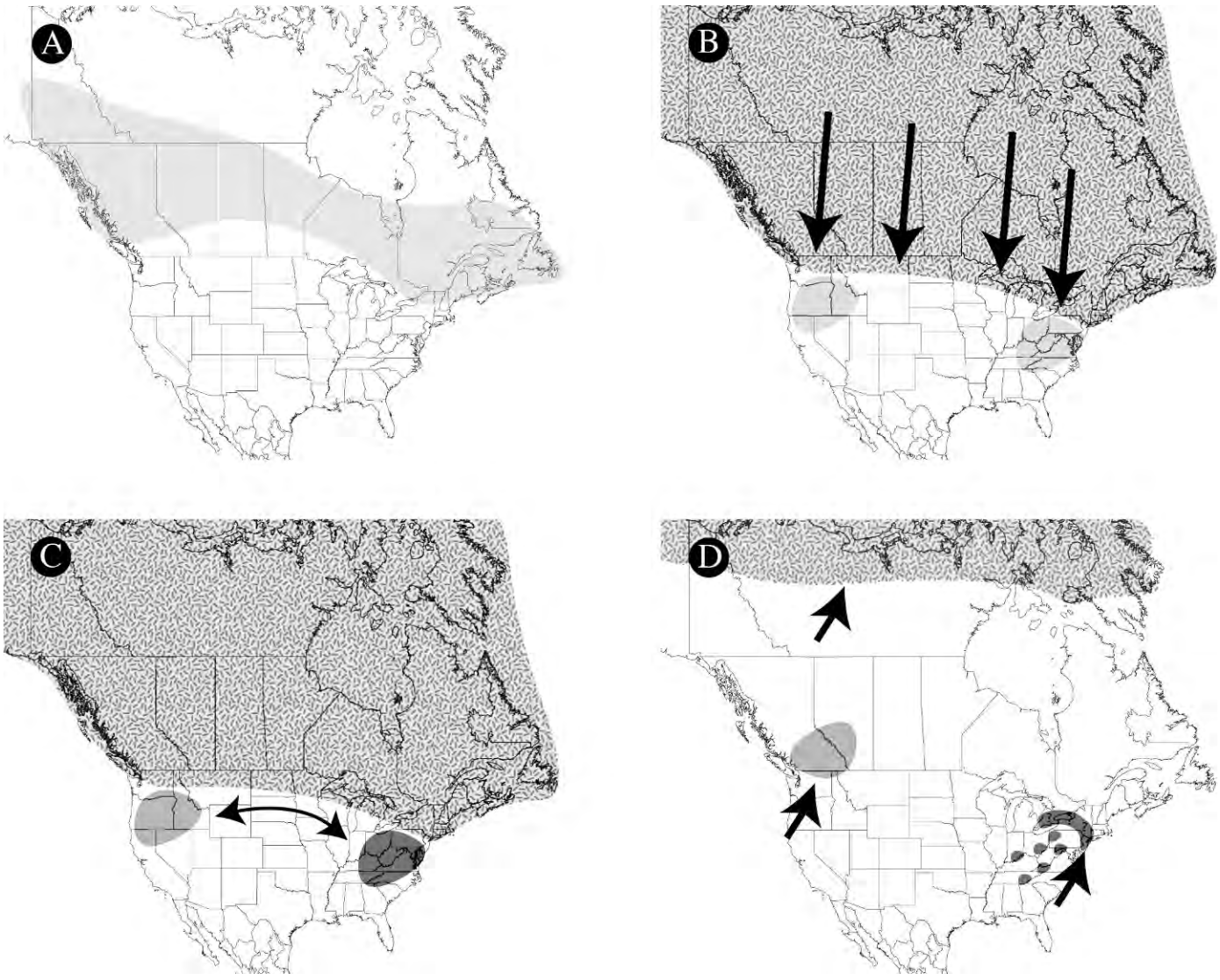


**Figure 29. Evolutive hypothesis of *O. beattyi* n.sp. and *O. flavus* proposed as sister species. A) Boreal distribution of the hypothesised ancestor associated with cool and moist forest habitats. B) Glaciations are sweeping down the ancestor into two areas defined by forest components. C) Isolation and speciation. D) Following the retreat of the Wisconsin glacial ice sheet, species shift up north. In the case of *O. beattyi* n.sp., the populations found in the southern limits are restricted to caves and northernmost probable records are surface ones; *O. flavus* is now found in previously glaciated areas.**

towards warmer and dryer climate, cryophilic species shifted their ranges northward, leaving behind pockets of populations in cool habitat such as bogs, mountain tops, scree slopes, or caves (Fig. 29). These areas are subsequently under warmer conditions, which lead to the extinction of epigean populations, and favor the survival in the subterranean habitat, or other suitable habitat. Such pressure differs or is absent at the northern edge, allowing species to survive on the surface.

Like many cave spiders from eastern North America, *Oreonetides beattyi* n.sp. has a broad distribution across multiple physiographic regions, including several karst areas of the Appalachians and Interior Low Plateaus (Hunt, 1974). The theoretical background for these broad distributions is unclear (but see Barr and Holsinger, 1985), particularly with such differences in the degree of cave adaptation for the different species. On one hand, this suggests that cave invasions by linyphiid species were not synchronized and are much more recent than cave formation, which would have limited and shaped the species distributions according to the physio-geographic evolution of these areas. For instance, a species restricted to a particular geological formation would suggest that the mechanisms driving such distribution are related to the evolution of the geological unit, but a distribution that encompasses several karst units suggests otherwise. On the other hand, the mechanisms behind the evolution and dispersal of troglobites are poorly understood and could

involve alternative scenarios. For instance, species may disperse by way of alternate hypogean habitats such as mammal burrows (Skelley and Kovarik, 2001), scree slopes (Ruszyka and Klimes, 2005), mesocavern or *espace sous-terrain superficiel* (subterranean underground compartments) (Juberthie et al., 1980), which provide a connection between apparently isolated cave systems. In addition, the perception of being isolated is often qualified by their actual state; apparently disconnected fragments may have been part of a complex network that evolved into a fragmented habitat, giving a biased impression of independence of its inherent units. Such fragmentation may not have been the physical conditions present when cave life evolved in these systems. Another possibility is that the distribution of these troglobites is the result of multiple cave colonizations by epigean ancestors. The intermediate stages of cave dependence suggested by the cryophilic affinities/relict population hypothesis provides a theoretical pathway for the evolution and distribution of troglobites that explains distributions by postulating surface connections between cave systems in colder times, followed by the isolation of disjunct cave populations as the climate warmed. Given the range of species mentioned above, it seems unlikely that a single scenario could explain their widespread distributions. The information presently available is not sufficient to conclusively favor any of these alternatives, but the widespread distribution and the different degrees of troglomorphism observed in eastern cave Linyphiidae likely represent different, and relatively early, stages in the evolution towards strict dependence on cave habitat when compared to the ~80 North American cave spiders that are totally eyeless, display highly fragmented distribution, or extremely narrow endemism (Gertsch, 1974; 1984; 1992).

## The Problematic Record from Sea Cliff (New York)

In the light of actual data, the identity of the specimen reported by van Helsdingen (1981) from Sea Cliff (New York) remains problematic (see Fig. 28). Given the similarity of both species, it is possible that this record is a misidentification of *O. beattyi* n.sp., as suggested by its location on the eastern side of the continent. Such record would be the first surface mention of the species, otherwise restricted to caves. A surface record would indicate similar affinities to those displayed by to *B. weyeri* and *C. latidens,* which are found at the surface at the northern edge of their distribution. However, it is also possible that this record is indeed of *O. flavus*, and the apparent distribution gap due to incomplete sampling or to a disjunct distribution like that of *Poeciloneta aggressa* (Chamberlin and Ivie 1943) (Paquin et al., 2001). Location of the Sea Cliff specimen, or the collection of additional specimens, is necessary to clarify the situation.

## Speciation Hypothesis

The study of *O. beattyi* n.sp. and *O. flavus* leaves no doubt about their close relatedness. Given the highly disjunct distribution of the two species and the clear affinities of *O. beattyi* n.sp. for cave habitat, we propose the following evolutionary scenario to explain their particular distribution. Like many Linyphiidae, and most North American *Oreonetides* species (van Helsdingen, 1981), the proto *beattyi/flavus* ancestor displayed affinities for cool and moist environments and had widespread boreal distribution (Fig. 29a). During the Wisconsinan age, most life forms occurring in northern latitudes were displaced southward by a glacier ice complex that covered nearly all of Canada (Prest et al., 1967; Matthews, 1979; Danks, 1993). In central North America, the ice-front habitat consisted of a thin band of mixed open conifer forest and tundra, with dry plains beyond. Some boreal species were able to live in this environment but many were not, and their populations were split into widely separated Cordilleran and eastern forest components (Scudder, 1979; Pielou, 1991) (Fig. 29b). Prolonged isolation led to speciation into western and eastern forms (*O. flavus* and *O. beattyi* n.sp.) (Fig. 29c). Such disjunct distribution of related species is similar to other pairs of taxa that display a similar eastern-western division (Scudder, 1979). For instance, the two North American species of *Cryphoeca* (Araneae, Hahniidae) are similarly distributed: *C. montana* Emerton 1909 is found in the East, while *C. exlineae* Roth 1988 is restricted to the West. Similar patterns also have been reported for several species of beetles such as Carabidae, Staphylinidae, Helodidae (Scudder, 1979). Such eastern-western distributions are well-known and used as broad categories in Danks (1994). The warming climate and retreat of the Wisconsin glacial ice sheet from 14 to 11 ka (Peck, 1988; Schwert, 1992) provided suitable habitat for rapid northward expansion for species with affinities for cold and moist conditions. The progressive northward movement of species with such requirements is well known (Schwert, 1992). Following the cryophilic affinities/relict population hypothesis proposed here, *O. beattyi* n.sp shifted northward in the east, leaving behind isolated populations in caves, while *O. flavus* reoccupied more northerly areas previously not available (Fig. 29d). This scenario is close to the speciation hypothesis proposed for the cave fauna of Illinois by Peck and Lewis (1978). It provides better theoretical support for the actual distribution of the species than treating *O. beattyi* n.sp. as a simple postglacial offshoot from *O. flavus*. Despite their clear phylogenetic affinities, the morphological differences observed between the two species are large enough to suggest a longer history than one originating only from the end of the last glaciation. The rarity of the species could result in incomplete sampling that may obscure an accurate assessment of their distributions, but the proposed hypothesis seems the most plausible one given available data. Hopefully, additional collections will either

confirm the proposed scenario by producing surface specimens of *O. beattyi* from northeastern North America or suggest a better one to explain the particular distributions and dynamics of these related species.

## Acknowledgments

We would like to thank Jeremy Miller, Nathaniel Mann, and David Caudle for their companionship during the field work related to that project. The molecular portion has been accomplished thanks to the generosity of Susan Masta (Portland State University). We are also grateful to Norman Platnick and Lou Sorkin (AMNH, New York, NY), Charles Dondale (CNC, Ottawa, ON), Laura Leibensperger and Gonzalo Giribet (MCZ Harvard, Cambridge, MA), Terry Wheeler (LEM, McGill University, Ste-Anne de Bellevue, QC) and Rod Crawford (UWBM, Washington University, Seattle, WA) who permitted us to work with the material under their responsibility. We are also grateful to Stewart B. Peck (Carleton University, Ottawa, ON) for an informative discussion on the topic. Finally, we appreciate the comments of two anonymous reviewers.

## References

Barr, T.C., 1967, Observations on the ecology of caves: The American Naturalist, v. 101, p. 475–491.

Barr, T.C., and Holsinger, J.R., 1985, Speciation in cave faunas: Annual Review of Ecology and Systematics, v. 16, p. 313–337.

Bender, S., Shelton, S., Bender, K.C., and Kalmbach, A., 2005, Texas comprehensive wildlife conservation strategy (TWAP), Texas Parks and Wildlife, p. i-xv + 1–1131.

Blest, A.D., and Vink, C.J., 2000, New Zealand spiders: Stiphidiidae: Records of the Canterbury Museum, v. 13, p. 1–27.

Buckle, D.J., Carroll, D., Crawford, R.L., and Roth, V.D., 2001, Linyphiidae and Pimoidae of America north of Mexico: Checklist, synonymy, and literature, *in* Paquin, P., and Buckle, D.J., eds., Contributions à la Connaissance des Araignées (Araneae) d'Amérique du Nord, Fabreries, Supplément 10, p. 89–191.

Cokendolpher, J.C., 2004, *Cicurina* spiders from caves in Bexar County, Texas: Texas Memorial Museum Speleological Monographs, v. 6, Studies on the cave and endogean fauna of North America, v. 4, p. 13–58.

Court, D.J., and Forster, R.R., 1988, Araneidae-Araneinae: The Spiders of New Zealand, v. 6, p. 68–124.

Crawford, R.L., 1988, An annotated checklist of the spiders of Washington: Burke Museum Contributions in Anthropology and Natural History, v. 5, p. 1–48.

Crosby, C.R., 1937, Studies in American spiders. The genus *Aigola* Chamberlin, *in* Proceedings of the Biological Society of Washington, v. 50, p. 35–42.

Danks, H.V., 1993, Patterns of diversity in the Canadian insect fauna, *in* Ball, G.E., and Danks, H.V., eds., Systematics and entomology: diversity, distribution, adaptation and application, Memoirs of the Entomological Society of Canada, v. 165, p. 51–74.

Danks, H.V., 1994, Regional diversity of insects in North America: American Entomologist, v. 41, p. 50–55.

Denis, J., 1949, Notes sur les Érigonides. XVI. Essai sur la détermination des femelles d'érigonides: Bulletin de la Société d'Histoire Naturelle de Toulouse, v. 83, p. 129–158.

Dondale, C.D., and Buckle, D.J., 2001, The genus *Maro* in North America (Araneae: Linyphiidae): Fabreries, v. 26, p. 9–15.

Dupérré, N., and Paquin, P., 2007, Description of five new spiders from Canada (Araneae, Linyphiidae): Zootaxa, v. 1632, p. 1–20.

Eberhard, W.G., 1986, Why are genitalia good species characters?, *in* Lubin, Y.D., Eberhard, W.G., and Robinson, B.C., eds., Proceedings of the Ninth International Congress of Arachnology, Panama, 1983, Washington, D.C., Smithsonian Institution Press, 333 p.

Emerton, J.H., 1882, New England spiders of the family Theridiidae: Transactions of the Connecticut Academy of Arts and Sciences, v. 6, p. 1–86 + pl. I–XXIV.

Emerton, J.H., 1915, Canadian spiders, II: Transactions of the Connecticut Academy of Arts and Sciences, v. 20, p. 147–156 + pl. II–III.

Eskov, K.Y., 1992, A restudy of the generic composition of the linyphiid spider fauna of the Far East (Araneida: Linyphiidae): Entomologica Scandinavia, v. 23, p. 153–168.

Gertsch, W.J., 1974, The spider family Leptonetidae in North America: Journal of Arachnology, v. 1, p. 145–203.

Gertsch, W.J., 1984, The spider family Nesticidae (Araneae) in North America, Central America, and the West Indies: Bulletin of the Texas Memorial Museum, v. 31, p. 1–91.

Gertsch, W.J., 1992, Distribution patterns and speciation in North American cave spiders with a list of the troglobites and revision of the cicurinas of the subgenus *Cicurella*: Texas Memorial Museum Speleological Monographs, v. 3, Studies on the endogean fauna of North America, Volume 2: Austin, Texas Memorial Museum, p. 75–122.

Hebert, P.D.N., Cywinska, A., Ball, S.L., and de Waard, J.R., 2003, Biological identifications through DNA barcodes, *in* Proceedings, Royal Society of London Series B, supplement, v. 270, p. 313–321.

Hedin, M.C., and Maddison, W.P., 2001, A combined molecular approach to phylogeny of the Jumping Spider subfamily Dendryphantinae (Araneae: Salticidae): Molecular Biology and Evolution, v. 18, p. 386–403.

Hormiga, G., 1994, Cladistics and the comparative morphology of linyphiid spiders and their relatives (Araneae, Araneoidea, Linyphiidae): Zoological Journal of the Linnean Society, v. 111, p. 1–71.

Hormiga, G., 2000, Higher level phylogenetics of erigonine spiders (Aranea, Linyphiidae, Erigoninae): Smithsonian Contributions to Zoology, v. 609, p. 1–160.

Hunt, C.B., 1974, Natural regions of the United States and Canada, Second edition, San Francisco, W.H. Freeman & Company, 725 p.

Juberthie, C., Delay, B., and Bouillon, M., 1980, Sur l'existence d'un milieu souterrain superficiel en zone non calcaire: Comptes rendus hebdomadaires des séances de l'Académie de Sciences de Paris (Série D), v. 290, p. 49–52.

Lewis, J.J., 2005, The subterranean fauna of the Tennessee Cumberland Plateau, Final Report, Nashville, The Nature Conservancy of Tennessee, 156 p.

Lewis, J.J., Burns, R., and Lewis, S., 2004, The subterranean fauna of the Hoosier National Forest, Bedford, Indiana, U.S. Department of Agriculture, Forest Service, 190 p.

Lewis, J.J., and Lewis, S., 2008a, The subterranean fauna of the Hoosier National Forest, Final Report, Bedford, Indiana, U.S. Department of Agriculture, Forest Service, 186 p.

Lewis, J.J., and Lewis, S., 2008b, The fauna of Sullivan Cave, Lawrence County, Indiana Final Report, Indianapolis, Indiana Department of Natural Resources, Division of Nature Preserves, 22 p.

Lewis, J.J., and Rafail, S., 2002, The subterranean fauna of the Big Oaks National Wildlife Refuge, U. S. Department of the Interior, Fish and Wildlife Service, Indiana Department of Natural Resources, Natural Heritage Program, 77 p.

Levi, H.W., 1971, The *diadematus* group of the orb-weaver genus *Araneus* north of Mexico (Araneae: Araneidae): Bulletin of the Museum of Comparative Zoology, v. 141, p. 131–179.

Longacre, C., 2000, Department of the Interior, Fish and Wildlife Service, 50 CFR part 17, RIN 1018-AF33, Endangered and threatened wildlife and plants, Final rule to list nine Bexar County, Texas Invertebrate species as endangered, Washington, D.C., Federal Register, v. 65(248), p. 81419–81433.

Maddison, D.R., and Maddison, W.P., 2003, MacClade 4, Release Version 4.07, Sunderland, MA, Sinauer Associates, Inc.

Matthews, J.V. jr., 1979, Tertiary and quaternary environments: historical background for an analysis of the Canadian insect fauna, *in* Danks, H.V., ed., Canada and its insect fauna, Memoirs of the Entomological Society of Canada, v. 108, p. 31–86.

Miller, J.A., 2005, A redescription of *Porrhomma cavernicola* Keyserling (Araneae, Linyphiidae) with notes on Appalachian troglobites: Journal of Arachnology, v. 33, p. 426–438.

Nice, C., Anthony, N., Gelembiuk, G., Ratermans, D., and French-Constant, R., 2005, The history and geography of diversification within the butterfly genus *Lycaeides* in North America: Molecular Ecology, v. 14, p. 1741–1754.

Nylander, J.A.A., 2004, MrModeltest v2., Evolutionary Biology Centre, Uppsala University.

Paquin, P., and Dupérré, N., 2009, A first step towards the revision of *Cicurina*: redescription of type specimens of 60 troglobitic species of the subgenus *Cicurella* (Araneae: Dictynidae), and a first visual assessment of their distribution: Zootaxa, v. 2002, p. 1–67.

Paquin, P., Dupérré, N., Cokendolpher, J.C., White, K., and Hedin, M., 2008, Fundamental importance of taxonomy in conservation biology: The case of the eyeless spider *Cicurina bandida* (Araneae: Dictynidae) of Central Texas, including new synonyms and the description of the male of the species: Invertebrate Systematics, v. 22, p. 139–149.

Paquin, P., and Hedin, M., 2004, The power and perils of 'molecular taxonomy': a case study of eyeless and endangered *Cicurina* (Araneae: Dictynidae) from Texas caves: Molecular Ecology, v. 13, p. 3239–3255.

Paquin, P., and Hedin, M., 2007, Genetic and morphological analysis of species limits in *Cicurina spiders* (Araneae, Dictynidae) from southern Travis and northern Hays Counties (Texas), with emphasis on *Cicurina cueva* Gertsch and relatives: Austin, Texas, Report to United States Fish and Wildlife Services, p. 1–40.

Paquin, P., LeSage, L., and Dupérré, N., 2001, First Canadian records of *Tenuiphantes cracens* and *Walckenaeria clavipalpis* (Araneae: Linyphiidae), plus thirteen new provincial records and a confirmation for Québec: Entomological News, v. 112, p. 271–277.

Parmesan, C., and Yohe, G., 2003, A globally coherent fingerprint of climate change impacts across natural systems: Nature, v. 421, p. 37–42.

Peck, S.B., 1973, A systematic revision and the evolutionary biology of the Ptomaphagus (*Adelops*) beetles of North America (Coleoptera; Leiodidae, Catopinae), with emphasis on cave-inhabiting species: Bulletin of the Museum of Comparative Zoology, v. 145, p. 29–162.

Peck, S.B., 1988, A review of the cave fauna of Canada, and the composition and ecology of the invertebrate fauna of caves and mines in Ontario: Canadian Journal of Zoology, v. 66, p. 1197–1213.

Peck, S.B., 1998, A summary of diversity and distribution of the obligate cave-inhabiting faunas of the United States and Canada: Bulletin of the National Speleological Society, v. 60, p. 18–26.

Peck, S.B., and Lewis, J.J., 1978, Zoogeography and evolution of the subterranean invertebrate faunas of Illinois and southeastern Missouri: The National Speleological Society Bulletin, v. 40, p. 39–63.

Pielou, E.C., 1991, After the Ice Age: The return of life to glaciated North America, Chicago, University of Chicago Press, 366 p.

Platnick, N.I., 2008, The World Spider Catalog, Version 8.5, American Museum of Natural History [accessed March 2008] http://research.amnh.org/entomology/saders/catalog

Posada, D., and Buckley, T.R., 2004, Model selection and model averaging in phylogenetics: Advantages of Akaike information criterion and Bayesian approaches over likelihood ratio tests: Systematic Biology, v. 53, p. 793–808.

Posada, D., and Crandall, K.A., 1998, MODELTEST: Testing the model of DNA substitution: Bioinformatics, v. 14, p. 817–818.

Prest, V.K., Grant, D.R., and Rampton, V.N., 1967, Glacial map of Canada: Geological Survey of Canada. Map 1253A: (Scale 1: 5 000 000).

Proszynski, J., 1968, Revision of the spider genus *Sitticus* Simon 1901 (Araneida, Salticidae), I. The *terebratus* group: Annales Zoologici (Warszawa), v. 26, p. 391–407.

Reeves, W.K., 2000, Invertebrate cavernicoles of the Great Smoky Mountains National Park, USA: Journal of the Elisha Mitchell Scientific Society, v. 116, p. 334–343.

Roberts, M.J., 1987, The Spiders of Great Britain and Ireland, Volume II, Description of Species - Linyphiidae; Check list of the British Spiders, Colchester, England, Harley Books Publishers, 204 p.

Ronquist, F., and Huelsenbeck, J.P., 2003, MRBAYES 3: Bayesian phylogenetic inference under mixed models: Bioinformatics, v. 19, p. 1572–1574.

Ruzicka, V., and Klimes, L., 2005, Spider (Araneae) communities of scree slopes in the Czech Republic: Journal of Arachnology, v. 33, p. 280–189.

Saaristo, M.I., 1972, Redelimitation of the genus *Oreonetides* Strand, 1901 (Araneae, Linyphiidae) based on an analysis of the genital organs: Annales Zoologici Fennici, v. 9, p. 69–74.

Saaristo, M.I., and Koponen, S., 1998, A review of northern Canadian spiders of the genus *Agyneta* (Araneae: Linyphiidae), with descriptions of two new species: Canadian Journal of Zoology, v. 76, p. 566–583.

Schikora, H.-B., 1995, Intraspecific variation in taxonomic characters, and notes on distribution and habitats of *Meioneta mossica* Schikora and *M. saxatilis* (Blackwall), two closely related spiders from northland and central Europe (Araneae: Linyphiidae): Bulletin of the British Arachnological Society, v. 10, p. 65–74.

Schwert, D.P., 1992, Faunal transitions in response to an ice age: the late Wisconsinan record of Coleoptera in the north-central United States: The Coleopterists Bulletin, v. 46, p. 68–94.

Scudder, G.G.E., 1979, Present patterns in the fauna and flora of Canada, *in* Danks, H.V., ed., Canada and its insect fauna, Memoirs of the Entomological Society of Canada, v. 108, p. 87–179.

Skelley, P.E., and Kovarik, P.W., 2001, Insect surveys in the southeast: investigating a relictual entomofauna: Florida Entomologist, v. 84, p. 552–555.

Swofford, D.L., 2002, PAUP* v. 4.0b10 PPC: Phylogenetic analysis using Parsimony, Sunderland, MA, Sinauer Associates.

van Helsdingen, P.J., 1981, The Nearctic species of *Oreonetides* (Araneae, Linyphiidae): Bulletin of the American Museum of Natural History, v. 170, p. 229–241.

Vink, C.J., Thomas, S.M., Paquin, P., Hayashi, C.Y., and Hedin, M., 2005, The effect of preservatives and temperatures on arachnid DNA: Invertebrate Systematics, v. 19, p. 99–104.

Vink, C.J., Sirvid, P.J., Malumbres-Olarte, J., Griffiths, J.M., Paquin, P., and Paterson, A.M., 2008, Species status and conservation issues of New Zealand's endemic *Latrodectus* spider species (Theridiidae: Araneae): Invertebrate Systematics, v. 22, p. 589–604.

Yagimuma, T., 1972, Spiders from tuff caves in Yamagata Prefecture, Japan: Faculty of Letters Review, Otemon Gakuin University, v. 6, p. 81–94.

J. De Waele, G.A. Brook, and A. Oertel – Monk seal (*Monachus monachus*) bones in Bel Torrente Cave (central-east Sardinia) and their paleogeographical significance. *Journal of Cave and Karst Studies,* v. 71, no. 1, p. 16–23.

# MONK SEAL (*MONACHUS MONACHUS*) BONES IN BEL TORRENTE CAVE (CENTRAL-EAST SARDINIA) AND THEIR PALEOGEOGRAPHICAL SIGNIFICANCE

Jo De Waele[1], George A. Brook[2], and Anke Oertel[3]

**Abstract:** Fragments of monk seal bones (*Monachus monachus*) discovered 7–12 m below water level in Bel Torrente Cave (central-east Sardinia) in 2004 have been AMS radiocarbon dated. The bones, probably of different individuals, have calibrated ages ranging from 5000–6500 calendar years B.P. and allow reconstruction of the paleogeography of the cave and the surrounding area during this time period. Monk seals living in large numbers along the Sardinian coast used the cave for shelter and to give birth to their pups. The lower sea level of the mid-Holocene, combined with cave morphology, allowed them to reach far into the main tunnel of the cave. The large number of bones found of approximately the same age seems to indicate that the monk seals used caves either to shelter from storm waves or to escape from natural predators during periods when human disturbance of the coast was minor. This could suggest the monk seals had other predators they were also trying to avoid.

## Introduction

During the summer of 2004, scuba divers exploring Bel Torrente Cave, one of the most interesting submarine karst resurgences in the Gulf of Orosei, central-east Sardinia, discovered several skeletons of monk seals (*Monachus monachus*) in an underwater passage. The skeletons were 750 m from the cave entrance and 8–12 m below the water surface (Sgualdini, 2004). A geomorphic study of the cave and AMS radiocarbon dating of some monk seal finger and toe bones were undertaken in an attempt to reconstruct the environmental conditions at the time this remarkable concentration of seal bones accumulated in what are now submerged passages.

## Monk Seal Biogeography

Recent genetic studies suggest that monk seals (genus *Monachus*) originated in the Tethys region during the Tortonian age (ca 12 Ma), and since have occupied the temperate waters of the Mediterranean (Mediterranean monk seal, *Monachus monachus*). They then spread from east to west to the Caribbean first (Caribbean monk seal, *Monachus tropicalis*, now extinct), and then to the Pacific Ocean (Hawaiian monk seal, *Monachus schauinslandi*, endemic to the Hawaiian Islands) (Fyler et al., 2005).

In the recent past, Mediterranean monk seals were present along coasts from the Black Sea through the entire Mediterranean to the Atlantic shores of Morocco and reaching as far south as Gambia and westwards to the Azores (Johnson et al., 2008). Monk seals were often mentioned during the Greek and Roman Periods as occurring along rocky shorelines and also on beaches. Since ancient times, the animal was hunted for its skin, meat, fat, and oil, but it was only in Roman times that the seal population was seriously depleted. There was a partial recovery in numbers after the fall of the Roman Empire, but monk seals were again endangered during the Middle Ages where they sought shelter along inaccessible coasts and often in sea caves, some only with underwater entrances. The inaccessible coasts of Sardinia must have been ideal places for important populations of monk seals to settle (Bareham and Furreddu, 1975). The vast territory formerly occupied by monk seals was rapidly limited by the increasing use and occupation of coastal areas by humans. Consequently, the animal has almost completely disappeared from France, Italy, Spain, Egypt, Israel, and Lebanon. Although there are still sporadic sightings of monk seals along some parts of these coasts, there do not appear to be permanent populations (Johnson et al., 2008).

Today, the major monk seal populations are found along the Cabo Blanco peninsula (Western Sahara-Mauritania) (Samaranch and Gonzalèz, 2000; Aguilar et al., 2007; Borrell et al., 2007), the Desertas Islands of Madeira archipelago (Karamandlidis et al., 2004; Pires et al., 2007), the Mediterranean coast between Morocco and Algeria (Borrell et al., 1997), the Cilician basin in Turkey (Gucu et al., 2004), and in Cyprus and the Greek Islands (Dendrinos et al., 2007a; 2007b). Monk seals are still occasionally sighted along the Sardinian coast, but the last permanent residents date back to at least 30 years ago. Before World War II monk seals were regularly hunted by local fishermen, but during the 1950s there were still tens of seals along the coast (Altara, 1995; Johnson, 1998). This number continued to decrease due to hunting, but also

[1] Dipartimento di Scienze della Terra e Geologico-Ambientali, University of Bologna, Via Zamboni 67 – 40127 Bologna, ITALY. E-mail: jo.dewaele@unibo.it
[2] Department of Geography, University of Georgia, Athens GA 30602, U.S.A. E-mail: gabrook@uga.edu
[3] Erentrudisstr. 19/11, A 5020, Salzburg, AUSTRIA. E-mail: anke.oertel@gmx.at

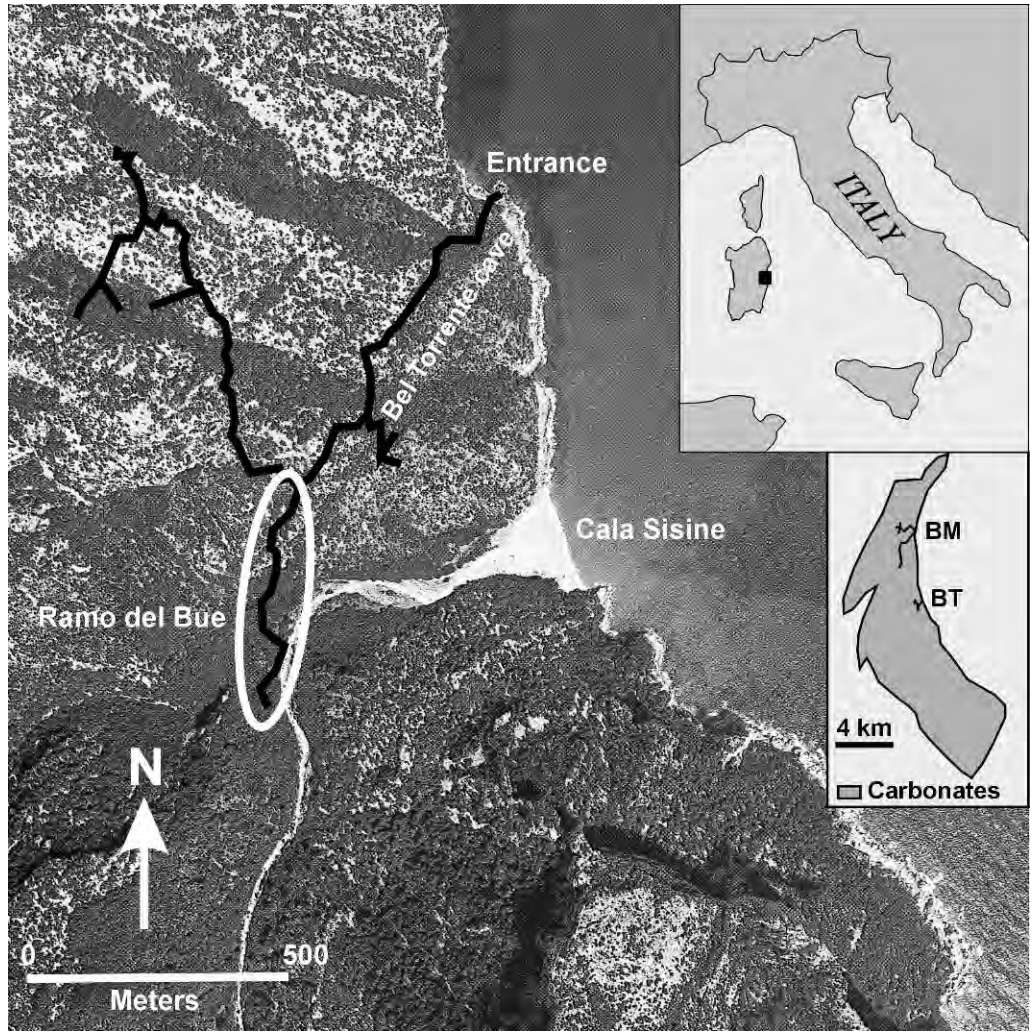


**Figure 1. Aerial photograph of the Bel Torrente Cave area. Cave passages are shown in black; the ellipse marks the Ramo del Bue area.**

because of increased tourism, with the famous Bue Marino Cave opening for visits in 1960 (Arisci et al., 2000). Tourism is one of the most important disturbances in karst areas in the central-eastern part of Sardinia and monk seals have been among the first to suffer (De Waele, 2008). The last monk seal reported in the Bue Marino Cave was killed by a fisherman in 1970, and about ten individuals were seen at the Grotta del Fico, a few kilometers south of Bue Marino, in the early 1970s (Bareham and Furreddu, 1975).

## Bel Torrente Cave

### Exploration

The Bel Torrente Cave is located 0.5 km north of Cala Sisine (Fig. 1). The cave was discovered and explored by Jochen Hasenmayer in the 1970s and the first 500 m was surveyed in the 1990s (Fancello et al., 2000; Morlock and Mahler, 1995). Cave diving expeditions in 2003, 2004, and 2006 explored and mapped the cave to more than 3 km. The side branch with the largest number of monk seal bones was discovered in the summer by two cave divers (Luca Sgualdini and Enrico Seddone) working for the diving club at Santa Maria Navarrese (Sgualdini, 2004).

The cave was surveyed with a wrist-held compass. Distances were determined using tags on the safety line spaced at 5-meter-intervals. Depth was measured with both analog- and digital-depth gauges. At survey points, distances to the cave floor and roof were estimated with an accuracy of about 1 m. Overall precision of the cave plan and profile is around 1%.

### Morphology

Bel Torrente Cave is characterised by a 5–20 m wide tunnel with an average height of 5 m and a depth of 12 m (Fig. 2). The cave extends to the southwest for the first 550 m and there are several air-filled passages separated by short sumps. Then the passage has a 22-m-deep sump (Sifone Centrale or Central Sump) that allows access to

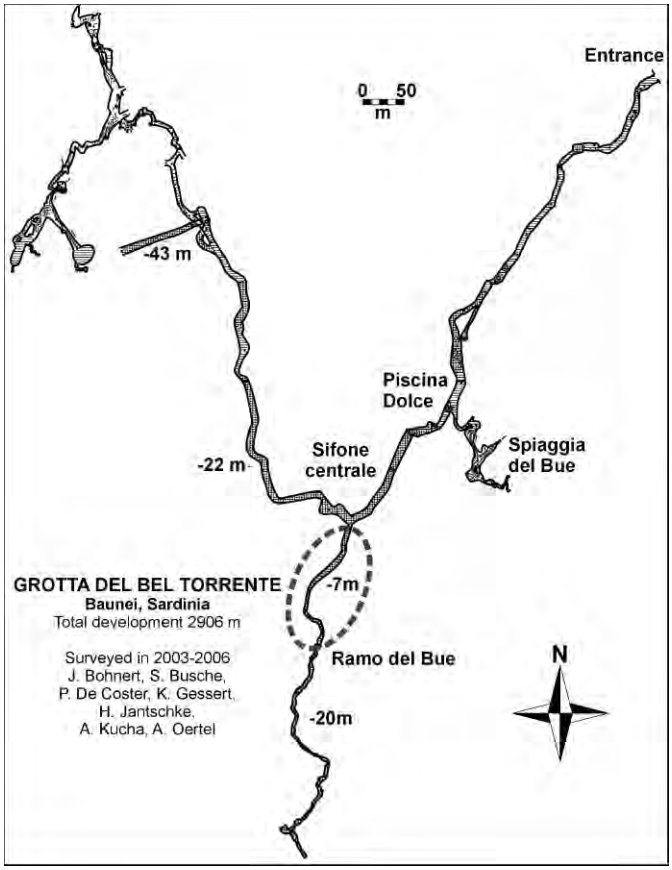


**Figure 2. Plan of Bel Torrente Cave. The ellipse defines the area from which monk seal bones were obtained.**

another air-filled chamber where a deep and only partially explored sump starts and a by-pass gives access to a series of air-filled galleries. Before the Sifone Centrale, there are two side passages to the left. The first side passage leads to the Spiaggia del Bue (ox beach), where bones of monk seal have been found on the sandy floor at 3–4 m depth and other remains of smaller vertebrates in several places on the rocky floor approximately 1 m above sea level. These bones have not been sampled and dated.

The second side passage, the Ramo del Bue (ox gallery) (Oertel and Patzner, 2007; Sgualdini, 2004), is entirely underwater and departs from the *Sifone Centrale* at 10 m below sea level. A 3-m-wide tunnel leads to the south and is 7–22-m-deep with the shallower section (−7 m measured at bottom of the gallery) located 50–100 m from the main tunnel and is characterized by a large flowstone entering from above (Fig. 3).

The floors of the main tunnel and the side passages are covered with sands and gravels containing both limestone and granite fragments with few fine sediments so that even after divers have passed through them water in the passages remains relatively clear. The lack of fine sediments is related to the regular flushing of the cave by freshwater floods. During normal conditions, the discharge of freshwater through the cave is only tens of liters per second so that the water current is hardly noticeable. Near the entrance, and up to 200–400 m inside the cave (depending on sea and climate conditions), there is a halocline at 1–2 m of water depth (Oertel and Patzner, 2007). Freshwater forms a ''surface blanket'' over brackish and sea water. After heavy rains, the main tunnel is flooded entirely by fresh water and flow velocities are up to 2 m $s^{-1}$ (Morlock and Mahler, 1995). These floods transport clastic deposits (including fine sediments) from the cave and erode/corrode the walls of the tunnel. As a result, the floor, ceiling, and walls display typical phreatic erosion and corrosion features. In several places, speleothems (flowstones, stalagmites, and stalactites) are present above water and also several meters below present sea level. These have been intensively corroded and eroded by flood waters below sea level and also up to at least one meter above sea level.

The morphology of the Bel Torrente Cave generally resembles that of the nearby Bue Marino Cave, except that the passages of Bel Torrente are mainly under water (De Waele and Forti, 2003). This difference may be due to neotectonic activity that resulted in the southwards tilting of the Tyrrhenian tidal notch, dated to 125,000 years B.P. and ranging in height between 10.5 m a.s.l. at Cala Gonone and 7.7 m a.s.l. at Santa Maria Navarrese (Antonioli et al., 1999). This slight tilting could be responsible for the altitude difference between the Bel Torrente and Bue Marino caves (De Waele, 2004; Forti and Rossi, 1991). If true, the Bel Torrente Cave system predates the tilting, and there is evidence suggesting that the main period of cave formation was more than 3 Ma. One convincing piece of evidence is Plio-Pleistocene basalts, dated between 2–3 Ma (Savelli et al., 1979) that fill karst conduits of the Bue Marino main gallery, indicating a karst phase older than this volcanic activity, which is thought to be of Mio-Pliocene age (De Waele, 2004; Mahler, 1979).

During the Quaternary, changes in sea level resulted in periodic drying and flooding of caves along the coast. The most recent drying episode was 22–18 ka B.P. when sea level dropped approximately 125 meters. From recent studies, especially on cave stalagmites, postglacial sea level had already risen to 6–10 m below present by about 6.5 ky B.P. (Antonioli et al., 2004), thus leaving most of the Bel Torrente galleries above water. As a result, 5–6 ka Bel Torrente may have resembled the present Bue Marino Cave, with an underground river flowing out of the mountains and easily accessible for at least 550 meters. Sea level continued to rise in the mid to late Holocene reaching 0.5–1 m below sea level 2 ky B.P. during Roman times.

## THE SEAL CEMETERY

Several monk seal skeletons were found in the shallow part of the Ramo del Bue passage, 50–100 m from the main gallery (720–790 m from the entrance). Bones and skulls of at least five monk seals have been found at depths of 8–


**Figure 3. Five skulls of monk seal discovered in the Ramo del Bue: A. Skull on a sandy floor in the center of the passage (cave diver for scale); B. Skull and bones with a black coating deposited in a fissure on the tunnel walls; C. Jaw with black coating and some spinal bones on a sandy floor of a side niche; D. Small blackened jaw lying on bare rock; other bones can be seen in the back; E. Jaw and bones with black coating on the bare rock surface in a lateral alcove.**

12 m, resting on the sandy floor or fallen in fissures or holes along the walls (Figs. 3 and 4). The cave divers who explored the passage report seeing the water surface in this area so that there could be an air-filled chamber above the flooded passage. Although only five skulls have been counted, more could be buried beneath sand, trapped in niches along the walls, or in a possible air-filled chamber above.

## Seal Bone Ages

### Sampling

Four samples of small finger and/or toe bones were collected from skeletal material 20–70 m from the entrance of the Ramo del Bue branch passage (720–790 m from cave entrance), at depths of 7.6–12 m (Table 1 and Fig. 4).

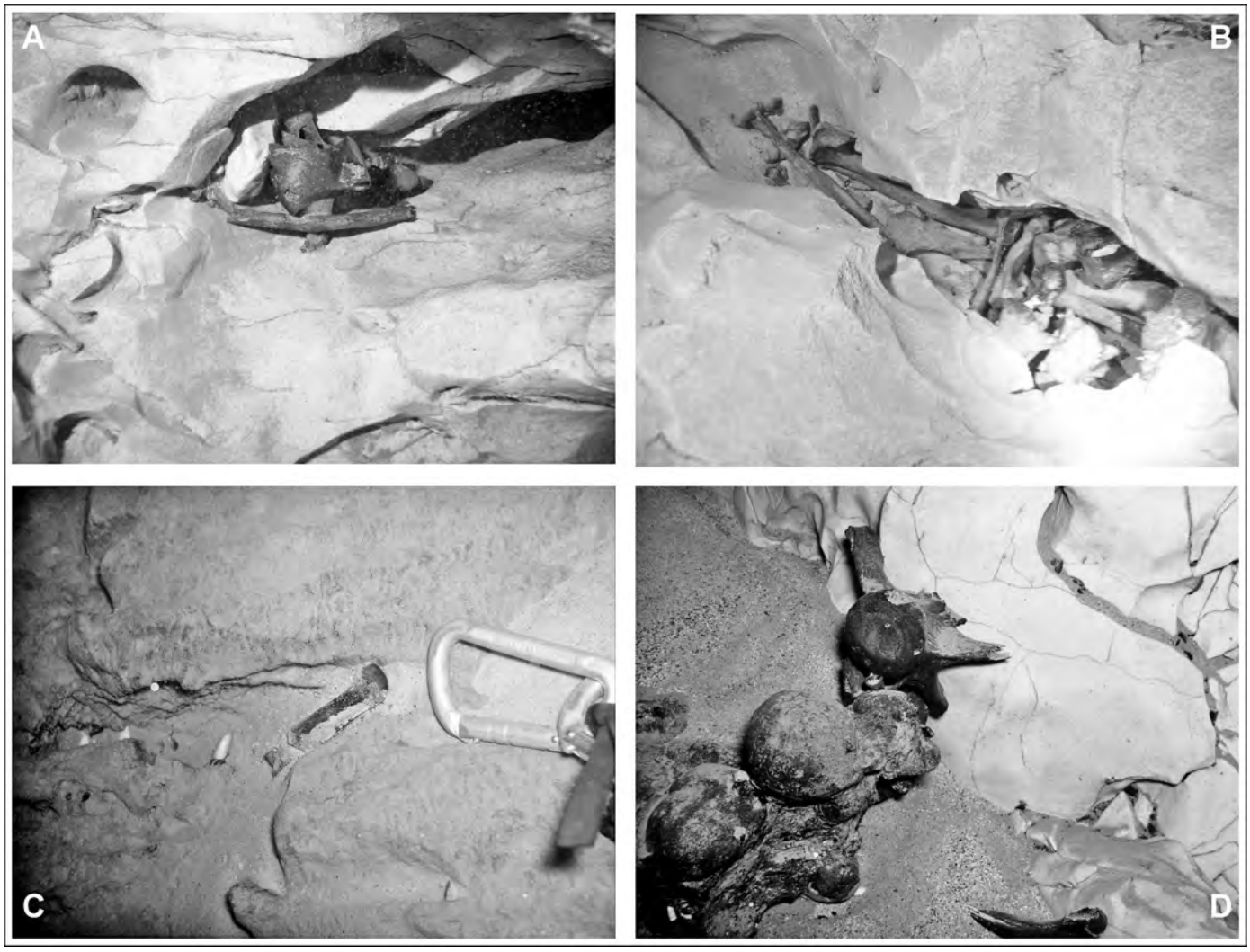


**Figure 4. Monk seal bones in the Ramo del Bue: (A) Rib and vertebra on bare rock on the side of the passage; (B) Deposit of long and short bones in a lateral fissure; (C) Small bone, probably toe, in a sandy fissure; (D) Vertebra and other bones in a lateral alcove.**

Smaller bones were selected for study as these were large enough to contain enough bone collagen for dating, which allowed leaving the skulls and larger bones to remain intact. When collected, the fragments were labelled and put in plastic bags together with the water. All of the bone fragments had a dark brown patina, and although composed of denser bone material, were relatively fragile. In the laboratory, samples were left to dry for several weeks and often lost consistency.

## RADIOCARBON DATING TECHNIQUES

To determine the ages of the monk seal bones, bone apatite (bioapatite) and bone collagen were dated. The bones were cleaned by abrasion and washed using an ultrasonic bath. The crushed bone was treated with diluted 1 N acetic acid to remove surface-absorbed and secondary carbonates. Periodic evacuation ensured that evolved carbon dioxide was removed from the interior of the sample fragments, and that fresh acid was allowed to reach even the interior micro-surfaces. The chemically cleaned sample was then reacted under vacuum with 1 N HCl to dissolve the bone mineral and release carbon dioxide from bioapatite.

The crushed bone was then treated with 1 N HCl at 4 °C for 24 hours. The residue was filtered, rinsed with deionized water, and under slightly acid conditions (pH = 3) heated at 80 °C for 6 hours to dissolve collagen and leave humic substances in the precipitate. The collagen solution was then filtered to isolate pure collagen and dried out. The purified collagen was combusted at 575 °C in an evacuated, sealed Pyrex ampoule in the presence of CuO.

The resulting carbon dioxide was cryogenically purified from the other combustion products and catalytically converted to graphite using the method of Vogel et al. (1984). Graphite $C^{14}/C^{13}$ ratios were measured using the 0.5 MeV accelerator mass spectrometer at the Center for

**Table 1. Location and description of the bone samples.**

| Sample | Distance from Entrance (m) | Depth (m) | Description |
|---|---|---|---|
| B | 770 | 7.6 | Bigger bone (10 cm) found in sand in the passage |
| C | 760 | 9.5 | Small bone (finger?) found on right side of passage in small sand filled cleft |
| D | 720 | 12 | Small bone (finger?) found on the sand in middle of passage |
| F | 760 | 9 | Small bone found in middle of passage on the sand between rocks |

Applied Isotope Studies at the University of Georgia. The sample ratios were compared to the ratio measured from the Oxalic Acid I standard (NBS SRM 4990). Sample $C^{13}/C^{12}$ ratios were measured separately using a stable isotope ratio mass spectrometer and expressed as $\delta^{13}C$ with respect to PDB, with an error of less than 0.1‰. The $\delta^{13}C$ of the bone collagen varied between −0.4 and −2.4‰ ± 0.1‰ relative to the PDB standard, while bone apatite varied between −7.2‰ and −7.5‰ ± 0.1‰. These values were subsequently used to calculate corrections for isotope fractionation.

The quoted uncalibrated dates are in radiocarbon years before 1950 (years BP), using the $^{14}C$ half-life of 5568 years (Table 2). The error is quoted as one standard deviation and reflects both statistical and experimental errors. The dates have been corrected for isotopic fractionation assuming that the samples originally had a $\delta^{13}C$ composition of −25‰. The ages shown in Table 2 were calibrated using OxCal version 3.9 (Ramsey, 1995, 2001) and the calibration curve of Stuiver et al. (1998).

## Results

Samples B and F were dated using both collagen and bio-apatite for comparison. In both samples the bio-apatite ages are several hundred years older than the collagen ages presumably because of the incorporation of old, dead carbon during accumulation or because of later contamination. Because the cave is a spring, discharging ground water contains significant quantities of old carbon that could explain this observation. The collagen ages are considered more reliable. Collagen samples C and F are statistically of the same age (6447 ± 106 cal yr B.P. and 6698 ± 150 cal yr B.P.) as are samples B and D (5124 ± 211 cal yr B.P. and 4896 ± 194 cal yr B.P.). This means that the samples recovered could have come from two individuals, one dying around 6500 cal yr B.P. and the other around 5000 cal yr B.P., or from several different seals that died at these times.

## Discussion

Based on the ages of the bones, and assuming that the seals could not have climbed to ledges in the cave much above water level, sea level was at most 10 m lower than present level by ca. 6.5 ka. In fact, sea level records for the Tyrrhenian show altitudes between 6 and 10 m below present at this time (Antonioli et al., 2004). At Alghero (N-Sardinia), Neolithic burials dated to around 7 ka B.P. have been found in the final sump of Grotta Verde 8–10 m below present sea level (Antonioli et al., 1994).

The longitudinal profile of the Bel Torrente Cave (precision ~1 m) shows that when sea level was 6 m lower than today, the monk seals would probably have been able to enter the first 500 meters of the cave (Fig. 5). This would have given them access to Spiaggia del Bue. Beyond this, the deep central sump reaching 22 m depth and completely submerged 6 ka may have been a significant obstacle to the seals. However, the Ramo del Bue gallery, with an initial section of limited depth and then two sumps around 15 m deep, may have been partly accessible. In fact, 6 ka Spiaggia del Bue and the first shallow section of Ramo del Bue, 500 m and 750–800 m from the entrance, respectively, may have been special resting places for monk seals and females giving birth on the sandy beaches alongside the underground river. Supporting this conclusion are observations of similar behavior by monk seals

**Table 2. AMS radiocarbon ages on seal bone collagen and bioapatite.**

| Sample ID | UGA CAIS ID[a] | Libby Age with Background Subtracted | $\delta^{13}C$ | Libby Age with $\delta^{13}C$ Correction | Calibrated Ages in cal. yr BC (95.4%) | Calibrated Age (cal yr before AD 2000) |
|---|---|---|---|---|---|---|
| B | R01879-B | 4957±50 | −7.53 | 5098±50 | 3989–3774 | 5881±107 |
| B | R01879-C | 4308±54 | −11.12 | 4421±54 | 3335–2913 | 5124±211 |
| C | R01880-C | 5501±57 | −11.19 | 5613±57 | 4553–4341 | 6447±106 |
| D | R01881-C | 4192±53 | −12.39 | 4293±53 | 3090–2702 | 4896±194 |
| F | R01882-B | 6798±55 | −7.22 | 6942±55 | 5978–5724 | 7851±127 |
| F | R01882-C | 5739±59 | −10.44 | 5857±59 | 4848–4548 | 6698±150 |

[a] B=bioapatite, C=collagen.

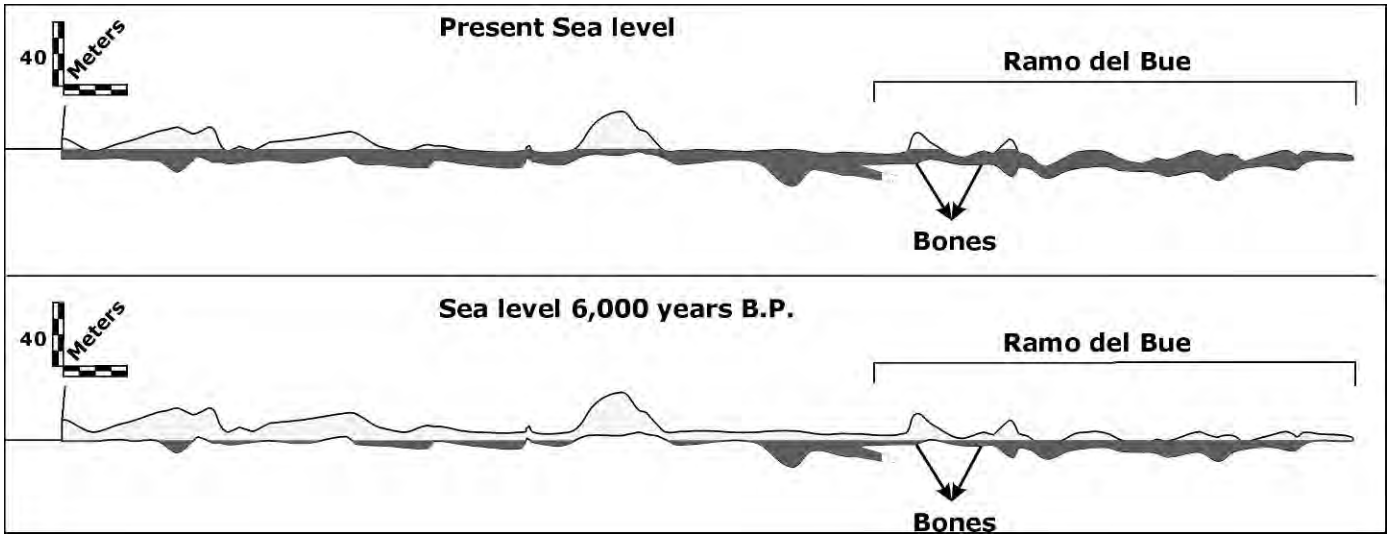


**Figure 5. Longitudinal profile of Bel Torrente Cave showing accessibility today and 6 ky B.P. when sea level was much lower.**

that used Bue Marino Cave. According to Johnson, these seals sheltered or gave birth almost 1 km from the entrance to this cave (Johnson, 1998).

## CONCLUSIONS

It has been suggested that monk seals in the Mediterranean sought out caves as refuges from sea waves during heavy storms, human interference, and killing. Our analysis of seal bones from Bel Torrente Cave suggest that even 6.5 ka, when human pressures were relatively low by modern standards, monk seals were using caves as refuges. The elevation of the bones indicates that by this time sea level was already within 10 m of the present position. The morphology of Bel Torrente Cave confirms that in the mid Holocene it was a coastal cave with an underground river, and monk seals would have been able to penetrate about 800 m without encountering severe difficulties such as deep sumps. Our data reveal that monk seals, even in periods of low human disturbance, had the habit of using coastal caves, penetrating as far as 800 m inside. This suggests that 6.5 ka humans were not the only predators of monk seals.

## ACKNOWLEDGEMENTS

The authors would like to thank the many cavers and cave divers who explored and surveyed the Bel Torrente system and documented the monk seal cemetery, especially Jürgen Bohnert, Karsten Gessert, Herbert Jantschke, Salvatore Busche, Peter de Coster, Andreas Kücha, Enrico Seddone, and Luca Sgualdini. Radiocarbon dating was performed at the Center for Applied Isotope Studies, University of Georgia. We additionally thank Jürgen Bohnert, Karsten Gessert, Anke Oertel, and Enrico Seddone for the photographs shown in Figures 3 and 4. Thanks also to the Centro Nautica Sub Navarrese for technical support during exploration of the cave. Finally two anonymous reviewers are thanked for their valuable comments.

## REFERENCES

Aguilar, A., Cappozzo, L.H., Gazo, M., Pastor, T., Forcada, J., and Grau, E., 2007, Lactation and mother-pup behaviour in the Mediterranean monk seal *Monachus monachus*: an unusual pattern for a phocid: Journal of the Marine Biological Association of the United Kingdom, v. 87, p. 93–99.

Altara, E., 1995, La Foca Monaca: Sottoterra, v. 101, p. 43–54.

Antonioli, F., Bard, E., Potter, E.K., Silenzi, S., and Improta, S., 2004, 215-ka history of sea-level oscillations from marine and continental layers in Argentarola cave speleothems (Italy): Global and Planetary Change, v. 43, no. 1–2, p. 57–78.

Antonioli, F., Ferranti, L., and Lo Schiavo, F., 1994, The submerged neolithic burials of the grotta Verde at Capo Caccia (Sardinia, Italy): Implication for the Holocene sea-level rise: Memorie descrittive della Carta Geologica d'Italia, v. 52, p. 329–336.

Antonioli, F., Silenzi, S., Vittori, E., and Villani, C., 1999, Sea level changes and tectonic mobility: precise measurements in three coastlines of Italy considered stable during the last 125 ky: Physics and Chemistry of the Earth (A), v. 24, no. 4, p. 337–342.

Arisci, A., De Waele, J., and Di Gregorio, F., 2000, Natural and scientific valence of the Gulf of Orosei Coast (central-east Sardinia) and its carrying capacity with particular regard to the pocket-beaches: Periodicum Biologorum, v. 102, no. suppl. 1, p. 595–603.

Bareham, J.R., and Furreddu, A., 1975, Observations on the use of grottos by Mediterranean monk seals (*Monachus monachus*): Journal of Zoology, v. 175, p. 291–298.

Borrell, A., Aguilar, A., and Pastor, T., 1997, Organochlorine pollutant levels in Mediterranean monk seals from the Western Mediterranean and the Sahara coast: Marine Pollution Bulletin, v. 34, no. 7, p. 505–510.

Borrell, A., Cantos, G., Aguilar, A., Androukaki, E., and Dendrinos, P., 2007, Concentrations and patterns of organochlorine pesticides and PCBs in Mediterranean monk seals (*Monachus monachus*) from Western Sahara and Greece: Science of the Total Environment, v. 381, p. 316–325.

De Waele, J., 2004, Geomorphologic evolution of a coastal karst: the Gulf of Orosei (Central-East Sardinia, Italy): Acta Carsologica, v. 33, no. 2, p. 37–54.

De Waele, J., 2008, Evaluating disturbance on Mediterranean karst areas: the example of Sardinia (Italy): Environmental Geology, (in print).

De Waele, J., and Forti, P., 2003, Estuari sotterranei, *in* Cicogna, F., Nike Bianchi, C., Ferrari, G., and Forti, P., eds., Grotte Marine: cinquant'anni di ricerca in Italia: Rapallo, Ministero per la Difesa dell'Ambiente, p. 91–104.

Dendrinos, P., Karamandlidis, A.A., Androukaki, E., and McConnell, B.J., 2007a, Diving development and behavior of a rehabilitated Mediterranean monk seal (*Monachus monachus*): Marine Mammal Science, v. 23, no. 2, p. 387–397.

Dendrinos, P., Tounta, E., Karamandlidis, A.A., Legakis, A., and Kolomatas, S., 2007b, A video surveillance system for monitoring the endangered Mediterranean monk seal (*Monachus monachus*): Aquatic Mammals, v. 33, no. 2, p. 179–184.

Fancello, L., Fileccia, A., and Mazzoli, M., 2000, La Grotta del Bel Torrente: Speleologia, v. 43, p. 67–69.

Forti, P., and Rossi, G., 1991, Idrogeologia ed evoluzione carsica della Codula di Luna (Sardegna): Atti e Memorie della Commissione "E. Boegan", v. 30, p. 53–79.

Fyler, C.A., Reeder, T.W., Berta, A., Antonelis, G., Aguilar, A., and Androukaki, E., 2005, Historical biogeography and phylogeny of monachine seals (Pinnipedia: Phocidae) based on mitochondrial and nuclear DNA data: Journal of Biogeography, v. 32, p. 1267–1279.

Gucu, A.C., Gucu, G., and Orek, H., 2004, Habitat use and preliminary demographic evaluation of the critically endangered Mediterranean monk seal (*Monachus monachus*) in the Cilician Basin (Eastern Mediterranean): Biological Conservation, v. 116, p. 417–431.

Johnson, W.M., 1998, Monk seal myths in Sardinia: The Monachus Guardian, v. 1, no. 1, p. 1–8.

Johnson, W.M., Karamandlidis, A.A., Dendrinos, P., Fèrnandez de Larrinoa, P., Gazo, M., Gonzaléz, L.M., Guclusoy, H., Pires, R., and Schnellmann, M., 2008, Mediterranean Monk Seal: www.monachus-guardian.org.

Karamandlidis, A.A., Pires, R., Carina Silva, N., and Costa Neves, H., 2004, The availability of resting and pupping habitat for the critically endangered Mediterranean monk seal *Monachus monachus* in the archipelago of Madeira: Oryx, v. 38, no. 2, p. 180–185.

Mahler, A., 1979, Verkarstung der Karbonatgebiete am Golfo di Orosei (Sardinien): Geologischer Palaeontologischer Mitteilungen Innsbruck, v. 7, no. 8–9, p. 1–49.

Morlock, W., and Mahler, A., 1995, La Grotta del Bel Torrente: la più importante risorgenza carsica del complesso calcareo del Golfo di Orosei: Sardegna Speleologica, v. 8, p. 35–36.

Oertel, A., and Patzner, R.A., 2007, The biology and ecology of a submarine cave: the Grotta del Bel Torrente (Central-East Sardegna, Italy): Marine Ecology, v. 28, no. suppl. 1, p. 60–65.

Pires, R., Costa Neves, H., and Karamandlidis, A.A., 2007, Activity patterns of the Mediterranean Monk Seal (*Monachus monachus*) in the Archipelago of Madeira: Aquatic Mammals, v. 33, no. 3, p. 327–336.

Ramsey, C.B., 1995, Radiocarbon calibration and analysis of stratigraphy: the OxCal Program: Radiocarbon, v. 37, no. 2, p. 425–430.

Ramsey, C.B., 2001, Development of the radiocarbon program OxCal: Radiocarbon, v. 43, no. 2A, p. 355–363.

Samaranch, R., and Gonzalèz, L.M., 2000, Changes in morphology with age in Mediterranean monk seals (*Monachus monachus*): Marine Mammal Science, v. 16, no. 1, p. 141–157.

Savelli, C., Beccaluva, L., Deriu, M., Macciotta, G., and Maccioni, L., 1979, K/ Ar geochronology and evolution of the Tertiary "calc-alkalic" volcanism of Sardinia (Italy): Journal of Volcanology and Geothermal Research, v. 5, no. 3–4, p. 257–269.

Sgualdini, L., 2004, Il cimitero delle foche: Anthèo, review of the Gruppo Speleo-Archeologico Giovanni Spano Cagliari, v. 8, p. 20–25.

Stuiver, M., Reimer, P.J., and Brazuinas, T.F., 1998, High-precision radiocarbon age calibration for terrestrial and marine samples: Radiocarbon, v. 40, no. 3, p. 1127–1151.

Vogel, J.S., Southon, J.R., Nelson, D.E., and Brown, T.A., 1984, Performance of catalytically condensed carbon for use in accelerator mass spectrometry: Nuclear Instruments and Methods in Physics Research, v. B5, p. 289–293.

A. Espino del Castillo, G. Castaño-Meneses, M.J. Dávila-Montes, M. Miranda-Anaya, J.B. Morales-Malacara, and R. Paredes-León – Seasonal distribution and circadian activity in the troglophile long-footed robber frog, *Eleutherodactylus longipes* (Anura: Brachycephalidae) at Los Riscos Cave, Querétaro, Mexico: Field and laboratory studies. *Journal of Cave and Karst Studies,* v. 71, no. 1, p. 24–31.

# SEASONAL DISTRIBUTION AND CIRCADIAN ACTIVITY IN THE TROGLOPHILE LONG-FOOTED ROBBER FROG, *ELEUTHERODACTYLUS LONGIPES* (ANURA: BRACHYCEPHALIDAE) AT LOS RISCOS CAVE, QUERÉTARO, MEXICO: FIELD AND LABORATORY STUDIES

Adriana Espino del Castillo[1], Gabriela Castaño-Meneses[2,4], Mayra J. Dávila-Montes[1,3], Manuel Miranda-Anaya[3], Juan B. Morales-Malacara[1,4,6], and Ricardo Paredes-León[5]

**Abstract:** Los Riscos Cave belongs to the El Abra limestone and its geographical location is in the Sierra Gorda in the State of Querétaro, Mexico. The cave has a high faunal diversity that includes arthropods and some vertebrates, such as vampire bats and anurans, and includes the robber frog *Eleutherodactylus longipes* (Baird, 1859). The abundance of the robber frog changes non-randomly between dry and rainy seasons and is related to the search for humid conditions inside the cave. In addition, the robber frog was located in areas where some scattered light may influence its dispersion inside the cave; and therefore, its activity. Frogs displayed spontaneous circadian rhythms of locomotor activity from the first days of the experimental observation in constant darkness. The average period of circadian rhythms was 24.85 ± 0.93 h indicating, in isolated conditions, a diurnal activity. When exposed to artificial light-dark cycles, the animals lacked daily activity rhythms, and ultradian activity was observed. The preference for high humidity and low illumination in the cave and a partial endogenous circadian rhythmicity confirm the troglophilic affinity of the robber frog to cave environments.

## Introduction

Caves represent windows to the lithosphere where different habitats are characterized by partial or total darkness, nearly constant temperature, often high levels of humidity, and a low flow of nutrients. Nevertheless, a variety of organisms have long colonized these subterranean environments. There are still constant incursions to caves by trogloxenes and troglophiles. In addition, there are unique troglobitic species that have developed diverse and specialized adaptations during their evolution to the lack of light.

In Mexico, there are records of 27 species of anurans that inhabit caves (Reddell, 1981; Hoffmann et al., 1986), which corresponds to approximately 7% of the total amphibian diversity of the country (363). This high percentage of use of this habitat for anurans is more frequent than expected (López-Ortega and Casas-Andreu, 2005).

Los Riscos Cave has been investigated for its fauna over many years and has a large diversity of fauna that includes arthropods and vertebrates, such as vampire bats *Desmodus rotundus* (Geoffroy, 1810) and *Diphylla ecaudata* Spix, 1823, the frugivorous bat *Artibeus lituratus* (Olfers, 1818), an insectivorous bat *Corynorhinus mexicanus* (Allen, 1916), and the fish *Astyanax mexicanus* (De Filipi, 1853), and anurans as *Incilius valliceps* (Wiegmann, 1833) (previously known as *Bufo valliceps*, see Frost, 2008), and the robber frog *Eleutherodactylus longipes* (Baird, 1859) (Fig. 1), which is a member of the family Brachycephalidae, following Frost et al., (2006).

*Eleutherodactylus longipes* is endemic to Mexico, being distributed along the Sierra Madre Oriental from the states of Nuevo Leon through Hidalgo, Tamaulipas, San Luis Potosí and Querétaro in isolated localities (Lynch, 1970; IUCN, 2006). It inhabits moderate elevations from 650 to 2000 m, and it shows a strong tendency to occupy caves (Taylor, 1939; Lynch, 1970; IUCN, 2006). The biology and natural history of this frog are unknown.

[1] Acarología & Bioespeleología, Departamento de Biología Comparada, Facultad de Ciencias, Universidad Nacional Autónoma de México, Coyoacán 04510, Distrito Federal, México
[2] Ecología y Sistemática de Microartrópodos, Departamento de Ecología y Recursos Naturales, Facultad de Ciencias, Facultad de Ciencias, Universidad Nacional Autónoma de México, Coyoacán 04510, Distrito Federal, México
[3] Biología animal experimental, Departamento de Biología Celular, Facultad de Ciencias, Universidad Nacional Autónoma de México, Coyoacán 04510, Distrito Federal, México
[4] Additional Address: Unidad Multidisciplinaría de Docencia e Investigación, Facultad de Ciencias, Universidad Nacional Autónoma de México, Campus Juriquilla, Boulevard Juriquilla 3001, C.P. 76230, Querétaro, Querétaro, México
[5] Departamento de Zoología, Instituto de Biología, Universidad Nacional Autónoma de México, Coyoacán 04510, Distrito Federal, México
[6] Corresponding Author (email: jbmm@hp.fciencias.unam.mx).

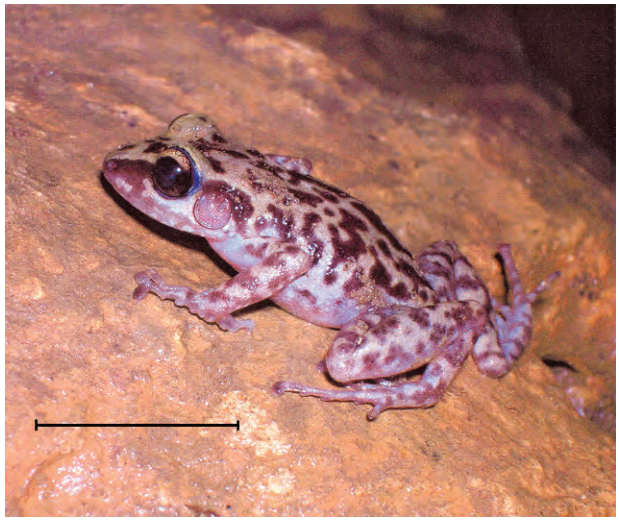

**Figure 1. Long-footed robber frog *Eleutherodactylus longipes* at Los Riscos Cave, Querétaro, Mexico. Scale bar is 2 cm.**

Caves provide a diversity of habitats where environmental signals may have different influences upon the circadian properties of the organisms that inhabit them. Near the main entry of a cave, natural day-night cycles, as well as changes in temperature and humidity, may play a significant role in the daily organization of animal activity. In deep regions of caves, constant or poorly fluctuating conditions lack the temporal periodicity to entrain endogenously generated circadian rhythms, and poor light conditions can also affect other physiological traits such as vision or skin color (Poulson and White, 1969; Lamprecht and Weber, 1992).

Diverse studies of circadian activity rhythms have been performed under laboratory conditions by monitoring the locomotor activity of fish (Trajano et al., 2005; Pati, 2001), crustaceans (De la O-Martínez et al., 2004), crickets (Hoenen 2005), millipedes (Koilraj et al., 2000), spiders (Gnaspini et al., 2003) and salamanders (Hervant et al., 2000), among others. Results have varied: some species are arrhythmic and others remain capable of displaying low-amplitude circadian rhythms, able to synchronize to artificial light-dark cycles.

Studying different morphological, ontogenetic or ethological adaptations to underground environments may help us understand the adaptive meaning of having a functional circadian clock in organisms that live in such unusual habitats.

Our aim is to present the habitat and seasonal distribution of *E. longipes* inside Los Riscos Cave, as well as its locomotor activity pattern in laboratory conditions, for understanding long-term circadian locomotor activity in natural settings and their response to artificial light-dark cycles.

## Materials and Methods

### Locality

Los Riscos Cave (21° 11′ 38″ N, 99° 30′ 50″ W: Lazcano Sahagún, 1986b) belongs to the El Abra limestone and its geographical location is in the Sierra Gorda in the State of Querétaro, Mexico (Alencaster et al., 1999). It is located 3 km northeast from Puente de Dios up the river Jalpan at 1122 m asl. Water persistence inside the cave varies between dry and rainy periods. Maximum precipitation occurs from June to November, and the driest period is from December to May. Average annual precipitation is about 48.9 mm $d^{-1}$ (CETENAL, 1986; CNA, 2004), and the average annual temperature is 24 °C (INEGI, 1996; CGSNEGI, 2004). The climate of the area is warm subhumid type (A)$C_1$(wo)(w) sensu Köppen and modified by Garcia (1981) and the category of vegetation is tropical dry forest (Carabias Lillo et al., 1999).

This cave represents a mixed underground system (horizontal and vertical) with eight zones, denoted with the letters A to H, including tunnels and galleries (Fig. 2). The cave is mainly horizontal, with a depth of 35 m and a length of 550 m (Lazcano Sahagún, 1986a, 1986b). Criteria for defining each zone are based on different topographical events and features inside the cave, like tunnels, areas of collapse or changing climatic conditions. The main entry, labeled as zone A, is surrounded by local vegetation and sunlight scatters about 35 m inside. Other zones have diminished amount of light or are totally dark. Zones B, C, D and E represent the largest transects, therefore average values of humidity, temperature, and light indicate the proximal (about 40 m deep, designated as 1) and distal (about 80 m deep, designated as 2) locations. Zone B2 represents the upper chamber at the end of this zone, which is 30 m high.

Zones G and H include narrow corridors and vertical pits and thus presented access challenges. These areas were not considered for this study because no frogs were found there.

### Field Techniques

All sampling activities were performed seasonally every three months from November 2005 to March 2008. Physical parameters such as temperature, humidity, and luminosity were recorded in different locations inside the cave using a thermohydrometer (IAQ- Calc 8760), and a luxometer (EXTECH instruments 0–2000 luxes). Readings were obtained every 20 m along search transects in both dry and rainy seasons.

The search for frogs was carried out along each one of the cave zones during day-twilight periods because we observed in preliminary explorations that apparently the frog's activity inside the cave is the same all times of the day. The frogs are not very visible. For example, in zone B they were more commonly observed at rest on top of walls or crevices on walls, whereas in other zones (E, F), the

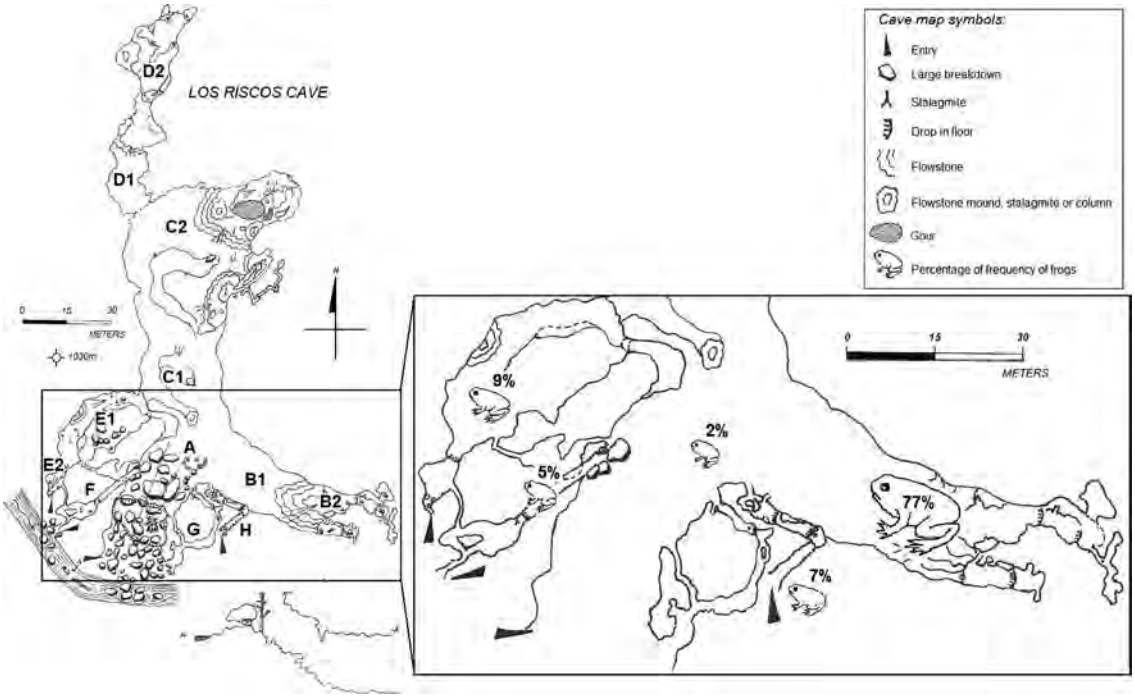


**Figure 2. Distribution and relative abundance of *E. longipes* in Los Riscos Cave, Querétaro, Mexico. Arrows represent cave entry points. The map, modified from Lazcano Sahagún (1986), shows in detail the zones of the cave, where frogs were sampled. Frog-like symbols indicate percentage of frequency of observation in each zone.**

frogs were found under rocks. Zones where the frogs were observed did not include puddles or pools of water. Some frogs were marked and released; others were collected and transported to the laboratory for circadian studies or to serve as voucher specimens at the Facultad de Ciencias, Universidad Nacional Autónoma de México (FC). In order to minimize possible dampening of endogenous activity rhythms, all animals used in the laboratory were transported in a dark styrofoam box slightly cooled with crushed ice and were recorded in the laboratory as soon as possible. A few individuals were examined for parasites and to confirm proper identification. These specimens will be deposited at the Universidad Nacional Autónoma de México (UNAM), in the Museo de Zoología de la Facultad de Ciencias (MZFC-UNAM) and Colección Nacional de Anfibios y Reptiles (CNAR-IBUNAM).

## LABORATORY TECHNIQUES

Nine frogs collected during different seasons (five in dry season and four in rainy season) were used for this portion of the study. Frogs were individually kept in glass aquaria (2.5 L) and were each equipped with infrared light crossings to detect locomotor activity as described elsewhere (Miranda-Anaya et al., 2003). These were kept in continuously ventilated, light-proof wooden boxes, and maintained at 23 ± 2 °C in environmentally-controlled rooms at the FC facilities. In order to maintain a sufficiently high humidity inside the recording chamber, each aquarium had a wet paper towel spread on its bottom which was moistened with clean water once a week. Locomotor activity data were summarized every 10 min for further analysis by means of a data acquisition board (NAFRI disp. México D. F.).

Every frog was initially monitored for at least nine days under continuous darkness (DD). As needed, a dim red light bulb (1–2 lx) was used for visual inspection and maintenance of aquaria. Then, light-dark cycles (LD 12:12) were used during at least ten days in order to observe any possible entrainment of locomotor activity rhythms. Light cycles were provided by means of a fluorescent lamp (Tecnolite F15T8D) controlled by a timer. The lamp was partially dimmed by using black tape and located at 30 cm above aquaria in order to provide half of the light intensity (150 lx). Frogs were fed once a week with juvenile crickets that were rendered legless to avoid their interfering with frog locomotor activities.

## DATA ANALYSIS

Seasonal means in abundance were compared by a student *t*-test for independent samples performed by Statistica software (StatSoft, 1999). A Fisher's exact test (Tocher, 1950) was used to evaluate the association between seasons and between different cave zones. We performed the Freeman and Halton (1951) analysis of the Fisher exact probability for a two-by-five contingency table. A two way Analysis of Variance (ANOVA) was

performed in order to evaluate the effect of the season and cave zone on the environmental parameters with a *post hoc* Tukey's test used to identify significant differences. A multiple correlation was performed between temperature, humidity, luminosity, and frog abundance in sites where frogs were recorded.

Locomotor activity data were analyzed in double-plotted actograms based on a day-by-day histogram in which each bar indicates the amount of activity observed in a time lapse of 10 min across a 24-hour series. In this presentation, the daily traces stacked vertically in chronological order give a lucid view of the activity envelope (DeCoursey, 2004).

The respective circadian periods for at least seven consecutive days ($\tau$) were calculated using $\chi^2$ periodograms (Sokolove and Bushell, 1978) at 0–30 h intervals. Ultradian activity was analyzed by means of Fast Fourier Transform Analysis using the software DISPAC (Instituto de Fisiología Célular (IFC), UNAM, Mexico; Aguilar-Roblero et al., 1997). Periodograms with spikes above the confidence interval ($p < 0.05$) were considered rhythmic. Results on period lengths of free-running activity bouts under different protocols were analyzed using a non-paired student *t*-test with the software program Statistica; differences were considered significant when $p < 0.05$. All results are presented as mean values ± standard deviations (SD) unless otherwise noted.

## Results

### Physical Parameters in Los Riscos Cave

The two-way ANOVA test showed no significant effect of season on temperature ($F_{1, 60} = 0.80$; $p > 0.05$), humidity ($F_{1, 60} = 3.18$ $p > 0.05$), or luminosity ($F_{1, 60} = 0.47$ $p > 0.05$). However, there were significant effects of cave zone on these parameters (temperature: $F_{9, 60} = 2.35$ $p < 0.05$; humidity: $F_{9, 60} = 5.81$ $p < 0.005$; luminosity: $F_{9, 60} = 37.72$ $p < 0.0005$). Temperature differences were found between zones B and D2 and between zones D1 and D2. The main differences for the humidity were found between zone A and zone D2. For the luminosity, zones B and C1 together were different from the other zones and zone A was different from all others (Fig. 3).

The zone with the highest temperature and humidity in both seasons was D2. This zone has permanent colonies of vampire bats (*Desmodus rotundus* and *Diphylla ecaudata*) present in the deepest part of the cave. Two other bat species, *Artibeus lituratus* and *Corynorhinus mexicanus*, were found in this zone, but only during a single sampling event.

### Distribution of *Eleutherodactylus longipes* in the Cave During Different Seasons

A total of 43 frogs was found in the cave during the three-year study. Seasonal average abundance for the rainy season was 5 ± 1.41 SD, and for the dry season was 11 ± 4.24 SD; the difference between the two seasons was significant ($t_4 = 2.82$; $p = 0.04$).

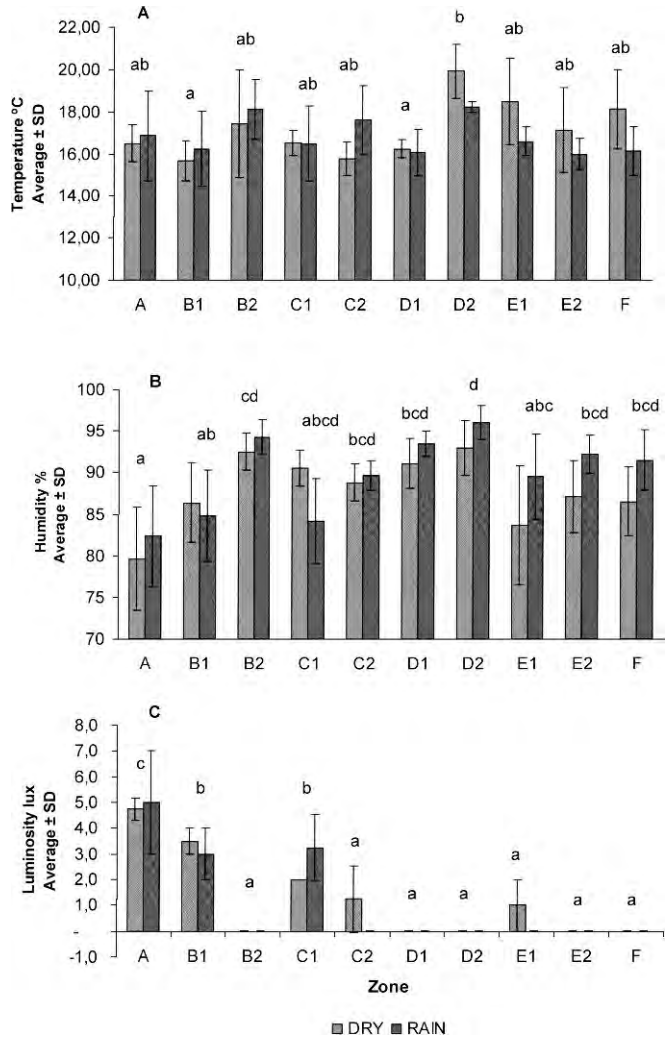


**Figure 3. Average temperature (A), humidity (B), and luminosity (C) along Los Riscos Cave. Letters denote significant differences between zones according to *post hoc* comparisons using Tukey's test ($p < 0.05$). Light gray bars mean dry season and dark gray bars mean rainy season.**

Frogs were located mainly between 1200 h and 1600 h in cave zones A, B, E, and F. Density was highest in zone B and lowest in zone F for both seasons (Fig. 4). In zone A, only one individual was found during the dry season, while during the rainy season, frogs were found outside of the cave on the external wall of zone B at midnight just one time. There was no association between cave depth and season (Fisher's exact test, $p = 0.29$). For both the dry and rainy seasons, the distribution of frogs in the cave was similar. The coefficient of multiple correlation between the environmental parameters and frog abundance was highly positive and significant ($r = 0.94$; $p < 0.05$). Humidity explained most of the observed variation in abundance ($r = 0.72$; $p < 0.005$), followed by luminosity ($r = 0.35$; $p <$

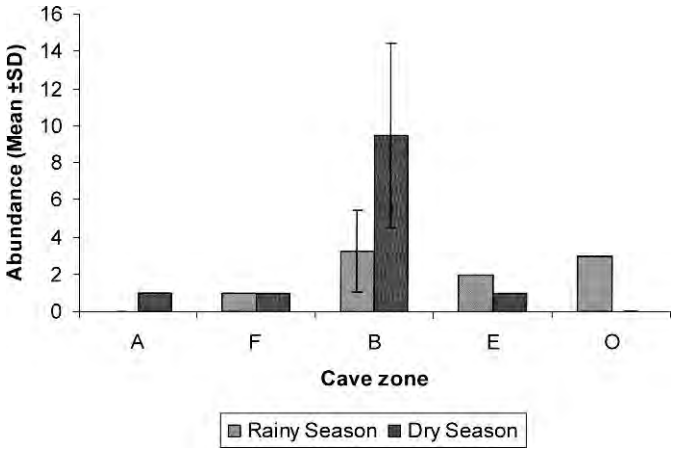


**Figure 4. Seasonal distribution of *E. longipes* in different zones at Los Riscos Cave, Querétaro, Mexico. Light gray bars mean rainy season and dark gray bars mean dry season.**

0.05). Temperature was not significantly correlated with abundance ($r = 0.24$; $p > 0.05$). This is unsurprising because this parameter was constant throughout the cave (Fig. 5). The simple correlation between luminosity and abundance was negative and significant ($r = -0.11$; $p < 0.05$).

### CIRCADIAN LOCOMOTOR ACTIVITY RHYTHMS

Figure 6 shows a double-plotted actogram (A) and correspondent activity profiles (B) for a typical recording of locomotor activity under different light conditions for a single frog. A significant circadian rhythm oscillated during the first nine days of recording in DD. The main bout of activity is projected for the external-light phase. When exposed to LD cycles (day 10), activity was still maintained during the diurnal phase of the cycle and crepuscular activity was observed in this first LD condition, as shown in the correspondent activity profile (see B in Fig. 6). However, when exposed again to constant DD, the rhythm faded away and a non-significant circadian period was observed. The next exposure to LD cycles did not show circadian activity.

In a second group of animals tested for a longer period, the initial free-running circadian rhythm in DD was observed again. However, the rhythm was dampened after 10 to 20 days and LD conditions did not reorganize the activity. Frequency analysis of ultradian rhythms by means of Fast Fourier transform shows that in LD, circadian frequencies were absent while ultradian rhythms of 1 to 6 h were observed.

## DISCUSSION

The factors determining the environmental characteristics of Los Riscos Cave are associated with the external agents imposed by local climate and season, and we found

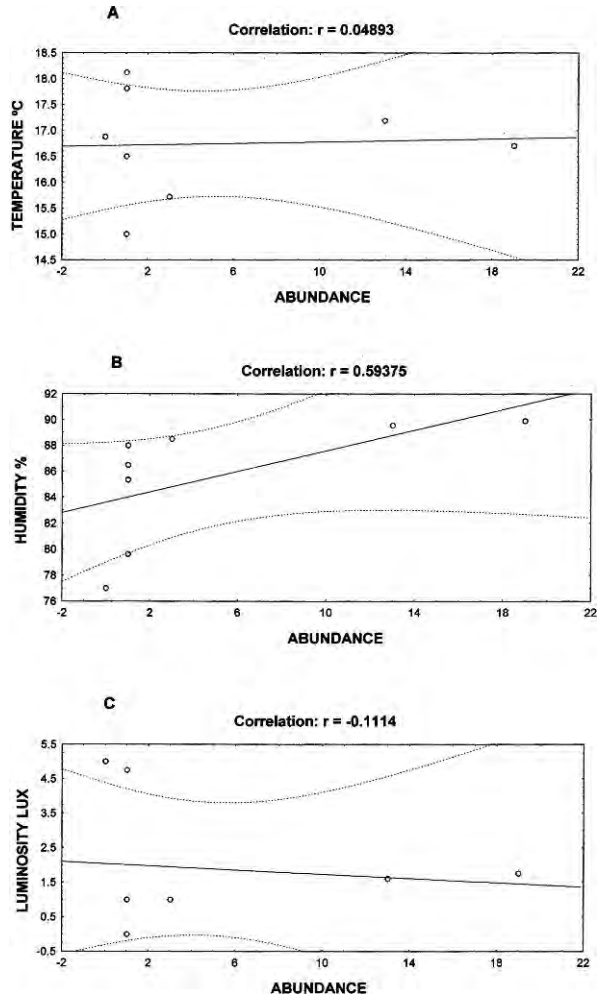


**Figure 5. Simple correlation analysis between temperature (A), humidity (B), and luminosity (C) with abundance of *E. longipes* in Los Riscos Cave. Data from November 2005 to March 2008 at Los Riscos Cave, Querétaro, Mexico. Solid lines mean the correlation that is adjusted to the data, and the dashed lines mean the range of dispersion of the data with regard to the correlation line.**

that differences of frog abundance between dry and rainy seasons can be related to humidity levels inside the cave, which is consistent with the necessity of frogs to avoid desiccation and light exposure. Also, amphibians of temperate areas display different strategies, such as hibernation, in order to avoid starvation and low environmental temperatures (Pinder et al., 1992). Among these strategies, there is use of refugia such as cracks in rocks, fallen trunks, stumps, caves and others (López-Ortega and Casas-Andreu, 2005). The study results confirmed that environmental variables such as temperature, solar radiation, and relative humidity determine the distribution of these organisms.

It is important to point out that all the individuals were found during the daytime inside the cave because Lynch and Duellman (1997) affirmed that all the *Eleutherodacty-*

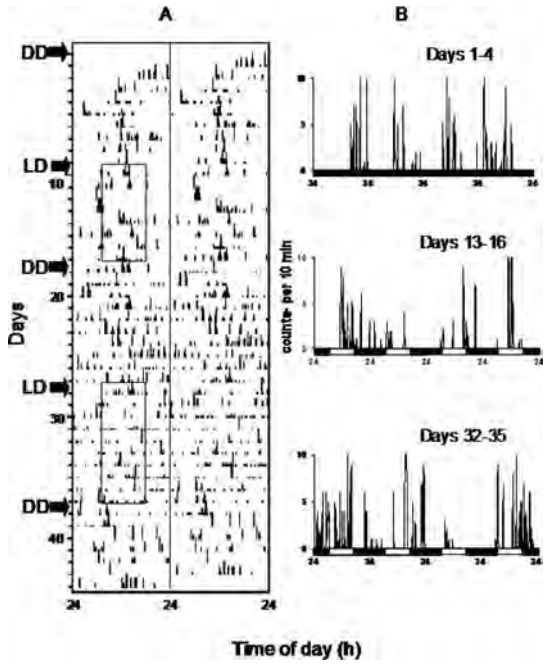


**Figure 6. Double-plotted actogram (left) and corresponding activity profiles of a single frog. Light conditions are indicated by arrows (DD = constant darkness, LD = light/dark cycles), light phase is also indicated by rectangles on left side of the actogram. Activity profiles on B show also the LD cycles. Days considered for the profiles are indicated.**

*lus* (with the exception of *E. hectus*) are nocturnal. The biotic (potential prey) and abiotic (temperature, humidity, and darkness) parameters inside the cave probably increase the range of crepuscular activity of the robber frog as shown in Figure 6B.

Inside the cave, zone B shows the main population of frogs and other records can be considered as accidental. The population living here apparently does not have contact with the exterior of the cave. However, we cannot discard the presence of little cracks that allow some movements to outside, which means the frogs could not remain in the cave full time. Additionally, the frogs were observed outside the cave at night and far from the main population of zone B.

Preliminary observations indicate that there is more diversity of invertebrates in zones A and F than in zones B and E. However, crickets and spiders in zone B can also serve as potential prey for the frogs. No frogs were observed feeding on cave animals while in the cave and, unfortunately, the contents of the few stomachs analyzed were in a state of advanced digestion, so it was not possible to identify the taxa in stomach contents. Zones C and D had appropriate temperature, humidity, and luminosity conditions, but their isolation from the external environment made these conditions difficult for the frogs to access.

Endogenous circadian rhythmicity was detected during the initial ten days of recording under laboratory conditions without acclimation, which indicates a functional circadian clock in this species. The average free-running period observed during the first 8–10 days of locomotor activity indicates a wide circadian variation, which according to Aschoff's rule, corresponds to a diurnal species (Aschoff, 1960).

This frog is visually reactive to the presence of living insects as prey. However, because the light intensity of artificial LD cycles used in the laboratory was higher than that available inside the cave, it is possible that bright light induced arhythmic patterns of ultradian expression in this species as is known to happen in vertebrates exposed to continuous bright light (Ohta, et al., 2005).

## Conclusions

Robber frog distribution among cave regions, being largely concentrated in zone B, suggests that the presence of some scattered light is necessary for its activity and may influence its dispersion inside the cave. The functional circadian clocks in cave animals may have different sensitivities to light according to the species, because fish or arachnids collected in deeper zones were able to entrain their circadian rhythms on similar artificial light-dark cycles (unpublished observations). Laboratory experiments did not include interaction with other species that coexist in the same cave areas. Therefore, it is possible that timing relationships among species inside the cave might be important to sustaining circadian rhythmicity under natural conditions as observed for different cave insects (Oda et al., 2000). Non-circadian data observed in different cave species in these conditions may require a different statistical analysis that can filter the noise pattern of small peaks as seen for the rhythm of the cave cricket *Strinatia brevipennis* (Hoenen et al, 2001). The arhythmic pattern observed may require different criteria of analysis than used in the present study, and the ecophysiological significance of these findings is yet to be fully understood.

Nonetheless, this is the first study of some aspects of the biology of *E. longipes*, and we can note that the environmental preference for caves and a partial endogenous circadian rhythmicity confirms the troglophilic nature of the robber frog. The paucity of information concerning the ecology and physiology of troglophilic anurans highlights the importance of generating detailed studies of these topics.

## Acknowledgments

For comments on an earlier draft of the manuscript, we express our appreciation to Joaquín Arroyo-Cabrales (Laboratorio de Arqueozoología, Instituto Nacional de Antropología e Historia, México), Fred Kraus (Bishop Museum, Hawaii), Gerardo López-Ortega (Universidad

Autónoma Metropolitana – Iztapalapa). We also thank Miguel Hernández, Sara Soriano, Yunuen Ávila, Marisol Vega, Itzel Sigala and Stephanie Ortega (Biospeleology group, Facultad de Ciencias, Universidad Nacional Autónoma de México) for their helpful assitance in the field expeditions. We thank Alejandro Martínez Mena and Ana Isabel Bieler Antolin, and José Antonio Hernández (Laboratorio de Microcine, Facultad de Ciencias, Universidad Nacional Autónoma de México) for their help with photographs. Financial assistance was provided by the Dirección General de Asuntos del Personal Académico, Universidad Nacional Autónoma de México, Grant IN221906 to J.B.M-M.

## REFERENCES

Aguilar-Roblero, R., Salazar-Juarez, A., Rojas-Castañeda, J., Escobar, C., and Cintra, L., 1997, Organization of circadian rhythmicity and suprachiasmatic nuclei in malnourished rats: American Journal of Physiology, Regulatory Integrative Comparative Physiology, v. 273, p. R1321–R1331.

Alencaster, G., Torres-Hernández, R., Tristán-González, M., Barbosa-Gudiño, R., López-Doncel, R., Pons, J.M., and Omaña, L., 1999, El Abra formation in the western part of the Valles-San Luis Potosí Platform (Mexico): Erlanger Geologische Abhandlungen, Sonderband, v. 3, p. 7–8.

Aschoff, J., 1960, Exogenous and endogenous components in circadian rhythms, *in* Proceedings, Cold Spring Harbor Symposia on Quantitative Biology, v. 25, p. 11–28.

Baird, S.F., 1859, Reptiles of the Boundary, *in* United States and Mexican Boundary Survey under the Order of Lieut. Col. W. H. Emory, Major First Cavalry, and United States Commisioner. 2, Rept., Pt. 2. Department of the Interior, Washington, 35 p.

Carabias Lillo, J., Provencio, E., de la Maza Elvira, J., and Ruiz Corzo, M., 1999, Programa de Manejo Reserva de la Biosfera Sierra Gorda, México, Instituto Nacional de Ecología, SEMARNAT (Secretaría de Medio Ambiente y Recursos Naturales), 172 p.

CETENAL (Comisión de Estudios del Territorio Nacional), 1986, Precipitación y probabilidad de la lluvia en la República Mexicana y su evaluación, Querétaro e Hidalgo, Serie climas, Instituto de Geografía, Universidad Nacional Autónoma de México.

CGSNEGI (Coordinación General de los servicios Nacionales de Estadística, Geografía e Informática), 2004, Carta de Climas, 1:1000 000, *in* Anuario Estadístico de Querétaro de Arteaga. http://www.queretaro.gob.mx/sedesu/deseco/esteco/perfeco/anuest/PDF/Capitulos/C1.pdf

CNA (Comisión Nacional del Agua), 2004, Registro mensual de precipitación pluvial en mm. Inédito, *in* Anuario Estadístico de Querétaro de Arteaga. http://www.queretaro.gob.mx/sedesu/deseco/esteco/perfeco/anuest/PDF/Capitulos/C1.pdf

De La O-Martínez, A., Verde, M.A., Valadez, R.L., Viccon-Pale, J.A., and Fuentes-Pardo, B., 2004, About the existence of circadian activity in cave crayfish: Biological Rhythm Research, v. 35, no. 3, p. 195–204.

DeCoursey, J.P., 2004, Overview of biological timing from unicells to humans, *in* Dunlap, J.C., Loros, J.J., and De Coursey, J.P., eds., Chronobiology, 1st ed.: Sunderland, Massachusetts, Sinauer Associates Incorporated Publishers, p. 3–27.

Freeman, G.H., and Halton, J.H., 1951, Note on exact treatment of contingency, goodness of fit and other problems of significance: Biometrika, v. 38, p. 141–149.

Frost, D.R., 2008, Amphibian Species of the World: An Online Reference, Version 5.2 (19 November, 2008), New York, American Museum of Natural History, Electronic Database accessible at http://research.amnh.org/herpetology/amphibia/index.php.

Frost, D.R., Grant, T., Faivovich, J., Bain, R.H., Haas, A., Haddad, C.F.B., Channing, A., Wilkinson, M., Donnellan, S.C., Raxworthy, C.J., Campbell, J.A., Blotto, B.L., Moler, P., Drewes, R.C., Nussbaum, R.A., Lynch, J.D., Green, D.M., and Wheeler, W.C., 2006, The amphibian tree of life: New York, Bulletin of the American Museum of Natural History, no. 297, 370 p.

García, E., 1981, Modificaciones al sistema de clasificación climática de köppen: México, D.F., 252 p.

Gnaspini, P., Santos, F.H., and Hoenen, S., 2003, The occurence of different phase angles between contrasting seasons in the activity patterns of the cave harvestman *Gnosioma spelaeum* (Arachnida, Opiliones): Biological Rhythm Research, v. 34, no. 1, p. 31–49.

Hervant, F., Mathieu, J., and Durand, J.P., 2000, Metabolism and circadian rhythms of the European blind cave salamander *Proteus anguinus* and a facultative cave dweller, the Pyrenean newt (*Euproctus asper*): Canadian Journal of Zoology, v. 78, no. 8, p. 1427–1432.

Hoenen, S., 2005, Circadian patterns in the activity of the Brazilian cave cricket *Strinatia brevipennis* (Ensifera Phalangopsidae): European Journal of Entomology, v. 102, no. 4, p. 663–668.

Hoenen, S., Schimmel, M., and Marques, M.D., 2001, Rescuing rhythms from noise: A new method of analysis: Biological Rhythm Research, v. 32, no. 2, p. 271–284.

Hoffmann, A., Palacios-Vargas, J.G., and Morales-Malacara, J.B., 1986, Manual de bioespeleología (con nuevas aportaciones de Morelos y Guerrero, México), Universidad Nacional Autónoma de México, 274 p.

INEGI (Instituto Nacional de Estadística, Geografía e Informática), 1986, Síntesis Geográfica, nomenclator y anexo cartográfico del estado de querétaro, 143 p.

IUCN (International Union for Conservation of Nature), Conservation International, and NatureServe, 2006, Global amphibian assessment. http://www.globalamphibians.org

Koilraj, A.J., Sharma, V.K., Marimuthu, G., and Chandrashekaran, M.K., 2000, Presence of circadian rhythms in the locomotor activity of a cave-dwelling millipede *Glyphiulus cavernicolus sulu* (Cambalidae, Spirostreptida): Chronobiology International, v. 17, no. 6, p. 757–765.

Lamprecht, G., and Weber, F., 1992, Spontaneous locomotion behaviour in cavernicolous animals: the regression of the endogenous circadian system, *in* Camacho, A.I., ed., The natural history of biospeleology: Madrid, Monografias del Museo Nacional de Ciencias Naturales, p. 225–262.

Lazcano Sahagún, C., 1986a, Cavernas de la Sierra Gorda. v. I, Universidad Autónoma de Querétaro, Mexico, 181 p.

Lazcano Sahagún, C., 1986b, Cavernas de la Sierra Gorda. v. II, Universidad Autónoma de Querétaro, Mexico, 206 p.

López-Ortega, G., and Casas-Andreu, G., 2005, A tunnel as hibernaculum of *Hyla plicata* (Anura: Hylidae) at Sierra Norte de Tlaxco, Tlaxcala, México: Revista de la Sociedad Mexicana de Historia Natural, 3ª época, v. 2, no. 1, p. 160–167.

Lynch, J., 1970, A Taxonomic Revision of the Leptodactylid Frog Genus *Eleutherodactylus* Cope: University of Kansas, Museum of Natural History, v. 20, no. 1, p. 1–45.

Lynch, J., and Duellman, W., 1997, Frogs of the Genus *Eleutherodactylus* (Leptodactylidae) in Western Ecuador: Systematics, Ecology, and Biogeography: University of Kansas Natural History Museum, Special Publication, no. 23, p. 50–165.

Miranda-Anaya, M., Barrera-Mera, B., and Ramírez-Lomelí, E., 2003, Circadian Locomotor Activity Rhythm in the Freshwater Crab *Pseudothelphusa americana* (De Saussure, 1857): Effect of Eyestalk Ablation: Biological Rhythm Research, v. 34, no. 2, p. 167–176.

Oda, G.A., Caldas, I.L., Piqueira, J.R.C., Waterhouse, J.M., and Marques, M.D., 2000, Coupled biological oscillators in cave insects: Journal of Theoretical Biology, v. 206, no. 4, p. 515–524.

Ohta, H., Yamazaki, S., and McMahon, D., 2005, Constant light desynchronizes mammalian clock neurons: Nature Neurosciences, v. 8, no. 3, p. 267–269.

Pati, A.K., 2001, Temporal organization in locomotor activity of the hypogean loach, *Nemacheilus evezardi*, and its epigean ancestor: Environmental Biology of Fishes, v. 62, no. 1–3, p. 119–129.

Pinder, A.W., Storey, K.B., and Ultsch, G.R., 1992, Estivation and hibernation, *in* Feder, M.E., and Burggren, W.W., eds., Environmental Physiology of the Amphibians: Chicago and London, The University of Chicago Press, p. 250–276.

Poulson, T.L., and White, W.B., 1969, The cave environment: Science, v. 165, no. 3897, p. 971–981.

Reddell, J.R., 1981, A review of the cavernicole fauna of México, Guatemala and Belize: Bulletin of the Texas Memorial Museum, v. 27, p. 1–327.

Sokolove, P.G., and Bushell, W.N., 1978, The Chi-Square periodogram: Its utility for analysis of circadian rhythms: Journal of Theoretical Biology, v. 72, p. 131–60.

StatSoft Inc., 1999, Statistical user guide: Complete Statistical System Statsoft. Oklahoma.

Taylor, E., 1939, New Species of Mexican Anura: The University of Kansas, Science Bulletin, v. 26, no. 11, p. 385–401.

Tocher, K.D., 1950, Extension of the Neyman-Pearson theory of tests to discontinuous variates: Biometrika, v. 37, p. 130–144.

Trajano, E., Duarte, L., and Menna-Barreto, L., 2005, Locomotor activity rhythms in cave fishes from Chapada Diamantina, northeastern Brazil (Teleostei: Siluriformes): Biological Rhythm Research, v. 36, no. 3, p. 229–236.

J.E. Mylroie and J.R. Mylroie – Caves as sea level and uplift indicators, Kangaroo Island, South Australia. *Journal of Cave and Karst Studies,* v. 71, no. 1, p. 32–47.

# CAVES AS SEA LEVEL AND UPLIFT INDICATORS, KANGAROO ISLAND, SOUTH AUSTRALIA

JOHN E. MYLROIE AND JOAN R. MYLROIE
*Department of Geosciences, Mississippi State University, Mississippi State, MS 39762 USA, mylroie@geosci.msstate.edu*

**Abstract:** Flank margin caves have been observed in Quaternary Bridgewater Formation eolianites on Kangaroo Island, South Australia. Horizons of flank margin cave development at 25 m, 30 m, and 35 m elevation demonstrate tectonic uplift of tens of meters during the Quaternary, as the cave elevations are higher than any reported Quaternary glacioeustatic sea-level highstand. Distinct cave horizons indicate that episodic uplift was possible. Wave-cut notches at Hanson Bay, at 30 to 35 m elevation, also support the interpretation from caves that relative sea level was once at the ~30-m-elevation range. Admirals Arch, previously presented as forming solely by wave erosion, is a flank margin cave breached and modified by wave erosion. Point Ellen contains a Late Pliocene subtidal carbonate unit that formed within the reach of wave base, was uplifted and cliffed by wave processes, and then was karstified before being buried by Quaternary Bridgewater Formation eolianites. A possible flank margin cave developed at Point Ellen at 3 m above modern sea level is consistent with earlier interpretations of notching of the nearby coast at a similar elevation during the last interglacial sea-level highstand (MIS 5e); and therefore, no tectonic uplift in the last 120 ka. In contrast, the tafoni of Remarkable Rocks present a cautionary note on evidence of cave wall morphological characteristics as proof of dissolutional origin.

## INTRODUCTION

Kangaroo Island is located 16 km southwest across the Backstairs Passage from Cape Jervis on the Fleurieu Peninsula, South Australia (Fig. 1). The island is a rectangle roughly 145 km east to west, and 60 km north to south with an area of 4,350 $km^2$ and a coastline length of 457 km (Short and Fotheringham, 1986). Kangaroo Island is a geologically diverse environment with rocks present from the Proterozoic through the Paleozoic, Mesozoic, and Cainozoic (Belperio and Flint, 1999). The island is a geologic extension of the Fleurieu Peninsula on the Australian mainland (Belperio and Flint, 1999; James and Clark, 2002). Although isolated Paleozoic outcrops of carbonate rock exist on Kangaroo Island, the dominant carbonate units are Cainozoic (James and Clark, 2002). Especially prevalent, primarily along the southern and western coasts, are eolian calcarenites of Late Pliocene through Holocene age (Ludbrook, 1983; Short and Fotheringham, 1986). The Cambrian Kanmantoo Group metasediments form the basement of the island (James and Clark, 2002), and commonly the eolianites rest directly upon them along the southern and western shore of Kangaroo Island. Cambro-Ordovician granites also outcrop at the southwest end of Kangaroo Island (James and Clark, 2002) and eolianites occasionally overlie those exposures.

The eolian calcarenites are assigned by most authors to the Bridgewater Formation, the name given to eolian calcarenites across South Australia and Victoria (Drexel and Preiss, 1995). These eolian calcarenites represent depositional episodes associated with glacioeustatic Quaternary sea-level fluctuations and consist of at least 16 separate events on the Australian mainland (Drexel and Preiss, 1995). On Kangaroo Island, the eolian depositional events are thought by some authors to represent only four glacial events because those authors recognize only the traditional, continental-based four Pleistocene glaciations (Twidale and Bourne, 2002), while other authors indicate that more than 16 sea-level highstands occurred in the Quaternary on Kangaroo Island (Short and Fotheringham, 1986). Most authors (e.g., Drexel and Preiss, 1995) consider the Bridgewater Formation to be Pleistocene in age. However, Ludbrook (1983) reports that eolian calcarenites of the Bridgewater Formation interfinger with Late Pliocene Point Ellen Formation subtidal facies at Point Reynolds, east of Point Ellen. This observation raises the possibility that the initial deposition of the Bridgewater Formation eolian calcarenites predates the Pliocene-Pleistocene boundary on Kangaroo Island. The Bridgewater Formation eolian calcarenites and the caves and karst features developed in them are the focus of this reconnaissance study.

Kangaroo Island was visited in September 2006 for five days as a reconnaissance expedition with the purpose of comparing cave development in the coastal eolian calcarenites on that island with those found in similar environments in the Bahamian Archipelago, half the world away. The observations reported here are necessarily brief and lack detail such as cave surveys. However, these brief observations establish important information regarding the nature of cave development on Kangaroo Island and

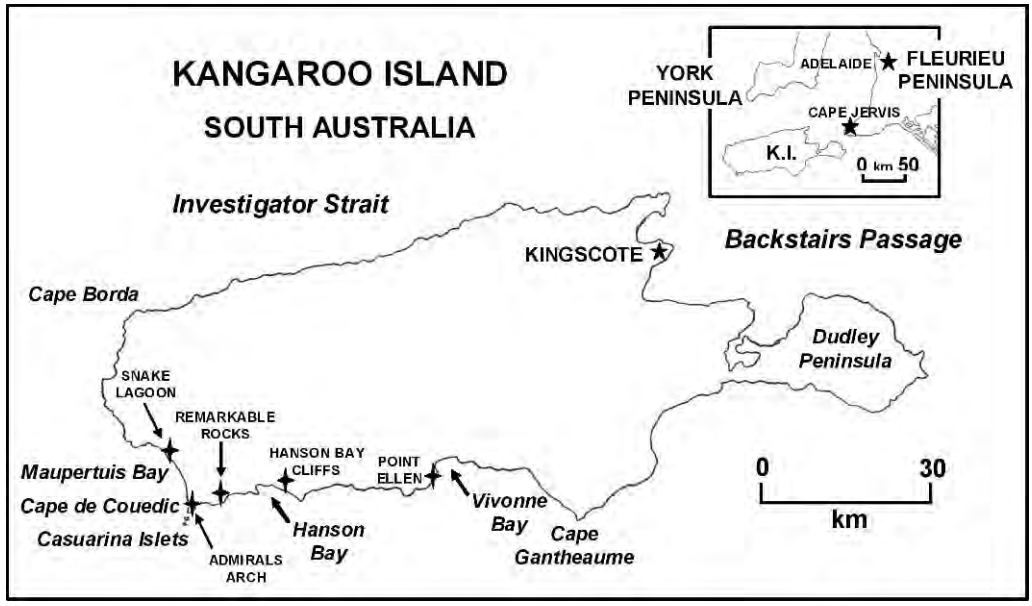


**Figure 1. Map of Kangaroo Island showing its position off the Australian coast, and locations discussed in the text.**

important sea level and tectonic interpretations that can be generalized from those observations.

Decades of work in the Bahamas (Mylroie, 1980; Vogel et al., 1990; Mylroie et al., 1995; Roth et al., 2006; Mylroie and Mylroie, 2007) developed an extensive database on cave development in eolian calcarenites. Those investigations led to the development of the flank margin cave model to explain rapid cave development in Bahamian eolianites as a result of mixing-zone dissolution. These caves develop in the distal margin of the fresh-water lens, under the flank of the enclosing landmass. At this location, the favorable dissolutional horizons at the top of the lens (vadose and phreatic fresh-water mixing) and at the base of the lens (sea-water and fresh-water mixing) are superimposed (Mylroie and Carew, 1990, 1995). These lens boundaries are also density interfaces, which collect organic material. Oxidation of these organics creates $CO_2$ to drive further dissolution, and with extreme organic loading, anoxic conditions develop and $H_2S$-mediated dissolution can occur (Bottrell et al., 1993). The decrease in lens cross-sectional area at the lens margin increases water-flow velocity, such that reactants and products move swiftly through the system (Raeisi and Mylroie, 1995). The model was expanded to non-eolianite carbonate islands of increasing complexity, such as Isla de Mona, Puerto Rico (Frank et al., 1998) and Guam in the Marianas (Mylroie et al., 2001). One of the prominent aspects of flank margin cave development is that the caves cut across carbonate facies without regard to grain size, porosity, or primary structures in the rock (Mylroie and Carew, 1995); fresh-water lens position, and hence sea level, is the primary factor in cave position. The flank margin cave model has evolved into the Carbonate Island Karst Model, or CIKM, which takes into account mixing dissolution, glacioeustasy, tectonics, carbonate/noncarbonate island relationships, and diagenetic maturity (Jenson et al., 2006; Mylroie and Mylroie, 2007). Flank margin caves form as isolated chambers or groups of chambers (i.e., they develop as mixing chambers without entrances). A similar rapid reconnaissance in August of 2006 at Rottnest Island, Australia, resulted in a number of new and important observations in the Quaternary eolianites and the flank margin caves there (Mylroie and Mylroie, 2009).

Flank margin cave development is controlled by the position of the fresh-water lens, which in turn, is tied to sea-level position. Other classic sea-level indicators on carbonate coasts, such as intertidal and subtidal deposits, and coastal notching, remain on the land surface after local uplift and/or eustatic sea-level fall. Flank margin caves also occur in a coastal setting, but inside the landmass. This difference in placement means that as surficial erosion strips away surface deposits and landforms, flank margin caves are still present. As surface erosion continues, the flank margin caves are breached and become visible to the surface observer. As a result, flank margin caves are not only sea-level indicators, but also indicators of rates of surface denudation (Figs. 2 and 3).

In the Bahamas, breached flank margin caves were once identified as fossil bioerosion notches before being recognized as erosionally-exposed subsurface features (Mylroie and Carew, 1991). The Bahamas are tectonically stable, subsiding at 1 to 2 m per 100 ka (Carew and Mylroie, 1995; McNeill, 2005), therefore, any sea-level indicators found in the subaerial environment today are the result of eustasy. As the surficial rocks of the Bahamas are less than 800,000 years old (Carew and Mylroie, 1997), this eustatic sea-level change is a result of glacial-deglacial cycles. The Bahamian situation is somewhat simplified, as


**Figure 2. West coast of Kangaroo Island, north of Snake Lagoon and Rocky River. A – Overall scene, with light-coloured Bridgewater Formation eolianites overlying darker Kanmantoo Group rocks. The white box denotes the area presented in (B). B – Isolated Bridgewater Formation eolian calcarenite outcrops (light-coloured patches) on Kanmantoo Group rocks, demonstrating that a once-continuous eolian calcarenite unit has been stripped away by Holocene coastal erosion.**

sea level or subtidal indicators above modern sea level today, such as fossil reefs, abandoned coastal notches, breached flank margin caves, or herringbone crossbedding, must be the result of a glacioeustatic sea-level highstand above modern levels. That highstand must also have been recent enough that its deposits have remained above modern sea level despite the isostatic subsidence rate of 1 to 2 m per 100 ka. Based on these constraints, the only sea-level highstand believed to be pervasively recorded in the Bahamas is that of the last interglacial, marine isotope substage 5e, or MIS 5e (Carew and Mylroie, 1997). In the Atlantic Basin, that highstand reached +6 m and lasted from 131 ka to 119 ka (Chen et al., 1991), a 12,000 year time window in which to create all the pre-modern sea-level indicators currently observed above sea level in the Bahamas, including the flank margin caves.

Kangaroo Island is in an environment that has been uplifted during the Quaternary (Short and Fotheringham, 1986; James and Clark, 2002; Twidale and Bourne, 2002); the debate has been over the amount of uplift. In high-relief coastal settings, such as on Kangaroo Island, cliff retreat under current sea-level conditions has removed many of the typical surface indicators of past, higher sea levels (Fig. 2), and uplift has displaced them from the elevation of their initial formation (Fig. 3). Numerous caves are found in the eolianite cliffs of the southern and western coasts of Kangaroo Island, and their location is potentially a representation of a past fresh-water lens position, and hence, a past sea-level position. This paper reports on how use of caves, especially flank margin caves, can help refine our understanding of Quaternary processes on Kangaroo Island.

## METHODOLOGY

Conceptually, the methodology is simple; walk the eolianite outcrops and record the location and elevation of flank margin caves. Ideally, all caves identified are representative of a paleo sea-level position, but care is needed because the caves can be of two main types: dissolutional caves; and pseudokarst caves produced by processes other than dissolution. A distinction must be made between the two main cave types. If the cave is determined to be a dissolutional cave, then the nature of that dissolution must be determined to establish whether the cave formed in the distal margin of a fresh-water lens as a flank margin cave.

Cliffed coastal settings in eolian calcarenites commonly have two main types of pseudokarst caves: sea caves, and tafoni caves. Sea caves are the result of wave energy and wave transported debris mechanically eroding a hollow or cave into a bedrock outcrop (Waterstrat, 2007 and references therein). Such caves form from the outside inward as the waves continue their work. Sea caves are a sea-level indicator, but because they are produced from the surface inward, they remain near the active erosive face of the land surface and are vulnerable to later removal by scarp retreat. Tafoni caves are voids and hollows produced by subaerial weathering processes that selectively remove rock grains from a specific area in an outcrop. The processes involve wind, crystal wedging of evaporite minerals, wetting and drying, and a variety of other activities (Owen, 2007 and references therein). Similar to sea caves, tafoni caves form from the outside inward and are vulnerable to removal by scarp retreat. Unlike sea caves, however, their position on a cliff face is random and not related to a specific past sea-level position. Recent work in Bahamian eolian calcarenites has resulted in the development of criteria to allow the differentiation of breached flank margin caves and sea caves (Waterstrat, 2007; Mylroie et al., 2008a), as well as the differentiation of sea caves and tafoni caves from each other and from


**Figure 3. Views of flank margin cave entrances in the lower Rocky River and Snake Lagoon area, developed in Bridgewater Formation eolianites. A – Valley north wall, showing a well-developed band of caves at ~30-m-elevation, and other caves at ~25-m-elevation. B – Valley south wall, showing three horizons of flank margin cave development, at ~25-, ~30- and ~35-m-elevation. As with the valley north wall, the best development is at ~30 m.**

breached flank margin caves (Owen, 2007; Mylroie et al., 2008a).

One of the primary criteria to differentiate the cave types is inspection of the interior rock surfaces for the unique curvilinear shapes associated with carbonate dissolutional surfaces. Such inspection can be problematic if a flank margin cave has been breached while still in the surf zone because wave-dominated mechanical processes may have scoured, obscured, and overprinted the original dissolutional surfaces. The use of metrics, such as the ratio of cave area over cave wall perimeter, and the ratio of cave entrance width over maximum cave width reliably differentiate flank margin caves, sea caves, and tafoni caves from each other in the Bahamas (Waterstrat, 2007, Owen, 2007, Mylroie et al., 2008a). These metrics have been demonstrated to work for sea caves and flank margin caves in coastal Puerto Rico (Lace, 2008). The dissolutional origin of the flank margin cave creates a very complex perimeter, whereas the sea cave and tafoni cave tend to have smooth perimeters. This difference creates distinct area to perimeter ratios for the cave types. Because the sea caves and tafoni caves are created by erosive forces working from the outside inward, they commonly have a cave entrance width over maximum cave width ratio of near one (the entrance is the widest part of the cave). Flank margin caves initiate as dissolutional chambers that are later breached by surface erosion. The entrances are commonly small or medium sized, and the cave entrance width to maximum cave width ratio is much less than one. When a flank margin cave displays a ratio near one, that result is an indication that the cave has been breached and denuded to the extent that it is approximately half or more destroyed (Stafford et al., 2005, their Fig. 11). Finally, sealed cave chambers with humidity near 100% precipitate dense, crystalline calcite speleothems such as stalactites, stalagmites, flowstone, and other forms as a result of $CO_2$ diffusion from drip water into the cave atmosphere. In open air environments, such calcite precipitation is not possible, as evaporation competes with $CO_2$ diffusion to control the $CaCO_3$ chemistry, and crumbly tuffaceous deposits form. Taboroši et al. (2006) provide examples and criteria to determine which calcite precipitates found in open cave chambers

formed inside a sealed cave and which are the result of open-air precipitation. Sea caves and tafoni caves originate as open voids and do not commonly contain dense calcite speleothems. Cave speleothems are commonly modified by surficial exposure, degrading into a more tuffaceous character, which can complicate interpretations (Taboroši et al., 2006)

Once it has been established that a given cave is the result of dissolution, that it is a karst cave, then the type of karst cave must be determined. Karst caves fall into two main groups (Palmer, 1991): epigenic caves that usually develop as conduit systems with rapid turbulent flow, that are directly coupled to the surface hydrology and hypogenic caves that develop in a laminar or slow flow system, decoupled from the surface hydrology. Flank margin caves, by this description, are similar to hypogenic caves because they are mixing chambers and do not have rapid turbulent conduit flow. Epigenic caves formed by conduit flow commonly contain wall markings that reveal the flow to be fast and turbulent. Dissolutional features called scallops are especially effective indicators of turbulent flow direction and velocity (Curl, 1966, 1974). Turbulent conduit flow commonly leaves behind diagnostic sedimentary deposits, and distinct passage shapes, such as vadose canyons. Other cave features, such as solution pipes and vadose shafts, can also be present. These other features represent part of the coupling system that connects the epikarst to the water table, and for epigenic caves, they couple the cave directly to the surface hydrology, but for hypogenic and flank margin caves, they represent random intersections. The Kelly Hill Caves on Kangaroo Island (Hill, 1984) are an example of conduit flow of water through an eolianite ridge, perched on underlying insoluble rocks. Subsequent collapse has created a maze of chambers and passageways within and above the collapse material, and the true nature of the original dissolutional passages is obscured in most of this epigenic cave.

Flank margin caves form entirely as phreatic features under laminar or slow flow conditions. Their wall sculpture consists of cuspate pockets, bedrock columns and spans commonly of delicate configuration, and curvilinear forms that cut across primary and secondary bedrock features (Mylroie and Carew, 1990, 1995). Flank margin caves contain no evidence of rapid turbulent flow, either as wall sculpture or as sedimentary deposits. Their development in the thin, distal margin of the fresh-water lens results in low, wide chambers that intersect randomly because each chamber was an initiation point for mixing dissolution (Roth, 2004; Labourdette, et al., 2007). This passage pattern is especially true of flank margin caves developed in diagenetically immature, or eogenetic, carbonate rocks such as Quaternary eolian calcarenites, where primary porosity can be as much as 30% and the waters are able to mix across a broad volume of the rock mass (Vacher and Mylroie, 2002). Flank margin cave size is controlled primarily by the duration of time that the fresh-water lens, and hence sea level, was in a stable position (Mylroie and Mylroie, 2007; Mylroie et al., 2008b).

The southern and western coasts of Kangaroo Island are areas of high wind and ocean energy (Short and Fotheringham, 1986). The coastal outcrops of eolianite are cliffed and have retreated landward. An idea of how much retreat has occurred can be seen on the west coast of the island where the eolian calcarenites rest unconformably on the Kanmantoo Group basement rocks. Remnants of eolian calcarenite can be seen that are tens of meters away from the current eolian calcarenite scarp, indicating significant Holocene erosional removal of eolian calcarenite material (Fig. 2). Such large-scale erosion not only strips off surface features such as intertidal deposits, but also removes sea caves, tafoni, and even flank margin caves, leaving no past sea-level record. To obtain a preserved eolian calacarenite section requires investigating embayments and stream valleys that are protected from direct marine assault, but which would have held a fresh-water lens in contact with sea water at a past, higher sea-level position. For these reasons, Rocky River, reaching the coast from Snake Lagoon to Maupertius Bay (Figs. 1, 3, and 4), was selected as the prime field investigation locality to search for flank margin caves and evidence of past sea-level highstands. Cape du Couedic was also investigated because offshore islands provided some wave protection (Fig. 5).

Each location was examined by preliminary reconnaissance and revealed its own set of observations. Follow-up quantitative mapping and subsequent map interpretation, as described in the Methods section, was not done due to lack of time at the field localities. As a result, the interpretations made as to the origin of these caves were based on physical configuration and appearance only. Each of the localities below is presented as an observation set and each locality is then used to generate a set of preliminary interpretations. The overall outcome of the study is then reviewed in the Summary section.

## RESULTS AND DISCUSSION

### SNAKE LAGOON

The Flinders Chase National Park trail along Rocky River from Snake Lagoon was used as the access route to the west coast (Fig. 1). At the location where the wooden footbridge crosses over Rocky River, Kanmantoo Group rocks are visible in the streambed, and cave openings can be seen back to the east, on the north bank, high up on the eolianite valley wall. These caves were not directly visited, but have the appearance of similar features in the Bahamas that are flank margin caves. Continuing west downstream, more cave openings are visible high on the north bank. While they have the appearance from a distance of flank margin caves, they were not visited and their origin cannot be confirmed. As Rocky River and the trail approach the coast, numerous cave openings appear in the cliffs on both

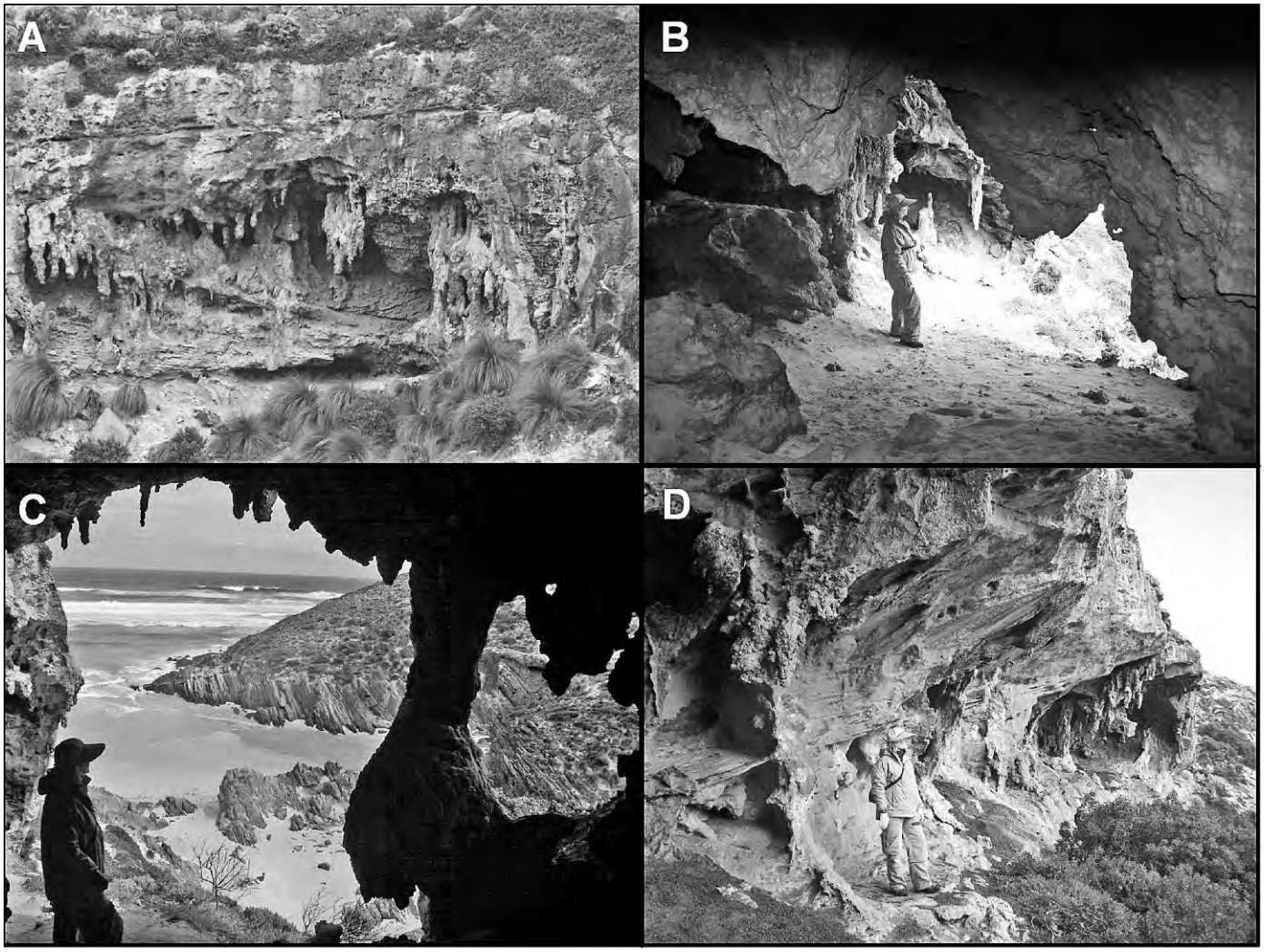


**Figure 4. Flank margin caves at Snake Lagoon. A – Cave entrance at ~25-m-elevation in the valley north wall, showing abundant flowstone, stalactite and stalagmite development. B – Cave at ~25-m-elevation in the valley south wall, showing interconnecting chambers and stalactites. C – Looking northwest from a flank margin cave in the valley south wall, showing the ocean and Kanmantoo Group basement rocks that underlie the Bridgewater Formation eolianites. D – Series of eroded flank margin cave chambers on the valley south wall, showing smooth phreatic dissolutional surfaces and secondary vadose stalactites.**

sides of the stream (Figs. 3 and 4). Those caves to the north were not visited because they were in a vertical wall (Figs. 3A and 4A), but the openings on the south bank were accessible and were thoroughly investigated (Figs. 3B, 4B, 4C, and 4D).

The single most obvious aspect of the caves is their development as a series of chambers that commonly connect internally. This observation is known as beads on a string (Mylroie et al., 2001) and reflects the degree to which individual flank margin cave chambers did or did not intersect as they grew by mixing dissolution in the distal margin of the fresh-water lens. The flank margin dissolutional origin of the caves is demonstrated by passage shape and configuration, abundant cave speleothems, and dissolutional wall morphologies (Fig. 4). The caves on the north side of the stream channel are found at two primary horizons, at approximately 25 m and 30 m elevation (Fig. 3A). The hill on the south side is higher, and contains evidence of three cave horizons at approximately 25 m, 30 m, and 35 m (Fig. 3B). The two horizons on the north side appear to correlate with the two lower horizons (at 25 m and 30 m) on the south side. At each cave horizon, the caves extend laterally over a distance of up to 100 m. The caves are not very deep, penetrating into the hillside generally less than 10 m. Because the caves have been breached by scarp retreat, the original voids had dimensions, perpendicular to the hillside, of over 10 m. The largest and most continuous band of caves, on each side of

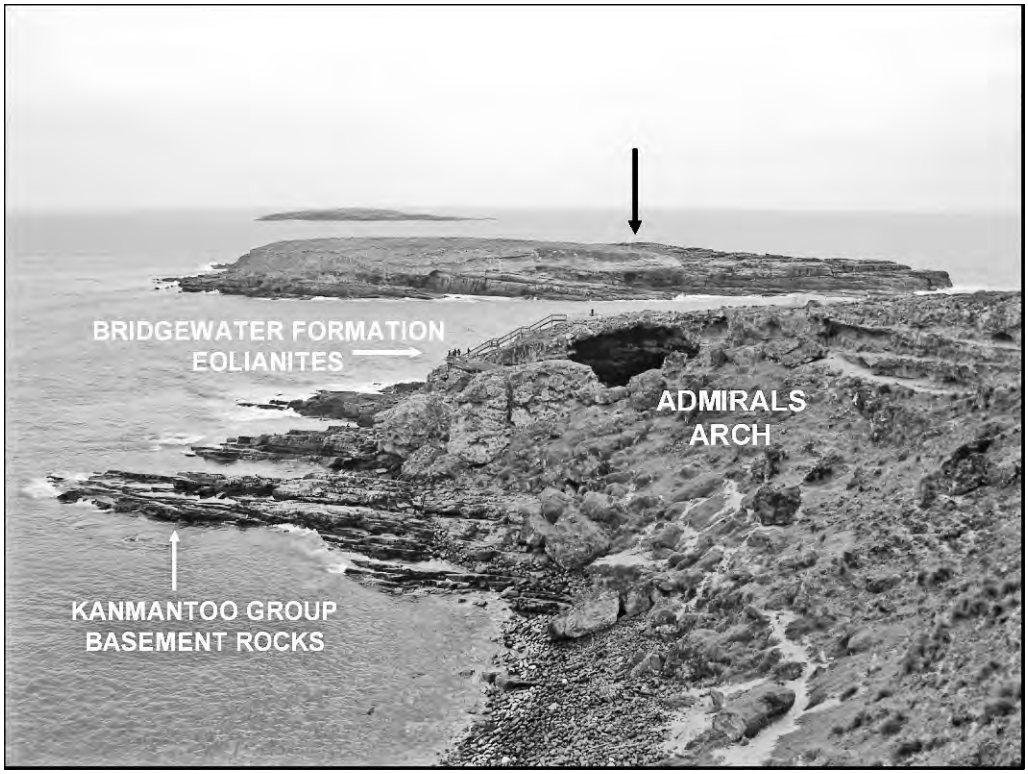


**Figure 5. Overview of Cape de Couedic, the Casuarina Islets, and Admirals Arch, Kangaroo Island. The two islands in the distance are the Casuarina Islets, also known as The Brothers. The east opening of Admirals Arch is labeled in the foreground. The black vertical arrow in the background points to the cave shown in Figure 6A. Light colored Bridgewater Formation eolianites overlie dark Kanmantoo Group basement rocks.**

the valley, is the one at 30 m, indicating perhaps a longer sea-level stillstand at that horizon than occurred at the 25 m or 35 m horizons.

The Snake Lagoon caves fit all the direct observational criteria that identify them as flank margin caves. As such, the caves represent past sea-level positions. All the caves described are above any past Quaternary glacioeustatic sea-level highstand. Therefore, uplift of Kangaroo Island is required to have occurred to place the caves at their current position with respect to modern sea level. Records of sea-level highstands on Kangaroo Island above 10 m are regarded as equivocal (Twidale and Bourne, 2002). However, Bauer (1961) indicated that a marine erosion terrace at 100 to 110 feet (30.5 to 33.5 m) was the most significant of the five terraces he recognized at 20 to 25 feet (6 to 7.6 m) and higher on Kangaroo Island. The cave observations presented here demonstrate a record of sea level well above 6 m, and at least three closely-spaced highstands are recorded. The duration of the highstands can be, in part, determined by how large the caves are. Cliff retreat since their formation has obviously decreased their size, but nonetheless, they are smaller than many flank margin caves in the Bahamas, which had 12,000 years to form. The development of the largest and most continuous caves at ~30-m-elevation agrees well with Bauer's (1961) best-developed terrace at that elevation. During glacioeustasy, the Bahamian record demonstrates that only when sea level is turning around from a lowstand or a highstand is it stable long enough to create large flank margin caves (Mylroie and Mylroie, 2007). If uplift is also involved, then the time of sea-level stability will be even less. The New Zealand flank margin cave record, in a tectonically active environment, provides time limits on lens stability (Mylroie et al., 2008b). The flank margin caves at Snake Lagoon indicate that uplift has definitely occurred, but it has been slow enough, and episodic enough, such that glacioeustatic stillstands can still leave a flank margin cave signature. Given that the last interglacial (oxygen isotope substage 5e) was 6 m higher than at present, such a eustatic sea-level elevation value should be considered when investigating the elevations of the caves found at Snake Lagoon today. In other words, the cave horizon at ~30-m-elevation could indicate an uplift of only 24 m, but that uplift would have had to occur in the last 120 ka, and other evidence at Point Ellen (below), suggests stability for the last 120 ka. The cluster of caves between ~25 m and ~35 m may represent two uplift events on a single glacioeustatic sea-level highstand, or no uplift episodes while three different glacioeustatic sea-level highstands occurred, or a combination of the two.

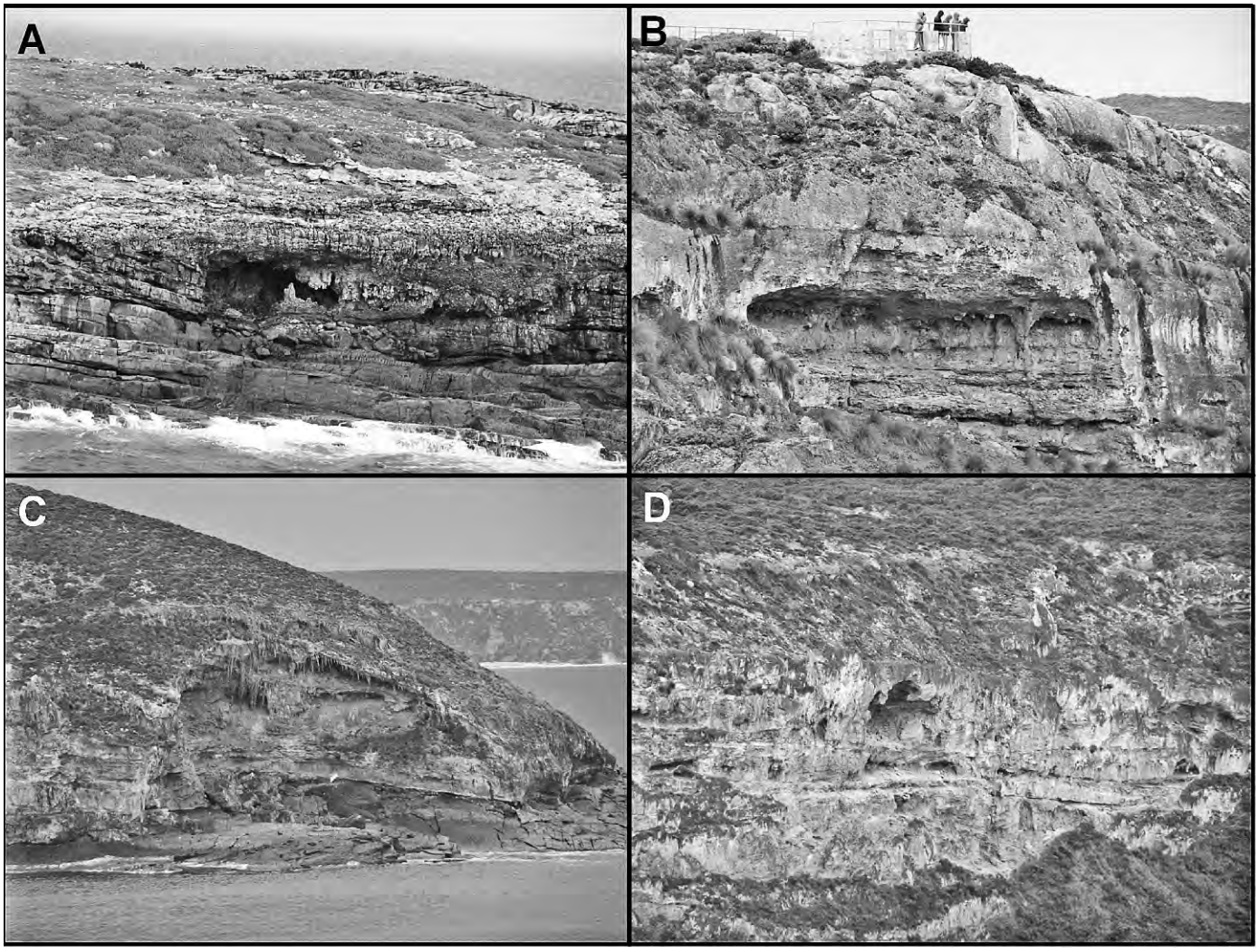


**Figure 6. Eroded flank margin caves in the Cape de Couedic area. A – Cave entrance at the eolianite-basement contact, showing stalactites and stalagmites, on the landward of the two Casuarina Islets (Figure 5). The prominent stalagmite in the cave entrance is ~1-m-high. B - Back wall of a flank margin cave intersected by cliff retreat, in a small point just east of Admirals Arch. People at top for scale. Note the curvilinear shape of the cave wall, and the stalactites and flowstone. C - Large breached flank margin cave at the major headland between Admirals Arch and Remarkable Rocks. Note the Bridgewater Formation contact with the Kanmantoo Group basement rocks near sea level, and the many stalactites and stalagmites present. D – Small flank margin cave, and associated phreatic pockets in cliff wall, between Admirals Arch and the breached cave seen in Figure 6B. The cave entrance is ~3-m-high.**

## Cape du Couedic

This location (Fig. 1) is famous for Admirals Arch, a large void penetrating a rocky point composed of Bridgewater Formation eolian calcarenites overlying Kanmantoo Group basement rocks (Fig. 5). The steep eolianite cliffs to the east contain a number of breached flank margin caves (Fig. 6). Unfortunately, Flinders Chase National Park access regulations prevented direct investigation. Visual examination demonstrates that these features have dissolutional wall morphologies, calcite speleoethems, and align horizontally with other caves on the same cliff face.

Admirals Arch was also not available for independent direct investigation, but public access places the observer where clear views can be had of the cave interior (Fig. 7). The public display on the tour path presents Admirals Arch as a product solely of wave erosion. However, visual examination of the north wall of the arch reveals that it has a series of phreatic dissolution pockets (Fig. 7C) and that the original floor of the arch was horizontal and developed in limestone above the dipping contact with the underlying Kanmantoo Group basement (Figs. 7A and 7D). The cave has abundant calcite speleothems.

Admirals Arch appears to be a breached flank margin cave, which has been modified by wave action on the current (and perhaps last interglacial) sea-level high-stand(s). The phreatic dissolution surfaces and abundant

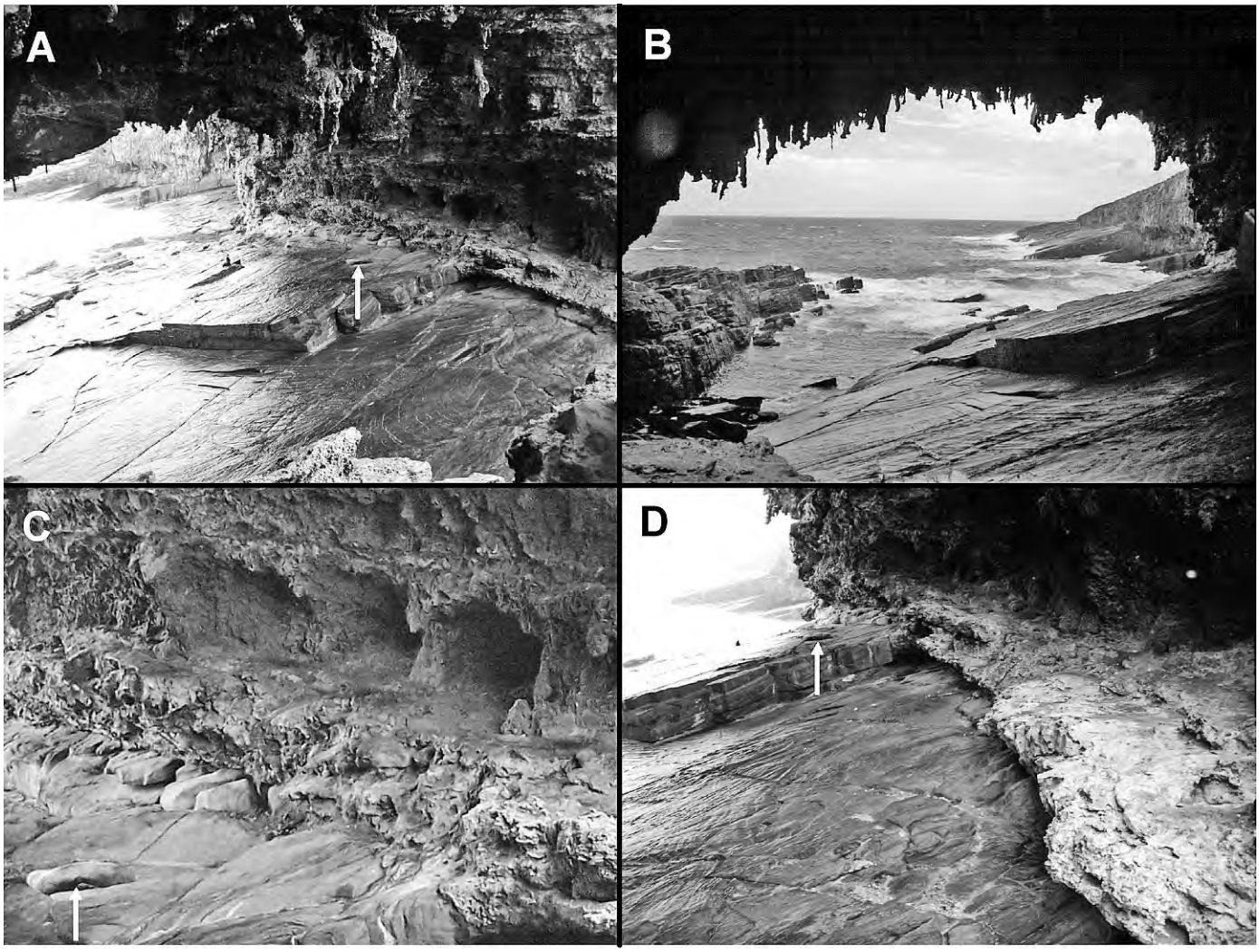


**Figure 7. Images from Admirals Arch. A – Looking northwest through the Arch. Note the steep dip of the Kanmantoo Group basement rocks, and stalactites in upper foreground. Reclining seal, 1.5-m-long, in the center of the image for scale (white arrow; same seal as in C and D). B – Looking west through the Arch, showing numerous stalactites silhouetted by the western entrance. The twisted and gnarly appearance of the stalactites is an outcome of modification by both evaporation and algal growth. C – Phreatic pockets along the north wall of the Arch, formed in the Bridgewater Formation eolianites along a horizontal datum, just above the sloping Kanmantoo Group basement rocks. Seal, ~1.5-m-long, in lower left foreground for scale (white arrow). D – Surviving section of the original horizontal floor of the Arch. The phreatic pockets of Figure 7C are in shadow ahead and to the right in the image. Seal lying in background for scale (white arrow).**

calcite speleothems indicate a cave that formed by phreatic, mixed-water dissolution, then was drained such that vadose speleothems could develop in a sealed cave chamber. The remnant flat limestone floor on the north side of the cave is another indication of flank margin cave development. That floor has been mostly stripped away by modern wave action ramping up the sloping Kanmantoo Group basement rocks.

Observation from a distance of the nearer of the two Casuarina Islets (The Brothers) revealed two caves in the eolian calcarenites on the cliff facing Admirals Arch (Figs. 5 and 6A). Remnant speleothems could be seen, but little of interior configuration was observable. The caves are quite close to the Kanmantoo Group basement contact. They appear to have phreatic morphologies, and as the islands are too small to support conduit flow, the most likely interpretation is that they are flank margin caves.

## POINT ELLEN

At Point Ellen, on the western side of Vivonne Bay (Fig. 1), a sequence of carbonate and non-carbonate rocks is exposed. As described by Ludbrook (1983), eolian calcarenites of the Bridgewater Formation overlie subtidal carbonates of the Late Pliocene Point Ellen Formation, which in turn rest unconformably on the Kanmantoo


**Figure 8. Point Ellen outcrop. A – Panorama photo of the major outcrop, looking north. The foreground is Kanmantoo Group basement rocks, the cave and laterally adjacent rocks are Point Ellen Formation marine carbonates, and the overlying rocks are Bridgewater Formation eolianites. Person in white oval for scale. B – Outcrop of the Point Ellen Formation, showing numerous mollusk shells. Pencil is 15-cm-long for scale (arrow). C – Closer view of the section in (A). Kanmantoo Group basement rocks in the foreground, grade upward into a Kanmantoo boulder and rubble facies interfingered with Point Ellen Formation, which forms the back wall of the cave. The Bridgewater Formation eolianites form the cave roof and top of the section. Person in black oval for scale.**

Group basement rocks (Fig. 8). Our observations indicate that the eolian calcarenites drape over the Point Ellen Formation, and a fossil epikarst with a terra rossa paleosol separates the two units. The eolian calcarenites extend seaward of the Point Ellen Formation and sit directly in contact with Kanmantoo Group basement rocks (Fig. 9A). The outcrop is very complex and contains a wealth of information. The contact of the Point Ellen Formation with the underlying Kanmantoo Group basement rocks commonly contains rounded clasts of the basement rocks in the first 1 to 2 meters of the Point Ellen Formation (Figs. 9B and 9C). Such evidence is an indication of wave base actively eroding the basement rocks at the time of Point Ellen Formation deposition. This wave-base evidence places limits on the depth of deposition of the Point Ellen Formation. The transport of these eroded Kanmantoo Group rocks down a submarine slope cannot be discounted, however. The report by Ludbrook (1983) that eolian calcarenites of the Bridgewater Formation interfinger with Late Pliocene Point Ellen Formation subtidal facies at Point Reynolds, east of Point Ellen, is another indication that the Point Ellen Formation was deposited in relatively shallow water.

The contact of the Point Ellen Formation with the overlying Bridgewater Formation is a paleokarst, a fossilized epikarst with a terra rossa paleosol. A paleokarst requires that the Point Ellen Formation was subaerially exposed for a substantial time. Subsequently, the Bridgewater Formation was deposited. The area where the Bridgewater Formation eolian calcarenites extend over the Point Ellen Formation has a relief of several meters (Fig. 10), and at this point, the Point Ellen Formation is cliffed and a paleo-talus occupies the space between the Bridgewater Formation and the Point Ellen Formation. The setting is suggestive that the Point Ellen Formation was deposited in waters within reach of wave base, and then as uplift occurred, the Point Ellen material was cliffed by wave action as it transited into the supratidal environment. It remained exposed for a period of time long enough to develop a mature epikarst and terra rossa

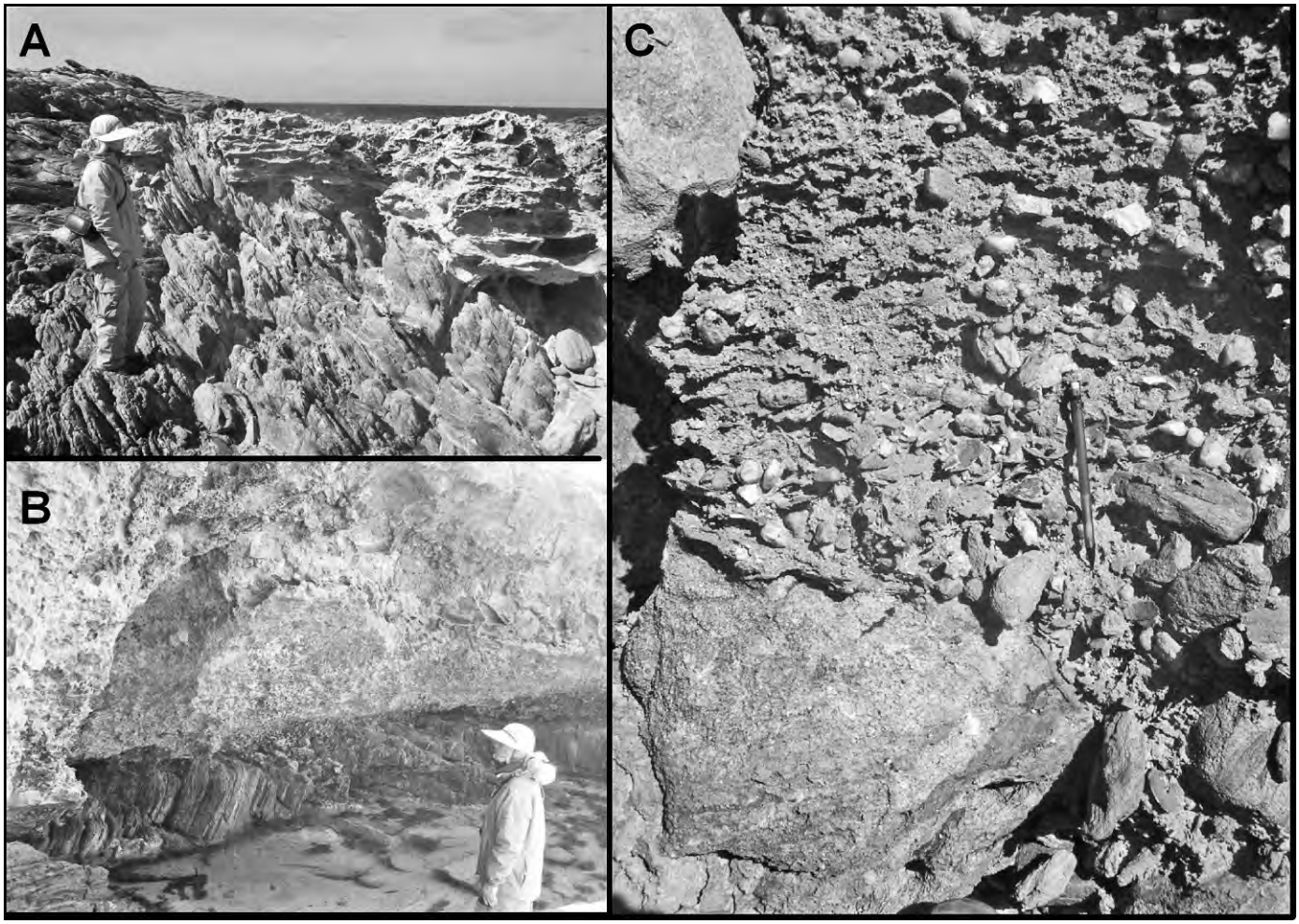


**Figure 9. A – Bridgewater Formation eolianites lying directly on deformed Kanmantoo Group basement rocks. The Point Ellen Formation is missing. The location is where the photograph of Figure 8A was taken, seaward of the main outcrop by about 30 m. B. – West (left) around the point shown in the far left of Figure 8A, the Point Ellen Formation rests on a planated bench of Kanmantoo Group basement rocks. Weathered boulders and cobbles of Kanmantoo Group basement rocks are visible 1 to 2 m above the contact. C – Point Ellen Formation rocks, with abundant subtidal fossils, intermixed with, and overlying, Kanmantoo Group basement rocks present as boulders and cobbles. Pencil is 15-cm-long for scale.**

soil. A talus formed along the former sea cliff. Based on Bahamian examples, the minimum time frame for terra-rossa palesol development would be in the 50 to 100 ka range (Carew and Mylroie, 1997). Subsequently, the Point Ellen Formation was entombed by Bridgewater Formation eolian calcarenites that overrode the unit, overrode the talus deposit, and extended on to the Kanmantoo Group basement rocks at a sea level lower than present.

The outcrop also has a cave in it (Figs. 8A and 8C). This cave is within reach of storm waves. It is difficult to determine if the cave is a breached flank margin cave or a sea cave. The cave contains floor to ceiling columns that are not speleothems, but rather remnant solution pipes (Milnes et al., 1983). Because the column walls became micritized when they were part of an active epikarst, they are now stronger than the host rock and weather out in relief (Fig. 11). Such features are common on coastal South Australia in Bridgewater Formation eolian calcarenites. The survival of these columns within a cave allows their connection to the original epikarst surface to be observed. The solution pipe columns to the east (right facing into the cave) are made up of paleosol material (Fig. 11C), but to the west (left facing into the cave) the material is strongly-indurated Point Ellen material that the solution pipe had drilled into (Fig. 11B). The correct interpretation of the cave is important. If it is a sea cave, produced as a result of storm activity on this coast, then it is a Holocene feature. If it is a flank margin cave, then it is at least 125 ka old and formed on the last interglacial sea-level highstand (MIS 5e). As benches at 3 m elevation from the last interglacial are reported on the southern shore of Kangaroo Island (Short and Fotheringham, 1986; Twideale and Bourne,

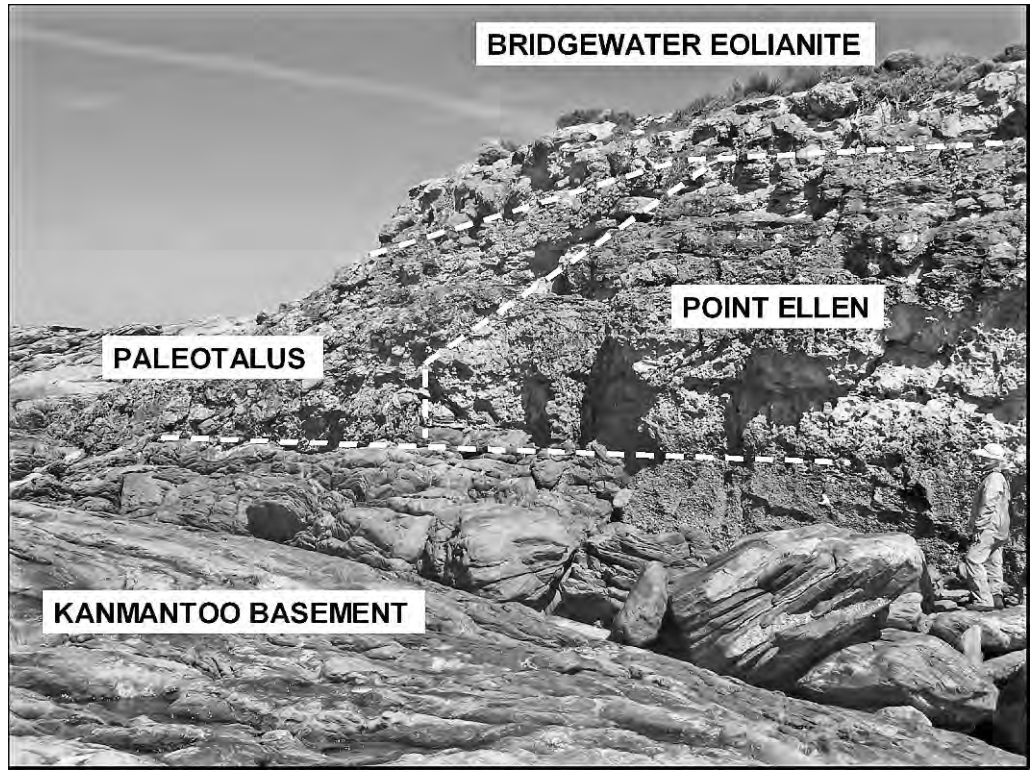


**Figure 10. Outcrop section at Point Ellen, the left portion of Figure 8A. Kanmantoo Group basement rocks at the bottom, passing through a rubble facies into Point Ellen Formation marine carbonates. A paleo-cliff separates the Point Ellen Formation laterally from a paleo-talus to the left (south). Bridgewater Formation eolianites overlie the Point Ellen Formation and the paleo-talus unit. Seaward (left or south) of this location, the Bridgewater Formation eolianites overlie the Kanmantoo Group basement rocks directly, as shown in Figure 9A.**

2002), a fresh-water lens could easily have existed in this outcrop during the last interglacial and a flank margin cave formed. If these benches, and the cave, are truly last interglacial, then uplift over the last 120 ka has been minimal and the uplift at Snake Creek was at least 30 m and occurred prior to MIS 5e.

### Remarkable Rocks

The tafoni developed in Cambro-Ordovician granite at Remarkable Rocks (Figs. 1 and 12) provide a cautionary tale. The interior of several of the larger tafoni have wall sculpture that is especially cuspate and dimpled and bare a striking resemblance to dissolutional wall morphology as found in flank margin caves (Fig. 12C versus Fig. 12D). They also have been misidentified. Twidale and Bourne (2002, their Figure 14c) presented a photograph of the interior of a tafoni at Remarkable Rocks, calling the wall surface mammillated. This error is a result of printing the picture upside down, such that lighting and shadows invert the apparent relief in the picture. The features are clearly cuspate and not mammillary, as seen in Figures 12B and C. Because such cuspate features are part of the visual inventory used to define a cave in limestone as phreatic in origin, the Remarkable Rocks example indicates that multiple lines of evidence should be used to identify a cave's origin. A review of tafoni, their mechanisms of formation, and the techniques utilized to differentiate them from dissolutional caves can be found in Owen (2007).

### Hanson Bay

The east side of Hanson Bay (Fig. 1) begins as a stretch of beach, and gradually trending southeastward, becomes a high eolian ridge with sea cliffs down to the ocean below. High up on these cliffs are a series of planated notches (Fig. 13A) that could easily represent small wave-eroded platforms. The platforms have a rubble deposit of rounded clasts in a grey matrix (Fig. 13B). These are clearly not a paleosol layer, in which the clasts would be more angular and the matrix would carry the red color of a terra rossa paleosol. Such deposits, when found in the Bahamas, indicate a back beach or rock platform rubble facies (Florea et al., 2001). It is therefore likely that these notches indicate a sea-level highstand approximately 30 m to 35 m above modern sea level, which would require tectonic uplift. Such a sea-level interpretation supports the observations of flank margin caves at similar elevations at Snake Lagoon to the west.

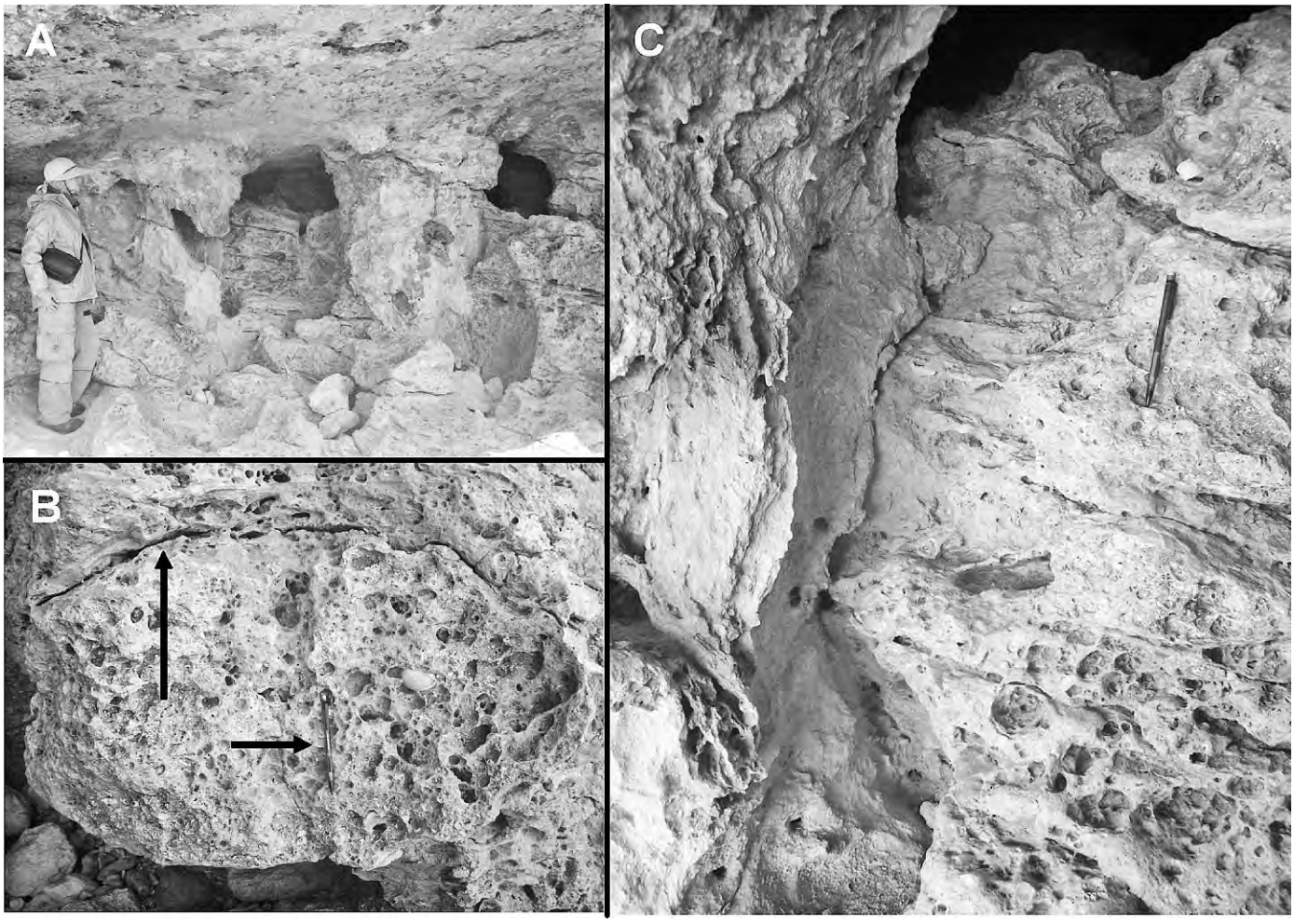


**Figure 11. The cave at Point Ellen. A – Looking into the cave, with the Bridgewater Formation eolianites forming the cave roof, and infilled solution pits descending into the Point Ellen Formation. B – Close up of Bridgewater Formation eolianites on top of Point Ellen marine carbonates. The contact is the upward convex line arching through the top portion of the photograph (long vertical arrow). Pencil is 15-cm-long for scale (short horizontal arrow). C – Vertical contact of Bridgewater Formation eolianites and paleosol infilling a solution pit to the left, with Point Ellen Formation marine carbonates to the right. Pencil is 15-cm-long for scale.**

## SUMMARY

The observations made on Kangaroo Island in September 2006 are admittedly cursory and superficial. They consist of simple visual descriptions at the macroscopic scale, without detailed site survey or rock-sample analysis. On the other hand, the simple observations allow new interpretations to be offered that may help illuminate geologic processes on the island. None of the previous workers who interpreted the Cainozoic geology of Kangaroo Island utilized the potential data stored in caves on the island.

It is clear that flank margin caves are present on Kangaroo Island, and this paper is the first report of their existence there. The positions of the flank margin caves at Snake Lagoon reveal sea-level highstands of at least three elevations: ~25 m, ~30 m, and ~35 m, substantiating early claims by Bauer (1961) that Twidale and Bourne (2002) later called into question. The absence of flank margin caves from many high-energy coasts underlain by Kanmantoo Group rocks verifies the vulnerability of flank margin caves to destruction by powerful wave-generated slope-retreat processes. In such locales, flank margin caves are preserved in embayments and surface water course incisions, as at Snake Lagoon, or by offshore barriers, as at Cape du Couedic. Observations from Hanson Bay show marine erosion features consistent with development during one or more sea-level highstands at approximately 30 m to 35 m, concurring with observations at Snake Lagoon, which would require tectonic uplift.

At Cape du Couedic, an arch in Bridgewater Formation eolianites resting on Kanmantoo Group rocks is presented to the public as being the result of wave erosion with wave energy being focused on the point by the presence of the

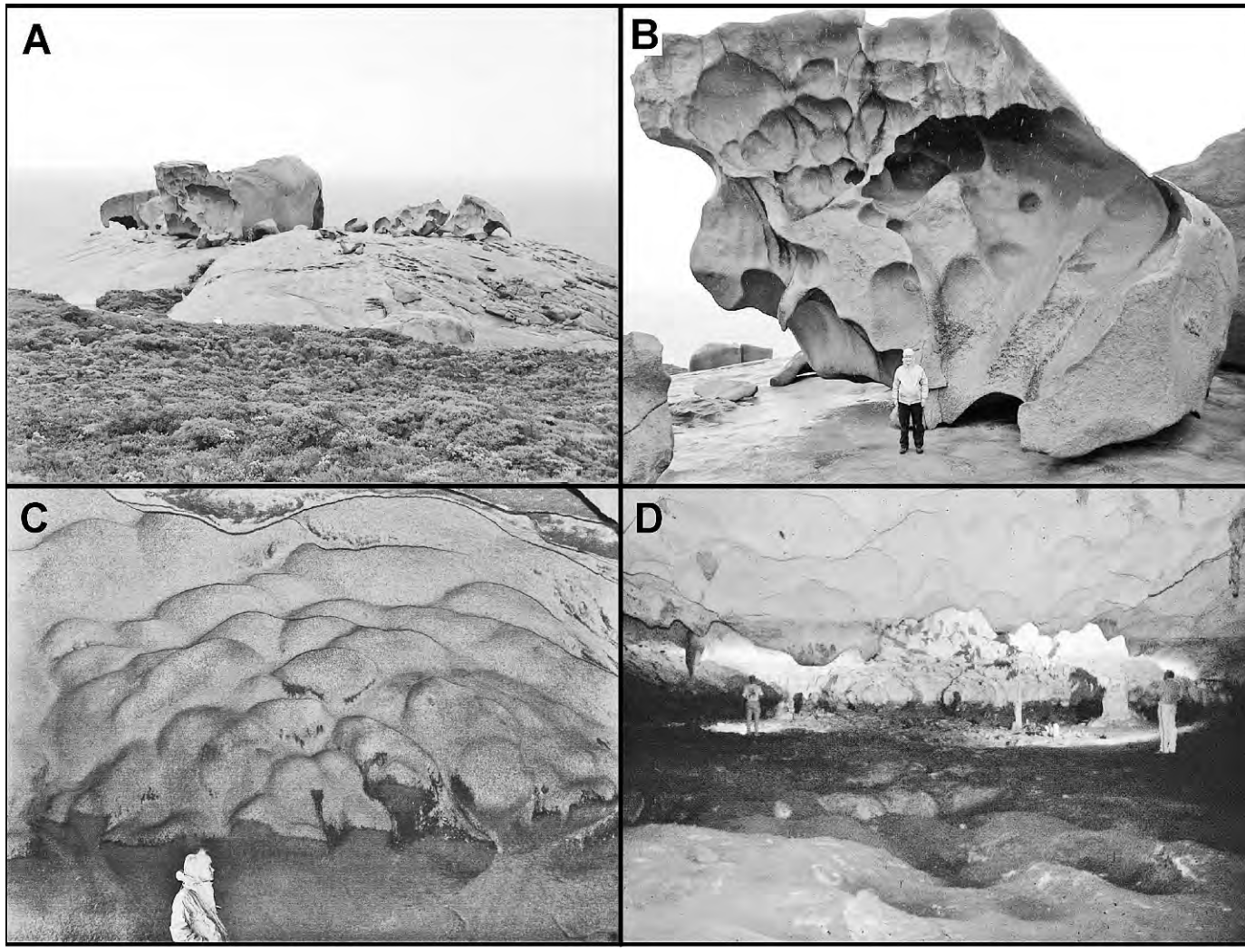


**Figure 12. Remarkable Rocks. A – The Remarkable Rocks, where tafoni have developed in granitic rocks. B – Classic cavernous weathering to produce a complicated tafoni. C – Inside one of the larger tafoni, with pockets or cusps eroded into the ceiling. D – Chamber in Salt Pond Cave, Long Island, Bahamas, in eolian calcarenites, showing the pockets and cusps considered as one of the diagnostic indicators of cave formation by phreatic dissolution. Compare with Figure 12C. Two people in background, left and right, for scale.**

islands offshore. The evidence from the eolianite portion of the arch suggests that the original void formed as a flank margin cave and was subsequently breached by wave erosion. The offshore islands not only acted as a focusing mechanism for wave energy, but also provided a barrier function that has prevented the entire eolianite section at Admirals Arch from being removed by wave erosion.

At Point Ellen, a cave has been useful in interpreting the stratigraphic section of eolian, marine, and basement rock relationships. The preserved fossil epikarst and paleosol at this location place boundary conditions on the timing of the carbonate-depositional events. A paleo-talus is described here for the first time. The cave itself is indeterminate in origin, but if it is a flank margin cave, it would provide a second line of evidence to suggest that uplift on Kangaroo Island has been minimal for the last 120 ka. Remarkable Rocks demonstrate how non-dissolutional erosive forces can produce surfaces in tafoni that mimic one of the classic indicators of flank margin cave development, and as such, are a warning about using single lines of evidence to make important cave origin interpretations.

## Acknowledgments

The authors thank the Department of Geosciences, Mississippi State University, for granting John Mylroie a sabbatical, and Joan Mylroie a leave of absence, and for providing support for the field expedition. Michael Kidd, Kelly Hill Cave, provided helpful information and guidance on Kangaroo Island. Peter Bell, Grant Gartrell, Ken Grimes, John Webb, Nick White and Sue White

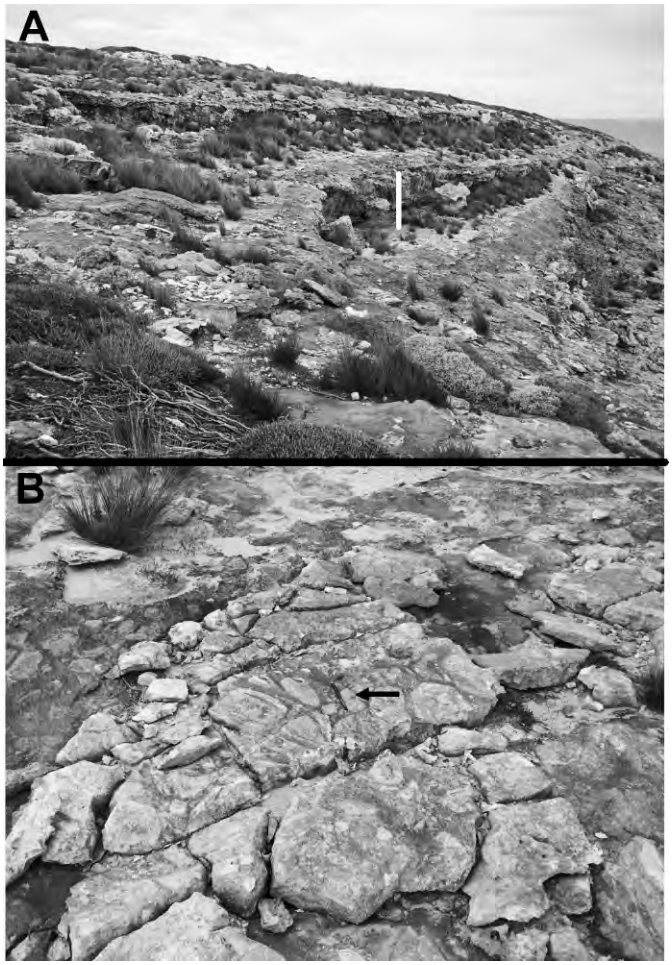


**Figure 13. Hanson Bay. A – Long, linear and level notches cut into the eolianites of the Bridgewater Formation. Vertical white bar 1-m-long for scale. B – Rubble facies found on the floor of the notches shown in Figure 13A. The matrix is sandy and white or gray, not red, and the clasts are more rounded than normally seen in a paleosol, and are interpreted as a back-beach rubble facies. Pencil 15-cm-long for scale (black arrow, same length as the pencil).**

provided significant logistical support and important scientific insight.

## REFERENCES

Bauer, F.H., 1961, Chronic problems of terrace study, South Australia: Zeitschrift für Geomorphologie, v. 3, p. 57–72.

Belperio, A.P., and Flint, R.B., 1999, Kangaroo Island biological survey: Geomorphology and geology, *in* Robinson, A.C., and Armstrong, D.M., eds., A biological survey of Kangaroo Island, South Australia: Department of Environment, Heritage, and Aboriginal Affairs, South Australia, p. 19–31.

Bottrell, S.H., Carew, J.L., and Mylroie, J.E., 1993, Bacterial sulphate reduction in flank margin environments: Evidence from sulphur isotopes, *in* White, B., ed., Proceedings of the 6th Symposium on the Geology of the Bahamas: Port Charlotte, Florida, Bahamian Field Station, p. 17–21.

Carew, J.L., and Mylroie, J.E., 1995, Quaternary tectonic stability of the Bahamian Archipelago: Evidence from fossil coral reefs and flank margin caves: Quaternary Science Reviews, v. 14, p. 144–153.

Carew, J.L., and Mylroie, J.E., 1997, Geology of the Bahamas, *in* Vacher, H.L., and Quinn, T.M., eds., Geology and hydrogeology of carbonate islands: Amsterdam, Elsevier, Developments in Sedimentology, v. 54, p. 91–139.

Chen, J.H., Curran, H.A., White, B., and Wasserburg, G.J., 1991, Precise chronology of the last interglacial period: $^{234}U$-$^{230}Th$ data from fossil coral reefs in the Bahamas: Geological Society of America Bulletin, v. 103, p. 82–97.

Curl, R.L., 1966, Scallops and flutes: Transactions of the Cave Research Group of Great Britain, v. 7, p. 121–160.

Curl, R.L., 1974, Deducing flow velocity in cave conduits from scallops: National Speleological Society Bulletin, v. 36, p. 1–5.

Drexel, J.F., and Preiss, W.V., 1995, The geology of South Australia, Volume 2, The Phanerozoic: Geological Survey of South Australia, Bulletin 54, 347 p.

Florea, L., Mylroie, J., and Carew, J., 2001, Karst genetic model for the French Bay Breccia deposits, San Salvador, Bahamas: Theoretical and Applied Karstology, v. 13–14, p. 57–65.

Frank, E.F., Mylroie, J., Troester, J., Alexander, E.C., and Carew, J.L., 1998, Karst development and speleologensis, Isla de Mona, Puerto Rico: Journal of Cave and Karst Studies, v. 60, no. 2, p. 73–83.

Hill, A.L., 1984, Origin of the Kelly Hill Caves: Helictite, v. 22, p. 6–10.

James, P.R., and Clark, I.F., 2002, Geology, *in* Davis, M., Twidale, C.R., and Tyler, M.J., eds., Natural History of Kangaroo Island: Richmond, Australia, Royal Society of South Australia, p. 1–22.

Jenson, J.W., Keel, T.M., Mylroie, J.R., Mylroie, J.E., Stafford, K.W., Taborosi, D., and Wexel, C., 2006, Karst of the Mariana Islands: The interaction of tectonics, glacioeustasy and fresh-water/sea-water mixing in island carbonates: Geological Society of America Special Paper 404, p. 129–138.

Labourdette, R., Lascu, I., Mylroie, J., and Roth, M., 2007, Process-like modeling of flank margin caves: From genesis to burial evolution: Journal of Sedimentary Research, v. 77, p. 965–979.

Lace, M.J., 2008, Coastal cave development in Puerto Rico: Journal of Coastal Processes, v. 24, no. 2, p. 508–518.

Ludbrook, N.H., 1983, Molluscan faunas of the Early Pleistocene Point Ellen Formation and Burnham Limestone, South Australia: Transactions of the Royal Society of South Australia, v. 107, p. 37–49.

McNeill, D.F., 2005, Accumulation rates from well-dated late Neogene carbonate platforms and margins: Sedimentary Geology, v. 175, p. 73–87.

Milnes, A.R., Ludbrook, N.H., Lindsay, J.M., and Cooper, B.J., 1983, The succession of Cainozoic marine sediments on Kangaroo Island, South Australia: Transactions of the Royal Society of South Australia, v. 107, p. 1–36.

Mylroie, J.E., 1980, Caves and Karst of San Salvador: Field Guide to San Salvador Island, Bahamas: Ft Lauderdale, Florida, College Center of the Finger Lakes, p. 67–91.

Mylroie, J.E., and Carew, J.L., 1990, The flank margin model for dissolution cave development in carbonate platforms: Earth Surface Processes and Landforms, v. 15, p. 413–424.

Mylroie, J.E., and Carew, J.L., 1991, Erosional notches in Bahamian carbonates: Bioerosion or groundwater dissolution?, *in* Bain, R.J., ed., Proceedings of the 5th Symposium on the Geology of the Bahamas: Port Charlotte, Florida, Bahamian Field Station, p. 185–191.

Mylroie, J.E., and Carew, J.L., 1995, Chapter 3, Karst development on carbonate islands, *in* Budd, D.A., Harris, P.M., and Saller, A., eds., Unconformities and Porosity in Carbonate Strata: American Association of Petroleum Geologists Memoir 63, p. 55–76.

Mylroie, J.E., Carew, J.L., and Vacher, H.L., 1995, Karst development in the Bahamas and Bermuda, *in* Curran, H.A., and White, B., eds., Terrestrial and Shallow Marine Geology of the Bahamas and Bermuda: Geological Society of America Special Paper 300, p. 251–267.

Mylroie, J.E., Jenson, J.W., Taborosi, D., Jocson, J.M.U., Vann, D.T., and Wexel, C., 2001, Karst features of Guam in terms of a general model of carbonate island karst: Journal of Cave and Karst Studies, v. 63, no. 1, p. 9–22.

Mylroie, J.E., and Mylroie, J.R., 2007, Development of the Carbonate Island Karst Model: Journal of Cave and Karst Studies, v. 69, p. 59–75.

Mylroie, J.R., Mylroie, J.E., Owen, A.M., and Waterstrat, W.J., 2008a, Coastal caves in Bahamian eolianites: Origin as flank margin caves,

sea caves, and tafoni caves [abs]: Journal of Cave and Karst Studies, v. 70, no. 3, p. 179–180.

Mylroie, J.E., Mylroie, J.R., and Nelson, C.N., 2008b, Flank margin cave development in telogenetic limestones of New Zealand: Acta Carsologica, v. 37, no. 1, p. 15–40.

Mylroie, J.E., and Mylroie, J.R., 2009, A rapid reconnaissance of a Quaternary eolianite island of Australia: Rottnest Island, with comparisons to the Bahamas, *in* Martin, J.B., and Siewers, F.D., eds., Proceedings of the 14th Symposium on the geology of the Bahamas and other carbonate regions, June 2008, Gerace Research Centre, San Salvador Island, Bahamas: (in press).

Owen, A.M., 2007, Tafoni caves in Quaternary carbonate eolianites: Examples from The Bahamas [MSc. thesis]: Mississippi State, Mississippi State University, 187 p. http://library.msstate.edu/etd/show.asp?etd=etd-05142007-143443

Palmer, A.N., 1991, Origin and morphology of limestone caves: Geological Society of America Bulletin, v. 103, p. 1–25.

Raeisi, E., and Mylroie, J.E., 1995, Hydrodynamic behavior of caves formed in the fresh-water lens of carbonate islands: Carbonates and Evaporites, v. 10, no. 2, p. 207–214.

Roth, M.J., 2004, Inventory and geometric analysis of flank margin caves of the Bahamas [MSc. thesis]: Mississippi State University, 117 p. http://library.msstate.edu/etd/show.asp?etd=etd-07062004-164930

Roth, M.J., Mylroie, J.E., Mylroie, J.R., Ersek, V., Ersek, C.C., and Carew, J.L., 2006, Flank Margin Cave Inventory of the Bahamas, *in* Davis, R.L., and Gamble, D.W., eds., Proceedings of the 12th Symposium on the Geology of the Bahamas and Other Carbonate Regions: San Salvador, Bahamas, Gerace Research Center, p. 153–161.

Short, A.D., and Fotheringham, D.G., 1986, Coastal morphodynamics and Holocene evolution of the Kangaroo Island coast, South Australia, Tech Report No. 86/1: Sidney, Australia, University of Sydney, Coastal Studies Unit, 92 p.

Stafford, K.W., Mylroie, J.E., Taboroši, D., Jenson, J.W., and Mylroie, J.R., 2005, Karst development on Tinian, Commonwealth of the Northern Mariana Islands: Controls on dissolution in relation to the carbonate island karst model: Journal of Cave and Karst Studies, v. 67, no. 1, p. 14–27.

Taboroši, D., Mylroie, J.E., and Kirakawa, K., 2006, Stalactites on tropical cliffs: Remnants of breached caves or subaerial tufa deposits? Zeitschrift fur Geomorphologie, v. 50, p. 117–139.

Twidale, C.R., and Bourne, J.A., 2002, The Land Surface, *in* Davis, M., Twidale, C.R., and Tyler, M.J., eds., Natural History of Kangaroo Island: Richmond, Australia, Royal Society of South Australia, p. 23–35.

Vacher, H.L., and Mylroie, J.E., 2002, Eogenetic karst from the perspective of an equivalent porous medium: Carbonates and Evaporites, v. 17, no. 2, p. 182–196.

Vogel, P.N., Mylroie, J.E., and Carew, J.L., 1990, Limestone petrology and cave morphology on San Salvador Island, Bahamas: Cave Science, v. 17, p. 19–30.

Waterstrat, W.J., 2007, Morphometric differentiation of flank margin caves and littoral, or sea caves [MSc. thesis]: Mississippi State University, 201 p. http://library.msstate.edu/etd/show.asp?etd=etd-04052007-150907

D. Lacelle, B. Lauriol, and I.D. Clark – Formation of seasonal ice bodies and associated cryogenic carbonates in Caverne de l'Ours, Québec, Canada: Kinetic isotope effects and pseudo-biogenic crystal structures. *Journal of Cave and Karst Studies,* v. 71, no. 1, p. 48–62.

# FORMATION OF SEASONAL ICE BODIES AND ASSOCIATED CRYOGENIC CARBONATES IN CAVERNE DE L'OURS, QUÉBEC, CANADA: KINETIC ISOTOPE EFFECTS AND PSEUDO-BIOGENIC CRYSTAL STRUCTURES

Denis Lacelle[1], Bernard Lauriol[2], and Ian D. Clark[3]

**Abstract:** This study examines the kinetics of formation of seasonal cave ice formations (stalagmites, stalactites, hoar, curtain, and floor ice) and the associated cryogenic calcite powders in Caverne de l'Ours (QC, Canada), a shallow, thermally-responsive cave. The seasonal ice formations, which either formed by the: (1) freezing of dripping water (ice stalagmite and stalactite); (2) freezing of stagnant or slow moving water (floor ice and curtain ice) and; (3) condensation of water vapor (hoar ice), all (except floor ice) showed kinetic isotope effects associated with the rapid freezing of calcium – bicarbonate water. This was made evident in the δD, $\delta^{18}O$ and *d* (deuterium excess) compositions of the formed ice where they plot along a kinetic freezing line. The cryogenic calcite powders, which are found on the surface of the seasonal ice formations, also show kinetic isotope effects. Their $\delta^{13}C$ and $\delta^{18}O$ values are among the highest measured in cold-climate carbonates and are caused by the rapid rate of freezing, which results in strong C-O disequilibrium between the water, dissolved C species in the water, and precipitating calcite. Although the cryogenic calcite precipitated as powders, diverse crystal habits were observed under scanning electron microscope, which included rhombs, aggregated rhombs, spheres, needles, and aggregated structures. The rhomb crystal habits were observed in samples stored and observed at room temperature, whereas the sphere and needle structures were observed in the samples kept and observed under cryogenic conditions. Considering that the formation of cryogenic calcite is purely abiotic (freezing of calcium – bicarbonate water), the presence of spherical structures, commonly associated with biotic processes, might represent vaterite, a polymorph of calcite stable only at low temperatures. It is therefore suggested that care should be taken before suggesting biological origin to calcite precipitates based solely on crystal habits because they might represent pseudo-biogenic structures formed through abiotic processes.

## Introduction

Most terrestrial freshwaters have a chemistry dominated by $Ca^{2+}$ and $HCO_3^-$ solutes that originates from the preferential dissolution of calcareous components of the bedrock. Even in crystalline bedrock environments, where the bedrock can comprise less than 1% carbonate, calcite dissolution will dominate over silicate weathering due to the higher solubility of calcite over silicate (White et al., 1999). Therefore, when a solution containing both $Ca^{2+}$ and $HCO_3^-$ solutes freezes, precipitation of cryogenic calcite ($CaCO_3$), or other forms of low-temperature carbonates, like vaterite (μ-$CaCO_3$) and ikaite ($CaCO_3 \cdot 6H_2O$), is expected, irrespective of the local geology. In the natural environment, cryogenic carbonates are quite common in areas where the air temperatures fall below the freezing point for at least a few months of the year. Freezing caves, located in areas of limestone bedrock, are among the most susceptible environments in which to find cryogenic carbonate precipitates (Clark and Lauriol, 1992; Zak et al., 2004; Lacelle, 2007; Zak et al., 2008; Richter and Riechelmann, 2008). However, cryogenic carbonates are also commonly encountered on the surface of aufeis or river icings (Hall, 1980; Pollard, 1983; Clark and Lauriol, 1997; Lacelle et al., 2006) and on the surface of clasts (Hallet, 1976; Fairchild et al., 1993; Marlin et al., 1993; Courty et al., 1994). The most commonly precipitated carbonate mineral is calcite, but vaterite and ikaite have also been reported from some high Arctic and Antarctic environments (Pauly, 1963; Suess et al, 1982; Marion, 2001; Omelon et al., 2001; Grasby, 2003). However, these metastable minerals have never been identified in freezing caves.

Experimental work done by Hallet (1976), Fairchild et al. (1996), and Killawee et al. (1998) have shown that the formation of cryogenic carbonate minerals involved a

[1] Planetary Exploration and Space Astronomy, Canadian Space Agency, 6767 route de l'aeroport, St-Hubert, QC, J3Y 8Y9, Canada. denis.lacelle@asc-csa.gc.ca
[2] Department of Geography, University of Ottawa, 60 University St., Ottawa, ON, K1N 6N5, Canada. blauriol@uottawa.ca
[3] Department of Earth Sciences, University of Ottawa, 140 Louis Pasteur, Ottawa, ON, K1N 6N5, Canada. idclark@uottawa.ca

series of chemical processes and unique kinetics of dissolution leading to the precipitation of carbonates. During initial freezing of a calcium bicarbonate solution, the $Ca^{2+}$ and $HCO_3^-$ solutes increase to a point where eventually their ion activity product might reach and exceed the calcite saturation point, causing calcite to precipitate from the solution. During their experimental work, Fairchild et al. (1996) identified the precipitation of both calcite and vaterite minerals, represented by rhombs (or aggregated rhombs) and spheres, respectively. For cryogenic calcite precipitated under equilibrium conditions, it was recently demonstrated by Lacelle et al. (2006) that in addition to the rate of freezing, the degree of C-O isotope fractionation is also controlled by the attainment of calcite saturation. However, when the rate of freezing is increased, the amount of C-O isotope fractionation between calcite and water results in strong C-O isotope disequilibrium, producing calcite with high stable C-O isotope composition (Clark and Lauriol, 1992). Therefore, the chemical processes and the rate at which they occur in the calcite-water-gas system play an important role in determining the stable C-O isotope composition and crystal habits of cryogenic carbonates.

In freezing caves, cryogenic carbonate precipitates are commonly observed on the surface of perennial/seasonal ice formations (i.e., ice plugs, stalagmites, and stalactites) as cryptocrystalline carbonate powders, or on the floor of freezing caves as loose calcite pearls or carbonate powders (e.g., Clark and Lauriol, 1992; Zak et al., 2004). In this study, we (1) examine the geochemical and stable O-H isotope composition of the various types of seasonal ice formations in Caverne de l'Ours (Québec, Canada), a thermally-responsive cave, and (2) analyze the mineralogy (XRD), micro-morphologies (SEM) and stable C-O isotope composition of the cryogenic carbonate powders associated with the formation of the various ice formations. We also document a new type of carbonate discovered in Caverne de l'Ours, spider silk calcite. The micro-morphologies of the cryogenic calcite powders were examined under cryogenic conditions and at room temperature to determine the potential presence of calcite polymorphs (vaterite or ikaite), which have shown characteristic crystal habits (e.g., Omelon et al., 2001; Grasby, 2003). To further understand the conditions and processes under which the cryogenic cave calcite precipitated, their micro-morphologies and stable C-O isotope composition are compared to those related to aufeis. Aufeis, which are sheet-like masses of horizontally layered ice that accumulate on river channels by successive overflow of perennial groundwater fed springs upon exposure to cold temperature, contain various cryptocrystalline powders, including calcite, vaterite and ikaite, within the individual ice layers. Consequently cryogenic aufeis and cave calcite powders are the only known types of cryogenic calcite precipitating as cryptocrystalline powders.

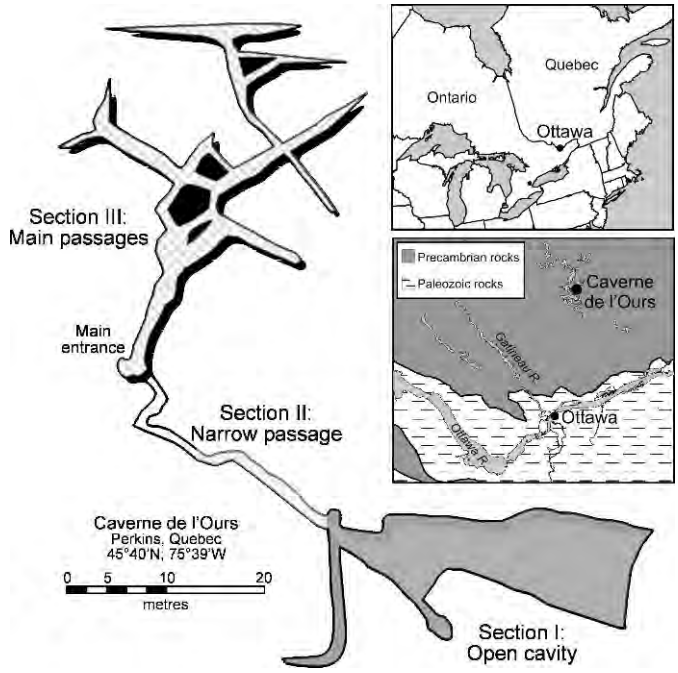


**Figure 1. Location and topography of Caverne de l'Ours (QC, Canada). The seasonal ice formations and associated cryogenic carbonates were collected in the open cavity (section I). Moonmilk deposits are found in the main passages (section III).**

## CAVERNE DE L'OURS

### SITE DESCRIPTION

Caverne de l'Ours (45°40′N; 75°39′W) is located in the Ottawa valley region on Precambrian Grenville marble outcrop and near the eastern limit of the Canadian Shield (Fig. 1). The cave is located in a region characterized by large seasonal temperature variations and relatively high precipitation. The mean annual air temperature $T$ (1970–2000) recorded at the Ottawa meteorological station is 6.0 ± 0.8 °C (January mean $T$: −10.8 ± 2.9 °C; July mean $T$: 20.9 ± 1.1 °C), and the area receives a total of 945 mm of precipitation annually, of which one-third falls as snow (Environment Canada, 2004). The vegetation surrounding the cave consists of a mixed-deciduous forest composed of spruce (*Picea*), hemlock (*Tsuga*), cedar (*Thuja*), birch (*Betula*), and maple (*Acer*), which is characteristic of the middle Ottawa zone of the Great Lakes – St. Lawrence forest region (Rowe, 1972). The soil overlying the cave consists of a slightly acidic organic matter and plant litter (pH of 4.5), typical of soils covered by a deciduous forest (Hagen-Thorn et al., 2004). The $pCO_2$ in the soil is approximately $10^{-3.3}$ to $10^{-3.1}$ ppmV in July and decreases to $10^{-3.5}$ to $10^{-3.4}$ ppmV in January, reflecting the biological activity of the overlying vegetation.

The age of formation of Caverne de l'Ours is unknown, but given the absence of glacial sediments inside the cave, it was probably initially scoured into the Precambrian

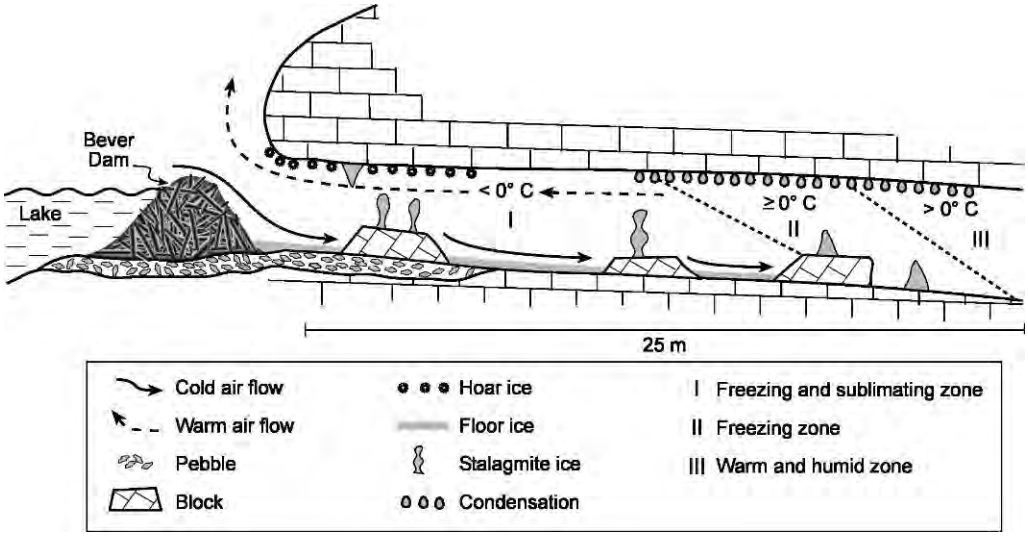


**Figure 2. Schematic diagram illustrating the micro-climatic zones in the open cavity in Caverne de l'Ours, QC, Canada, in relation to the various types of seasonal ice formations.**

Grenville marble outcrop by subglacial meltwater flowing from the Laurentide ice sheet. The Grenville marble, which consists of metamorphosed limestone ($CaCO_3 > 95\%$; $\delta^{18}O = -7.9‰$; $\delta^{13}C = 2.3‰$) (Kretz, 1980, 2001), is highly soluble and contains numerous inclusions of quartz, gabbro, garnet and feldspar (Dresser and Denis, 1946; Prévost and Lauriol, 1994).

Caverne de l'Ours, which measures up to 280 m in length, is divided into three sections: (1) a large open cavity measuring 30-m-long and 5-m-wide; (2) the main underground section consisting of 250 m of narrow subhorizontal passages; and (3) a 30-m-long and very narrow passage that connects the open cavity to the main underground passages (Fig. 1). The open cavity and main passages both reach a few meters in height. There is a small closed-basin lake adjacent to the entrance of the open cavity, and the presence of a beaver dam prevents the lake water from filling most of the open cavity. However, the beaver dam allows for a small stream to flow (ca. 4–5 L $s^{-1}$) along the floor of the open cavity, and the stream reaches the main passages of the cave through a narrow network of fissures. Near the entrance of the cavity, the stream partially freezes during winter, but it remains unfrozen (stream temperature near 4 °C) at the end of the cavity. The cryogenic cave calcite deposits discussed in this study are only found in the open cavity; inside the remainder of the cave, moonmilk is the dominant type of speleothem, although a few Holocene-age flowstones are also present (Lacelle et al., 2004).

## MICROCLIMATE, SEASONAL ICE DISTRIBUTION AND CRYOGENIC CALCITE POWDERS

The microclimate inside the main underground passages of the cave was described in Lacelle et al. (2004), and it was found that the seasonal air temperature and relative humidity fluctuated between 5–15 °C and 85–100%, respectively. However, the microclimate in the open cavity tends to reflect that of the outside air temperature. January air temperatures range from −10 °C near the entrance, to near 0 °C at the end of the cavity. Therefore, the cold dense air that enters the cavity in winter circulates along the floor. As it progresses in the open cavity, the air warms up, rises, and flows back towards the entrance along the roof (Fig. 2). The distribution of ice formations in the cavity is in part controlled by the winter 0 °C isotherm, which extends to approximately 20 m inside the cavity.

In Caverne de l'Ours, as in most freezing caves in Canada (Ford and Williams, 2007), the seasonal ice formations formed either by the: (1) freezing of dripping water (ice stalagmite and stalactite), (2) freezing of stagnant or slow moving water (floor ice and curtain ice), or (3) condensation of water vapor (hoar ice) (Fig. 3). Figure 2 presents the various forms of seasonal cave ice formations in relation to the microclimatic zones in the cavity. Within the first 5 m from the entrance, a few small ice stalagmites (5- to 15-cm-high) are found on the limestone blocks, and the ceiling is covered by hoar ice. Between 5 and 10 m from the entrance, the ice stalagmites, shaped as inverse bowling pins, are more abundant and measure up to 1-m-high and 20-cm-wide. Numerous ice stalactites are also present in this section. The stalactites have a conical shape that tapers at their tips and measure up to 1-m-long. These two types of ice formations, which are formed from the freezing of dripping water, grow more rapidly when the air temperatures in the cavity are very cold, whereas when the air temperatures are slightly below 0 °C, the dripping water slowly circulates on their surface, resulting in a thickening of the ice formations. In this middle section (5 to 10 m) and near the entrance of the cavity, the shapes of the ice stalagmites and stalactites are not only controlled by the

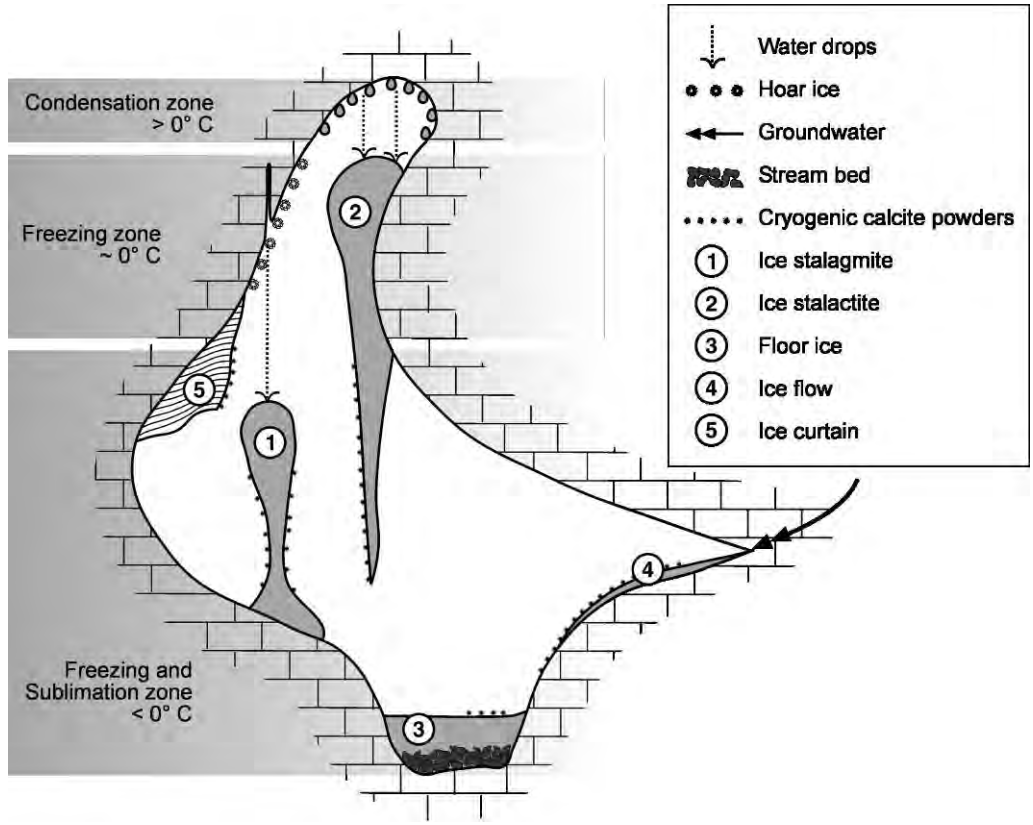


**Figure 3. Schematic diagram of various types of seasonal ice formations encountered in the open cavity in Caverne de l'Ours, QC, Canada.**

freezing of dripping water, but also by sublimation of the ice surfaces. This process lies in the equilibrium between temperature and humidity differences between the air and the ice formations. The cold and dry air that enters the open cavity flows around the ice stalagmites and stalactites, and the interaction of the water molecules at the boundary layer between the ice and air masses causes a transfer (removal) of ice to the air. Also found in the middle section of the cavity is hoar ice along the roof and curtain ice growing perpendicular on the upper walls. Further away from the entrance (10 to 20 m), the ice stalagmites have a tubular form and measure up to 1.2-m-high, indicating that sublimation is no longer active in the farthest section. Ice stalactites and hoar ice are absent in this section because the air temperature along the roof is greater than 0 °C, except on very cold winter days. Throughout the open cavity (except near the end), the floor is covered by ice. This ice forms by the freezing of lake water passing beneath the beaver dam in winter. Near the entrance, the floor ice measures 25-cm-thick, and is composed of candle ice crystals up to 5-cm-long. These characteristics approach those of aufeis, and as such, the formation of the floor ice resembles that of aufeis in the Arctic, albeit at a much smaller scale (discussed further in text).

Cryogenic calcite powders, which form during the freezing of a solution containing dissolved calcium and bicarbonate solutes, are visible on the surface on the floor ice and also on the sublimated sections of the ice stalagmites and stalactites. Deeper in the open cavity, where the ice formations are not modified by sublimation, no calcite powders are found on their surface; however, it should be noted that the melting of ice stalagmites growing deeper in the cave also released calcite powders. The cryogenic calcite powders have a whitish to yellowish color and become progressively thicker on the ice surfaces as the winter months advance, with maximum accumulations reaching 1–2 mm in March.

Calcite powders are not only found on the surface of ice formations, but also were observed on spider webs attached to the tips of the small ice stalagmites growing at the entrance of the cavity. In the literature, this type of calcite is rarely documented, but Murase et al. (2001) named it spider silk calcite, following their discovery in a laboratory experiment. The only spider species observed in the summer in the entrance of Caverne de l'Ours was *Meta ovalis*, and this species is the most common spider living in the entrance of caves in North America (Dondale et al., 2003). The spider silk has a strong ability for water condensation; and therefore, the condensation and subse-

quent freezing of water vapor containing cave aerosols on the spider silk could produce cryogenic spider silk calcite, assuming the cave aerosols contain some dissolved calcium and bicarbonate species.

## FIELD SAMPLING AND ANALYTICAL PROCEDURES

### CAVE ICE

In the winters of 2006–2007, various types of seasonal cave ice formations (hoar, curtain, floor, stalagmite, and stalactite ice) found in the open cavity of Caverne de l'Ours were collected for geochemical and stable O-H isotopes. Since the hoar and curtain ice could readily be broken off, they were collected and transferred directly into sealed plastic bags, whereas the floor ice was sampled using an ice axe and then transferred into sealed plastic bags. Near the entrance of the cavity, an entire ice stalagmite (50 cm) and stalactite (80 cm) were broken off from their limestone block and ceiling, respectively, and brought back to the laboratory in a thermally insulated box. Water dripping from the ceiling in the open cavity was also collected during the months of October and December 2006 and April 2007 in glass amber bottles for geochemical and stable O-H-C isotope measurements.

Prior to geochemical and stable O-H isotope analyses, all ice samples were melted in the laboratory, filtered through 0.45 μm pore diameter filters, and transferred in 20 ml pre-rinsed polyethylene bottles. However, the ice stalagmite and stalactite were sectioned with a pre-cleaned saw into 2-cm-thick slices along their growth axis to verify the chemical and stable isotope (O-H) variations during their accretion. The pH of the melted ice samples, which represents an equilibrium value between the water and potentially any dissolved cryogenic calcite under the laboratory partial pressure of $CO_2$, was determined using a Fisher Accumet 610A pH meter calibrated with pH 4 and 7 buffer solutions. Major cations ($Ca^{2+}$, $Mg^{2+}$, $Na^{+}$ and $K^{+}$) were analyzed and acidified to pH 2 using ultra-pure nitric acid by Inductively Coupled Plasma Atomic Emission Spectroscopy (ICP-AES). All samples were run in duplicate at the University of Ottawa (Department of Earth Sciences) and the analytical reproducibility was ±5%.

The $^{18}O/^{16}O$ ratio of the melted ice samples was determined on $CO_2$ equilibrated with the water at 25 °C. The D/H ratio was measured on $H_2$ isotopically equilibrated with the water at 25 °C using a Pt based catalyst. Both stable isotope measurements were made on the same sample using a Gas Bench II interfaced with a Finnigan Mat Delta$^{+}$ XP isotope mass spectrometer at the G.G. Hatch Laboratory (University of Ottawa). Results are presented using the δ-notation, where δ represents the parts per thousand difference of $^{18}O/^{16}O$ or D/H in a sample with respect to Vienna Standard Mean Ocean Water (VSMOW). Analytical reproducibility was of ±0.1‰ for $\delta^{18}O$ and ±1.5‰ for δD.

### CRYOGENIC CAVE CALCITE

The mineral composition of the cryogenic carbonate deposits, identified as calcite in all cases, was determined a few months after collection. The samples were powdered, mixed with acetone and spread over a glass slide and analyzed using a Phillips PW-1800 x-ray diffractometer with a step size of 0.02 and scanning speed of 0.4 seconds per step to record the x-ray diffraction spectra.

The cryogenic calcite powders were also collected from the ice formations using different methods and examined under scanning electron microscope (SEM) either under cryogenic or room temperature conditions to verify the effect of post-field storing on their micro-morphologies and to determine the potential presence of calcite polymorphs. Four methods were used:

(1) Cryogenic calcite powders were collected directly from the surface of the ice formations, placed in sterile roll-top plastic bags and kept at room temperature until analyzed under SEM.
(2) Cryogenic calcite powders were collected along with the ice on which they rested, stored, and analyzed using a SEM under cryogenic conditions to verify the undisturbed micro-morphologies.
(3) The third method consisted of collecting a section of ice stalagmite that was melted in a glass beaker back in the laboratory. The calcite powders were retrieved from the beaker after the water had completely evaporated and then examined under SEM at room temperature.
(4) For the final method, an ice stalagmite was sectioned into small blocks, placed in a beaker covered by an aluminum sheet and desiccated (1 atm and temperature of −5 °C) in a commercial dessicator (Labconco Freezone) at the Geological Survey of Canada. The residual calcite powders were collected from the beaker and kept at sub-freezing temperature until SEM examination under cryogenic conditions.

Calcite powders were also collected from the spider webs attached on the small ice stalagmites near the entrance of the cavity to examine the morphology of the crystals. The cryogenic spider silk calcite was collected directly on a carbon tape mounted onto an aluminum stub and kept at sub-freezing temperature until examination under SEM. Prior to examination under SEM, all calcite powders (except for the powder collected with the ice substrate, which was put directly uncovered onto an aluminum stub) were mounted onto an aluminum stub using doubled-sided carbon tape and then sputter-coated with gold for 60 seconds. The micro-morphologies of calcite precipitates were examined using a JEOL 6400 SEM at the Université du Québec à Montréal.

The $^{18}O/^{16}O$ and $^{13}C/^{12}C$ ratios of the cryogenic cave calcite powders were determined on $CO_2$ gas produced by reacting the powdered calcite with 100% phosphoric acid ($H_3PO_4$) in glass septum vials for 24 hours at 25 °C. The

evolved $CO_2$ gas was analyzed in continuous flow using a Gas Bench II interfaced with a Finnigan Mat Delta$^+$ XP isotope mass spectrometer at the G.G. Hatch Isotope Laboratory, University of Ottawa. Stable isotope data for C and O are expressed in δ-notation, where δ represents the parts per thousand difference of $^{13}C/^{12}C$ and $^{18}O/^{16}O$ in a sample with respect to the Vienna Pee-Dee Belemnite standard (VPDB). Analytical reproducibility is ±0.15‰ for both isotopes.

## RESULTS

### CAVE ICE FORMATIONS

The geochemical and stable O-H isotope compositions of the various seasonal cave ice formations in Caverne de l'Ours are presented in Figures 4 and 5. The ice formations have similar geochemical and isotopic compositions: a pH ranging between 7 and 8, a $Ca^{2+}$ concentration averaging 15.9 ± 6.7 mg $L^{-1}$, typical of karst water in the area (Prévost and Lauriol, 1994), and $\delta^{18}O$ and δD values averaging −8.2 ± 0.2‰ and −57.6 ± 2.8‰, respectively (Fig. 4A). Although the $\delta^{18}O$ compositions of the ice stalagmite, ice stalactite, curtain and hoar ice are similar, separate regression lines are obtained in a $\delta D - \delta^{18}O$ diagram. Individual regression slopes of 5.1 ($\delta D = 5.1\ \delta^{18}O - 16.2$; $R^2 = 0.58$), 5.6 ($\delta D = 5.6\ \delta^{18}O - 11.1$; $R^2 = 0.57$), and 2.7 ($\delta D = 2.7\ \delta^{18}O - 37.6$; $R^2 = 0.40$) are calculated for the ice stalactite, ice stalagmite, and ice curtain, respectively (Fig. 4B), suggesting potentially unique mechanism of formation for each type of ice.

Sampling along the growth axis of the ice stalactite and stalagmite revealed slight geochemical and isotopic variations related to their separate accretion processes (Fig. 5). In the 80-cm-long ice stalactite, the pH increases from 6.8 at the base to 7.3 at its tip. The geochemical composition of the ice stalactite is dominated by $Ca^{2+}$ (14 ± 2.3 mg $L^{-1}$), followed by $Na^+$ (1.7 ± 0.9 mg $L^{-1}$) and $K^+$ (1.2 ± 0.8 mg $L^{-1}$), but their concentrations do not show any trends from the base to the summit. It is interesting to observe that the concentrations of $K^+$ and $Na^+$ fluctuate together, whereas the variation in the concentration of $Ca^{2+}$ is independent. The source of $K^+$ and $Na^+$ is probably related to some clastic component, which can be either clay transported together by the drip water or cave aerosols deposited on the wet surface of the ice stalactite. The $\delta^{18}O$ composition of the ice stalactite shows a progressive depletion trend from −7.1‰ at its base to −8.7‰ at its tip.

In the 50-cm-long ice stalagmite, the pH also progressively increases as it grew, ranging from 6.9 at the base to 7.9 at its tip. The $K^+$ and $Na^+$ concentration in the ice stalagmite is similar to that of the stalactite. However, the $Ca^{2+}$ solutes concentration reaches a much greater concentration (up to 47.2 mg $L^{-1}$). Like the ice stalactite, the solute concentrations in the stalagmite do not show any trends during ice accretion (Fig. 5). The $\delta^{18}O$ of the ice stalagmite varies between −7.9 and −8.9‰. It was interesting to observe that once thawed, the color of the water of the ice stalagmite and stalactite was yellowish, suggesting the presence of amino acids. In fact, the cave drip water has a measured dissolved organic content (DOC) ranging from 4.1 to 6.9 mg $L^{-1}$ (unpublished data).

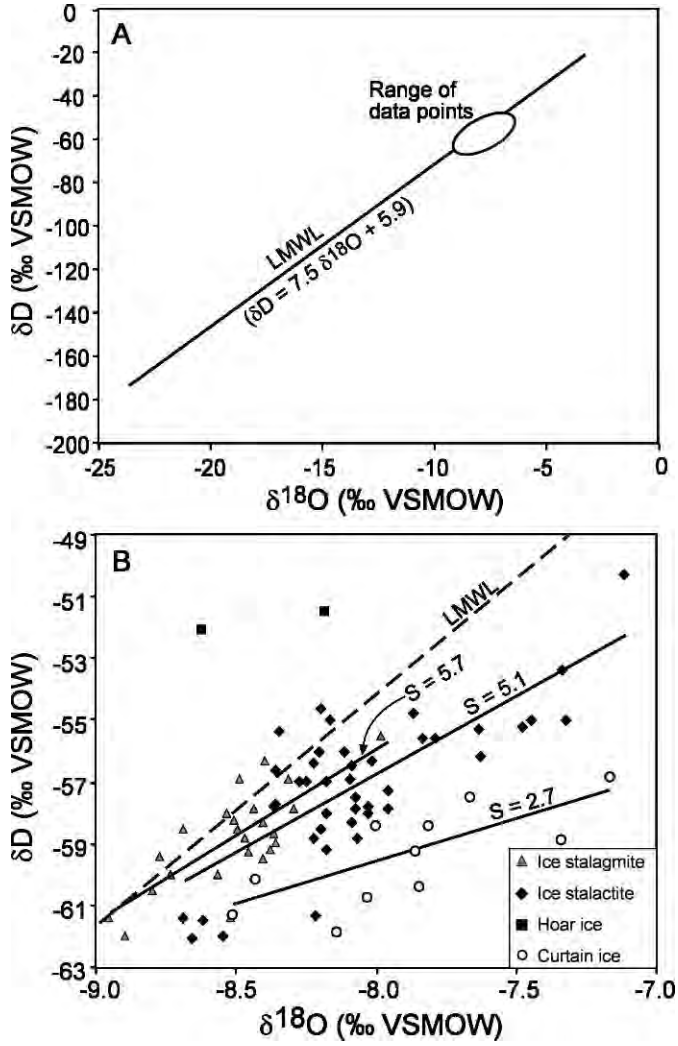


**Figure 4. A) Range of stable O-H isotope composition of seasonal ice formations in Caverne de l'Ours, QC, Canada, compared to that of the seasonal precipitation recorded in Ottawa, which is defined by the Local Meteoric Water Line (LMWL: $\delta D = 7.5\ \delta^{18}O + 5.9$; IAEA/WMO, 2004). B) Stable O-H isotope composition of seasonal ice formations (ice stalagmite, ice stalactite, hoar ice and curtain ice) in Caverne de l'Ours and their respective regression line (*S*).**

### CRYOGENIC CAVE CALCITE POWDERS

The $\delta^{18}O$ and $\delta^{13}C$ composition of the cryogenic calcite powders is presented in Figure 6. The stable isotopic composition of the cryogenic calcite powders is invariant of the cave ice formation from which they were collected and

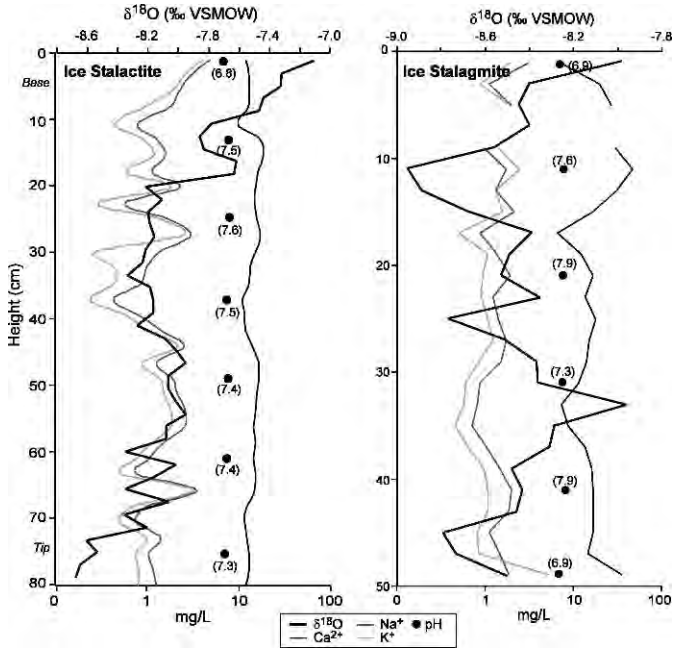


**Figure 5. Geochemical ($Ca^{2+}$, $Na^{+}$, $K^{+}$ and pH) and $\delta^{18}O$ composition along growth axis of an ice stalactite and ice stalagmite found in the open cavity in Caverne de l'Ours, QC, Canada.**

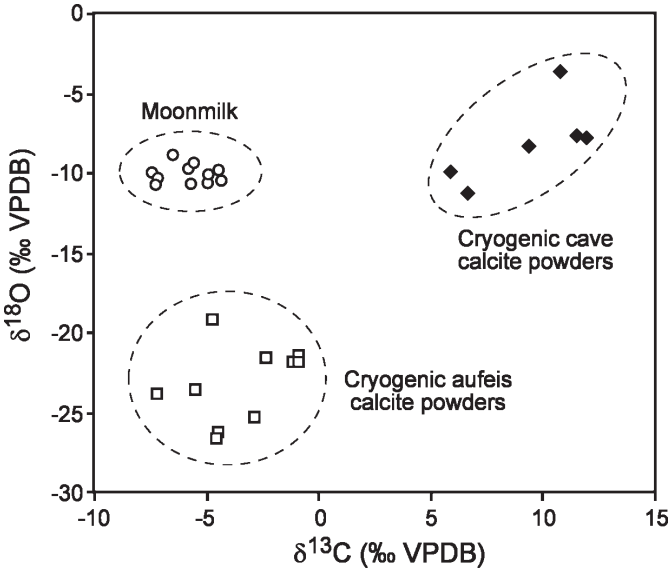


**Figure 6. Stable C-O isotope composition of cryogenic calcite powders found on the surface of the various seasonal ice formations in Caverne de l'Ours. Also shown for comparison purposes is the $\delta^{13}C$ and $\delta^{18}O$ composition of moonmilk found in the main passages of Caverne de l'Ours (Fig. 1), and cryogenic aufeis calcite powders (sampled from limestone terrain in the northern Yukon, Canada), the only other known type of cryogenic calcite precipitating as cryptocrystalline powders. $\delta^{13}C$ and $\delta^{18}O$ data for moonmilk and cryogenic aufeis calcite powders derived from Lacelle et al. (2004) and Clark and Lauriol (1997), respectively.**

of the post-sampling handling. The cryogenic calcite powders all have $\delta^{18}O$ values ranging from −11.3 to −3.7‰ and $\delta^{13}C$ values between 5.8 and 11.9‰, which are among the most positive values in the literature. The $\delta^{18}O$ and $\delta^{13}C$ of calcite powders collected from the sublimated ice stalagmite fall also within this isotopic range. Cryogenic calcite powders collected from the surface of floor ice in the nearby Lusk cave (45°39′N; 75°38′W) yielded very similar $\delta^{18}O$ and $\delta^{13}C$ values (Clark and Lauriol, 1992).

Unlike the $\delta^{18}O$ and $\delta^{13}C$ values, the cryogenic calcite powders produced varied crystal arrangements depending on the post-sampling storage and analytical methods (room or sub-freezing temperature) during examination under SEM (Figs. 7 and 8). The crystal arrangement of the first group of cryogenic calcite powders, which were collected from the surface of the ice stalagmites and stalactites and stored at room temperature prior to analysis, is composed of 3–8 μm rhombohedral crystals (Fig. 7A–C). The surface of the calcite crystals is often pitted and their edges are etched, suggesting calcite disintegration after precipitation by local dissolution. In contrast, the cryogenic calcite powders analyzed directly from the surface of the ice and those collected from sublimated ice stalagmites under cryogenic conditions showed crystal habits different from the first group (Fig. 8). These calcite crystals are composed of spheres ranging from <1 to 2 μm in diameter and thick calcite needles up to 20 μm long. In some instances, several spheres aggregate together, producing a chain-like appearance (Fig. 8B, D). Finally, the cryogenic calcite powders analyzed from evaporated melted ice stalagmites and stalactites are composed of 3–10 μm rhombohedral crystals that are often stacked together (Fig. 7D–F). The surface of the crystals is smooth, but their edges are etched, similar to the first group of calcite powders (collected from the surface of the ice formations and kept at room temperature prior to analysis). Overall, none of these crystal habits resemble that of ikaite, which is typically composed of anhedral calcite crystals (Omelon et al., 2001). However, the spherical-shaped crystal aggregates observed under cryogenic conditions closely resemble those of vaterite precipitated under natural and laboratory setting (e.g., Turnbull, 1973; Fairchild et al., 1996; Vecht and Ireland, 2000; Grasby, 2003).

The spider silk calcite produced a unique crystal habit (Fig. 9). The calcite attached to the spider's silk showed elongated crystals up to 3 μm long that formed clusters less than 10 μm wide along the spider's silk (Fig. 9 C–F). These dimensions of single clusters are probably constrained by the weight of the calcite crystals on the silk.

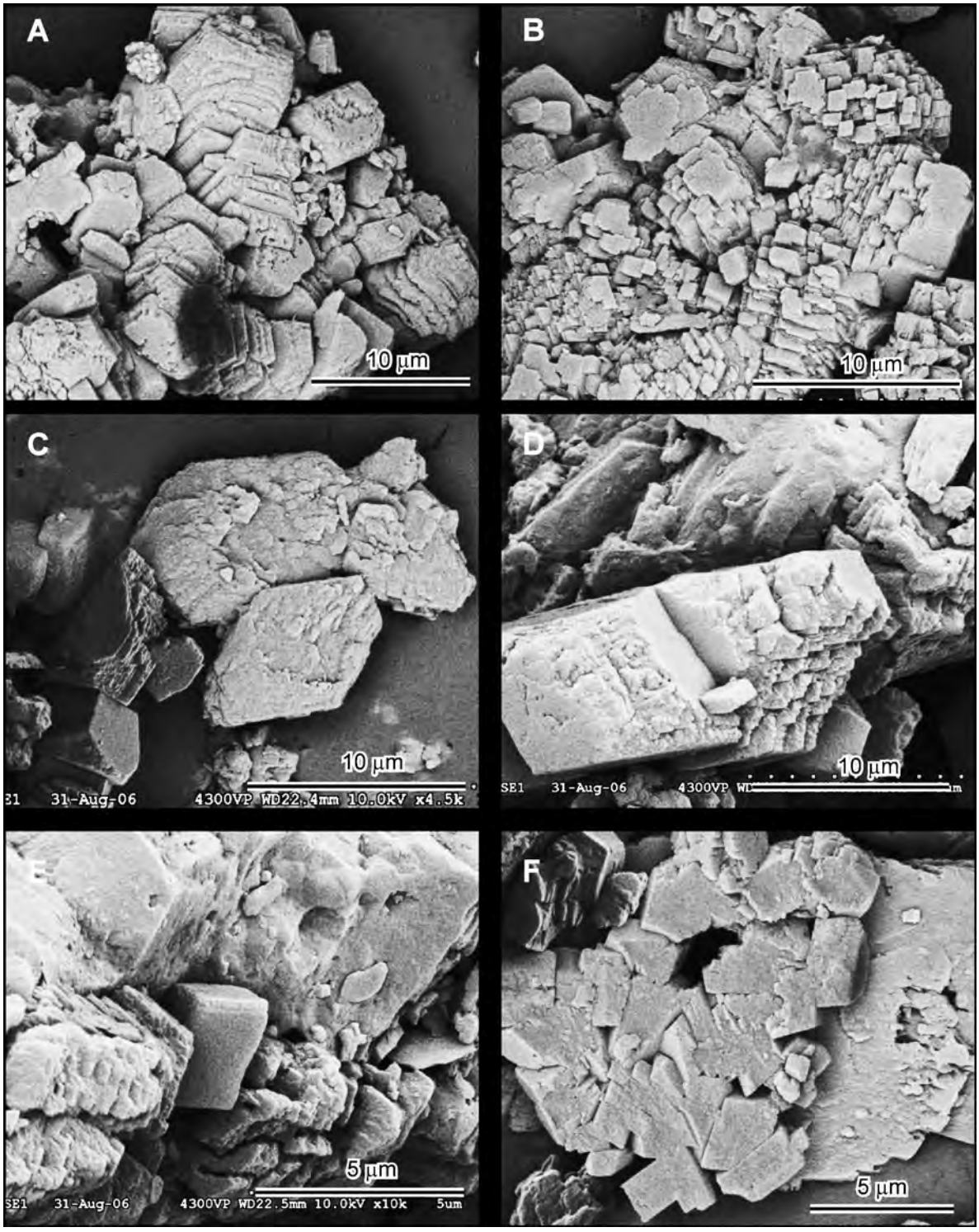


**Figure 7. Secondary electron images of cryogenic calcite powders collected on the surface of various ice formations in Caverne de l'Ours. The images were acquired at room temperature with a SEM. A–C) cryogenic calcite powders collected from the surface of ice stalagmites and stalactites; and D–F) calcite powders recovered from a beaker in which a section of ice stalagmite was melted and left to evaporate in the laboratory.**

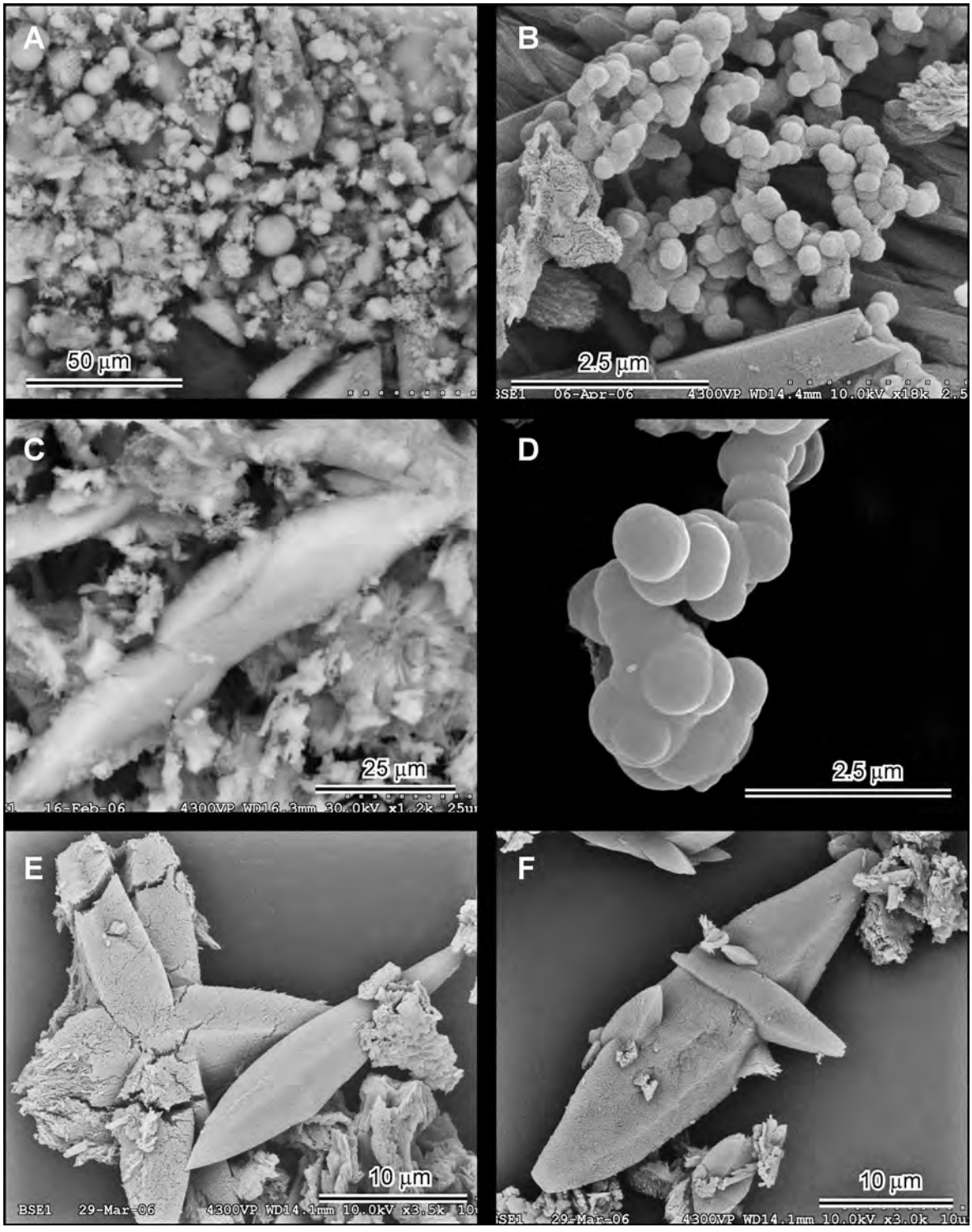


**Figure 8. Secondary electron images of cryogenic calcite powders collected on the surface of various ice formations in Caverne de l'Ours. The images were acquired at sub-freezing temperature with a SEM. A–C) cryogenic calcite powders collected from the surface of ice stalagmite using cryogenic sample transport and analysis; and D–F) calcite powders recovered from a beaker in which a section of ice stalagmite was sublimated in the laboratory under cryogenic condition, transport, and analysis.**

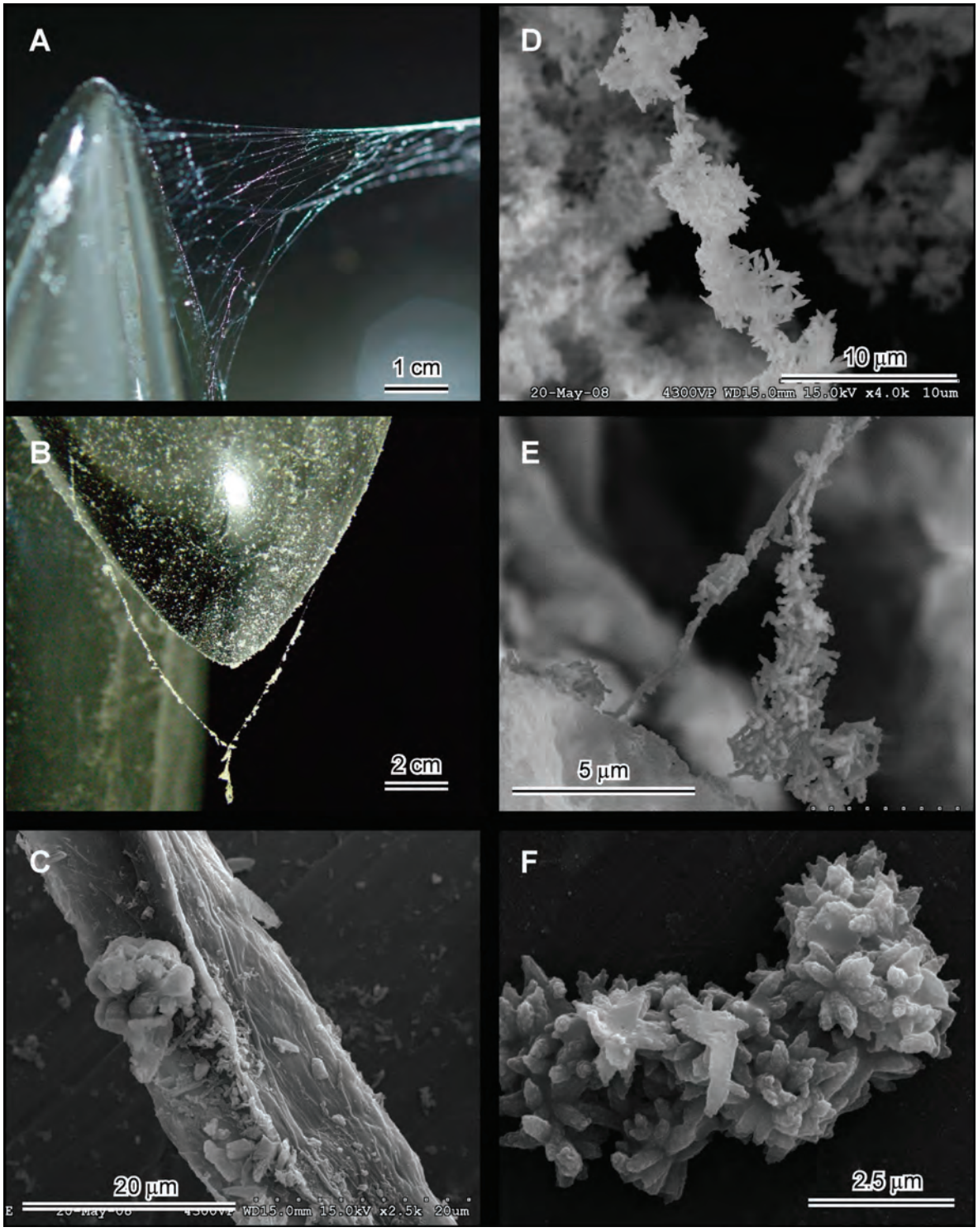


**Figure 9. A–B) Field photographs of calcite powders on spider silk attached to a small ice stalagmite near the entrance of the open cavity of Caverne de l'Ours. C–F) Secondary electron images of spider silk calcite acquired at room temperature with a SEM.**

## DISCUSSION

### ORIGIN OF THE SEASONAL CAVE ICE FORMATIONS: EVIDENCE FOR KINETIC ISOTOPE EFFECTS

The formation of the seasonal cave ice formations examined in this study is well known in the literature (i.e., Ford and Williams, 2007) and it has been described here in a previous section. However, little is known regarding the degree of isotope equilibrium/disequilibrium during the formation of the hoar, curtain, stalagmite and stalactite ice bodies. Such information can be provided by examining the $\delta D - \delta^{18}O$ relation in the ice formations (Fig. 4). During equilibrium freezing, the ice samples are aligned along a regression line that will be lower than the local meteoric water line (LMWL; $\delta D = 7.5\ \delta^{18}O + 5.9$; $R^2 = 0.97$; IAEA/WMO, 2004) because the amount of incorporation of the heavier isotopes in the ice (D and $^{18}O$), which follows a Rayleigh-type fractionation, is slightly different for both isotopes (Jouzel and Souchez, 1982; Souchez and Jouzel, 1984). According to Jouzel and Souchez (1982), the slope of the freezing line depends mainly on the initial isotopic composition of the water, with the more depleted waters having a lower slope value. The conditions prevailing during freezing (open versus closed system), and the rate of supply of water to the freezing fronts, have little effect on the freezing slope (Souchez and Jouzel, 1984). Based on the Jouzel and Souchez (1982) model and using an initial water $\delta^{18}O$ and $\delta D$ values of −11.4‰ and −78.8‰, respectively, and the average annual precipitation values in Ottawa (IAEA/WMO, 2004), the ice formations in the cave resulting from equilibrium freezing should plot along a slope of 5.9.

Another parameter that provides clues into the rate of freezing during the formation of ice bodies is the $d - \delta D$ relation, where $d$ represents the deuterium excess ($d = \delta D - 8\ \delta^{18}O$) (Dansgaard, 1961). During equilibrium freezing, the first ice that forms has a greater $\delta D$ (and $\delta^{18}O$) value due to the preferential partitioning of the D isotope in the ice (i.e., with an associated depletion of heavy isotopes in the residual water), but as freezing progresses, the $\delta D$ values of the ice become progressively lower. This is accompanied by a concurrent increase in $d$ values because the freezing equilibrium slope has a value lower than the LMWL. As a result, a negative relation is expected between $d$ and $\delta D$ during equilibrium freezing (Souchez et al., 2000).

If we examine the $\delta D - \delta^{18}O$ and $d - \delta D$ relations in the Caverne de l'Ours seasonal ice formations, a few key features emerge. First, all cave ice formations have $\delta^{18}O$ and $\delta D$ values within the range of summer precipitation and of the stream flowing inside the open cavity (Fig. 4A). Secondly, the stalagmite and stalactite ice formations lie on positive slopes that are less than the LMWL (7.5), but similar to the theoretical freezing slope (5.9) (Fig. 4B). Individual regression slopes of 5.1 ($\delta D = 5.1\ \delta^{18}O - 16.2$; $R^2 = 0.58$) and 5.6 ($\delta D = 5.6\ \delta^{18}O - 11.1$; $R^2 = 0.57$) are calculated for the ice stalactite and ice stalagmite, respectively (Fig. 4B). By contrast, the curtain ice samples plot along a regressive slope ($\delta D = 2.7\ \delta^{18}O - 37.6$; $R^2 = 0.40$) that is much less than the LMWL and predicted freezing slope. Thirdly, there is no negative relation between $d - \delta D$ in all cave ice formations (Fig. 10), suggesting the non-existence of a freezing slope; or in other words, freezing occurred under non-equilibrium conditions. In fact, even though regression slopes were calculated for the various ice formations, their correlation coefficient is rather weak ($R^2 < 0.58$). Finally, the hoar ice on the ceiling of the cave shows strong enrichment in D, as it plots well above the LMWL (Fig. 4B). Overall, these unusual isotopic features cannot be explained by the progressive freezing of water under equilibrium conditions, but can be attributed to kinetic isotope effects during the successive freezing of thin layers of water. The arguments in favor of non-equilibrium freezing for the formation of each seasonal ice type formations are presented below.

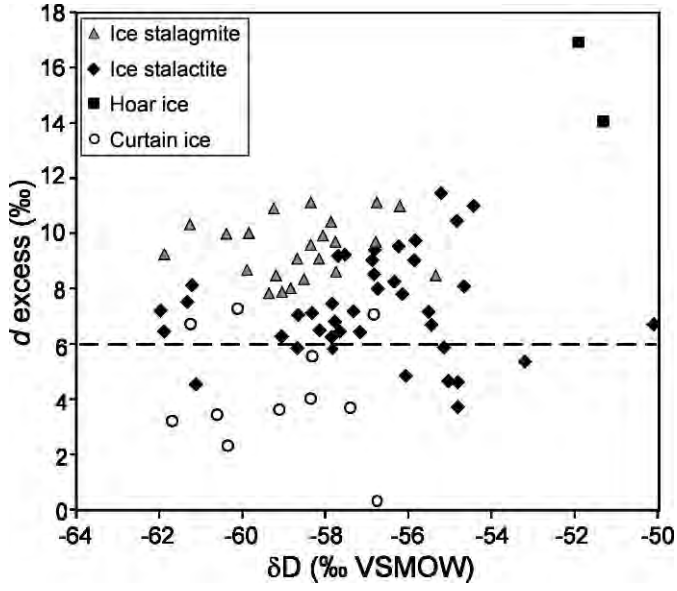


**Figure 10. Deuterium excess ($d$) and stable D isotope composition of the various seasonal ice formations in Caverne de l'Ours, QC, Canada. Horizontal dashed line represents $d$ in local precipitation.**

By definition, hoar ice forms by direct condensation of water vapor on the cold ceiling. The effect of condensation is evident in the $\delta D - \delta^{18}O$ diagram, where the hoar ice samples plot well above the LMWL (Fig. 4B). This is attributed to the effect of air circulation dynamics inside the open cavity. The non-equilibrium evaporation of the stream inside the open cavity would produce water vapor plotting above the LMWL, followed by equilibrium condensation of the water vapor along the LMWL (Fig. 11). This process produces $d$ values much greater than 10‰ that are increasing under decreasing relative humidity conditions. A simple calculation using the

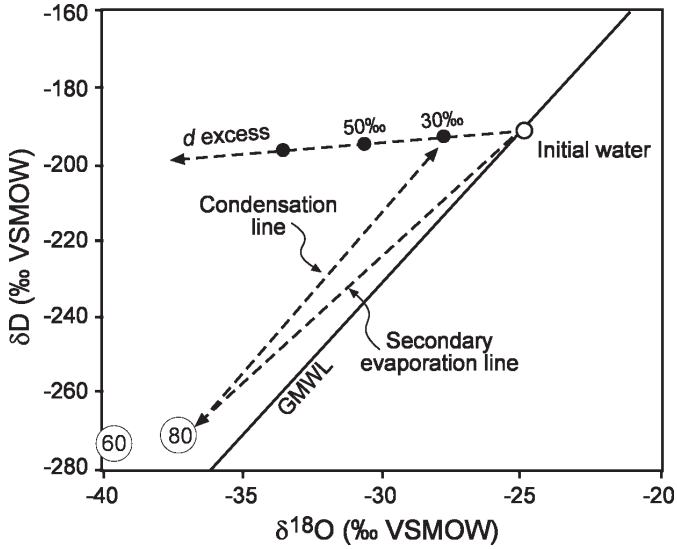


**Figure 11. δD − $\delta^{18}$O systematic during condensation of secondary evaporated water (i.e., small stream on the floor of the open cavity). When humidity conditions are near 100%, precipitation plots close to the local meteoric water line, however, under decreasing relative humidity conditions, the vapor (evaporated water) becomes strongly depleted and precipitation formed by equilibrium condensation plots further above the GMWL (global meteoric water line) along a condensation line with a slope very similar to the GMWL.**

average $\delta^{18}$O and δD of the small stream in the open cavity in winter (−7.5 ± 1.0‰ and −56.6 ± 2.1‰, respectively) (Lacelle et al., 2004), the fractionation factor between ice and vapor ($\delta^{18}$O ice-vapor = 14.7‰; δD ice-vapor = 127‰, both at 0 °C; Majoube, 1971), and average relative humidity in winter (74.7%; this value is probably slightly less in the open cavity since the air becomes warmer), shows that the condensing ice would have a $\delta^{18}$O and δD composition of −7.9‰ and −39.2‰, respectively, and a *d* excess of 24.7‰. These predicted values are similar to the measured $\delta^{18}$O, δD and *d* values of the hoar ice in Caverne de l'Ours (Figs. 4B and 10), indicating that the stable O-D isotope composition of hoar preserved the condensation signature.

Ice stalagmites and stalactites and ice curtains originate from the freezing of dripping water. As the $\delta^{18}$O values of these ice formations are within the range of summer precipitation (Fig. 4A), the percolating water in the open cavity during the winter originates from rainfall ground water stored in the overlying soil (epikarst zone), and not from snow meltwater. In the δD and $\delta^{18}$O diagram (Fig. 4B), the ice stalagmite and stalactite plot near the predicted equilibrium freezing slope of 5.9, although they have a weak correlation coefficient ($R^2 \sim 0.58$). However, the ice curtain plots along a much lower slope (δD = 2.7 $\delta^{18}$O −37.6). In the *d* − δD diagram, the three ice types do not show a clear relation, as they are scattered across broad horizontal bands (Fig. 10). These observations, and the fact that no trend is displayed in the vertical distribution of heavy isotopes ($^{18}$O and D) during the accretion of the ice stalagmite and stalactite (Fig. 5), indicate that they grew from the successive freezing of water dripping from the ceiling under non-equilibrium conditions. The sublimation of the ice formations by air circulation would not affect the stable O-H isotope of the remaining ice, as sublimation is a physical surface phenomenon.

## Formation of Cryogenic Cave Calcite Powders: A Comparison with Cryogenic Aufeis Calcite Powders

Cryogenic cave calcite and cryogenic aufeis calcite are the only two known types of calcite powders formed by the freezing of calcium-bicarbonate waters. In the simplest form, the formation (and dissolution) of calcite can be expressed by this reaction:

$$CO_2(aq) + H_2O + CaCO_3 \leftrightarrow Ca^{2+} + 2HCO_3^- \quad (1)$$

During the formation of calcite minerals under equilibrium conditions, the heavy isotopes ($^{18}$O and $^{13}$C) are preferentially incorporated from the aqueous phase into the minerals in a proportion governed by the isotope fractionation factor, and by such, the C-O isotope composition of calcite is controlled by the $\delta^{18}$O and $\delta^{13}C_{DIC}$ composition of the parent water and temperature at which precipitation occurs. However, it is well known that freezing can modify the isotope composition of the aqueous phase as the products are being isolated immediately after their formation (Rayleigh distillation), leading to a progressive depletion in $\delta^{18}$O and enrichment in $\delta^{13}C_{DIC}$ in the residual water (Lacelle et al., 2006). However, it was shown in the previous section that the seasonal cave ice formations examined in this study formed through non-equilibrium (rapid) freezing of waters. Therefore, the kinetic isotope effect during the formation of the ice stalagmites and stalactites by water freezing rapidly should also create isotopic disequilibrium between the aqueous phase and the precipitating calcite, the latter showing an increase in heavy isotopes. Clark and Lauriol (1992) demonstrated that the rapid freezing of a calcium bicarbonate solution that is at or near calcite saturation led to strong C isotope disequilibrium between the precipitating calcite and the escaping $CO_2$ ($\varepsilon^{13}$C $CaCO_3$-$CO_2$ = 31.2 ± 3.1‰) (Clark and Lauriol, 1992). By contrast, the stable O isotope fractionation between water and calcite during kinetic freezing ($\varepsilon^{18}$O $CaCO_3$-$H_2O$ = 36.7 ± 1.3‰ VSMOW) (Clark and Lauriol 1992) is only slightly greater than equilibrium values ($\varepsilon^{18}$O $CaCO_3$-$H_2O$ = 33.6‰ VSMOW) (Kim and O'Neil, 1997). According to these kinetic isotope enrichment factors and the average $\delta^{13}C_{DIC}$ of drip waters (−11.9 ± 1.3‰; unpublished data) and $\delta^{18}$O of the various ice formations (−8.2 ± 0.2‰ VSMOW), the

$\delta^{13}C$ (9.4 ± 2.6‰) and $\delta^{18}O$ values (−8.9 ± 1.6‰ VPDB) of the cryogenic calcite powders in Caverne de l'Ours are within the range expected of a formation by kinetic freezing.

Cryogenic cave calcite powders have highly distinct $\delta^{13}C$ and $\delta^{18}O$ values from those measured in the cryogenic calcite powders formed in association with aufeis, the latter having much lower $\delta^{13}C$ and $\delta^{18}O$ values (Fig. 6). Aufeis (icings) are sheet-like masses of horizontally layered ice that form on river channels by successive freezing of overflow of perennial groundwater-fed springs upon exposure to cold air. Stable isotope profiles within the ice layers indicate that the growth of aufeis occurs under closed-system equilibrium conditions (Elver, 1994; Clark and Lauriol, 1997). As a result, unlike the seasonal cave ice formations discussed in this study, the residual water is covered by a sheet of ice that grows downwards, leading to saturation in the residual water of various minerals, including calcite ($CaCO_3$) and ikaite ($CaCO_3 \cdot 6H_2O$), and their precipitation within the ice (Hall, 1980; Clark and Lauriol, 1997; Heldmann et al., 2005; Lacelle et al., 2006). Accordingly, a closed system Rayleigh-type fractionation process occurs during the aggradation of aufeis. Although Jouzel and Souchez (1982) and Souchez and deGrotte (1985) demonstrated the O isotope systematics associated with the slow freezing of low ionic strength waters under equilibrium conditions, much remains to be known about the C isotope. It can be expected that the C isotope fractionation during freezing under equilibrium conditions involves a C isotope mass balance in the $CO_2$-$HCO_3$-$CO_3$-$CaCO_3$ system. Considering that the DIC species ($CO_{2aq}$-$HCO_3$-$CO_3$) fractionate differently among them, and that their relative concentration is set by pH, the $\delta^{13}C_{DIC}$ and $\delta^{13}CCaCO_3$ during equilibrium freezing is not simply controlled by the initial geochemical and isotopic composition of the source water, but also by changing physical and geochemical conditions as freezing progresses (i.e., pH and exolved $CO_2$ during the precipitation of calcite). Given the different conditions of formation for the aufeis (closed system equilibrium freezing), the cryogenic aufeis calcite powders are characterized by $\delta^{13}C$ and $\delta^{18}O$ values that are in equilibrium with that of the water from which they precipitated (Lacelle et al., 2006). These characteristics indicate that the limiting process affecting the degree of deviation between the stable C-O isotope composition of the cryogenic aufeis calcite (formed under equilibrium conditions) and water from which they precipitated is the attainment of calcite saturation, whereas for the cryogenic cave calcite powders (formed under kinetic conditions), it is the rate of precipitation of calcite.

## Micromorphologies of Cryogenic Cave Calcites: Abiotic and Pseudo-Biogenic Signatures

In natural environments, such as in caves, calcite crystals commonly display a wide range of crystal micromorphologies. Although rhombohedral habit is highly suggestive of an inorganic precipitation of calcite, the formation of spherical crystal aggregates is usually attributed to an organic influence (Folk, 1993; Braissant et al., 2003). In this study, it was shown that the cryogenic cave-calcite powders, which are produced by freezing, an abiotic process, revealed highly different crystal habits depending on the procedures used to collect the sample, and the conditions under which it was examined under SEM. The samples analyzed under room temperature all produced rhombohedral crystals (either single or stacked) (Fig. 7), whereas the ones examined under cryogenic conditions showed small spheres (<2 μm) and thick needle structures (Fig. 8). Needle-like crystals are also the dominant type of crystal habit observed in cryogenic aufeis calcite (e.g., Lacelle, 2007). The samples examined under cryogenic conditions probably preserved the undisturbed nature of the calcite powders, whereas those examined at room temperature were probably altered and recrystallized before analysis. The latter effect would not greatly affect the stable C-O isotope composition of the calcite.

Considering that the formation of cryogenic carbonate powders is purely abiotic and that vaterite is stable at low temperature (<10 °C and 1 atm; Albright, 1971) and precipitates in a spherical shape with crystals ranging from 0.05 to 2 μm (Kralj et al., 1990; Vecht and Ireland, 2000), the most plausible explanation for the observation of small spheres (<2 μm) in the crystal habits of the cryogenic powders is that they consist of vaterite. This metastable polymorph of calcite recrystallizes to calcite when in contact with water (Silk, 1970), which would explain why spheres were not observed in the samples examined at room temperature because they were exposed to water during melting of the ice formations. The formation of vaterite during freezing is not unusual and was also observed by Fairchild et al. (1996) during laboratory experiments, and by Grasby (2003) in spring deposits in the high Arctic. Although higher pH values (between 9.3 and 10.0; Kralj et al., 1990) than what was measured in the ice formations (Fig. 5) are necessary to precipitate vaterite, it is possible that favorable microenvironments were created within the accretion of the various annual ice formations that allowed vaterite to precipitate. Vaterite was not identified in our XRD measurements because the samples were not kept frozen for these analyses. It is therefore suggested that care should be taken before suggesting biological origin of calcite precipitates based solely on crystal habits because they might represent pseudo-biogenic structures formed through abiotic processes.

## Conclusions

Based on the results presented in this study, the following conclusions can be reached regarding the formation of seasonal cave ices and the associated cryogenic calcite powders in Caverne de l'Ours, QC, Canada:

1. The seasonal ice formations, which either formed by (1) freezing of dripping water (ice stalagmite and stalactite); (2) freezing of stagnant or slow moving water (floor ice and curtain ice) and; (3) condensation of water vapor (hoar ice), all (except floor ice) showed kinetic isotope effects during the freezing of water. This is made evident in the $d - \delta D$ diagram where the ice formations show no relation because they are scattered across broad horizontal bands.
2. The cryogenic calcite powders, which precipitate during the formation of the seasonal ice formations, also show kinetic isotope effects. Their $\delta^{13}C$ values are among the highest measured in cold-temperature carbonates and are caused by the rapid rate of freezing, which results in strong C disequilibrium between the water and precipitating calcite, the latter showing an increase in heavy isotopes. The $\delta^{18}O$ composition of the cryogenic calcite powders also show elevated values associated with kinetic freezing.
3. The cryogenic calcite powders showed varied crystal habits. Rhombs, aggregated rhombs, spheres and needles were all observed under SEM. The rhombs crystal habit was observed at room temperature whereas the spheres and needles were observed at sub-freezing temperatures with cryogenic storage of the samples. This suggests that the sphere structures might represent vaterite, a polymorph of calcite stable only at low temperature. This indicates that not all sphere crystal habits can be attributed to biogenic origin for calcite, as in Caverne de l'Ours, the formation of cryogenic calcite is purely abiotic.

## Acknowledgements

This work was supported by a Canadian Space Agency internal research fund to DL and Natural Sciences and Engineering Research Council of Canada (NSERC) grants to BL and IDC. We would like to thank R. Mineau, W. Abdy and P. Middlestead for their technical assistance in the laboratories. M.S. Field (editor), I. Sasowsky (associate editor), K. Zak, and an anonymous referee provided helpful reviews of the manuscript.

## References

Albright, J.N., 1971, Vaterite stability: American Mineralogy, v. 56, p. 620–624.

Braissant, O., Cailleau, G., Dupraz, C., and Verrecchia, E.P., 2003, Bacterially induced mineralization of calcium carbonate in terrestrial environments: The role of exopolysaccharides and amino acids: Journal of Sedimentary Research, v. 73, p. 485–490.

Clark, I.D., and Lauriol, B., 1992, Kinetic enrichment of stable isotopes in cryogenic calcite: Chemical Geology, v. 102, p. 217–228.

Clark, I.D., and Lauriol, B., 1997, Aufeis of the Firth River basin, Northern Yukon, Canada: Insights into permafrost hydrogeology and karst: Arctic and Alpine Research, v. 29, p. 240–252.

Courty, M.A., Marlin, C., Dever, L., Tremblay, P., and Vachier, P., 1994, The properties, genesis and environmental significance of calcitic pendants from the high Arctic (Spitsbergen): Geoderma, v. 61, p. 71–102.

Dansgaard, W., 1961, The isotopic composition of natural waters: Meddelelser om Gronland, v. 165, p. 1–120.

Dondale, C.D., Redner, J.H., Paquin, P., and Levi, H.W., 2003, The Insects and Arachnids of Canada: Part 23, The Orb-weaving Spiders of Canada and Alaska. Ottawa, Canada, National Research Council of Canada, 371 p.

Dresser, J.A., and Denis, T.C., 1946, La géologie de Québec, géologie descriptive: Quebec, Canada, Ministère des Mines, Québec, Rapport géologique 20, 647 p.

Elver, M.S., 1994, The stratigraphic and isotopic characteristics of an Arctic Icing, Bylot Island, N.W.T. [M.Sc. thesis]: Ottawa, Canada, Carleton University, http://www.climate.weatheroffice.ec.gc.ca/climate_normals/

Fairchild, I.J., Bradly, L., and Spiro, B., 1993, Carbonate diagenesis in ice: Geology, v. 21, p. 901–904.

Fairchild, I.J., Killawee, J.A., Spiro, B., and Tison, J.-L., 1996, Calcite precipitates formed by freezing processes: kinetic controls on morphology and geochemistry, *in* Bottrell, S., ed., Proceedings of the fourth International Symposium on the Geochemistry of the Earth's Surface, Ilkley, Yorkshire, Wiley, p. 178–183.

Folk, R.L., 1993, SEM imaging of bacteria and nanobacteria in carbonate sediments and rocks: Journal of Sedimentary Petrology, v. 63, p. 990–999.

Ford, D.C., and Williams, P., 2007, Karst hydrogeology and geomorphology: West Sussex, U.K., Wiley, 576 p.

Grasby, S.E., 2003, Naturally precipitating vaterite (i-$CaCO_3$) spheres: unusual carbonates formed in an extreme environment: Geochimica et Cosmochimica Acta, v. 67, p. 1659–1666.

Hagen-Thorn, A., Callesen, I., Armolaitis, K., and Nihlgård, B., 2004, The impact of six European tree species on the chemistry of mineral topsoil in forest plantations on former agricultural land: Forest, Ecology and Management, v. 195, p. 373–384.

Hall, D.K., 1980, Mineral precipitation in North Slope river icings: Arctic, v. 33, p. 343–348.

Hallet, B., 1976, Deposits formed by subglacial precipitation of $CaCO_3$: Geological Society of America Bulletin, v. 87, p. 1003–1015.

Heldmann, J.L., Pollard, W.H., McKay, C.P., Andersen, D.T., and Toon, O.B., 2005, Annual development cycle of an icing deposit and associated perennial spring activity on Axel Heiberg Island, Canadian High Arctic: Arctic, Antarctic and Alpine Research, v. 37, p. 127–135.

IAEA/WMO (International Atomic Energy Agency/World Meterology Organization), 2004, Global Network of Isotopes in Precipitation. The GNIP Database, http://isohis.iaea.org

Jouzel, J., and Souchez, R.A., 1982, Melting—refreezing at the glacier sole and the isotopic composition of the ice: Journal of Glaciology, v. 28, p. 35–42.

Killawee, J.A., Fairchild, I.J., Tison, J.L., Janssens, L., and Lorrain, R., 1998, Segregation of solutes and gases in experimental freezing of dilute solutions: implication for natural glacier systems: Geochimica et Cosmochimica Acta, v. 62, p. 3637–3655.

Kim, S.T., and O'Neil, J.R., 1997, Equilibrium and nonequilibrium oxygen isotope effects in synthetic carbonates: Geochimica et Cosmochimica Acta, v. 61, p. 3461–3475.

Kralj, D., Brecevic, L., and Nielson, A.E., 1990, Vaterite growth and dissolution in aqueous solution: 1. Kinetics of crystal growth: Journal of Crystal Growth, v. 104, p. 793–800.

Kretz, R., 1980, Occurrence, mineral chemistry and metamorphism of Precambrian carbonate rocks in a portion of the Grenville Province: Journal of Petrology, v. 21, p. 573–620.

Kretz, R., 2001, Oxygen and carbon isotopic composition of Grenville marble, and an appraisal of equilibrium in the distribution of isotopes between calcite and associated minerals, Otter Lake, Quebec, Canada: The Canadian Mineralogist, v. 39, p. 1455–1472.

Lacelle, D., 2007, Environmental setting, (micro)morphologies, and stable C-O isotope composition of cold climate carbonate precipitates – a review and evaluation of their potential as paleoclimatic indicators: Quaternary Science Reviews, v. 26, p. 1670–1989.

Lacelle, D., Lauriol, B., and Clark, I.D., 2004, Seasonal isotopic imprint in moonmilk from Caverne de l'Ours: implications for climatic reconstruction: Canadian Journal of Earth Sciences, v. 41, p. 1411–1423.

Lacelle, D., Lauriol, B., and Clark, I.D., 2006, Effect of chemical composition of water on the oxygen-18 and carbon-13 signature preserved in cryogenic carbonates, Arctic Canada: implications in paleoclimatic studies: Chemical Geology, v. 234, p. 1–16.

Majoube, M., 1971, Fractionnement en oxygene-18 et en deuterium entre l'eau et sa vapeur. Journal of Chemical Physics, v. 197, p. 1423–1436.

Marion, G.M., 2001, Carbonate mineral solubility at low temperatures in the Na-K-Mg-Ca-H-Cl-$SO_4$-OH-$HCO_3$-$CO_3$-$CO_2$-$H_2O$ system: Geochimica et Cosmochimica Acta, v. 65, p. 1883–1896.

Marlin, C., Dever, L., Vachier, P., and Courty, M-A., 1993, Variations chimiques et isotopiques de l'eau du sol lors de la reprise en gel d'une couche active sur pergélisol continu (Presqu'ile de Brogger, Svalbard): Canadian Journal of Earth Sciences, v. 30, p. 806–813.

Murase, N., Ruike, H., Matsunaya, N., Hagakawa, M., Kaneko, Y., and Ono, Y., 2001, Spider silk has an ice nucleation activity: Naturwissenschaften, v. 88, p. 117–118.

Omelon, C.R., Pollard, W.H., and Marion, G.M., 2001, Seasonal formation of ikaite ($CaCO_3$ $6H_2O$) in saline spring discharge at Expedition Fjord, Canadian High Arctic: assessing conditional constraint for natural crystal growth: Geochimica et Cosmochimica Acta, v. 65, p. 1429–1437.

Pauly, H., 1963, Ikaite, a new mineral from Greenland: Arctic, v. 16, p. 263–264.

Prévost, C., and Lauriol, B., 1994, Variabilité de l'érosion actuelle et Holocene: le cas des marbres de Grenville en Outaouais Québécois: Géographie Physique et Quaternaire, v. 48, p. 297–303.

Pollard, W., 1983, A study of seasonal frost mounds, North Fork Pass, northern interior Yukon Territory [Ph.D. thesis]: Ottawa, Canada, University of Ottawa.

Richter, D.K., and Riechelmann, D.F.C., 2008, Late Pleistocene cryogenic calcite spherolites from the Malachitdom Cave (NE Rhenish Slate Mountains, Germany): origin, unusual internal structure and stable C-O isotope composition: International Journal of Speleology, v. 37, p. 119–129.

Rowe, J.S., 1972. Forest Regions of Canada. Environment of Canada, Canadian Forestry Service, Publication No. 1300, 172 p.

Silk, S.T., 1970, Factors governing polymorph formation in calcium carbonate [PhD thesis]: New York, New York University.

Souchez, R.A., and Jouzel, J., 1984, On the isotopic composition in δD and $\delta^{18}O$ of water and ice during freezing: Journal of Glaciology, v. 30, p. 369–372.

Souchez, R.A., and deGrotte, J.M., 1985, δD- $\delta^{18}O$ relationships in ice formed by subglacial freezing: paleoclimatic implications: Journal of Glaciology, v. 109, p. 599–602.

Souchez, R.A., Jouzel, J., Lorrain, R., Sleewaegen, S., Stiévenard, M., and Verbeke, V., 2000, A kinetic isotope effect during ice formation by water freezing: Geophysical Research Letters, v. 27, p. 1923–1926.

Suess, E., Balzer, W., Hesse, K.-F., Muüller, P.J., Ungerer, C.A., and Wefer, G., 1982, Calcium carbonate hexahydrate from organic-rich sediments of the antarctic shelf: Precursors of glendonites: Science, v. 216, p. 1128–1131.

Turnbull, A.G., 1973, A thermodynamic study of vaterite: Geochimica et Cosmochimica Acta, v. 37, p. 1593–1601.

Vecht, A., and Ireland, T.G., 2000, The role of vaterite and aragonite in the formation of pseudo-biogenic carbonate structures: implications for martian exobiology: Geochimica et Cosmochimica Acta, v. 64, p. 2719–2725.

White, A.F., Bullen, T.D., Vivit, D.V., Schultz, M.S., and Clow, D.W., 1999, The role of disseminated calcite in the chemical weathering of granitoid rocks: Geochimica et Cosmochimica Acta, v. 63, p. 1939–1953.

Zak, K., Urban, J., Cilek, V., and Hercman, H., 2004, Cryogenic cave calcite from several Central European caves: age, carbon and oxygen isotopes and a genetic model: Chemical Geology, v. 206, p. 119–136.

Zak, K., Onac, B.P., and Persoiu, A., 2008, Cryogenic carbonates in cave environments: a review: Quaternary International, v. 187, p. 84–96.

A. Muñoz, A.K. Sen, C. Sancho, and D. Genty – Wavelet analysis of Late Holocene stalagmite records from Ortigosa Caves in Northern Spain. *Journal of Cave and Karst Studies,* v. 71, no. 1, p. 63–72.

# WAVELET ANALYSIS OF LATE HOLOCENE STALAGMITE RECORDS FROM ORTIGOSA CAVES IN NORTHERN SPAIN

A. Muñoz[1], A.K. Sen[2], C. Sancho[1], and D. Genty[3]

**Abstract:** We have deduced short-term climatic changes from millennial to annual scales from the study of laminae thickness and radiocarbon analysis of Holocene stalagmite records from two caves in Ortigosa de Cameros (Iberian Range, northern Spain). Speleothems are made up of dark compact laminae (DCL) and white porous laminae (WPL) of seasonal origin. Couplets seasonality is deduced from monitoring calcite laminae growth, drip water rates, and soil organic matter flushed into the caves. The thickness variations of the couplets are analyzed using a continuous wavelet transform and the various periodicities at interannual, decadal, multidecadal, and centennial scales are revealed from the wavelet power spectrum. The periodicities at decadal, multidecadal and centennial scales, with periods around 9.7, 10.4, 14, 16, 22, 43, 73, 83 and 180 years, are mainly related to solar activity. Among the interannual periodicities, oscillations around the 2.4-yr-period may be linked to the Quasi-Biennial Oscillation (QBO), whereas periods ranging from 4 to 7 years may be associated with the El Niño-Southern Oscillation (ENSO) and/or the North Atlantic Oscillation (NAO).

## Introduction

The understanding of Holocene paleoclimatic evolution in the north-central Iberian Peninsula has significantly improved during the past few years from the studies of lacustrine (Luque, 2003), tufaceous (Sancho et al., 1997), fluvial (Thorndycraft and Benito, 2006), alluvial (Sancho et al., 2008), and slope (Gutiérrez et al., 2006) records. In general, from the analysis of the reported data, it has been possible to deduce a prevailing climate with high variability and millennial scale cycles. As a consequence, a link between North Atlantic circulation and weather in Iberia during the Holocene period has been established. However, the contribution to climate variability made from speleothem records still remains at a preliminary level (Durán et al., 2000; Labonne et al., 2002; Muñoz-García et al., 2004; 2007; Martín-Chivelet et al., 2006).

Speleothems are widely used for paleoclimatic and paleoenvironmental reconstructions essentially because they can be well dated and their isotopic compositions record changes in temperature, rainfall, and vegetation-soil activity (McDermott, 2004). In addition, growth patterns of speleothems can be used to establish paleoclimatic sequences made up of cycles with variable frequency. From radiometric ages and stable isotope analysis of speleothems, several studies have detected short-term or high frequency climatic changes at regional/local scale (Dorale et al., 1992; Frumkin et al., 1999; Burns et al., 2001). Furthermore, very high frequency climatic cycles have been identified by performing statistical analysis of (1) laminaeted structure of the stalagmites (Quinif et al., 1994; Genty and Quinif, 1996; Ming et al., 1998; Qin et al., 1999; Frisia et al., 2003; Soubiès et al., 2005), and (2) $\delta^{18}O$ high resolution records (Niggemann et al., 2003; Holzkämper et al., 2004; Dykoski et al., 2005).

In this paper we examine stalagmite records from two caves in Ortigosa de Cameros (La Rioja, Spain). We used radiometric chronological data to deduce short-term environmental changes. We also use wavelet analysis of the laminaeted structure of the stalagmites to deduce very high frequency periodicities. As a result of this analysis, the present state of knowledge of environmental changes during Holocene times, in the northern sector of the Iberian Peninsula, can be significantly improved. Preliminary information about paleoenvironmental meaning of the speleothem records from Ortigosa Caves has been reported by Muñoz et al. (2001, 2004).

## Study Area

The study area is located in the westernmost sector of the Cameros Range (Iberian Mountain System, Northern Spain (Fig. 1a). The geological framework is made up of a Paleozoic basement surrounded by a Mesozoic stratigraphic sequence dipping to the S-SE. Specifically, the Ortigosa cave system is composed of 185-m-thick Middle Jurassic limestones of a high energy shallow shelf sequence (ITGE, 1990).

La Paz and La Viña Caves are located in the Encinedo Mountain near Ortigosa de Cameros village (La Rioja). The mean annual temperature is 9 °C and the mean annual precipitation is 630 mm. The Ortigosa cave system is one of the most important endokarstic features in the Iberian Range. La Viña Cave is 114-m-long and is located at a

[1] Departamento de Ciencias de la Tierra, Universidad de Zaragoza, 50009 Zaragoza, Spain, armunoz@unizar.es csancho@unizar.es
[2] Department of Mathematical Sciences, Indiana University, 402 N, Blackford Street, Indianapolis, IN 46202, USA, asen@iupui.edu
[3] Laboratoire des Sciences du Climat et de l'Environnement, LSCE UMR CEA/CNRS, 91191 Gif sur Yvette cedex, France, dominique.genty@lsce.ipsl.fr

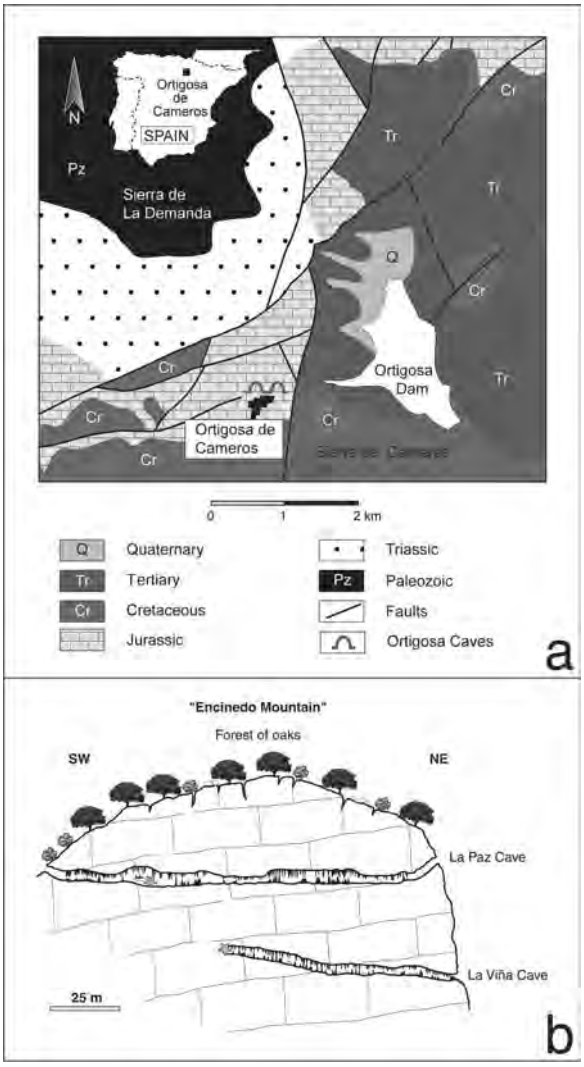


**Figure 1. (a) Location and geological setting of the Ortigosa Caves. (b) NE-SW section of the Encinedo Mountain showing the morphological features of the Caves. The asterisk in La Paz Cave illustrates the position of the OR-P1 artificial carbonate plate (Fig. 3b, c, d). The asterisk in La Viña Cave shows the location of the HOBORG3 Data Logging Rain Gauge to measure the drip water flow rates (see Fig. 4).**

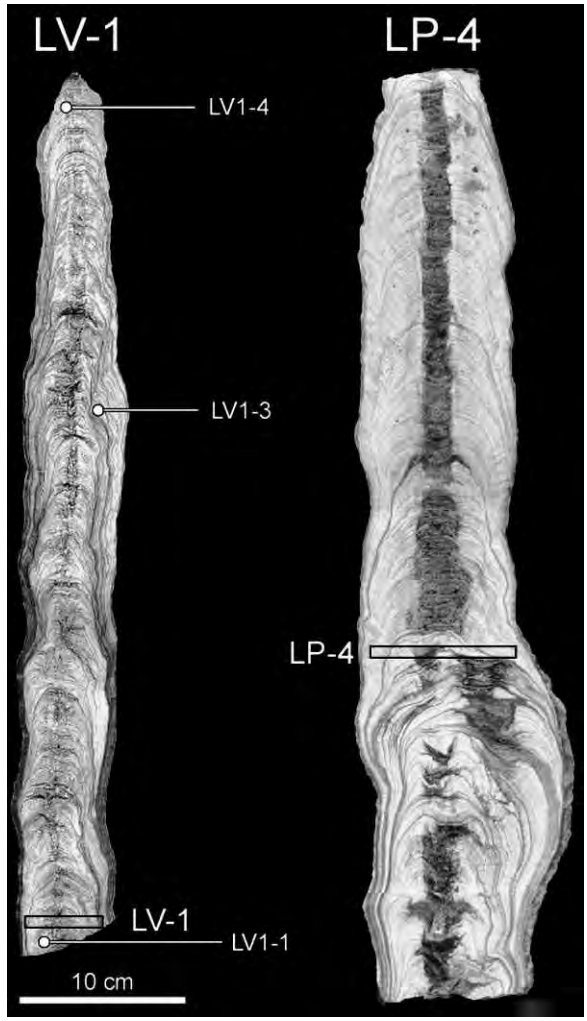


**Figure 2. Laminated structure of the LV-1 stalagmite from La Viña Cave, and of the LP-4 stalagmite from La Paz Cave. Locations of samples used in U/Th dating and radiocarbon-AMS analysis are denoted by rectangles and dots, respectively.**

lower elevation with an altitude of about 1080 m above the sea level. La Paz Cave is longer (236 m), and it is located 20 m above the former. Both La Paz Cave and La Viña Cave exhibit horizontal development and a geometry that is controlled by the direction of the main regional NE-SW fault system (Fig. 1b).

## MATERIAL AND METHODOLOGY

The Ortigosa Caves contain a large variety of speleothems. Three speleothem development stages have been differentiated after a detailed morphostratigraphic and chronological analysis (Muñoz et al., 2001). The oldest period began more than 400,000 Ma and is represented by flowstones that are very well exposed in La Viña Cave. The intermediate stage is associated with a greater development of stalagmites in both caves. It includes Isotopic Stages 7, 5, and 3 separated by periods of inactivity. The final development stage is related to smaller stalagmites and corresponds to Isotopic Stage 1. In this study, we use two stalagmite deposits from La Paz Cave (LP-4) and La Viña Cave (LV-1) related to the youngest stage, Holocene in age. The stalagmite from the La Viña Cave was still active when samples were taken (Fig. 2).

The sampled stalagmites were cut along their growth axis showing a very well-marked internally banded structure characterized by an alternation of white porous laminae (WPL) and dark compact laminae (DCL) (Figs. 2 and 3a, b, c). This terminology (WPL/DCL) has been used by Quinif et al. (1994) and Genty et al. (1997b). An

elongated columnar or fibrous fabric was the most prevalent fabric identified in these stalagmites according to the differentiation made by Frisia et al. (2000).

One of the two symmetrical portions was used to select samples in order to carry out mineralogical studies, as well as radiometric dating. X-ray diffraction analysis data indicate that the stalagmite deposits are largely made up of low-Mg calcite. The average molar ratio of $MgCO_3$ in calcite is 0.51% and its maximum value reaches 1.05%.

Several samples were designed to estimate the radiometric ages by using U/Th isotopic ratios and radiocarbon-AMS techniques. The U and Th isotopic ratios were determined by alpha spectrometry and the activities were calibrated by addition of known quantities of artificial radioactive spikes ($^{232}U$-$^{228}Th$ in radioactive equilibrium). Chemical preparation was carried out at the Isotopic Geochemistry Laboratory of the Centre d'Etudes et de Recherches Appliquées au Karst de la Faculté Polytechnique de Mons (Belgium). The $^{14}C$-AMS ages have been corrected for an arbitrary dead carbon proportion (also called dcp where the carbon comes mainly from the limestone dissolution and is $^{14}C$ free) of 10%, which is an average value for several European sites (Genty et al., 1997b, 1998, 2001; Genty and Massault, 1999). The ages have been calibrated using dendrochronological and coral curves (Stuiver and Kra, 1986; INTCAL 04, Reimer et al., 2004). These calibrations were carried out at the Hydrology and Isotopic Geochemistry Laboratory of the Université de Paris-Sud and TANDETRON, CNRS-CEA, UMS T2004, Gif sur Yvette (France).

The second symmetrical portion of the stalagmites was carefully polished to carry out a spectral-temporal analysis of the internal laminaetion using wavelets. First, the samples were photographed and the images were stored in a digital format. Then the laminae thickness was measured using the software OPTIMA V5 at the Instituto Jaume Almera (Barcelona). Subsequently, we applied wavelet analysis on the thickness variation data to detect very high frequency periodicities. In addition, to detect the various periodicities in the internal laminaetions, wavelet analysis can delineate the time intervals over which these periodicities persist. Wavelet-based methods have been used for signal analysis in a wide variety of applications (Addison, 2001; Sen and Dostrovsky, 2007; Sen et al., 2008a, b) including analysis of speleothem records (Holmgren et al., 2003; Lachniet et al., 2004; Tan et al., 2006). The various periodicities are discerned from the wavelet power spectrum of the thickness variations. A brief description of the wavelet analysis methodology is given in the Appendix.

In order to test the seasonal growth pattern of the laminae, on March 27, 2003 a carbonate plate (25 × 15 × 2 cm) (OR-P1) was placed under a drip water point to sample the present day stalagmite growth in La Paz Cave. It was removed on November 8, 2007 and was studied by using a petrographic microscope incorporating fluores-

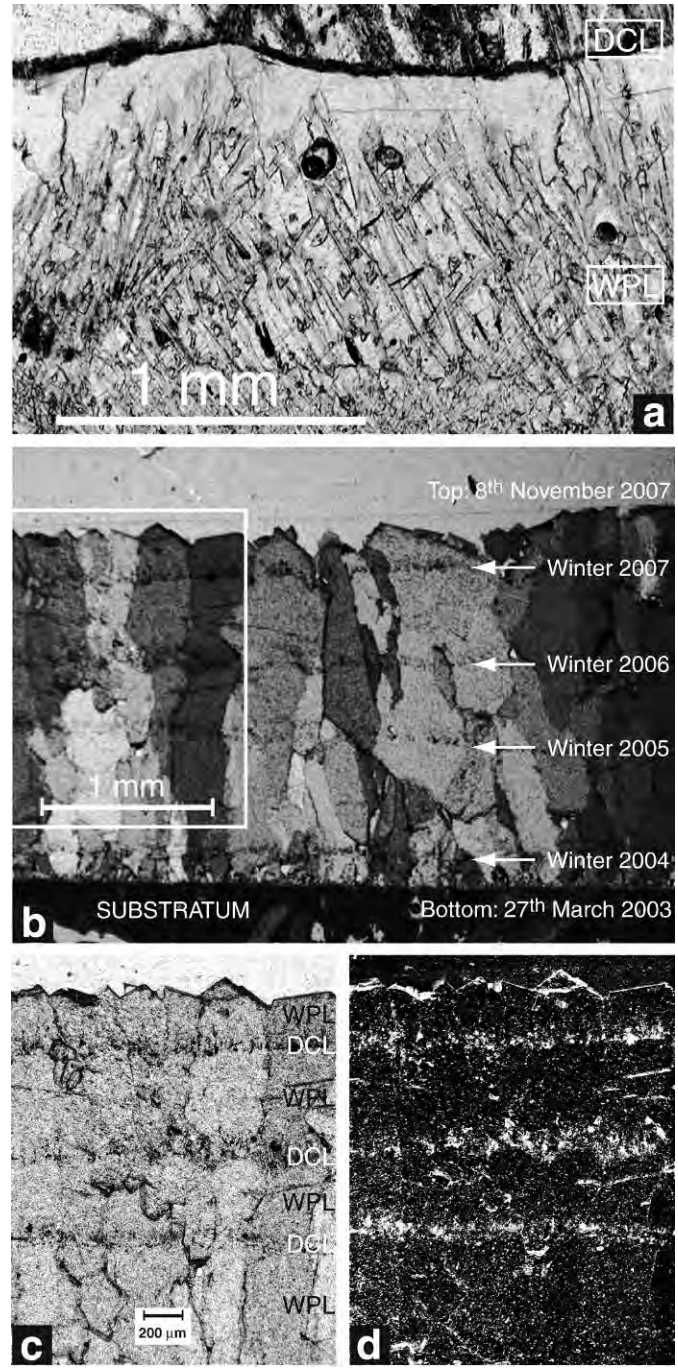


**Figure 3. (a) Annual microsequence from the LV-1 stalagmite showing the white porous lamina (WPL) and dark compact lamina (DCL). (b) General view of stalagmite growing over the OR-P1 carbonate plate located in La Paz Cave (between March 27, 2003 and November 8, 2007). Dark compact lamina (DCL) would correspond to the increase of water drip rate in winters (see Fig. 4). Non-polarized (c) and fluorescence (d) photographs of the stalagmite area indicated in b). The luminescence lines (DCL) correlate with the trends in seasonal water excess which flushes organic materials through the aquifer to the speleothem (Baker et al., 1997, 1999; Genty et al., 1997a).**

**Table 1. Analytical data of U/Th dating.**

| Sample No. | Lab. No. | $[U]_{ppm}$ | $^{234}U/^{238}U$ | $^{230}Th/^{234}U$ | $^{230}Th/^{232}Th$ | $[^{234}U/^{238}U]_{t=0}$ | Age (ky BP) |
|---|---|---|---|---|---|---|---|
| LP-4 | 6173 | 0.043 ± 0.001 | 1.100 ± 0.027 | 0.068 ± 0.006 | 3.0 ± 0.5 | 1.102 | 7.6[+0.7/−0.7] |
| LV-1 | 6174 | 0.031 ± 0.001 | 1.148 ± 0.029 | 0.193 ± 0.022 | 4 ± 1 | 1.158 | 23.2[+3.0/−2.9] |

cence analysis. The images obtained with non-polarized light show couplets of dark and clear laminae related to DCL/WPL pairs (Fig. 3b). In fact, five clear laminae (WPL) and four dark laminae (DCL) were identified.

Luminescence intensity reflects organic matter concentration (Baker et al., 1997) and was observed to correlate with the trends in seasonal water excess (Genty et al., 1997a). In order to obtain a fluorescence image from the stalagmite growing over the carbonate plate (Fig. 3d), we used an excitation wavelength of 450–480 nm. It was filtered by U-MWB filter and the fluorescence emission was detected at 515–700 nm. Finally, drip water flow inside the caves was continuously recorded by using a HOBO RG3 Data Logging Rain Gauge from September 22, 2005 in order to know the hydrological response of the karstic system to seasonally controlled external rainfall events.

## RESULTS

### CHRONOLOGY

Based on preliminary morphostratigraphic arrangement of speleothems in the Ortigosa Caves, as well as on radiometric ages (Muñoz et al., 2001), stalagmites LP-4 and LV-1 have been associated with the Isotopic Stage 1. The U/Th ages are found to be 23.2 (+3.0/−2.9) ky BP (bottom LV-1) and 7.6 (+0.7/−0.7) ky BP (middle LP-4) (Table 1). However, all the samples show a very low $^{230}Th/^{232}Th$ isotopic ratio (3 ± 0.5 for LP-4 and 4 ± 1 for LV-1) which means that they are contaminated with detrital Th ($^{232}Th$). Therefore the U/Th ages obtained are uncertain and any correction is unreliable as we don't know the initial $^{230}Th/^{232}Th$ ratio. Moreover, the 23.2 ky BP dating from LV-1 stalagmite occurs during a very cold period (Last Glacial Maximum) when the growth of speleothems was not likely. As a consequence, this chronological result should be used with caution.

In order to improve the estimation of U/Th age of the stalagmite LV-1, three additional analyses by radiocarbon-AMS were carried out. The obtained ages (Table 2) of the different samples from bottom to top are 3.4 ± 0.6 ky BP, 1.2 ± 0.4 ky BP, and 0.7 ± 0.35 ky BP, respectively. Despite the uncertainties due to the unknown dcp, these results demonstrate that the stalagmite is Late Holocene in age.

### STALAGMITE LAMINATION FREQUENCY ANALYSIS

The internal alternating structure of white porous laminae (WPL) and dark compact laminae (DCL) in the stalagmite samples (Figs. 2 and 3) may be seasonally controlled and, as a consequence, the paired microsequence may be annually developed (Baker et al., 1993; Quinif et al., 1994; Railsback et al., 1994; Shopov et al., 1994; Genty and Quinif, 1996; Genty et al., 1997b; Baker et al., 1998). In addition, Mitchell (1976) deduced that the magnitude of the seasonal cycle power is one order greater than any other cycle-generating mechanism.

In order to validate the seasonal control on stalagmite laminaetion in Ortigosa Caves, we use present day karstic activity in caves, based on both the hydrological response model and the stalagmite growth pattern. By using the stalagmite grown on the artificial tablet (OR-P1, Fig. 3b), it can be deduced that the first clear laminae developed on the sample would correspond to 2003 spring/summer and the first dark laminae to 2004 winter. The last laminae corresponds to 2007 spring/summer period. On the basis of the water-drip rates inside the cave (Fig. 4), we interpret the dark compact laminae (DCL) would form at the moment of a more intense dripping (winter), whereas the clear (white) porous laminae (WPL) would form during the slow dripping that takes place during spring and summer. Genty and Quinif (1996) indicate that the precipitation of the WPL in the microsequence most likely took place during summer and is related to a low water excess and a more regular and chemically more efficient flow rate, while the DCL was probably formed during the winter season, is related to a high water excess, and a chemically less efficient water flow.

On the other hand, the most prominent fluorescence emission in the OR-P1 sample occurs in the dark compact laminae (Fig. 3c, d). This would also indicate that they have been formed during winters when soil organic matter is flushed into the cave. The white porous laminae would form later in the hydrological cycle when the drip rate is lower.

Within this premise, the stalagmite samples LV-1 and LP-4 are made up of 1276 and 638 annual cycles, respectively. In the sample LV-1, chronologically analyzed by radiocarbon, 900 annual cycles have been counted between 3400 ± 600 yr BP and 1200 ± 400 yr BP, 326 cycles between 1200 ± 400 yr BP and 700 ± 350 yr BP, and 50 cycles between 700 ± 350 yr BP and present time.

Wavelet analysis of the couplet thickness variations of the LP-4 stalagmite laminaetions from the La Paz cave indicates the occurrence of very high frequency climatic cycles. Figure 5a depicts the time series of thickness variations in the LP-4 stalagmite laminaetions. The wavelet power spectrum (WPS) of this time series is shown in

**Table 2. Analytical data of radiocarbon-AMS dating.**

| Sample No. | Lab. No. | Distance to Top (mm) | Age (years BP) |
|---|---|---|---|
| LV1-4 | PA764/H2410 | 20 | 700 |
| LV1-3 | PA763/H2409 | 210 | 1200 |
| LV1-1 | PA762/H2401 | 540 | 3400 |

Figure 5b. In Figures 5a and 5b the horizontal axis is labeled as the number of annual cycles. In Figure 5b, the dark contour lines represent 95% confidence level with respect to red noise spectrum, and the area below the thin U-shaped curve denotes the cone of influence (see Appendix for details). Several periodicities, and the time intervals (i.e., the number of annual cycles) over which the periodicities persist, can be discerned from Figure 5b. For example, there is a strong periodic band around the 9.7-yr-period. This band persists over the time interval between 250 and 285 annual cycles. A similar periodic band is present around the 10.4-yr period. Another periodic band is found around the 43-yr period spanning approximately the time interval between 160 to 260 annual cycles. We also observe time-varying periodicities with periods from 22 to 31 years. In addition, several very high frequency cycles in the 2–4-yr band are seen in Figure 5b. These periodicities appear in an intermittent fashion. Figure 5c depicts the global wavelet spectrum (GWS) of the LP-4 stalagmite thickness time series. The dominant spectral modes can be identified from the various peaks in Figure 5c (see Appendix for details).

The results of wavelet analysis of the LV-1 stalagmite from La Viña cave are shown in Figure 6. Figure 6a, b, and c illustrate, respectively, the time series of thickness variations, wavelet power spectrum, and global wavelet spectrum. The following periodicities can be observed in Figure 6b. There is a strong periodic band around the 180-yr-period persisting continuously over the interval from 260 to 775 annual cycles. There are also strong periodic bands around the 73-yr and 83-yr periods persisting continuously over several annual cycles. In addition, we observe oscillations around the 14-yr and 16-yr periods. These bands persist approximately over 46 annual cycles. Several very high-frequency periodicities with peaks at the 2.4-yr, 4.0-yr, and 5.6-yr periods are also seen in Figure 6. These periodicities appear in an intermittent pattern. The dominant spectral modes can also be identified from the global wavelet spectrum of the time series shown in Figure 6c.

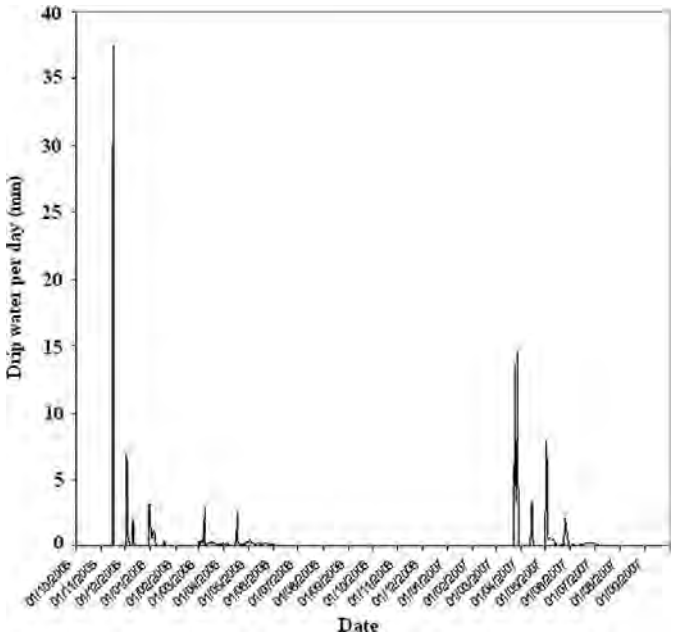


**Figure 4. Drip-water flow in La Viña cave (September 2005–September 2007). The drip water shows an initial intense flow generating the dark sheet of the seasonal cycle and another stage of more slow and effective drip-water flow that generates the clear sheet.**

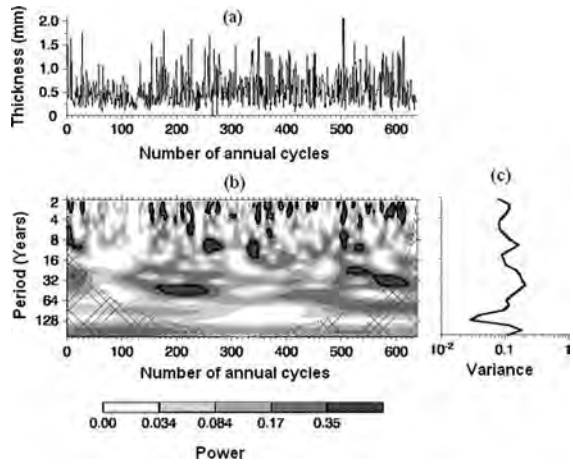


**Figure 5. (a) Time series of the thickness variations in LP-4 stalagmite from La Paz cave. (b) Wavelet power spectrum of the time series of LP-4 stalagmite thickness variations shown in (a). The dark contour lines represent 95% confidence level with respect to a red noise background and the area below the thin U-shaped curve denotes the cone of influence (COI). Inside the COI, the edge effects may become important and the results should be used with caution (Torrence and Compo, 1998). (c) Global wavelet spectrum of the time series shown in (a).**

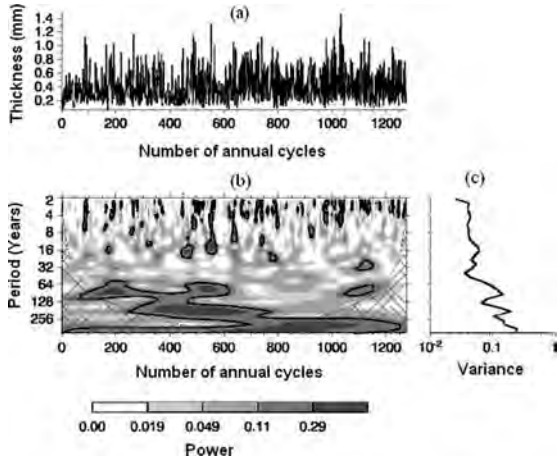


**Figure 6. (a) Time series of the thickness variations in LV-1 stalagmite from La Viña cave. (b) Wavelet power spectrum of the time series of LV-1 stalagmite thickness variations shown in (a). The dark contour lines and the cone of influence have the same meaning as in Figure 5(b). (c) Global wavelet spectrum of the time series shown in (a).**

## DISCUSSION

### SHORT-TERM ENVIRONMENTAL CHANGES

Taking into account the chronological data obtained from LP-4 and LV-1 stalagmites, we propose that the youngest morphostratigraphic stalagmite growth period in Ortigosa Caves may be Late Holocene in age and is related to the warm Isotopic Stage 1 at global scale (Henning et al., 1983). The occurrence of this period on the Iberian Peninsula and Balears Islands is shown in the geochronological dating scenario compiled by Durán (1989). This Holocene warm period deduced from stalagmites can be related to other morphosedimentary records in the Iberian Range. Radiometric ages of regional fluvial tufa deposits indicate an extensive period of tufa building during warm Isotopic Stage 1 (Martínez-Tudela et al., 1986; Ordóñez et al., 1990; Sancho et al., 1997; Peña et al., 2000).

This climatic period based on speleothem growth could be correlated with the paleoenvironmental evolution in high latitude regions (see for example, Gordon et al., 1989). However, in addition to the temperature, rainfall changes must be considered as an important factor in the speleothem development stages due to the location of the Iberian Peninsula near the low latitude arid belts (Brook et al., 1990; Bar-Matthews et al., 1996, 1997).

From the radiocarbon ages, it is possible to establish that the LV-1 stalagmite started to grow 3400 ± 600 Ma and finished at present-day time. On the other hand, 1276 annual cycles have been recorded from the internal laminaetions of the stalagmite. As a consequence, it is likely that either we missed a lot of laminae during counting because they were not visible, or there are growth hiatuses. A description of the Late Holocene speleothem sequence can be proposed considering that 900 annual cycles have been counted between 3400 ± 600 yr BP and 1200 ± 400 yr BP, 326 cycles between 1200 ± 400 yr BP and 700 ± 350 yr BP, and 50 cycles between 700 ± 350 yr BP and present time. In spite of the high chronological uncertainty, these data indicate an important lack of cycles between 3400 ± 600 yr BP and 1200 ± 400 yr BP, and also between 700 ± 350 yr BP and present time. Tentatively, we propose to correlate the occurrence of growth hiatuses in stalagmites from the Ortigosa karst system with the Iron Age Cold Phase (the coldest maximum is at 2700–2500 yr BP) and with the Little Ice Age (XVI-XIX centuries) (Muñoz et al., 2001; Peña et al., 2004). However, at this time and with the currently available chronological data, it is not possible to locate exactly both activity and inactivity periods. Similar short-term climatic records ($10^2$–$10^3$ years) have been deduced using Holocene stalagmites in Israel (Frumkin et al., 1999), South Africa (Repinski et al., 1999), Oman (Burns et al., 2001), and Germany (Niggemann et al., 2003).

High climate variability during Late Holocene has been proposed by different authors at regional scale by using different morphosedimentary records and multiproxy data (Peñalba et al., 1997; Perrette, 1999; Sánchez Goñi and Hannon, 1999; Luque, 2003; González-Sempériz et al., 2006; Martín-Chivelet et al., 2006; Thorndycraft and Benito, 2006; Luzón et al., 2007; Vegas, 2007; Sancho et al., 2008). Holocene climatic changes in Iberia, and particularly variations in rainfall, are connected with large-scale atmospheric processes such as the North Atlantic Oscillation (NAO) (Zorita et al., 1992; Trigo et al., 2004). A close relationship has also been proposed between North Atlantic Oscillation and solar activity (Luque, 2003).

### VERY HIGH FREQUENCY CLIMATIC CYCLES

Some of the short term and very high frequency periodicities revealed by wavelet analysis can be related to solar activity cycles, as well as to natural climatic oscillations, such as El Niño-Southern Oscillation (ENSO), North Atlantic Oscillation (NAO), Quasi-Biennial Oscillation (QBO), etc. (O'Sullivan et al., 2002; Burroughs, 2003). Climatic cycles corresponding to the solar activity (1–100 years) have been recognized in Holocene as well as Pleistocene stalagmites by several authors and in different parts of the world (Baker et al., 1993; Shopov et al., 1994; Genty et al., 1994; Genty and Quinif, 1996; Qin et al., 1999; Niggemann et al., 2003; Frisia et al., 2003; Holzkämper et al., 2004; Dykoski et al., 2005; Soubiès et al., 2005).

First, cycles with strong decadal scale periodicities (e.g., 9.7-yr and10.4-yr-periods in LP-4, and 14-yr period in LV-1 stalagmites) can be associated with the sunspot cycle (9–14 years). The 14-yr-period is related to lake drying phases in Gallocanta (Iberian Range) and is interpreted as influencing of the low-frequency component of ENSO (Rodó et al., 1997). Genty et al. (1994) and Genty and

Quinif (1996) found a similar periodicity in a Pleistocene stalagmite from Belgium. This periodicity is also observed by Baker et al. (1993) and Shopov et al. (1994) in their studies of the laminaeted structure in stalagmites using ultraviolet light. Spectral analysis performed on high resolution $\delta^{18}O$ records by Niggemann et al. (2003), Holzkämper et al. (2004) and Dykoski et al. (2005), and on stalagmite laminae thickness records (Qin et al., 1999; Frisia et al., 2003; Soubiès et al., 2005) show strong periodicities at subdecadal and decadal scales. The 22-yr-period may be associated with the Hale cycle of sunspot activity.

On the other hand, the 4–7-year-periodic band can be related to ENSO as well as NAO. Similar periodicities in Holocene stalagmites are described by Genty et al. (1994), Frisia et al. (2003), Dykoski et al. (2005), Rasbury and Aharon (2006), and Soubiès et al. (2005), among others.

The presence of very high frequency periodicities around the 2.4-yr-period can be related to the Quasi-Biennial Oscillation (QBO). This climatic cycle is mainly observed in rainfall and temperature records and has been identified in different varved sediments (Sonett et al., 1992; Muñoz et al., 2002). Oscillations with this period have been found in stalagmite laminae by Qin et al. (1999), and Frisia et al. (2003).

Finally, periodicities at decadal, multidecadal, and centennial scales that are observed in Ortigosa Cave stalagmites and related to solar activity (such as the Gleissberg cycle) have also been found in other cave deposits (see Qin et al., 1999; Niggemann et al., 2003; Holzkämper et al., 2004, and Dykoski et al., 2005).

The way that the solar forcing drives Earth's climate system has been fully discussed (Friis-Christensen and Lassen, 1991; Hoyt and Schatten, 1997; Kelly and Wigley, 1992; Schlesinger and Ramankutty, 1992; Schonwiese et al., 1994; Van Geel et al., 1999; Scafetta and West 2006, 2007). The climatic information provided by the speleothem cycles would be translated into a variation of the cycle thickness due to a more or less intense development of the soil-vegetation system over the cave. During warm and humid climatic periods, the intense soil activity favors a greater amount of percolating water with high concentration in biogenic $CO_2$ in the karst system. The result is a thicker annual cycle through years with higher temperature (more biogenic $CO_2$ and rainfall) and thinner in years with lower temperature.

In the same way, a close relation has been observed between NAO and the distribution of winter rainfall in the Iberian Peninsula. Periods with the NAO in a negative phase are associated with wet conditions in the western Mediterranean and northern Africa (Wanner et al., 1994) whereas periods with positive NAO are related to droughts in the Iberian Peninsula. Moreover, Rodó et al. (1997) relate warm periods of ENSO to periods of reduced rainfall and higher temperatures in the eastern half of Spain. Although the relationship between NAO and ENSO events and atmospheric teleconnections in Europe, and specifically Spain, is not clear, it is possible to correlate higher growth rates in the Ortigosa speleothems with NAO negative phases. The simple relationship between growth rates in the Ortigosa Caves and solar forcing and NAO phases may become more complex with the occurrence of ENSO teleconnections.

## Conclusions

Based on the studies of chronological control and the wavelet analysis of thickness variations of stalagmite deposits in the Ortigosa Caves (La Paz and La Viña), we have deduced environmental and climatic changes with multiple periodicities during Late Holocene. From our analysis, the following conclusions can be made.

1. Late Holocene period (from 4000 yr BP to the present) is a very active stage of speleothem growth in the northern sector of the Iberian Peninsula.
2. Short-term ($10^2$–$10^3$ years) climatic changes can be deduced from radiocarbon-AMS dating combined with annually developed laminae number. However, with the available chronological data, it is not possible to establish a precise sequence of activity and inactivity periods on centennial-millennial time scales.
3. The stalagmites belonging to the Late Holocene stage have developed a banded structure characterized by an alternating sequence of light and dark laminae, which constitute a seasonally controlled microsequence. The wavelet power spectrum analysis of the thickness variations in the stalagmites indicates climatic cycles at centennial, decadal, multidecadal, and interannual scales with periods around 2.4, 4–7, 9.7, 10.4, 14, 16, 22, 43, 73, 83 and 180 years.
4. Very high frequency climatic changes obtained from wavelet analysis are related to astronomical and atmospheric controls. Higher growth rates in the Ortigosa speleothems could be related to warm and humid climatic periods as a consequence of high solar activity and negative phases of NAO.

## Acknowledgements

This work has been supported by the La Rioja Government and Ortigosa de Cameros Town Council. We thank Professor Ives Quinif (Faculté Polytechnique de Mons) for his collaboration on U/Th dating, and Dr. Antonio Vázquez (Instituto Jaume Almera C.S.I.C., Barcelona) for his support on image analysis. This is a contribution by the PaleoQ and Cuencas Sedimentarias Continentales groups (Aragón Regional Government). We thank Dr. Ira D. Sasowsky (Associate Editor) and two anonymous reviewers for valuable suggestions.

## REFERENCES


Addison, P.S., 2001, The illustrated wavelet transform handbook, Bristol, U. K., Institute of Physics Publishing, 353 p.

Baker, A., Smart, P.L., Edwards, R.L., and Richards, D.A., 1993, Annual growth banding in a cave stalagmite: Nature, v. 364, p. 518–520, doi: 10.1038/364518a0.

Baker, A., Barnes, W.L., and Smart, P.L., 1997, Variations in the discharge and organic matter content of stalagmite drip waters in Lower Cave: Hydrological Processes, v. 11, p. 1541–1555.

Baker, A., Genty, D., Dreybrodt, W., Barnes, W.L., Mockler, N.J., and Grapes, J., 1998, Testing theoretically predicted stalagmite growth rate with recent annually laminaeted samples: implications for past stalagmite deposition: Geochimica et Cosmochimica Acta, v. 62, p. 393–404.

Baker, A., Mockler, N.J., and Barnes, W.L., 1999, Fluorescence intensity variations of speleothem-forming groundwaters: Implications for paleoclimate reconstruction: Water Resources Research, v. 35, no. 2, p. 407–413.

Bar-Matthews, M., Ayalon, A., Matthews, A., Sass, E., and Halicz, L., 1996, Carbon and oxygen isotope study of the active water-carbonate system in a karstic Mediterranean cave: implications for paleoclimate research in seimiarid regions: Geochimica et Cosmochimica Acta, v. 60, p. 337–347.

Bar-Matthews, M., Ayalon, A., and Kaufman, A., 1997, Late Quaternary paleoclimate in the Eastern Mediterranean region from stable isotope analysis of speleothems at Soreq Cave, Israel: Quaternary Research, v. 47, p. 155–168.

Brook, G.A., Burney, D.A., and Cowart, J.B., 1990, Desert paleoenvironmental data from cave spelothems with examples from the Chihuahuan, Somali-Chalbi, and Kalahari deserts: Palaeogeography, Palaeoclimatology, Palaeoecology, v. 76, p. 311–329.

Burns, S.J., Fleitmann, D., Matter, A., Neff, U., and Mangini, A., 2001, Speleothem evidence from Oman for continental pluvial events during interglacial periods: Geology, v. 29, p. 623–626.

Burroughs, W., 2003, Weather cycles: Real or imaginary?: Cambridge, U.K., Cambridge University Press, 317 p.

Dorale, J.A., Gonzalez, L.A., Regan, M.K., Pickett, D.A., Murrel, M.T., and Baker, R.G., 1992, A high resolution record of Holocene climate change in speleothem calcite from Cold Water Cave, Northeast Iowa: Science, v. 258, p. 1626–1630.

Durán, J.J., 1989, Geocronología de los depósitos asociados al karst en España, *in* Durán, J.J., and López, J., eds., El karst en España. Monografía, 4, Sociedad Española de Geomorfología, p. 243–256.

Durán, J.J., López, J., Dallai, L., Bruschi, G., Caballero, E., Jiménez, C., and Julia, R., 2000, Paleoenvironmental reconstruction based on a detailed stable isotope analysis and dating of a Holocene speleothem from Valporquero Cave, Northern Spain: Geogaceta, v. 27, p. 63–67.

Dykoski, C.A., Edwards, R.L., Cheng, H., Yuan, D., Cai, Y., Zhang, M., Lin, Y., Qing, J., An, Z., and Revenaugh, J., 2005, A high-resolution, absolute-dated Holocene and deglacial Asian monsoon record from Dongge Cave, China: Earth and Planetary Science Letters, v. 233, p. 71–86.

Friis-Christensen, E., and Lassen, K., 1991, Length of the solar cycle: an indicator of solar activity closely associated with climate: Science, v. 254, p. 698–700.

Frisia, S., Borsato, A., Fairchild, I.J., and Mcdermott, F., 2000, Calcite fabrics, growth mechanisms and environments of formation in speleothems from the Italian Alps and Southwestern Ireland: Journal of Sedimentary Research, v. 70, p. 1183–1196.

Frisia, S., Borsato, A., Preto, N., and McDermott, F., 2003, Late Holocene annual growth in three Alpine stalagmites records the influence of solar activity and the North Atlantic Oscillation on winter climate: Earth and Planetary Science Letters, v. 216, p. 411–424.

Frumkin, A., Ford, D.C., and Schwarcz, P., 1999, Continental oxygen isotopic record of the last 170,000 years in Jerusalem: Quaternary Research, v. 51, p. 317–327.

Genty, D., and Massault, M., 1999, Carbon transfer dynamics from bomb-$^{14}C$ and $\delta^{13}C$ time series of a laminaeted stalagmite from SW-France: Modelling and comparison with other stalagmite: Geochimica et Cosmochimica Acta, v. 63, p. 1537–1548.

Genty, D., and Quinif, Y., 1996, Annually laminaeted sequences in the internal structure of some Belgian stalagmites-Importance for paleoclimatology: Journal of Sedimentary Research, v. 66, p. 275–288.

Genty, D., Quinif, Y., and Deflandre, G., 1994, Microsequences des lamines annuelles dans deux stalagmites du massif de Han-Sur-Lesse (Belgique): Spelochronos, v. 6, p. 9–22.

Genty, D., Baker, A., and Barnes, W., 1997a, Comparaison entre les lamines luminescentes et les lamines visibles annuelles de stalagmites: Comptes rendus de l'Académie des sciences, Série 2, v. 325, no. 3, p. 193–200.

Genty, D., Deflandre, G., Quinif, Y., and Verheyden, S., 1997b, Les lamines de croissance des speleothemes: origine et interet paleoclimatique: Bulletin de la Société Belge de Géologie, v. 106, p. 63–77.

Genty, D., Vokal, B., Obelic, B., and Massault, M., 1998, Bomb 14C time history recorded in two modern stalagmites: Importance for soil organic matter dynamics and bomb 14C distribution over continents: Earth and Planetary Science Letters, v. 160, p. 795–809.

Genty, D., Baker, A., Massault, M., Proctor, Ch., Gilmour, M., Pons-Branchu, E., and Hamelin, B., 2001, Dead carbon in stalagmites: Carbonate bedrock paleodissolution vs. ageing of soil organic matter: Implications for 13C variations in speleothems: Geochimica et Cosmochimica Acta, v. 65, no. 15, p. 3443–3457.

González-Sempériz, P., Valero-Garcés, B.L., Moreno, A., Jalut, G., García-Ruiz, J.M., Martí-Bono, C., Delgado-Huertas, A., Navas, A., Otto, T., and Dedoubat, J.J., 2006, Climate variability in the Spanish Pyrenees during the last 30,000 yr revealed by the El Portalet sequence: Quaternary Research, v. 66, p. 38–52.

Gordon, D., Smart, P.L., Ford, D.C., Andrews, J.N., Atkinson, T.C., Rowe, P., and Christopher, N.S.J., 1989, Dating of late Pleistocene Interglacial and Interstadial periods in the United Kingdom from speleothems growth frequency: Quaternary Research, v. 31, p. 14–26.

Gutiérrez, M., Gutiérrez, F., and Desir, G., 2006, Considerations on the chronological and causal relationships between talus flatirons and paleoclimatic changes in central and northeastern Spain: Geomorphology, v. 73, p. 60–63.

Henning, G.J., Grun, R., and Brunnacker, K., 1983, Speleothems, Travertines and Paleoclimates: Quaternary Research, v. 20, p. 1–29.

Holmgren, K., Lee-Thorp, J.A., Cooper, G.R.J., Lundblad, K., Partridge, T.C., Scott, L., Sithaldeen, R., Talma, A.S., and Tyson, P.D., 2003, Persistent millennial-scale climate variability over the past 25,000 years in Southern Africa: Quaternary Science Reviews, v. 22, p. 2311–2326.

Holzkämper, S., Mangini, A., Spötl, C., and Mudelsee, M., 2004, Timing and progression of the Last Interglacial derived from a high alpine stalagmite: Geophysical Research Letters, v. 31, L07201, doi: 10.1029/2003GL019112.

Hoyt, D.V., and Schatten, K.H., 1997, The Role of the Sun in Climate Change, Oxford, Oxford University Press, 397 p.

ITGE, 1990, Mapa geológico de España. Escala 1:50.000. 2ª Serie (241) Anguiano, Madrid, Servicio de Publicaciones del Ministerio de Industria y Energía.

Kelly, P.M., and Wigley, T.M.L., 1992, Solar cycle length, green-house forcing and global climate: Nature, v. 360, p. 328–330.

Labonne, M., Hillaire-Marcel, C., Ghaleb, B., and Goy, J.L., 2002, Multi-isotopic age assessment of dirty speleothem calcite: an example from Altamira Cave, Spain: Quaternary Science Reviews, v. 21, p. 1099–1110.

Lachniet, M., Burns, S.J., Piperno, D.R., Asmerom, Y., Polyak, V.J., Moy, C.M., and Christenson, K., 2004, A 1500-year El Nino/Southern oscillation and rainfall history for the isthmus of Panama from speleothem calcite: Journal of Geophysical Research, v. 109, D20117, doi: 10.1029/2004JD004694.

Luque, J.A., 2003, Lago de Sanabria: un sensor de las oscilaciones climáticas del Atlántico Norte durante los últimos 6.000 años [PhD thesis], Barcelona, Universitat de Barcelona, 384 p.

Luzón, A., Pérez, A., Mayayo, M.J., Soria, A.R., Sánchez-Goñi, M.F., and Roc, A.C., 2007, Holocene environmental changes in the Gallocanta lacustrine basin, Iberian Range, NE Spain: Holocene, v. 17, p. 649–663.

Martín-Chivelet, J., Muñoz-García, M.B., Domínguez-Villar, D., Turrero, M.J., and Ortega, A.I., 2006, Comparative analysis of stalagmites from two caves of northern Spain: Implications for Holocene paleoclimate studies: Geologica Belgica, v. 9, no. 3–4, p. 323–335.

Martínez-Tudela, A., Cuenca, F., Santisteban, C., Grun, R., and Hentzsch, B., 1986, Los travertinos del Río Matarraña, Beceite (Teruel) como indicadores paleoclimáticos del Cuaternario, *in* López-Vera, F., ed., Quaternary Climate in Western Mediterranean, p. 307–324.

McDermott, F., 2004, Paleoclimate reconstruction from stable isotope variations in speleothems: A review: Quaternary Science Reviews, v. 23, p. 901–918.

Ming, T., Tungsheng, L., Xiaoguang, Q., and Xianfeng, W., 1998, Signification chronoclimatique de spéléothèmes laminés de Chine du Nord: Karstologia, v. 32, p. 1–6.

Mitchell, J.M., 1976, An overview of climatic variability and its causal mechanism: Quaternary Research, v. 6, p. 481–493.

Muñoz, A., Peña, J.L., Sancho, C., and Martínez, M.A., 2001, Los espeleotemas de las cuevas de Ortigosa de Cameros (La Rioja): Datos cronológicos y consideraciones paleoambientales: Geogaceta, v. 30, p. 95–98.

Muñoz, A., Ojeda, J., and Sanchez-Valvede, B., 2002, Sunspots-like and ENSO/NAO-like periodicities in lacustrine laminaeted sediments of the Pliocene Villarroya Basin (La Rioja, Spain): Journal of Paleolimnology, v. 27, no. 4, p. 453–463.

Muñoz, A., Sancho, C., Peña, J.L., Sánchez-Valverde, B., Valero-Garcés, B., Durán, J.J., and Genty, D., 2004, Ciclos climáticos de alta frecuenta en los espeleotemas de las Cuevas de Ortigosa de Cameros (La Rioja), *in* Liesa, C., Pocoví, A., Sancho, C., Colombo, F., González, A., and Soria, A.R., eds., Geo-Temas, v. 6, no. 5, p. 141–144 (VI Congreso Geológico de España).

Muñoz-García, M.B., Martín-Chivelet, J., and Rossi, C., 2004, Implicaciones paleoclimáticas de la distribución geocronológica de espeleotemas en la Cueva del Cobre (Palencia): Geogaceta, v. 35, p. 179–182.

Muñoz-García, M.B., Martín-Chivelet, J., Rossi, C., Ford, D.C., and Schwarcz, H.P., 2007, Chronology of Termination II and the Last Interglacial Period in North Spain based on stable isotope records of stalagmites from Cueva del Cobre (Palencia): Journal of Iberian Geology, v. 33, no. 1, p. 17–30.

Niggemann, S., Mangini, A., Mudelsee, M., Richter, D.K., and Wurth, G., 2003, Sub-Milankovitch climatic cycles in Holocene stalagmites from Sauerland, Germany: Earth and Planetary Science Letters, v. 216, p. 539–547.

O'Sullivan, P.E., Moyeed, R., Cooper, M.C., and Nicholson, M.J., 2002, Comparison between instrumental, observational and high resolution proxy sedimentary records of Late Holocene climatic change — a discussion of possibilities: Quaternary International, v. 88, p. 27–44.

Ordóñez, S., González, J.A., and García Del Cura, M.A., 1990, Datación radiogénica (U-234/U-238 y Th-230/U-234) de sistemas travertínicos del Alto Tajo (Guadalajara): Geogaceta, v. 8, p. 53–56.

Peña, J.L., Sancho, C., and Lozano, M.V., 2000, Climatic and tectonic significance of Late Pleistocene and Holocene tufa deposits in the Mijares river canyon (Eastern Iberian Range, NE Spain): Earth Surface Processes and Landforms, v. 25, p. 1403–1417.

Peña, J.L., Julián, A., Chueca, J., Echeverría, M.T., and Ángeles, G., 2004, Etapas de evolución holocena en el valle del río Huerva: Geomorfología y Geoarqueología, *in* Peña, J.L., Longares, L.A., and Sánchez, M., eds., Geografía Física de Aragón: aspectos generales y temáticos, Universidad de Zaragoza-Institución Fernando el Católico, p. 289–302.

Peñalba, M.C., Arnold, M., Guiot, J., Duplessy, J.C., and de Beaulieu, J.L., 1997, Termination of the Last Glaciation in the Iberian Península inferred from the pollen sequence of Quintanar de la Sierra: Quaternary Research, v. 48, p. 205–214.

Perrette, Y., 1999, Les stalagmites: archives environnementales et climatiques à haute résolution. Présentation des protocoles d'étude et premiers résultats sur les spéléothèmes du Vercors: Karstologia, v. 34, no. 2, p. 23–44.

Qin, X., Tan, M., Liu, T., Wang, X., Li, T., and Lu, J., 1999, Spectral analysis of a 1000-year stalagmite laminae-thickness record from Shihua Cavern, Beijing, China, and its climatic significance: Holocene, v. 9, p. 689–694.

Quinif, Y., Genty, D., and Maire, R., 1994, Les spéléothèmes: un outil perfomant pour les études paléoclimatiques: Bulletin Societé Géologique France, v. 165, p. 603–612.

Railsback, L.B., Brook, G.A., Chen, J., Kalin, R., and Fleisher, J., 1994, Environmental controls on the petrology of a late Holocene speleothem from Botswana with annual layers of aragonite and calcite: Journal of Sedimentary Research, v. A64, p. 147–155.

Rasbury, M., and Aharon, A., 2006, ENSO-controlled rainfall variability records archived in tropical stalagmites from the mid-ocean island of Niue, South Pacific: Geochemistry, Geophysics, Geosystems, v. 7, p. 1–15.

Reimer, P.J., Baillie, M.G.L., Bard, E., Bayliss, A., Beck, J.W., Bertrand, C., Blackwell, P.G., Buck, C.E., Burr, G., Cutler, K.B., Damon, P.E., Edwards, R.L., Fairbanks, R.G., Friedrich, M., Guilderson, T.P., Hughen, K.A., Kromer, B., McCormac, F.G., Manning, S., Bronk Ramsey, C., Reimer, R.W., Remmele, S., Southon, J.R., Stuiver, M., Talamo, S., Taylor, F.W., Van der Plicht, J., and Weyhenmeyer, C.E., 2004, IntCal04 terrestrial radiocarbon age calibration, 26-0 ka BP: Radiocarbon, v. 46, p. 1029–1058.

Repinski, P., Holmgren, K., Lauritzen, S.E., and Lee-Thorp, J.A., 1999, A late Holocene climate record from a stalagmite, Cold Air Cave, Northern province, South Africa: Palaeogeography, Palaeoclimatology, Palaeoecology, v. 150, p. 269–277.

Rodó, X., Baert, E., and Comín, F.A., 1997, Variations in seasonal rainfall in Southern Europe during the present century: relationships with the North Atlantic Oscillation and the El Niño-Southern Oscillation: Climate Dynamics, v. 13, p. 275–284.

Sánchez Goñi, M.F., and Hannon, G.E., 1999, High-altitude vegetational pattern on the Iberian Mountain Chain (north-central Spain) during the Holocene: Holocene, v. 9, p. 39–57.

Sancho, C., Peña, J.L., and Meléndez, A., 1997, Controls on Holocene and present-day travertine formation in the Guadalaviar River (Iberian Chain, NE Spain): Zeistchrift fur Geomorphologie, v. 41, p. 289–307.

Sancho, C., Peña, J.L., Muñoz, A., Benito, G., McDonald, E., Rhodes, E., and Longares, L.A., 2008, Holocene alluvial morphopedosedimentary record and environmental changes in the Bardenas Reales Natural Park (NE Spain): Catena, v. 73, p. 225–238.

Scafetta, N., and West, B.J., 2006, Phenomenological solar signature in 400 years of reconstructed Northern Hemisphere temperature record: Geophysical Research Letters, v. 33, L17718, doi: 10.1029/2006GL027142.

Scafetta, N., and West, B.J., 2007, Phenomenological reconstructions of the solar signature in the Northern Hemisphere surface temperature records since 1600: Journal of Geophysical Research, v. 112, D24S03, doi: 10.1029/2007JD008437.

Schlesinger, M.E., and Ramankutty, N., 1992, Implications for global warming of intercycle solar irradiance variations: Nature, v. 360, p. 330–333.

Schonwiese, C.D., Ullrich, R., Beck, F., and Rapp, J., 1994, Solar signals in global climatic change: Climate Change, v. 27, p. 259–281.

Sen, A.K., and Dostrovsky, J.O., 2007, Evidence of intermittency in the local field potentials recorded from patients with Parkinson's disease — A wavelet-based approach: Computational and Mathematical Methods in Medicine, v. 8, p. 165–171.

Sen, A.K., Longwic, R., Litak, G., and Gorski, K., 2008a, Analysis of cycle-to-cycle pressure oscillations in a diesel engine: Mechanical Systems and Signal Processing, v. 22, p. 362–373.

Sen, A.K., Filippelli, G., and Flores, J., 2008b, An application of wavelet analysis to paleoproductivity records from the Southern Ocean: Computers and Geosciences (in press).

Shopov, Y.Y., Ford, D.C., and Schwarcz, H.P., 1994, Luminescent microbanding in speleothems: high-resolution chronology and paleoclimate: Geology, v. 22, p. 402–410.

Sonett, C.P., Williams, C.R., and Mörner, N.A., 1992, The Fourier spectrum of Swedish riverine varves: evidence of sub-arctic quasi-biennial (QBO) oscillations: Palaeogeography, Palaeoclimatology, Palaeoecology, v. 98, p. 57–65.

Soubiès, F., Seidel, A., Mangin, A., Genty, D., Ronchail, J., Plagnes, V., Hirooka, S., and Santos, R., 2005, A fifty-year climatic signal in three Holocene stalagmite records from Mato Grosso, Brazil: Quaternary International, v. 135, p. 115–129.

Stuiver, M., Kra, R.S., and editors, 1986, Calibration issue, Proceedings of the 12th International 14C Conference: Radiocarbon, v. 28, p. 805–1030.

Tan, M., Baker, A., Genty, D., Smith, C., Esper, J., and Cai, B., 2006, Applications of stalagmite laminae to paleoclimate reconstructions: Comparison with dendrochronology/climatology: Quaternary Science Reviews, v. 25, p. 2103–2117.

Thorndycraft, V.R., and Benito, G., 2006, The Holocene fluvial chronology of Spain: Evidence from a newly compiled radiocarbon database: Quaternary Science Reviews, v. 25, p. 223–234.

Torrence, C., and Compo, G.P., 1998, A practical guide to wavelet analysis: Bulletin of the American Meteorological Society, v. 79, p. 61–78.

Trigo, R.M., Pozo, D., Osborne, T., Castro, Y., Gámiz, S., and Esteban, M.J., 2004, North Atlantic Oscillation influence on precipitation, river flow and water resources in the Iberian Peninsula: International Journal of Climatology, v. 24, p. 925–944.

Van Geel, B., Raspopov, O.M., Renssen, H., Van der Plicht, J.R., Dergachev, V.A., and Meijer, H.A.J., 1999, The role of solar forcing upon climate change: Quaternary Science Review, v. 18, p. 331–338.

Vegas, J., 2007, Caracterización de eventos climáticos del Pleistoceno superior-Holoceno mediante el estudio sedimentológico de la Laguna Grande (Sierra de Neila, NO Sistema Ibérico): Revista de la Sociedad Geológica de España, v. 20, p. 53–70.

Wanner, H., Brazdil, R., Frich, P., Frydendahl, K., Jonsson, T., Kington, J.A., Pfister, C., Rosenorn, S., and Wishman, E., 1994, Synoptic interpretation of monthly weather maps for the late Maunder Minimum (1675–1704), *in* Frenzel, B., Pfister, C., and Glaser, B., eds., Climatic Trends and Anomalies in Europe, Stuttgart, Gustav Fischer Verlag, p. 401–424.

Zorita, E., Kharin, V., and von Storch, H., 1992, The atmospheric circulation and sea surface temperature in the North Atlantic area in winter: Their interaction and relevance for Iberian precipitation: Journal of Climate, v. 5, p. 1097–1108.

## APPENDIX

### WAVELET ANALYSIS METHODOLOGY

A wavelet is a small wave with zero mean and finite energy. The continuous wavelet transform (CWT) of a function $x(t)$ with respect to a wavelet $\psi(t)$ is given by the convolution of the function with a scaled and translated version of $\psi(t)$. The function $\psi(t)$ is referred to as an analyzing wavelet or a mother wavelet. The convolution is expressed by the integral:

$$W(s,\tau) = \int_{-\infty}^{+\infty} x(t)\psi^*_{s,\tau}(t)dt \qquad (1)$$

where

$$\psi_{s,\tau}(t) = \frac{1}{\sqrt{s}}\psi\left(\frac{t-\tau}{s}\right) \qquad (2)$$

is a scaled and translated version of the mother wavelet $\psi(t)$ and an asterisk on $\psi$ denotes its complex conjugate. The symbols $s$ and $\tau$ are the scale parameter and translation parameters, respectively. The scale parameter controls the dilation ($s > 1$) and contraction ($s < 1$) of the mother wavelet. The factor $1/\sqrt{s}$ is introduced in Equation (2) so that the function $\psi_{s,\tau}(t)$ has unit energy at every scale. The translation parameter $\tau$ indicates the location of the wavelet in time; in other words, as $\tau$ varies, the signal is analyzed in the vicinity of this point. The amount of signal energy contained at a specific scale $s$ and location $\tau$ is given by the squared modulus of the CWT, $P(s,\tau) = |W(s,\tau)|^2$.

For a time series $\{x_i\}$ with $i = 1, 2, 3, \ldots, N$, the integral formulation shown in Equation (1) can be discretized as (Torrence and Compo, 1998):

$$W_n(s) = \sum_{n=1}^{N}\left(\frac{\delta t}{s}\right)^{1/2} x_{n'}\psi^*\left[\frac{(n'-n)}{s}\right] \qquad (3)$$

Here $n$ is the time index, $s$ is the wavelet scale, and $\delta t$ is the sampling interval. The wavelet power spectrum (WPS) of the time series is defined by $|W_n(s)|^2$, which is a measure of the fluctuation of the variance at different scales or frequencies. This power spectrum, which depends on both scale and time, is represented by a surface. By plotting contours of this surface on a plane, a time-scale representation of the spectrum may be derived.

A time-scale representation is found to be useful for extracting important features of signals arising in many applications. An alternate representation, namely, a time-frequency representation, has also been used. A scale-to-frequency conversion, which follows a reciprocal relationship, can be easily made by use of the formula, $f = f_0 f_*/s$, where $f$ is the instantaneous frequency of the signal, $f_*$ is the sampling frequency, and $f_0$ is the center frequency of the mother wavelet (see below). In our analysis, we used a complex Morlet wavelet as the mother wavelet. A complex Morlet wavelet consists of a plane wave modulated by a Gaussian function and is described by

$$\psi(\eta) = \pi^{-1/4} e^{i\omega_0\eta} e^{-\eta^2/2} \qquad (4)$$

where $\omega_0 = 2\pi f_0$, is the order of the wavelet, with $f_0$ being the center frequency. In our computations we have used a Morlet wavelet of order 6 as the mother wavelet. This choice provides a good balance between time and frequency localizations. For this choice, the scale is also approximately equal to the Fourier period and thus the terms scale and period can be used interchangeably.

The wavelet power spectrum (WPS) displays a contour plot of power as a function of scale (period) and time and is sometimes referred to as a local wavelet spectrum. Additional information about the spectral properties of the time series can be obtained by averaging the WPS at each scale over all time, and thereby calculating the global wavelet spectrum (GWS). The GWS is given by

$$\overline{W}^2_S = \frac{1}{N}\sum_{n=1}^{N}|W_n(s)|^2 \qquad (5)$$

(Torrence and Compo, 1998). The GWS displays power as a function of period or frequency and is similar to a smoothed Fourier power spectrum. The dominant spectral modes of the time series can be identified from the various peaks in the GWS.

J.A. Dorale and Z. Liu – Limitations of hendy test criteria in judging the paleoclimatic suitability of speleothems and the need for replication. *Journal of Cave and Karst Studies,* v. 71, no. 1, p. 73–80.

# LIMITATIONS OF HENDY TEST CRITERIA IN JUDGING THE PALEOCLIMATIC SUITABILITY OF SPELEOTHEMS AND THE NEED FOR REPLICATION

JEFFREY A. DORALE[1] AND ZAIHUA LIU[2,3,*]

**Abstract:** Carbon and oxygen isotopes in calcite speleothems are powerful proxies for understanding past climate change. For calcite deposited under isotopic equilibrium conditions, variations in $\delta^{18}O$ values directly reflect changes in cave temperature and the isotopic composition of meteoric water. Speleothem $\delta^{13}C$ values have bedrock, atmospheric, and soil gas sources. Soil gases can be traced to the overlying vegetation, which is related to climate. Both $\delta^{13}C$ and $\delta^{18}O$ values are therefore potentially powerful tracers of climate change. Processes that could alter speleothem $\delta^{13}C$ and/or $\delta^{18}O$ values, and thereby mask primary environmental signals, fall in the categories of 1) kinetic processes, including deposition of calcite out of isotopic equilibrium, and 2) vadose processes, including evaporation of water at or near the land surface. In truth, there is no absolute test for the absence of these kinetic/vadose-zone processes. However, the Hendy Test is widely used for assessing whether isotopic equilibrium existed during the time of calcite deposition. Criterion (1) of the Hendy Test (i.e., that $\delta^{18}O$ values remain constant along a single growth layer) may not be a valid control of equilibrium conditions because isotopic equilibrium could theoretically occur in the center of the speleothem at the same time that kinetic fractionation occurs at the flanks. Moreover, the concept of sampling along a single growth layer is flawed in both theory and practice. Criterion (2) of the Hendy Test (i.e., that there is no relationship between $\delta^{13}C$ and $\delta^{18}O$) is based on the assumption that speleothem $\delta^{13}C$ values are not linked to climate. However, speleothem $\delta^{13}C$ values may well be linked to climate because climate provides a first-order control on soil productivity and the type of vegetation. Therefore, Hendy Test criterion (2) is not a prerequisite to isotopic equilibrium in all cases. We propose instead the Replication Test (i.e., the demonstration of similar isotopic profiles among two or more speleothems) for evaluating the likelihood of calcite deposition under isotopic equilibrium conditions. Replication of isotopic profiles among two or more speleothems is possible only if kinetic/vadose-zone processes are either: 1) absent or 2) have affected spatially separated speleothems in exactly the same way. Because the second scenario is highly unlikely, we propose that the Replication Test is effectively sufficient in ruling out kinetic/vadose-zone overprinting processes. We further suggest that the Replication Test is far more robust in testing for the absence of the wide range of processes described above than is the traditional Hendy Test.

## INTRODUCTION

Carbon- and oxygen-isotopic variations in speleothems have been studied for more than 40 years (Galimov and Grinenko, 1965; Hendy and Wilson, 1968; Duplessy et al., 1970), commonly with the central goal of reconstructing past environmental and/or climatic conditions. In a seminal paper, Hendy (1971) outlined the various equilibrium and nonequilibrium processes that govern $\delta^{18}O$ and $\delta^{13}C$ values during calcite speleothem formation and discussed the means of recognizing whether speleothem stable isotopic signatures might serve as appropriate paleoclimatic indicators.

Continued refinements in U/Th dating techniques (Edwards et al., 1987; Shen et al., 2002; Dorale et al., 2004; Hellstrom, 2006) and construction of high-resolution $\delta^{18}O$ time series comparable to ice core records (Bar-Matthews et al., 1997; Dorale et al., 1998; Wang et al., 2001; Yuan et al., 2004; Spötl et al., 2006; Wang et al., 2008; Zhang et al., 2008) have generated a surge of renewed interest in using speleothems as high-resolution paleoclimatic archives. Thus, the fidelity with which $\delta^{18}O$ and $\delta^{13}C$ variations in speleothems might be interpreted as paleoclimatic indicators remains a basic and critical issue. This

*Corresponding author. Tel: 86-851-5892338; Fax: 86-851-5891721; E-mail addresses: liuzaihua@vip.gyig.ac.cn (Z. Liu)
[1] Department of Geoscience, University of Iowa, Iowa 52242-1379, USA
[2] The State Key Laboratory of Environmental Geochemistry, Institute of Geochemistry, Chinese Academy of Sciences, 550002 Guiyang, China
[3] The Key Laboratory of Karst Dynamics, Ministry of Land and Resources, Institute of Karst Geology, Chinese Academy of Geological Sciences, 541004 Guilin, China

paper considers the widely used Hendy Test method for evaluating the presence or absence of isotopic equilibrium in speleothems. We reach the long overdue conclusion that the Hendy Test criteria for judging speleothems (Hendy, 1971) are not reliably effective at screening stalagmites for paleoclimatic suitability. We therefore suggest that the widespread application of Hendy Test should be discontinued. We propose instead the Replication Test (i.e., the demonstration of similar isotopic profiles among two or more speleothems) for evaluating the likelihood of calcite deposition under isotopic equilibrium conditions (e.g. Dorale et al., 1998; Wang et al., 2001; Constantin et al., 2007; Denniston et al., 2007; Wang et al., 2008). Replication of isotopic profiles among two or more speleothems is possible only if kinetic/vadose-zone processes are either: 1) absent or 2) have affected spatially separated speleothems in exactly the same way. As the second scenario is highly unlikely because of the spatial heterogeneity of the karst aquifer (Perrin et al., 2003), we propose that the Replication Test is effectively sufficient in ruling out kinetic/vadose-zone-overprinting processes.

## OXYGEN AND CARBON ISOTOPES IN SPELEOTHEMS

The $\delta^{18}O$ and $\delta^{13}C$ values of speleothem $CaCO_3$ are related to the primary sources of oxygen and carbon in the cave seepage water. In the case of oxygen, this is meteoric water. In the case of carbon, this is soil $CO_2$, atmospheric $CO_2$, and carbonate bedrock. In most cases, the process of speleothem deposition can be traced back to the soil layer where biological activity produces high levels of $CO_2$. This soil $CO_2$ acidifies seepage waters, which in turn dissolve carbonate bedrock enroute to underlying caves. Upon entering a cave passage of lower $CO_2$ partial pressure (relative to the soil atmosphere), the seepage water releases $CO_2$ and $CaCO_3$ deposition takes place in accordance with the equation below (Holland et al., 1964):

$$Ca^{2+} + 2HCO_3^- \rightarrow CO_2 + CaCO_3 + H_2O \quad (1)$$

Because $HCO_3^-$ concentrations in karst ground waters are typically in the parts per thousand range, $\delta^{18}O$ values of the water and the dissolved carbonate species are dominated by the water molecules themselves, which originated as meteoric precipitation. Therefore, the $\delta^{18}O$ values of speleothems are generally not significantly influenced by bedrock $\delta^{18}O$ values (Harmon, 1979).

Paleoclimatic interpretation of speleothem $\delta^{18}O$ variations requires knowledge and quantitative estimation of processes that may affect the isotopic composition of water during the course of the hydrologic cycle and during calcite deposition. The cave temperature effect of Williams et al. (1999) represents isotopic fractionation between water and calcite during calcite deposition. The temperature dependence of the fractionation has been experimentally determined as $\sim -0.24$‰ per °C (O'Neil, 1969), meaning that there is greater fractionation at low temperatures relative to high temperatures. The rainwater composition effect represents established empirical relationships between precipitation $\delta^{18}O$ values and certain climatic parameters such as temperature and rainfall intensity (Dansgaard, 1964). Different parts of the globe are represented by fundamentally different relationships, depending on the prevailing meteorological pattern of precipitation. In tropical regions and regions that experience a strong monsoon or a Mediterranean climate, for example, the rainwater composition effect may not have a strong link to temperature. Other factors, such as the intensity of the rainfall (Dansgaard's (1964) Amount Effect), or the partitioning of multiple moisture sources over the course of the year, may dominate variations in the $\delta^{18}O$ values of precipitation (Wang et al., 2001; Bar-Matthews et al., 2003; Wang et al., 2008). However, at many middle and high-latitude sites, the rainwater composition effect is linked to temperature. The modern day spatial slope for Greenland, for example, is 0.67‰ per °C (Johnsen et al., 1989). For many mid-latitude regions, the $\delta^{18}O_{MAP(\text{mean annual precipitation})} - MAT_{(\text{mean annual temperature})}$ slope is generally also positive, but the slope is typically smaller than 0.67‰ per °C.

Caves are excellent environments for temperature reconstructions because the ambient temperature within sufficiently deep caves is constant year-round, and reflects the mean surface temperature averaged over several years (Wigley and Brown, 1976). The $\sim -0.24$‰ per °C fractionation that defines the cave temperature effect, therefore, reflects the mean annual temperature of the area. If the cave drip water can be assumed to approximate $\delta^{18}O_{MAP}$ (Yonge et al., 1985), the rainwater composition effect and the cave temperature effect may be combined to yield an $\delta^{18}O_{speleothem} - MAT$ slope that is either positive, negative, or zero, depending on the exact sign and slope of the $\delta^{18}O_{MAP} - MAT$ relationship (Hendy and Wilson, 1968; Harmon et al., 1978; Gascoyne et al., 1980; Dorale et al., 1992; Winograd et al., 1992; Dorale et al., 1998; Lauritzen and Lundberg, 1999b; Williams et al., 1999). If the $\delta^{18}O_{MAP} - MAT$ slope has a value larger than +0.24‰ per °C, then the $\delta^{18}O_{speleothem} - MAT$ slope will be positive (i.e. more positive $\delta^{18}O_{speleothem}$ values indicate warmer temperatures). If the $\delta^{18}O_{MAP} - MAT$ slope is less than +0.24‰ per °C, the $\delta^{18}O_{speleothem} - MAT$ slope will be negative, in which case more positive $\delta^{18}O_{speleothem}$ values indicate lower temperatures.

What mostly limits robust quantitative temperature reconstructions back through time is the incomplete knowledge of how the slope for $\delta^{18}O_{MAP} - MAT$ has varied through time. Possible reasons for $\delta^{18}O_{MAP} - MAT$ slope variations include fundamental changes in the seasonality or the moisture source of the precipitation (Jouzel et al., 1997). In the case of speleothems, the problems of an unknown, but presumably variable rainwater composition effect could be circumvented if

there was some way of accessing directly the water from which the calcite was precipitated. Fluid inclusions in speleothems are tiny trapped parcels of the original drip water from which the calcite was deposited. Henry Schwarcz and his students pioneered the early ideas of fluid inclusion work (Schwarcz et al., 1976; Harmon et al., 1979; Yonge, 1982), but technical difficulties in extracting an unfractionated sample of the water stymied the approach for many years. Recent work shows considerable promise in having overcome the technical challenges (Rowe et al., 1998; Matthews et al., 2000; Vonhof et al., 2006; Zhang et al., 2008).

Most recently, the clumped isotope technique has been developed as a type of quantitative paleothermometer for carbonates that requires no information or assumptions about the $\delta^{18}O$ values of waters from which carbonates grew (Eiler, 2007; Affek et al., 2008). This is an exciting development, although application of the clumped isotope paleothermometer to speleothems is in its infancy and we would think there will be significant challenges (although not insurmountable) in accurately applying the technique to speleothems because of issues with sample size and precision.

Unlike $\delta^{18}O$ values, speleothem $\delta^{13}C$ values are significantly influenced by the isotopic composition of the bedrock and the soil $CO_2$ (Deines et al., 1974). Vegetation is a major controlling factor of speleothem $\delta^{13}C$ values because soil $CO_2$ is generated largely by root respiration and the microbial oxidation of soil organic matter, which is derived from vegetation. Whereas bedrock characteristics are generally stable over the timescales of U/Th dating, vegetation can be dynamic. Most of the world's plants utilize either the $C_3$ photosynthetic pathway or the $C_4$ pathway (a minor group is the CAM pathway). The $C_3$ and $C_4$ photosynthetic pathways produce large differences in $\delta^{13}C$ values. $C_3$ plants have $\delta^{13}C$ values averaging ca. $-26‰$, whereas $C_4$ plants average ca. $-12‰$ (Deines, 1986). $C_4$ plants are typically warm-season grasses and a few herbs found in tropical and temperate grasslands, whereas $C_3$ plants include most trees, shrubs, cool-season grasses, and most herbs. Where $C_3$ and $C_4$ plant types coexist, their biomass ratio will be reflected in the soil $CO_2$ $\delta^{13}C$ values. Proxies capable of preserving soil $\delta^{13}C$ signatures such as speleothems (Dorale et al., 1992; 1998; Holmgren et al., 1995) are thus capable of recording the proportion of $C_3$ to $C_4$ plant biomass through time, and are indirectly linked to climate. Thus, we do not necessarily agree with the generalized assertion of Dreybrodt (2008), that "...oxygen isotope records of stalagmite are more promising for extracting paleo-climatic signals than those of carbon".

## Limitations of the Hendy-Test Criteria

### Equilibrium Versus Non-Equilibrium Deposition of Calcite

Although it is clear that speleothem $\delta^{18}O$ values are controlled by temperature and the isotopic composition of meteoric water and that $\delta^{13}C$ values are controlled by the isotopic composition of bedrock and soil organic matter, the degree to which the $\delta^{18}O$ and $\delta^{13}C$ values of speleothem calcite reflect only these primary environmental variables is possibly a more complex issue. It is possible that other processes may mask these primary environmental variables (Hendy, 1971). These processes may fall into the category of kinetic processes during calcite crystallization. Hendy (1971) distinguished such kinetic effects from the more desirable isotopic-equilibrium condition. That is the condition defined by sufficiently slow degassing rates and with no evaporation, such that the fractionation of heavy and light isotopes between aqueous and solid phases is only a function of temperature. Although useful paleoenvironmental information may be recorded in speleothems deposited out of isotopic equilibrium (Talma and Vogel, 1992; Spötl and Mangini, 2002), equilibrium deposition is generally more desirable because, under such conditions, temporal variations in $\delta^{18}O$ and $\delta^{13}C$ values most likely reflect changes in the primary environmental variables of interest directly, not indirectly through complicated controls on varying degrees of non-equilibrium effects.

Recently, a number of field, experimental, and modeling studies have focused directly on the issue of isotopic equilibrium in stalagmites (e.g., Mickler et al., 2004; Mickler et al., 2006; Mühlinghaus et al., 2007; Romanov et al., 2008; Dreybrodt, 2008). All have provided valuable insight into this important issue of equilibrium versus non-equilibrium deposition, but none have seriously challenged the general applicability of the Hendy Test in screening stalagmites for paleoclimatic suitability.

### The Hendy-Test Criteria and Their Limitations

In many recent studies, researchers have applied Hendy Test criteria to a single stalagmite to ascertain whether the calcite was deposited under isotopic equilibrium conditions (e.g., Fleitmann et al., 2004; Dykoski et al., 2005; Vacco et al., 2005; Williams et al., 2005; Johnson et al, 2006a; Spötl et al., 2006; Mangini et al., 2007; Hu et al., 2008; Zhang et al., 2008; Zhou et al., 2008). The Hendy Test approach requires drilling subsamples along a growth layer in the stalagmite, from the center outward and down the flanks. The Hendy Test criteria are: (1) $\delta^{18}O$ values remain constant along a single growth layer; (2) there are no simultaneous enrichments of $^{13}C$ and $^{18}O$ in the speleothem calcite (i.e., there is no correlation between $\delta^{13}C$ and $\delta^{18}O$ values). The basis for $^{13}C$ enrichments is thought to be linked to Rayleigh distillation of the $HCO_3^-(aq)$ reservoir during degassing of $\delta^{13}C$-depleted $CO_2$ (Hendy, 1971; Mickler et al., 2006; Romanov et al., 2008). In contrast, $^{18}O$ may not be nearly as affected by Rayleigh distillation during degassing because $CO_2$ hydration and hydroxylation reactions will buffer the oxygen isotopic composition of the $HCO_3^-(aq)$ reservoir (Mickler et al., 2006). However, if the effects of Rayleigh distillation manifest themselves in the oxygen isotopic system, they will result in

$\delta^{18}O$ enrichment in the $HCO_3^-$ (aq) reservoir and ultimately in the precipitated $CaCO_3$.

Based on the above argument, criterion (1) may at face value appear to have a sound theoretical basis, but it may not be a perfect test for the presence of equilibrium conditions because isotopic equilibrium fractionation could occur in the center of a stalagmite at the same time that kinetic fractionation occurs at the flanks (Talma and Vogel, 1992; Spötl and Mangini, 2002; Dreybodt, 2008). In this particular case, criterion (1) of the Hendy Test could fail to indicate that isotopic equilibrium was maintained in any sector of the studied stalagmite. An additional, and largely underappreciated, problem with criterion (1) revolves around the issues of sampling resolution and sampling errors. In practice, criterion (1) is difficult (if not impossible) to apply, in part, because even small sampling errors could invalidate the within growth layer comparison, and in part, because the geometry of a typical stalagmite is not well-suited for the task. A typical growth layer is commonly thickest along the top surface of the stalagmite and becomes progressively thinner along the sides. If growth layers were of uniform thickness, stalagmites would be twice as wide as they are tall, which is seldom, if ever, the case. Therefore, when a constant diameter drill bit is used, drillings from the sides of the stalagmite (where the targeted layer is thinner) will likely include calcite that is younger and/or older relative to drillings from the top surface. This errantly sampled young and old calcite (possibly even including small growth hiatuses not present in the stalagmite center) may have a significantly different isotopic composition than that of targeted growth layer. Thus, a comparison of coeval sub-samples from the top and the sides is not truly valid, and a negative result of the Hendy Test does not, therefore, necessarily indicate kinetic fractionation during deposition (Lauritzen and Lundberg, 1999a). A truly valid attempt at executing criterion (1) would by necessity use multiple drill bits of variable diameter. This approach has never, to our knowledge, been reported in the literature.

Another, possibly more critical issue with regard to sampling resolution, involves the large temporal mismatch between drilled subsamples and the actual timescale of calcite-formation processes. Subsamples drilled using modern techniques are time integrations typically on the order of months to centuries, depending on calcite deposition rates. Even the short end of this timescale is clearly incompatible with the seconds to hours timescale of drip rate, $CO_2$ degassing, calcite precipitation, and other reaction processes being evaluated as equilibrium versus non-equilibrium by Hendy Test criterion (1). In other words, since drilled sub-samples often incorporate years to centuries of material into a single isotopic value, criterion (1) implicitly assumes that any level of apparent isotopic disequilibrium detected by criterion (1) was maintained at some constant level for the entire time of integration. This is highly unlikely, as numerous studies of cave drip waters have shown high variability in seasonal drip and related isotopic phenomena (e.g. Bar-Matthews et al., 1996; Treble et al., 2005; Johnson et al., 2006b; Cobb et al., 2007).

The same temporal mismatch is problematic for the same reason to studies of modern drip waters and associated speleothems, which has been claimed by some to offer the most convincing case for assessing whether isotopic equilibrium exists in a given cave setting (e.g., Bar-Matthews et al., 1996; Mickler et al., 2006; Harmon et al., 2004). The problem again is that drip waters collected in modern settings represent isotopic snapshots of seconds-to-minutes while calcite collected for comparison (due to sample size constraints) may represent much longer time integrations. Furthermore, this mismatch in water volume versus calcite volume (normalized to time) to enable measurements on both probably results in significant bias in modern drip/calcite studies toward fast-growing calcites. Unfortunately, this may well be the type of calcite most likely to have been deposited out of isotopic equilibrium.

Hendy Test criterion (2) is based on the assumption that there is no systematic change in the $\delta^{13}C$ value of soil $CO_2$ with a change in climate as reflected by $\delta^{18}O$ values (Hendy, 1971). While this scenario is theoretically possible, it would appear to be unlikely in the majority of cases. In fact, the concentration and $\delta^{13}C$ values of soil $CO_2$ are tied to climate, which controls the soil bio-productivity (Cerling and Quade, 1993; Hellstrom et al., 1998; Hellstrom et al, 2000; Genty et al., 2006) and the type of vegetation (Cerling, 1984; Deines, 1986). As one example, vegetation could change with a change in climate (Cerling, 1984; Dorale et al., 1992; 1998). Clearly in this case, simultaneous changes in speleothem $\delta^{13}C$ and $\delta^{18}O$ values could be expected (Dorale et al., 1992; Baker et al., 1998; Holmgren et al., 1995; Bar-Matthews et al., 1997; Dorale et al., 1998; Denniston et al., 2000; Frumkin et al., 2000; Denniston et al., 2001; Xia et al., 2001; Burns et al., 2002; Vaks et al., 2003, McDermott et al., 2004; Zhang et al., 2004, 2006; Frisia et al., 2005; Vacco et al., 2005; Cruz Jr. et al., 2006; Vaks et al., 2006; Mangini et al., 2007). Thus, in some cases, such a coupling of $\delta^{13}C$ and $\delta^{18}O$ values is not related to the kinetic isotope effects, but is instead an indication of climatic change. Several examples follow below.

The work of Dorale et al. (1998) provides a highly illustrative example of this type of coupling in their study of several stalagmites from Crevice Cave, Missouri, USA. They found that multiple stalagmites yielded highly replicating $\delta^{13}C$ and $\delta^{18}O$ profiles throughout part of the last glacial period (Fig. 1). Temperatures interpreted from $\delta^{18}O$ values and $C_4$ plant biomass interpreted from $\delta^{13}C$ values were both relatively high from 59–55 ka (Fig. 1). Declining $\delta^{13}C$ and $\delta^{18}O$ values were interpreted as a cooling climate with forest replacing grassland around 55 ka. The key element in interpreting the coupled changes in $\delta^{13}C$ and $\delta^{18}O$ values as climate-driven versus kinetic-driven (as might be concluded from a Hendy Test

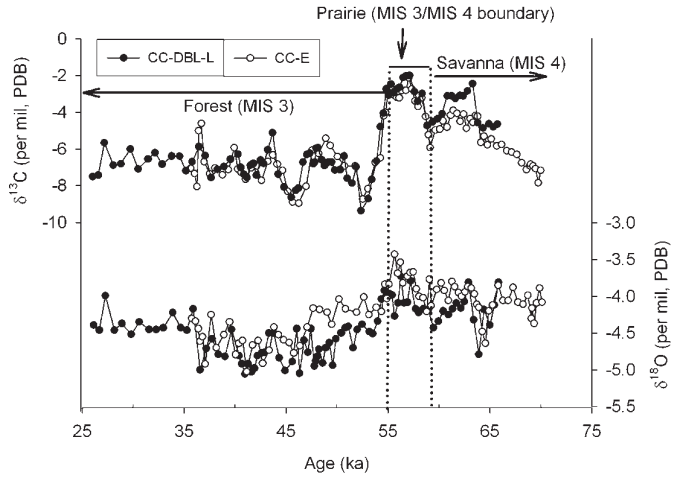


**Figure 1. The $\delta^{13}C$ and $\delta^{18}O$ values vs. time, for stalagmites CC94-DBL-L and CC94-E (after Dorale et al., 1998), showing that the simultaneous enrichment of $^{13}C$ and $^{18}O$ (or a negative result of the Hendy Test) is the indication of change in both climate and vegetation type, but not the result of nonequilibrium isotopic fractionation. That means a negative result of the Hendy Test does not necessarily indicate kinetic fractionation.**

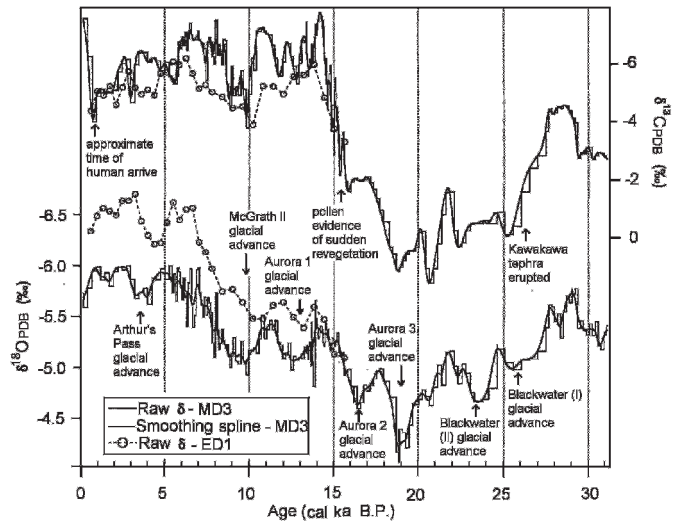


**Figure 2. The $\delta^{13}C$ and $\delta^{18}O$ values vs. time, for adjacent increments of cores MD3 and ED1 (after Hellstrom et al., 1998), showing that the simultaneous enrichment of $^{13}C$ and $^{18}O$ (or a negative result of the Hendy Test) is not related to the kinetic isotope effects in this case, but rather an indication of changes in both climate and forest productivity.**

approach) was the replication. The stalagmites differed in growth rates, diameters, and a number of other characteristics that could be considered reflective of drip rates, $CO_2$ degassing rates, and calcite precipitation rates (all thought to influence equilibrium versus non-equilibrium deposition), yet $\delta^{13}C$ and $\delta^{18}O$ values replicated. The replication implies that the differences in hydrologic characteristics between specific drip pathways cannot account for the long-term changes in speleothem $\delta^{13}C$ and $\delta^{18}O$ values. Instead, these $\delta^{13}C$ and $\delta^{18}O$ trends likely reflect a more pervasive influence, such as the climate driven changes in $\delta^{13}C$ values of the overlying soil and vegetation.

Hellstrom et al. (1998) produced a detailed record of climate and vegetation change from the $\delta^{13}C$ and $\delta^{18}O$ profiles of two New Zealand speleothems (Fig. 2). The $\delta^{13}C$ record (Fig. 2) is interpreted in terms of inorganic processes acting on carbon derived purely from $C_3$ plants (as $C_4$ plants do not exist in New Zealand), and appears to be closely related to changes in soil $CO_2$ concentration above the cave. As such, it is considered a proxy for forest productivity above the cave, a conclusion strongly supported by its similarity to pollen-based records of forest extent in the region. Notably, an extremely rapid increase in forest cover (indicated by steep decrease in $\delta^{13}C$ values (Fig. 2)) coincident with a significant increase in speleothem growth rate, was centered on 15 ka and marking the end of glacial maximum conditions (indicated by the highest speleothem $\delta^{18}O$ values and highest speleothem $\delta^{13}C$ values at ~19 ka (Fig. 2)) in the region. Close examination of Figure 2 reveals a short delay in the decline of $\delta^{13}C$ values relative to $\delta^{18}O$ values, which may capture a small lag between the time of climate change and soil microbe re-activation induced by the climate change. Similar to the example from Crevice Cave, the systematic co-variation between $\delta^{13}C$ and $\delta^{18}O$ values is again not necessarily related to kinetic isotopic fractionation, but instead, is likely forced by climate change.

In our last example, Baldini et al (2005) found that increases in calcite deposition rates, combined with decreases in $\delta^{13}C$ and $\delta^{18}O$ values in three modern stalagmites from Brown's Folly Mine, Wiltshire, England, are correlative with a well-documented re-vegetation above the mine. Increased soil $pCO_2$ resulted in greater amounts of dissolved $CaCO_3$ in the drip waters, which consequently increased annual calcite deposition rates. Lower $\delta^{13}C$ values through time may reflect the increased input of isotopically light biogenic carbon to the total dissolved inorganic carbon (DIC). In this case, $\delta^{18}O$ values decreased synchronously with $\delta^{13}C$ values, reflecting the increased importance of isotopically light winter recharge due to greater biomass-induced summer evaportranspiration.

Finally, in view of his recent modeling results Dreybrodt (2008) concluded that stalagmites collected for paleoclimatic studies should have grown with drip intervals of less than 50 seconds, which results in diameters of at least 10 cm and predicts oxygen isotopic equilibrium in the calcite. We find this result intriguing and perhaps reflective of the situation in several recently published Chinese cave $\delta^{18}O$ records, which are derived from fast-growing, large diameter, replicating stalagmites (e.g., Wang et al., 2001; Yuan et al., 2004). On the other hand, the replicating fossil stalagmites from Crevice Cave are characteristically slow-

growing (typical range: 1–10 μm $yr^{-1}$) and with diameters typically in the range of 4–7 cm. Therefore, our field evidence from Crevice Cave would not appear to support the predictions of Dreybrodt's (2008) model. We suspect instead that slow degassing and calcite precipitation rates, as reflected in the slow growth rates of these particular speleothems, likely contributed to their replicating profiles, which we interpret as equilibrium deposition.

## CONCLUSIONS

The argument for replication is simple, straightforward, and powerful. Imagine the scenario where two coeval stalagmites from a given cave contain disparate $\delta^{13}C$ and $\delta^{18}O$ profiles. Which stalagmite contains the correct climatic signal, stalagmite A, stalagmite B, or neither? Traditionally the Hendy Test would be employed to sort out this mystery, but we have shown here that the Hendy Test is prone to producing invalid comparisons and false negative results; and therefore, cannot be considered accurate in its approach. In truth and in practice, the Hendy Test is an easily executed exercise widely used in the review and editorial process to validate speleothem climate records, but, unfortunately, it is not a reliable exercise.

To help resolve the conundrum of our stalagmite A versus B scenario, should we instead adopt the advice from modeling studies such as Dreybrodt (2008) and choose the larger diameter stalagmite over the smaller diameter one? Should we choose the stalagmite with the less porous fabric, or the one less colored? Should we choose the stalagmite with flat layering or the one with arced layering? In truth, we cannot know from these types of basic observations which one, if either, reflects equilibrium deposition. Had a single stalagmite been used in the study, the entire issue of disparity would have been avoided, but we would be no closer to the truth in deciphering the status of equilibrium deposition.

We would argue that only in the case where two or more stalagmites replicate $\delta^{18}O$ and $\delta^{13}C$ values can we have any significant measure of confidence that isotopic equilibrium was maintained. Others have argued that the only real test of equilibrium deposition is to directly measure and monitor the isotopic composition of drip waters and calcites, along with the environmental conditions the calcite is precipitated under, in modern systems, and then use this information to help interpret the ancient speleothem record (e.g., Bar-Matthews et al., 1996; Mickler et al., 2004; 2006; Harmon et al., 2004). While we do not necessarily disagree with the wisdom of this approach, it may not be feasible in many cases, and also, there is no guarantee that modern conditions mimic ancient ones. In fact, with large differences in climate and the whole range of carbonate chemistry and water flow parameters linked to climate, it may even be likely that modern systems are poor analogs for ancient ones. We would argue, again, that replication is a key, as is a high level of agreement with independent indicators of paleoclimatic conditions, such as paleovegetation or ice cores.

Finally, our advocacy for replication has implications for cave conservation. Speleothem collection should always be carried out with the very highest standards of conservation. In some cases, the collection of multiple speleothems simply may not be justifiable. Instead, we should focus our efforts on those systems that have an adequate resource to allow for sampling with minimal impact. In the case of Crevice Cave, for example, literally hundreds of speleothems, naturally broken, exist in the cave. We might also consider increasing our depth of understanding of those systems that have already displayed promise of faithfully capturing paleoclimatic conditions, versus racing around the globe attempting to collect samples from pristine settings.

## ACKNOWLEDGMENTS

This work was supported by the U.S. National Science Foundation Grant ATM-0402482 to J.A.D. Support to Z.L. includes the Hundred Talents Program of Chinese Academy of Sciences, the foundation of the Chinese Academy of Sciences for Innovation (Grant No. kzcx2-yw-306), National Natural Science Foundation of China (Grant Nos. 40572017 and 40872168), and Ministry of Science and Technology of China (Grant No. 2005DIB3J067). We thank P.J. Mickler and an anonymous reviewer for comments that helped improve the manuscript.

## REFERENCES

Affek, H.P., Bar-Matthews, M., Ayalon, A., Matthews, A., and Eiler, J.M., 2008, Glacial/interglacial temperature variations in Soreq cave speleothems as recorded by 'clumped isotope' thermometry: Geochimica et Cosmochimica Acta, v. 72, p. 5351–5360.

Baker, R.G., González, L.A., Raymo, M., Bettis, E.A., Reagan, M.K., and Dorale, J.A., 1998, Comparison of multiple proxy records of Holocene environments in the Midwestern United States: Geology, v. 26, p. 1131–1134.

Baldini, J.U.L., McDermott, F., Baker, A., Baldini, L.M., Mattey, D.P., and Railsback, L.B., 2005, Biomass effects on stalagmite growth and isotope ratios: A 20th century analogue from Wiltshire, England: Earth and Planetary Science Letters, v. 240, p. 486–494.

Bar-Matthews, M., Ayalon, A., Matthews, A., Sass, E., and Halicz, L., 1996, Carbon and oxygen isotope study of the active water-carbonate system in a karstic Mediterranean cave: Implications for paleoclimate research in semiarid regions: Geochimica et Cosmochimica Acta, v. 60, p. 337–347.

Bar-Matthews, M., Ayalon, A., and Kaufman, A., 1997, Late Quaternary paleoclimate in the Eastern Mediterranean region from stable isotope analysis of speleothems at Soreq Cave, Israel: Quaternary Research, v. 47, p. 155–168.

Bar-Matthews, M., Ayalon, A., Gilmour, M., Matthews, A., and Hawkesworth, C.J., 2003, Sea–land oxygen isotopic relationships from planktonic foraminifera and speleothems in the Eastern Mediterranean region and their implication for paleorainfall during interglacial intervals: Geochimica et Cosmochimica Acta, v. 67, p. 3181–3199.

Burns, S.J., Fleitmann, D., Mudelsee, M., Neff, U., Matter, A., and Mangini, A., 2002, A 780-year annually resolved record of Indian Ocean monsoon precipitation from a speleothem from South Oman:

Journal of Geophysical Research—Atmospheres, v. 107, doi: 10.1029/2001JD001281.

Cerling, T.E., 1984, The stable isotope composition of modern soil carbonate and its relationship to climate: Earth and Planetary Science Letters, v. 71, p. 229–240.

Cerling, T.E., and J. Quade, 1993, Stable carbon and oxygen isotopes in soil carbonates, *in* Swart, P.K., Lohmann, K.C., McKenzie, J.A., and Savin, S.M., eds., Climate Change in Continental Isotopic Records, Washington, D.C., American Geophysical Union Geophysical Monograph, v. 78, p. 217–231.

Cobb, K.M., Adkins, J.F., Partin, J.W., and Clark, B., 2007, Regional-scale climate influences on temporal variations of rainwater and cave dripwater oxygen isotopes in northern Borneo: Earth and Planetary Science Letters, v. 263, p. 207–220.

Constantin, S., Bojar, A., Lauritzen, S., and Lundberg, J., 2007, Holocene and Late Pleistocene climate in the sub-Mediterranean continental environment: A speleothem record from Poleva Cave (Southern Carpathians, Romania): Palaeogeography, Palaeoclimatology, Palaeoecology, v. 243, p. 322–338.

Cruz, Jr., F.W., Burnsa, S.J., Karmann, I., Sharp, W.D., Vuillea, M., and Ferrari, J.A., 2006, A stalagmite record of changes in atmospheric circulation and soil processes in the Brazilian subtropics during the Late Pleistocene: Quaternary Science Reviews, v. 25, p. 2749–2761.

Dansgaard, W., 1964, Stable isotopes in precipitation: Tellus, v. 16, p. 436–468.

Deines, P., Langmuir, D., and Harmon, R.S., 1974, Stable carbon isotope ratios and the existence of a gas phase in the evolution of carbonate waters: Geochimica et Cosmochimica Acta, v. 38, p. 1147–1164.

Deines, P., 1986, The isotopic composition of reduced organic carbon, *in* Fritz, P., and Fontes, J.C., eds., Handbook of Environmental Geochemistry: The Terrestrial Environment, Amsterdam, Elsevier, p. 331–406.

Denniston, R.F., Gonzalez, L.A., Asmerom, Y., Reagan, M.K., and Recelli-Snyder, H., 2000, Speleothem carbon isotopic records of Holocene environments in the Ozark Highlands, USA: Quaternary International, v. 67, p. 21–27.

Denniston, R.F., Gonzalez, L.A., Asmerom, Y., Polyak, V., Reagan, M.K., and Saltzman, M.R., 2001, A high-resolution speleothem record of climatic variability at the Allerod-Younger Dryas transition in Missouri, central United States: Palaeogeography, Palaeoclimatology, Palaeoecology, v. 176, p. 147–155.

Denniston, R.F., DuPree, M., Dorale, J.A., Asmerom, Y., Polyak, V.J., and Carpenter, S.J., 2007, Episodes of late Holocene aridity recorded by stalagmites from Devil's Icebox Cave, central Missouri, USA: Quaternary Research, v. 68, p. 45–52.

Dorale, J.A., González, L.A., Reagan, M.K., Pickett, D.A., Murrell, M.T., and Baker, R.G., 1992, A high–resolution record of Holocene climate change in speleothem calcite from Cold Water Cave, northeast Iowa: Science, v. 258, p. 1626–1630.

Dorale, J.A., Edwards, R.L., Ito, E., and Gonzalez, L.A., 1998, Climate and vegetation history of the mid-continent from 75 to 25 ka: A speleothem record from Crevice Cave, Missouri, USA: Science, v. 282, p. 1871–1874.

Dorale, J.A., Edwards, R.L., Alexander, Jr., E.C., Shen, C.-C., Richards, D.A., and Cheng, H., 2004, Uranium-series disequilibrium dating of speleothems: Current techniques, limits, and applications, *in* Mylroie, J., and Sasowsky, I.D., eds., Studies of Cave Sediments: Physical and Chemical Records of Paleoclimate, New York, Kluwer Academic/Plenum Publishers, p. 177–197.

Dreybrodt, W., 2008, Evolution of the isotopic composition of carbon and oxygen in a calcite precipitating $H_2O$-$CO_2$-$CaCO_3$ solution and the related isotopic composition of calcite in stalagmites: Geochimica et Cosmochimica Acta, v. 72, p. 4712–4724.

Duplessy, J.C., Labeyrie, J., Lalou, C., and Nguyen, H.V., 1970, Continental climatic variations between 130,000 and 90,000 years B.P.: Nature, v. 226, p. 631–633.

Dykoski, C.A., Edwards, R.L., Cheng, H., Yuan, D., Cai, Y., Zhang, M., Lin, Y., Qing, J., An, Z., and Revenaugh, J., 2005, A high-resolution, absolute-dated Holocene and deglacial Asian monsoon record from Dongge Cave, China: Earth and Planetary Science Letters, v. 233, p. 71–86.

Edwards, R.L., Chen, J.H., and Wasserburg, G.J., 1987, $^{238}U$-$^{234}U$-$^{230}Th$-$^{232}Th$ systematics and the precise measurement of time over the past 500,000 y: Earth and Planetary Science Letters, v. 81, p. 175–192.

Eiler, J.M., 2007, "Clumped-isotope" geochemistry—The study of naturally-occurring, multiply-substituted isotopologues: Earth and Planetary Science Letters, v. 262, p. 309–327.

Fleitmann, D., Burns, S.J., Neff, U., Mudelsee, M., Mangini, A., and Matter, A., 2004, Paleoclimatic interpretation of high-resolution oxygen isotope profiles derived from annually laminated speleothems from Southern Oman: Quaternary Science Reviews, v. 23, p. 935–945.

Frisia, S., Borsato, A., Spòtl, C., Villa, I.M., and Cucchi, F., 2005, Climate variability in the SE Alps of Italy over the past 17000 years reconstructed from a stalagmite record: Boreas, v. 34, p. 445–455.

Frumkin, A., Ford, D.C., and Schwarcz, H.P., 2000, Paleoclimate and vegetation of the last glacial cycles in Jerusalem from a speleothem record: Global Biogeochemical Cycles, v. 14, p. 863–870.

Galimov, E.M., and Grinenko, V.A., 1965, The effect of leaching under surface conditions on the isotopic composition of carbon in secondary calcite: Geochemistry International, v. 1, p. 79–82.

Gascoyne, M., Schwarcz, H.P., and Ford, D.C., 1980, A paleotemperature record for the mid-Wisconsin in Vancouver Island: Nature, v. 285, p. 474–476.

Genty, D., Blamart, D., Ghaleb, B., Plagnes, V., Causse, C.h., Bakalowicz, M., Zouari, K., Chkir, N., Hellstrom, J., Wainer, K., and Bourge, F., 2006, Timing and dynamics of the last deglaciation from European and North African $\delta^{13}C$ stalagmite profiles—comparison with Chinese and South Hemisphere stalagmites: Quaternary Science Reviews, v. 25, p. 2118–2142.

Harmon, R.S., Thompson, P., Schwarcz, H.P., and Ford, D.C., 1978, Late Pleistocene paleoclimates of North America as inferred from stable isotope studies of speleothems: Quaternary Research, v. 9, p. 54–70.

Harmon, R.S., 1979, An isotopic study of groundwater seepage in the central Kentucky karst: Water Resources Research, v. 15, p. 476–480.

Harmon, R.S., Schwarcz, H.P., and O'Neil, J.R., 1979, D/H ratios in speleothem fluid inclusions: A guide to variations in the isotopic composition of meteoric precipitation: Earth and Planetary Science Letters, v. 42, p. 254–266.

Harmon, R.S., Schwarcz, H.P., Gascoyne, M., Hess, J.W., and Ford, D.C., 2004, Paleoclimate information from speleothems: The present as a guide to the past, *in* Mylroie, J., and Sasowsky, I.D., eds., Studies of Cave Sediments: Physical and Chemical Records of Paleoclimate, New York, Kluwer Academic/Plenum Publishers, p. 199–226.

Hellstrom, J., McCulloch, M., and Stone, J., 1998, A detailed 31,000-year record of climate and vegetation change from the isotope geochemistry of two New Zealand speleothems: Quaternary Research, v. 50, p. 167–178.

Hellstrom, J., and McCulloch, M.T., 2000, Multi-proxy constraints on the climatic significance of trace element records from a New Zealand speleothem: Earth and Planetary Science Letters, v. 179, p. 287–297.

Hellstrom, J., 2006, U-Th dating of speleotherns with high initial Th-230 using stratigraphical constraint: Quaternary Geochronology, v. 1, p. 289–295.

Hendy, C.H., and Wilson, A.T., 1968, Palaeoclimatic data from speleothems: Nature, v. 216, p. 48–51.

Hendy, C.H., 1971, The isotopic geochemistry of speleothems-I: The calculations of the effects of different modes of formation on the isotopic composition of speleothems and their applicability as paleoclimate indicators: Geochimica et Cosmochimica Acta, v. 35, p. 801–824.

Holland, H.D., Kirsipu, T.V., Huebner, J.S., and Oxburgh, U.M., 1964, On some aspects of the chemical evolution of cave waters: Journal of Geology, v. 72, p. 36–67.

Holmgren, K., Karlen, W., and Shaw, P.A., 1995, Palaeoclimatic significance of the stable isotopic composition and petrology of a Late Pleistocene stalagmite from Botswana: Quaternary Research, v. 43, p. 320–328.

Hu, C., Henderson, G.M., Huang, J., Xie, S., Sun, Y., and Johnson, K.R., 2008, Quantification of Holocene Asian monsoon rainfall from spatially separated cave records: Earth and Planetary Science Letters, v. 266, p. 221–232.

Johnsen, S.J., Dansgaard, W., and White, J.W.C., 1989, The origin of Arctic precipitation under present and glacial conditions: Tellus, v. 41, p. 452–468.

Johnson, K.R., Ingram, B.L., Sharp, W.D., and Zhang, P., 2006a, East Asian summer monsoon variability during Marine Isotope Stage 5

based on speleothem $\delta^{18}O$ records from Wanxiang Cave, central China: Palaeogeography, Palaeoclimatology, Palaeoecology, v. 236, p. 5–19.

Johnson, K.R., Hu, C., Belshaw, N.S., and Henderson, G.M., 2006b, Seasonal trace-element and stable-isotope variations in a Chinese speleothem: The potential for high-resolution: Earth and Planetary Science Letters, v. 244, p. 394–407.

Jouzel, J., Alley, R.B., Cuffey, K.M., Dansgaard, W., Grootes, P., Hoffman, G., Johnsen, S.J., Koster, R.D., Peel, D., Shuman, C.A., Stievenard, M., Stuiver, M., and White, J., 1997, Validity of the temperature reconstruction from water isotopes in ice cores: Journal of Geophysical Research, v. 102, p. 26,471–26,487.

Lauritzen, S.-E., and Lundberg, J., 1999a, Speleothems and climate: A special issue of The Holocene: The Holocene, v. 9, p. 643–647.

Lauritzen, S.-E., and Lundberg, J., 1999b, Calibration of the speleothem delta function: An absolute temperature record for the Holocene in northern Norway: The Holocene, v. 9, p. 659–669.

Mangini, A., Blumbacha, P., Verdesa, P., Spotl, C., Scholz, D., Machel, H., and Mahon, S., 2007, Combined records from a stalagmite from Barbados and from lake sediments in Haiti reveal variable seasonality in the Caribbean between 6.7 and 3 ka BP.: Quaternary Science Reviews, v. 26, p. 1332–1343.

Matthews, A., Ayalon, A., and Bar-Matthews, M., 2000, *D*/*H* ratios of fluid inclusions of Soreq cave Israel speleothems as a guide to the Eastern Mediterranean Meteoric Line relationships in the last 120 ky: Chemical Geology, v. 166, p. 183–191.

McDermott, F., 2004, Paleoclimate reconstruction from stable isotope variations in speleothems: a review: Quaternary Science Reviews, v. 23, p. 901–918.

Mickler, P.J., Banner, J.L., Stern, L., Asmerom, Y., Edwards, R.L., and Ito, E., 2004, Stable isotope variations in modern tropical speleothems: Evaluating equilibrium vs. kinetic isotope effects: Geochimica et Cosmochimica Acta, v. 68, p. 4381–4393.

Mickler, P.J., Stern, L.A., and Banner, J.L., 2006, Large kinetic isotope effects in modern speleothems: Geological Society of America Bulletin, v. 118, p. 65–81.

Mühlinghaus, C., Scholz, D., and Mangini, A., 2007, Modelling stalagmite growth and $\delta^{13}C$ as a function of drip interval and temperature: Geochimica et Cosmochimica Acta, v. 71, p. 2780–2790.

O'Neil, J.R., Clayton, R.N., and Mayeda, T.K., 1969, Oxygen isotope fractionation in divalent metal carbonates: Journal of Chemical Physics, v. 51, p. 5547–5559.

Perrin, J., Jeannin, P.Y., and Zwahlen, F., 2003, Implications of the spatial variability of infiltration-water chemistry for the investigation of a karst aquifer: a field study at Milandre test site, Swiss Jura: Hydrogeology Journal, v. 11, p. 673–686.

Romanov, D., Kaufmann, G., and Dreybrodt, W., 2008, $\delta^{13}C$ profiles along growth layers of stalagmites: comparing theoretical and experimental results: Geochimica et Cosmochimica Acta, v. 72, p. 438–448.

Rowe, P.J., Dennis, P.F., Atkinson, T.C., Lauritzen, S.-E., and Lundberg, J., 1998, A high resolution deuterium record from fluid inclusions in a late Holocene speleothem from S.W. Britain, *in* Proceedings, PAGES Open Science Meeting, London, University of London, 112 p.

Schwarcz, H.P., Harmon, R.S., Thompson, P., and Ford, D.C., 1976, Stable isotope studies of fluid inclusions in speleothems and their paleoclimatic significance: Geochimica et Cosmochimica Acta, v. 40, p. 657–665.

Shen, C., Edwards, R.L., Cheng, H., Dorale, J.A., Thomas, R.B., Moran, S.B., Weinstein, S.E., and Edmonds, H.N., 2002, Uranium and thorium isotopic and concentration measurements by magnetic sector inductively coupled plasma mass spectrometry: Chemical Geology, v. 185, p. 165–178.

Spötl, C., and Mangini, A., 2002, Stalagmite from the Austrian Alps reveals Dansgaard-Oeschger events during isotope stage 3: Implications for the absolute chronology of Greenland ice cores: Earth and Planetary Science Letters, v. 203, p. 507–518.

Spötl, C., Mangini, A., and Richards, D.A., 2006, Chronology and paleoenvironment of Marine Isotope Stage 3 from two high-elevation speleothems, Austrian Alps: Quaternary Science Reviews, v. 25, p. 1127–1136.

Talma, A.S., and Vogel, J.C., 1992, Late Quaternary paleotemperatures derived from a speleothem from Cango Caves, Cape Province, South Africa: Quaternary Research, v. 37, p. 203–213.

Treble, P.C., Chappell, J., Gagan, M.K., McKeegan, K.D., and Harrison, T.M., 2005, In situ measurement of seasonal $\delta^{18}O$ variations and analysis of isotopic trends in a modern speleothem from southwest Australia: Earth and Planetary Science Letters, v. 233, p. 17–32.

Vacco, D.A., Clark, P.U., Mix, A.C., Cheng, H., and Edwards, R.L., 2005, A speleothem record of Younger Dryas cooling, Klamath Mountains, Oregon, USA: Quaternary Research, v. 64, p. 249–256.

Vaks, A., Bar-Matthews, M., Ayalon, A., Schilman, B., Gilmour, M., Hawkesworth, C.J., Frumkin, A., Kaufman, A., and Matthews, A., 2003, Paleoclimate reconstruction based on the timing of speleothem growth and oxygen and carbon isotope composition in a cave located in the rain shadow in Israel: Quaternary Research, v. 59, p. 182–193.

Vaks, A., Bar-Matthews, M., Ayalon, A., Matthews, A., Frumkin, Dayan, A.U., Halicz, L., Almogi-Labin, A., and Schilman, B., 2006, Paleoclimate and location of the border between Mediterranean climate region and the Saharo—Arabian Desert as revealed by speleothems from the northern Negev Desert, Israel: Earth and Planetary Science Letters, v. 249, p. 384–399.

Vonhof, H.B., van Breukelen, M.R., Postma, O., Rowe, P.J., Atkinson, T.C., and Kroon, D., 2006, A continuous-flow crushing device for on-line $\delta^{2}H$ analysis of fluid inclusion water in speleothems: Rapid Communications Mass Spectrometry, v. 20, p. 2553–2558.

Wang, Y., Cheng, H., Edwards, R.L., An, Z., Wu, J., Shen, C., and Dorale, J.A., 2001, A high-resolution absolute-dated late Pleistocene monsoon record from Hulu Cave, China: Science, v. 294, p. 2345–2348.

Wang, Y., Cheng, H., Edwards, R.L., Kong, X., Shao, X., Chen, S., Wu, J., Jiang, X., Wang, X., and An, Z., 2008, Millennial- and orbital-scale changes in the East Asian monsoon over the past 224,000 years: Nature, v. 451, p. 1090–1093.

Wigley, T.M.L., and Brown, M.C., 1976, The physics of caves, *in* Ford, T.D., and Cullingford, C.H.P., eds., The Science of Speleology, London, Academic Press, p. 329–350.

Williams, P.W., Marshall, A., Ford, D.C., and Jenkinson, A.V., 1999, Palaeoclimatic interpretation of stable isotope data from Holocene speleothems of the Waitomo District, North Island, New Zealand: The Holocene, v. 9, p. 649–657.

Williams, P.W., King, D.N.T., Zhao, J.-X., and Collerson, K.D., 2005, Late Pleistocene to Holocene composite speleothem $^{18}O$ and $^{13}C$ chronologies from South Island, New Zealand—did a global Younger Dryas really exist?: Earth and Planetary Science Letters, v. 230, p. 301–317.

Winograd, I.J., Coplen, T.B., Landwehr, J.M., Riggs, A.C., Ludwig, K.R., Szabo, B.J., Kolesar, P.T., and Revesz, K.M., 1992, Continuous 500,000-Year Climate Record from Vein Calcite in Devils Hole, Nevada: Science, v. 258, p. 255–260.

Xia, Q., Zhao, J., and Collerson, K.D., 2001, Early-Mid Holocene climatic variations in Tasmania, Australia: multi-proxy records in a stalagmite from Lynds Cave: Earth and Planetary Science Letters, v. 194, p. 177–187.

Yonge, C.J., 1982, Stable isotope studies of water extracted from speleothems, [Ph.D. thesis], Hamilton, Canada, McMaster University, 298 p.

Yonge, C.J., Ford, D.C., Gray, J., and Schwarcz, H.P., 1985, Stable isotope studies of cave seepage water: Chemical Geology, v. 58, p. 97–105.

Yuan, D., Cheng, H., Edwards, R.L., Dykoski, C.A., Kelly, M.J., Zhang, M., Qing, J., Lin, Y., Wang, Y., Wu, J., Dorale, J.A., An, Z., and Cai, Y., 2004, Timing, duration, and transitions of the last interglacial Asian Monsoon: Science, v. 304, p. 575–578.

Zhang, M., Yuan, D., Lin, Y., Cheng, H., Qin, J., and Zhang, H., 2004, The record of paleoclimatic change from stalagmites and the determination of termination II in the south of Guizhou Province, China: Science in China (Ser. D), v. 47, p. 1–12.

Zhang, M., Cheng, H., Yuan, D., Zhu, X., Lin, Y., Qin, J., and Edwards, R.L., 2006, Carbon and oxygen isotope records and paleoclimate reconstruction (140–250 ka B.P.) from a stalagmite of Shuinan Cave, Guilin, China: Environmental Geology, v. 49, p. 752–764.

Zhang, R., Schwarcz, H.P., Ford, D.C., Schroeder, F.S., and Beddows, P.A., 2008, An absolute paleotemperature record from 10 to 6 Ka inferred from fluid inclusion D/H ratios of a stalagmite from Vancouver Island, British Columbia, Canada: Geochimica et Cosmochimica Acta, v. 72, p. 1014–1026.

Zhou, H., Zhao, J., Feng, Y., Gagan, M.K., Zhou, G., and Yan, J., 2008, Distinct climate change synchronous with Heinrich event one, recorded by stable oxygen and carbon isotopic compositions in stalagmites from China: Quaternary Research, v. 69, p. 306–315.

R. Henry L. Disney – Scuttle flies (Diptera: Phoridae) from caves in Meghalaya, India. *Journal of Cave and Karst Studies,* v. 71, no. 1, p. 81–85.

# SCUTTLE FLIES (DIPTERA: PHORIDAE) FROM CAVES IN MEGHALAYA, INDIA

R. Henry L. Disney
*Department of Zoology, University of Cambridge, Downing Street, Cambridge CB2 3EJ, U. K., rhld2@hermes.cam.ac.uk*

**Abstract:** Four scuttle fly species (family Phoridae) were collected from caves in Meghalaya, India, of which one was from deep inside the caves, while the others were restricted to the vicinity of the cave entrances. Illustrated notes are provided to aid future recognition of these species.

## Introduction

Since the early 1990s the Meghalayan Adventurers Association (based in Shillong), in partnership with European speleologists, has conducted a series of expeditions with the objective of mapping and documenting caves in Meghalaya, India. To date, over 280 km of cave passages have been surveyed, but much more remains to be discovered. The quantity and length of caves in Meghalaya exceed that of any other known karst region of India. Due to a major expansion of the limestone-extraction industry in recent years in the Jaintia Hills, there is a strong case for documenting the biospeleology of the region before significant loss or damage occurs. During the course of these investigations, a number of scuttle flies (Diptera: Phoridae) were collected. Dr. Dan Harries (School of Life Sciences, Heriot-Watt University, Edinburgh) passed these samples on to me for identification.

## Methods

The specimens were preserved in alcohol and subsequently mounted on slides in Berlese Fluid (Disney, 2001). Voucher specimens have been deposited in the Cambridge University Museum of Zoology.

## The Species

### *Conicera kempi* Brunetti 1924

This species was described from the female only, but its male has since been described (Disney, 1982), its critical features as shown in Figures 1 and 2. A key to the Oriental species of *Conicera* Meigen (Disney, 1990b) only allows identification of males and likewise using the key to the species recorded from China (Liu, 2001).

Females can normally only be named when associated with their males. Three species whose females have been described (Disney, 1990b; Bänziger and Disney, 2006) differ from *C. kempi* in one or more of the following features. The labrum is devoid of longitudinal ridges in the median band or more. The postpedicel is clearly shorter, and/or the abdominal tergite 6 (T6) is of a different shape. Other species, whose females are unknown, can be excluded because there is a hair at the base of vein 3 in their males. The females reported below have been compared with a female from Nepal that had previously been compared with the type material of *C. kempi* (Disney, 1982). In this species, while the female postpedicel is not as long as in the male (Fig. 3), it is unusually long for a female (Fig. 4). The labrum is as shown in Figure 5 and T5 and T6 are as shown in Figure 6.

#### *Material*

Twenty females, 6 larvae, Krem Shynrong Labbit (25°21′1.2″N, 92°30′105″E) collected >500 m into the cave and 200 m below surface on February 17, 2001 (KSL4 and KSL4.2 (larvae), CUMZ, 38–55). Five females, Krem Kotsati Lawan (25°10′46″N, 92°22′29″E) collected about 85 m from the cave entrance on February 18, 2002 (KUL2, CUMZ, 38–56). Two females, Liat Prah (25°22′31.5″N, 92°32′18.6″E) collected about 50 m into the cave, February 26, 2002 (LP5.4, CUMZ, 38–55). Five females were collected at the same locality, but about 10 m from the cave entrance, on February 26, 2002 (LP5.2, CUMZ, 38–56). Twenty females were collected at the same locality, but about 1000 m from the cave entrance, on February 26, 2002 (LP3.1, CUMZ, 38–56).

#### *Natural History*

Brunetti (1924) recorded six females collected 120–150 m from the entrance of Siju Cave. The new material confirms that this species is a cave dweller. Furthermore, it was sometimes common near bat roosts. Mature eggs are about 0.84-mm-long and 0.27-mm-wide with a surface microsculpture of numerous short ridges. Gravid females with about 50 eggs. Most specimens had an infestation of worms in the abdomen. These are blunt at each end, colorless, featureless (at 240× magnification) and are more than 2-mm-long but only about 0.001-mm-wide. They look like miniature hairworms, rather than Nematoda.

### *Diplonevra* Species IC

Species recognition is primarily based on the male sex in the genus *Diplonevra* Lioy. However, a key covering the Oriental species (Disney, 1990a) included some poorly known species only known in the female sex. The species below runs to couplets 11 and 12 with the former based on species only known in the female sex, and the latter based only on the male sex. In couplet 11, the female of *D.*

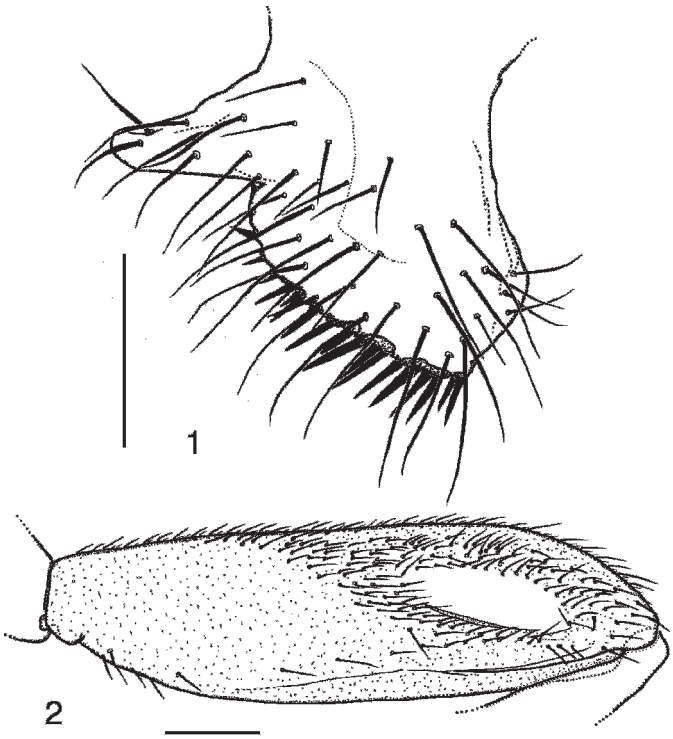


**Figures 1–2. *Conicera kempi* male. 1, right clasper of hypopygium; 2, posterior face of mid femur. Scale bars = 0.1 mm.**

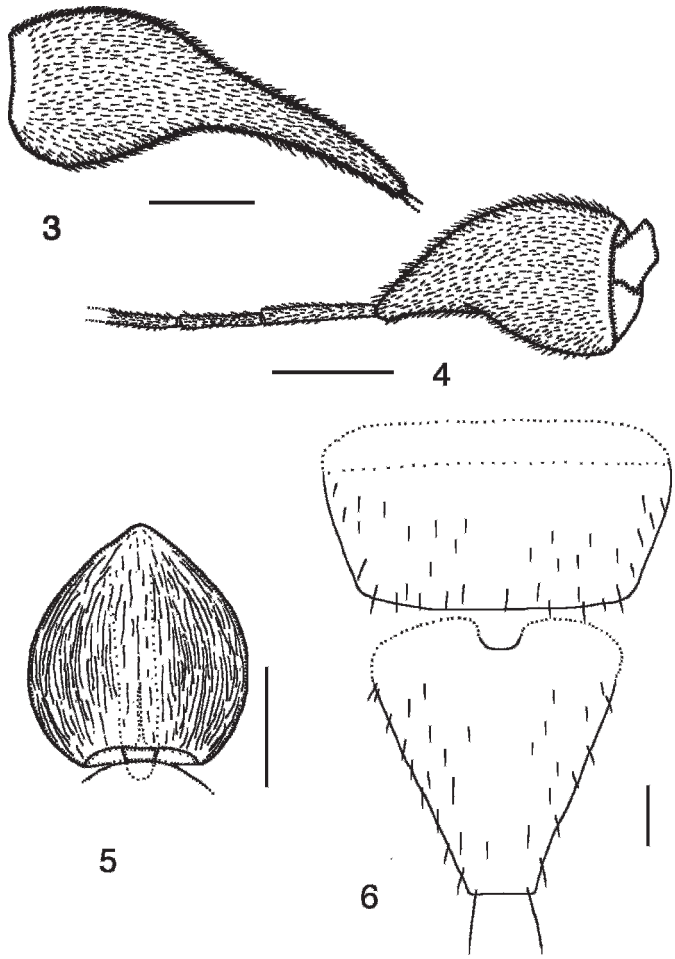


**Figures 3–6. *Conicera kempi*. 3, male, right postpedicel; 4, female, left postpedicel; 5, female, labrum; 6, female abdominal tergites 5 and 6. Scale bars = 0.1 mm.**

*evanescens* (Brues) differs by having a more yellowish wing membrane and a broader abdominal tergite 3. *D. fasciiventris* (Brues), has much darker hind femora and tibiae, and lacks a hair at the base of vein 3. In couplet 12, the female of *D. assmuthi* (Schmitz) was described under its synonym *D. ater* (Brunetti). It is immediately distinguished by having its distiproboscis clearly longer than the basiproboscis (see figure in Schmitz, 1931). *D. varians* Beyer (1958) was described from a series of males from Burma. The species below could be the hitherto unknown female of this species. Until the two sexes are associated, this cannot be resolved. The species characterized below could not be run down in Liu's (2001) key to Chinese species.

*Female*

Frons orange brown to more yellowish in the lower part with about 40 small hairs (which are absent from median band) and minute microsetae. The supra-antennal bristles almost as long as antials, which are closer to anterolaterals than to midline, with the ALs being slightly higher on the frons. The bristles of the middle row almost equally spaced but mediolaterals a little lower on frons than pre-ocellars. A short, but robust, bristle on cheek and a much longer one on jowl. The yellowish brown postpedicels are small (both the length and greatest breadth being about 0.18 mm). The straw yellow palps appear dusky in distal third or more because of the dense dark pubescence. They measure about 0.41-mm-long, the second segment being about 0.36-mm-long (and its greatest breadth being about 0.11 mm), with five bristles at tip and up to 30 hairs below. The basiproboscis is yellowish brown, but with narrow dark brown bands at sides of the basal half. The length is about 0.59 mm and the maximum breadth is about 0.26 mm. The distiproboscis colored as postpedicels and about 0.50-mm-long and 0.32 mm at its greatest width. The combined width of the pale labella is only slightly greater. Thorax orange brown, but darker on top. Each side of scutum with a humeral, a notopleural, a prealar, an intra-alar, a postalar, and a pre-scutellar dorsocentral bristle. Scutellum with four bristles. Abdomen dark greyish brown apart from the tergites and the yellow tip and cerci. The tergites are mainly orange brown with minute hairs, but T1 is more straw yellow in the middle. T2, as shown in Figure 7, with the missing anteromedian band grey and the anterolateral wings straw yellow until they encounter a brown patch on the pleural region. T3 (Fig. 7) and T4 greatly reduced and T5 and T6 absent. Legs with coxae, mid and hind femora and hind tibia largely orange brown; the rest straw yellow. Front tibia with a neardorsal bristle near middle and 4–7 short spines in distal third to quarter. Front

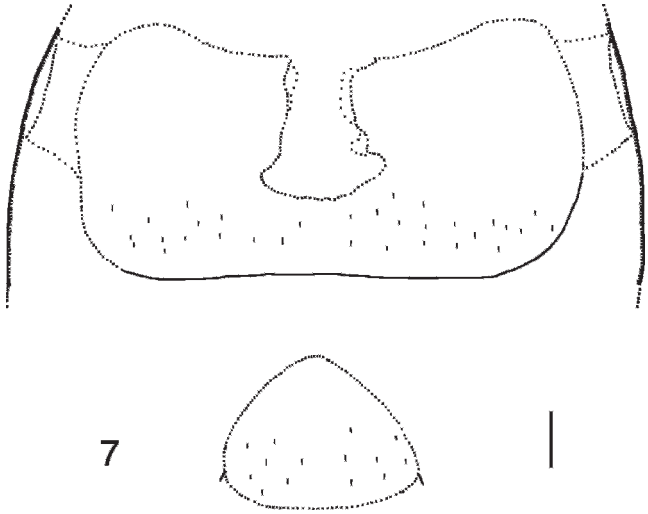


**Figure 7. *Diplonevra* species IC female, abdominal tergites 2 and 3. Scale bar = 0.1 mm.**

tarsus with posterodorsal hair palisades on segments 1–3 and 5 longer than 4. Mid tibia with the normal pair of bristles at end of basal quarter, and apart from the dorsal hair palisade, there is an anterodorsal one that ends at the start of the distal third, which has a series of anterodorsal transverse combs. Hind femur with hairs below basal half not differentiated from those of anterior face. Hind tibia with two anterodorsal bristles, one just before the end of the basal third and the other a little before the end of the middle third. Wing about 1.8 mm long. The costal index is about 0.6. The costal ratios about 6:3.5:1. The costal cilia (of section 3) are 0.07–0.08-mm-long. The thick veins yellowish brown. Veins 4–6 fine and grey. Vein 7 very pale. Vein 4 originates well before fork of vein 3 and is evenly concave towards the front in the basal four fifths and then runs straight to the margin in the last fifth. Sc reduced and only evident at extreme base. A fine hair at base of vein 3. With five bristles on axillary ridge. Membrane almost colorless. Haltere knob brown.

### *Material*

Five females, Krem Kotsati Lawan (25°10′46″N, 92°22′29″E) were collected at the cave entrance. Collection was on February 18, 2002 (KUL1, CUMZ, 38–56).

### *Natural History*

This species was only procured at a cave's entrance and was probably only sheltering there. It is probably not a specialist cave dweller. Mature eggs with a smooth surface and about 0.87-mm-long and 0.34-mm-wide. Gravid females with about 22–24 eggs.

### *Megaselia malaisei* Beyer 1958

This species was described from a series of females from Burma and has subsequently been reported from Thailand in a flower of *Aristochia baenzigeri* Hansen and Phuphathanaphong (Bänziger and Disney, 2006). The male

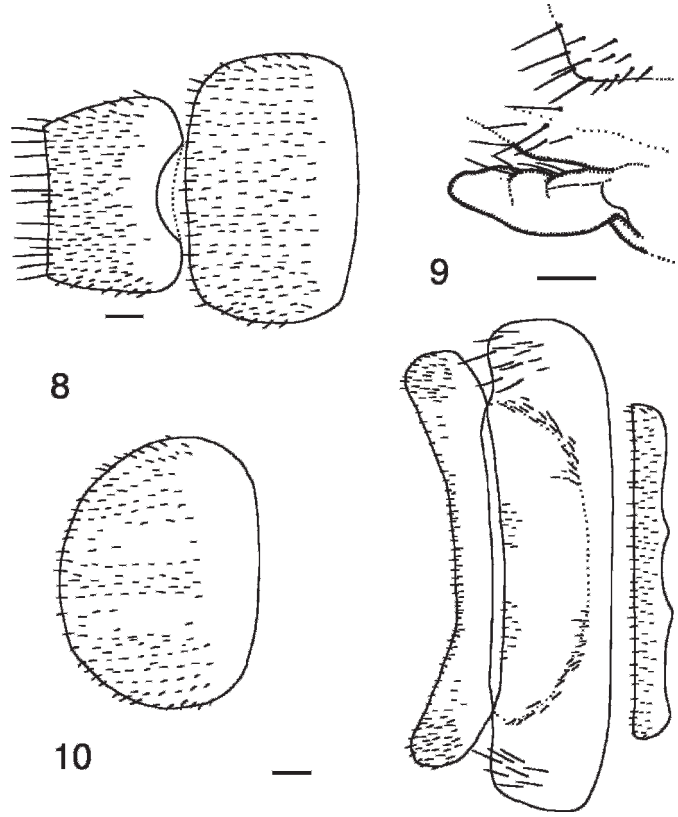


**Figures 8–10. *Megaselia malaisei* female, details of abdomen; 8, tergites 5 and 6; 9, right retractile lobe of segment 6; 10, tergites 1–4. Scale bars = 0.1 mm.**

remains unknown. Beyer's description was not illustrated, so the distinctive abdominal tergites 1–6 are illustrated here (Figs. 8 and 10) and also the pair of retractile, finger-like processes on the sides of segment 6 (Fig. 9), which Beyer failed to observe (as they are likely to have been withdrawn in a pinned specimen).

### *Material*

One female, Krem Pyrda (25°20′29″N, 92°29′23″E) was collected about 50 m into the cave on February 10, 2001 (KP3, CUMZ, 38–55). One female, Liat Prah (25°22′31.5″N, 92°32′18.6″E) was collected about 50 m into the cave on February 26, 2002 (LP5.4, CUMZ, 38–55).

### *Natural History*

This species was only procured close to the entrance of the caves and was probably only sheltering there. It is probably not a specialist cave dweller. One female retained eight mature eggs, but this was probably an incomplete batch following the deposition of some eggs. These eggs have a smooth surface and are about 0.58-mm-long and 0.22-mm-wide.

### *Megaselia* species IC

Apart from species described from females only in the past (such as the distinctive species above), the recognition

of species in the giant genus *Megaselia* Rondani is now based on the males for the first time. The species characterized below cannot be named until associated with its male. In the key covering the relevant Group VII of the Oriental species (Borgmeier, 1967) it readily runs to couplet 65, which is based on the relative darkness of the antennal postpedicels. Taking the first option at couplet 66 the distinction is based on the male sex only. However, the female of its first option, *M. palpella* Beyer, is smaller (wing length <2 mm), and it has a well-elongated abdominal tergite 6. Taking the second lead of couplet 66 one then proceeds to couplet 70, to *M. apposita* Brues. The latter's female is immediately distinguished by its yellow, as opposed to brownish grey, abdominal venter. If one takes the second option of couplet 65, one readily proceeds to couplet 89, where the distinction is based on the degree of darkening of the thorax. The first option leads to couplet 94 to *M. tetricifrons* Beyer, which has the costal section one less than the combined lengths of 2+3 (as opposed to more) and half as many differentiated posterodorsal hairs on the hind tibia. Taking the second lead of couplet 89, one runs to couplet 110, where neither lead applies but the first option, *M. rutilipes* Beyer (only known in the male sex) is closest, but it has a darker frons and darker legs.

*Female*

Frons brown, but not dark, and clearly broader than long, with 20–24 hairs and dense, but very fine, microsetae. The supra-antennal bristles unequal in length, the lower pair being a little shorter and less robust. The antials slightly lower on frons than anterolaterals, which are about level with the upper SAs, and closer to the ALs than to the upper SAs. Pre-ocellars about as far apart as either is from a mediolateral bristle, which is very slightly higher on frons. Cheek with four bristles and jowl with two longer bristles. The subglobose postpedicels light brown, about 0.12-mm-wide, and with about three dozen SPS vesicles, which are a little smaller than sockets of lower SA bristles. Palps are about 0.21-mm-long and 0.04-mm-wide, pale straw yellow, and with five bristles and 7–10 hairs (of which 1–2 are a little stronger than the rest). Labrum a little darker than palps and about 0.45-mm-wide. Labella greyish white and at most with only a dozen short spinules below. Thorax brown. Two notopleural bristles and no cleft in front of these. Mesopleuron bare. Scutellum with an anterior pair of hairs (subequal to those in middle of scutum) and a posterior pair of bristles. Abdominal tergites brown. T4–T7 as shown in Figure 11. Venter brownish grey, and with small hairs below segments 3–6. Sternite 7 as long as T7 but a narrow isosceles triangle with two longer hairs at its rear margin and half a dozen smaller ones further forward. Posterolateral lobes at rear of sternum eight short, but broad and with three long hairs near rear margin. Cerci whitish grey and about twice as long as broad. With four rectal papillae. Furca not evident. Dufour's crop mechanism about 0.40-mm-long, but the posterior part is 0.15 mm and comprises a pair of pale

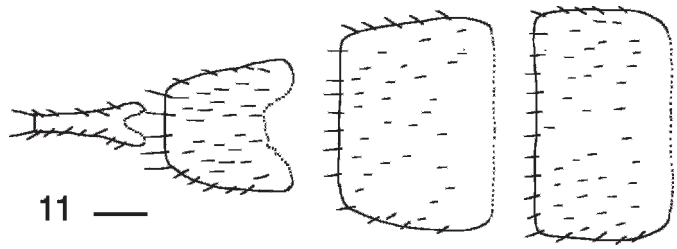


**Figure 11. *Megaselia* species IC female, abdominal tergites 4–7. Scale bar = 0.1 mm.**

divergent lobes. The greatest breadth of anterior part is about 0.25 mm. Legs straw yellow apart from brown patch on mid coxa and a light brown tip to hind femur. Fore tarsus with posterodorsal hair palisade on segments 1–5 and 5 longer than 4. Dorsal hair palisade of mid tibia extends almost two thirds of its length. Hairs below basal half of hind femur clearly longer than those of anteroventral row of outer half. Hind tibia with 17–20 differentiated posterodorsal hairs and spinules of apical combs simple. Wings 2.0–2.4-mm-long. Costal index 0.54–0.56. Costal ratios 3.4–3.7:2.1–2.5:1. Costal cilia (of section 3) 0.07-mm-long. No hair at base of vein 3. With 4–6 axillary bristles, all of which are longer than costal cilia. Sc strong and its tip fused to R1. Thick veins yellowish grey, thin veins grey, but 7 paler. Vein 4 originates beyond fork of vein 3 and is distinctly recurved at its base. Membrane lightly tinged grey. Haltere brown.

*Material*

One female, Krem Pyrda (25°20′29″N, 92°29′23″E) was collected about 50 m into the cave, on February 10, 2001 (KP3, CUMZ, 38–55). Two females, Krem Kotsati Lawan (25°10′46″N, 92°22′29″E) were collected at the cave entrance on February 18, 2002 (KUL1, CUMZ, 38–56). Six females, Liat Prah (25°22′31.5″N, 92°32′18.6″E) were collected about 10 m into the cave on February 26, 2002 (LP5.4, CUMZ, 38–54); 16 females were collected at the same locality but about 50 m into the cave on February 26, 2002 (LP5.2, CUMZ, 38–56).

*Natural History*

This species was only procured close to the entrance of caves and was probably only sheltering there. It is probably not a specialist cave dweller. Mature eggs with a smooth surface and about 0.61-mm-long and 0.24-mm-wide. Twenty to twenty-four eggs are matured at a time.

## Acknowledgements

Thanks are due to Nigel Wyatt (Natural History Museum, London) for the loan of a female of *Conicera kempi.* My studies of Phoridae are currently supported by a grant from the Balfour-Browne Trust Fund (University of Cambridge).

## Postscript

Since the acceptance of this manuscript, a general review of these caves has been published (Harries et al., 2008).

## References


Beyer, E., 1958, Die ersten Phoriden von Burma (Dipt. Phor.): Commentationes Biologicae, Helsingfors, v. 18, p. 3–72.

Bänziger, H., and Disney, R.H.L., 2006, Scuttle flies (Diptera: Phoridae) imprisoned by *Aristolochia baenzigeri* (Aristolochiaceae) in Thailand: Mitteilungen der Schweizerischen Entomologischen Gesellschaft, v. 79, p. 29–61.

Borgmeier, T., 1967, Studies on Indo-Australian phorid flies, based mainly on material of the Museum of Comparative Zoology and the United States National Museum, Part II: Studia Entomologica, Petropolis, v. 10, p. 81–276.

Brunetti, E., 1924, Diptera of the Siju Cave, Garo Hills, Assam. 1. Tipulidae, Tabanidae, Anthomyidae, Acalyptratae, Muscidae and Phoridae: Records of the Indian Museum, Calcutta, v. 26, p. 99–106.

Disney, R.H.L., 1982, The undescribed male of *Conicera kempi* Brunetti (Dipt., Phoridae): Entomologist's Monthly Magazine, v. 118, p. 29–30.

Disney, R.H.L., 1990a, A key to *Diplonevra* males of the Australasian and Oriental Regions, including two new species (Diptera, Phoridae): Entomologica Fennica, v. 1, p. 33–39.

Disney, R.H.L., 1990b, A revised key to Australasian and Oriental *Conicera* (Diptera: Phoridae), with three new species: Entomologica Scandinavica, v. 21, p. 339–344.

Disney, R.H.L., 2001, The preservation of small Diptera: Entomologist's Monthly Magazine, v. 137, p. 155–159.

Harries, D.B., Ware, F.J., Fischer, C.W., Biswas, J., and Kharpran-Daly, B.D., 2008, A review of the biospeleology of Megahalaya, India: Journal of Cave and Karst Studies, v. 70, p. 163–176.

Liu, G., 2001, A Taxonomic Study of Chinese Phorid Flies Diptera: Phoridae (part 1), China, Neupress.

Schmitz, H., 1931, Ueber die Gattung *Phorynchus* Brunetti: Natuurhistorisch Maandblad, v. 20, p. 43–44.

J.J. Fornós, J. Ginés, and F. Gràcia – Present-day sedimentary facies in the coastal karst caves of Mallorca island (western Mediterranean). *Journal of Cave and Karst Studies,* v. 71, no. 1, p. 86–99.

# PRESENT-DAY SEDIMENTARY FACIES IN THE COASTAL KARST CAVES OF MALLORCA ISLAND (WESTERN MEDITERRANEAN)

Joan J. Fornós[1], Joaquín Ginés[1], and Francesc Gràcia[1,2]

**Abstract:** In spite of the increasing number of papers on cave sediments published during the last few decades, no one has focused from a sedimentological point of view on the processes that take place specifically within the coastal karst areas of carbonate islands. The objective of the present investigations is to deal with the sedimentary processes that take place inside two littoral caves of Mallorca (western Mediterranean), characterizing the different facies existing in the particular geological, geochemical, and hydrological setting that represents this very specific cave sedimentary environment. The recent exploration of extensive underwater galleries and chambers into some outstanding coastal caves of the island, has permitted the recognition of important accumulations of present-day sedimentary infillings in their drowned passages. Both the Pirata-Pont-Piqueta cave system and the Cova de sa Gleda have floors covered by muddy and/or sandy sediments which, in a wide sense, fit into two well-differentiated categories. On one hand we have allochthonous reddish mud sediments (mainly siliciclastic) and on the other hand autochthonous yellowish carbonate mud or sands. The mixing of both materials is also frequent as well as the accumulation of large blocks and debris due to the breakdown of roof and cave walls. A series of 21 manual cores was obtained by scuba-divers in both caves, in order to collect the full thickness of sedimentary fill. Soil samples at the entrance of the two caves, as well as rock samples of the walls of both sites, were also obtained for a later comparison. Several sedimentary facies can be distinguished, which include coarse-grained deposits (entrance facies and breakdown blocks), fine-grained siliceous sediments (silts and muddy deposits with very variable organic matter content), carbonate deposits composed of calcite raft accumulations and/or weathering-released limestone grains, and mixed facies including diverse proportions of the other sediment types. There are also some relict deposits composed of siliceous red silts, which are affected by polygonal desiccation cracks. In all the cases, the siliciclastic elements (quartz and feldspars, mainly) are related to rain events supplying dust of Saharan origin. The deposits and facies described herein correspond to different sedimentary environments that can be individualized inside the caves (collapse entrances, breakdown chambers, fully drowned passages and chambers, pools with free water surface…), and reflect very specific hydrological, geochemical, and mechanical processes related to the coastal nature of the studied karst caves.

## Introduction

During the last decade, there has been a great increase in speleological and karst research on Mallorca island, especially in those peripheral areas where the coastal karst attains noteworthy development. The recent explorations of extensive underwater galleries and chambers into some outstanding littoral caves of the island are particularly important (Gràcia et al., 2007a), allowing for the detailed observation and survey of some tens of kilometers of drowned passages. These investigations have permitted the recognition of the morphological characteristics of the underwater part of these caves, which exhibit an outstanding variety of present-day sedimentary infillings in most of the explored chambers and passages (Gràcia et al., 2006, 2007b).

Cave sediments have been recognized and described since scientific interest in caves began. Nevertheless, we can consider, in general, that in-depth investigations on the subject have not been performed until recently by karst researchers. When scientists realized that sediments contain both hydrogeological and paleoclimatical records, together with the development of absolute dating techniques, the study of cave sediments become one of the most interesting topics in karst literature (White, 2007). In spite of the increasing number of references on this matter, published during the last few decades, only a few are specific synthesis works dealing with the topic (Ford, 2001; Sasowsky and

[1] Dept. Ciències de la Terra. Universitat de les Illes Balears, Crta. Valldemossa, km 7.5, 07122 Palma (BalearicIslands), joan.fornos@uib.es; jginesgracia@yahoo.es
[2] Grup Nord Mallorca, Federació Balear d'Espeleologia, xescgracia@yahoo.es

Mylroie, 2004). In the meantime, there have also appeared some general texts that include reviews of current understanding of its hydrological and geomorphological significance (Ford and Williams, 2007; Gillieson, 1996; Palmer, 2007). However, among the great number of recent papers devoted to cave sediments, no one has focused from a sedimentological point of view on the processes that take place specifically in the coastal karst areas of carbonate islands.

The flank margin model of littoral speleogenesis, developed in the Bahamas from the 1980s onwards (Mylroie and Carew, 1990), recognized the importance of dissolution processes occurring in the mixing zone between fresh and sea waters, whose position is complicated by Quaternary sea-level oscillations due to glacioeustatic phenomena. This model has evolved during the 1990s until now (Mylroie and Mylroie, 2007) leading to the elaboration of a Carbonate Island Karst Model (CIKM), in which speleogenesis is strongly conditioned by the particular behavior of diagenetic immature (eogenetic) carbonate rocks. The CIKM progressively integrated more components into the model, taking into account both the presence and disposition of an impervious basement, if it exists, as well as the overprinting of tectonic activity and sea-level changes. Recently, Ginés and Ginés (2007) focused their work on the littoral caves of Mallorca island, adding new morphogenetic insights to the evolution of this eogenetic coastal karst. These authors particularly emphasize the role of breakdown processes, together with the recurrent glacioeustatic sea-level oscillations and the subsequent falls and rises of the water table. This cyclicity would provoke during the glacial periods the triggering of collapse by the loss of buoyant support of phreatic waters and, during the subsequent drowning associated with warm events, the underwater dissolution of boulders and collapse debris. These mechanisms will enable the enlargement of a nonintegrated array of caves and vug-porosity connected to the sea (developed in the mixing zone) rather than conventional karstic flow through conduits.

Framed into the geomorphological context above described, the objective of the present paper is to deal with the sedimentary processes that take place inside the coastal caves of Mallorca, characterizing the different facies existing in the particular geomorphological and hydrological settings that represent this very specific underground sedimentary environment. In this sense, the peculiarities of coastal karst include specific geochemical processes linked to the mixing zone (dissolution, dolomitization…) together with the decisive fact that drowning of cave passages is controlled by the sea-level position, instead of by a local base level plus the possible floods associated with events of intense recharge of the aquifer. As a consequence of its hydrogeological behavior and the low amount of precipitation, the stability of the water-table position in Mallorcan littoral areas is remarkable even at a millennial time-span, although at a longer time-scale there were important fluctuations related to glacioeustatic variability. In general terms we are dealing with a very low energy aquatic environment, framed in a high permeability context (Upper Miocene calcarenites) without a fully karstic hydrogeological behavior: recharge is limited and dispersed, with no sinking superficial streams or flood high waters, and conduit flow is relatively less important than diffuse flow.

## Regional Geological Setting

The two studied caves, Pirata-Pont-Piqueta system and Cova de sa Gleda, are developed in Upper Miocene limestones that crop out along the southern and eastern areas of Mallorca forming the best featured coastal karst region of the island, called Migjorn. Its littoral landscapes are characterized by significant phenomena including different types of karstic and/or marine caves, paleokarst features, littoral karren and fluvio-karstic bights or coves. The Upper Miocene limestone constitutes a post-orogenic platform that surrounds the mountain ranges (Serres de Llevant and Serra de Tramuntana) built up during the Alpine orogeny (Fig. 1). Showing a mean thickness around 70 m, that can occasionally exceed 120 m, they onlap a very irregular alpine folded and thrusted basement composed by Mesozoic dolomites and limestones with minor marl intercalations. The Upper Miocene carbonate sequence corresponds to an alternance of sedimentary bodies (Pomar, 1991) of calcilutites and very porous calcarenites, with a complex geometry, that were formed by the progradation of a Tortonian reef complex. The sequence ends with a series of carbonate tabular deposits with oolitic and mangrove facies, Messinian in age.

The Upper Miocene carbonate sequence forms a slab that stretches as a flat surface behind the coastal decametric-scale cliffs of the southern and eastern shores of the island. This characteristic tabular landscape is interrupted only by incised dry valleys filled up by Holocene sediments, ending at littoral coves whose presence and morphology are conditioned by the extensional processes occurring from the Neogene to the Quaternary. Furthermore, they were responsible for the present-day coastal morphology that is controlled by recent normal faults; also notable is a small tilting that affects the Migjorn plateau along a north-south profile and provokes the variation of sedimentary facies cropping out near the sea level.

## Cave Locations and Descriptions

The Pirata-Pont-Piqueta cave system is located at Can Frasquet farm-house, in the so called Marina de Manacor (Migjorn region, eastern Mallorca), near Cala Falcó small bight (UTM ED-50, 525 590/4 373 360-33) and some 0.4 km from the coast. It is composed of a series of independently explored caves that were recently connected

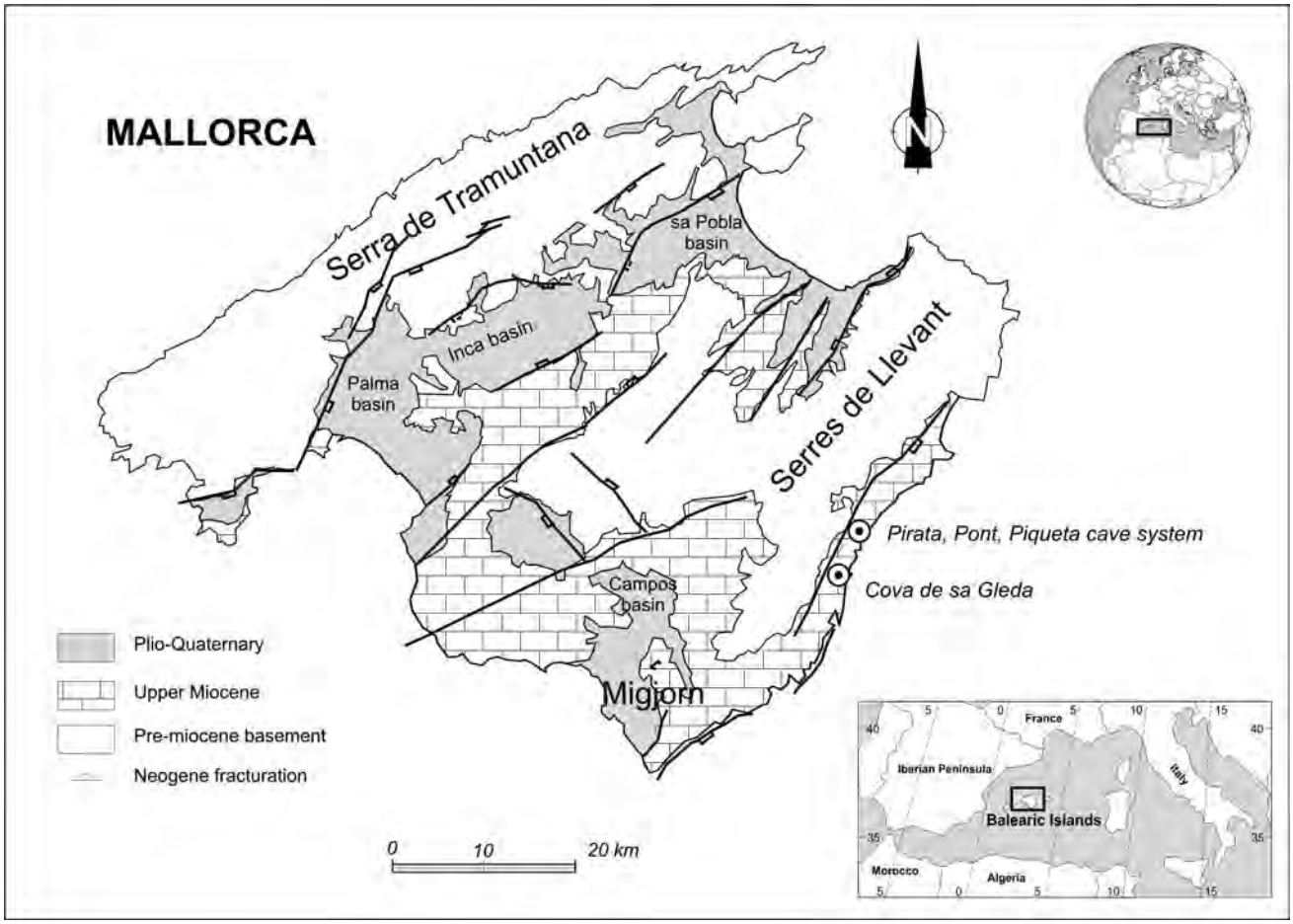


**Figure 1. Geological map of Mallorca depicting the main geologic units of the island and the location of the studied caves.**

by underwater exploration (Gràcia et al, 2006). The system presents a series of breakdown differentiated units, three of them corresponding to the entrance chambers. Up to date explorations include a series of chambers and galleries reaching 3,020 m of development, 1,190 m of which are underwater (Fig. 2); the surface area occupied by subterranean pools with an air surface reaches 5,000 $m^2$. Its maximum depth is 44 m, including 11 m below the present-day sea level. The passages show solution morphologies that are restricted to those sections located beneath the current phreatic level. In that sense the water column has four different well stratified water masses according to their salinity and temperature that constitute a rather complex mixing zone showing two haloclines (Gràcia et al., 2006). The linear penetration of these caves perpendicularly from the coast line is about 700 m. The speleogenesis of the system corresponds to the mixing processes between continental and marine waters that affected the Miocene calcarenites and provoked the initial void creation. Subsequent breakdown processes were induced by the glacioeustatic sea-level falls giving large block accumulations, together with spectacular speleothem ornamentation that is observed through most of the caves.

The Cova de sa Gleda is also located on the Marina de Manacor (Migjorn region) at Son Josep Nou farm-house (UTM ED-50, 523 805/4 372 315-36), 36 m above sea level and some 1.7 km from the coast. It corresponds to a subterranean complex of chambers and galleries related to some collapse sinkholes at the surface, having today a surveyed development near 10,500 m with a maximum underwater depth of 25 m (it is the largest littoral mixing-zone cave in Europe). The morphological frame of the cave shows a series of breakdown chambers (Fig. 2) which are connected to each other by phreatic galleries and passages showing circular, elliptic or irregular sections. Some of the galleries are clearly structurally controlled. The water profile in the submerged passages shows up to five different saline layers, with defined haloclines that give varied types of clearly marked corrosion morphologies (Gràcia et al., 2007b), the most interesting being the corrosion notches that affect both the cave walls and ancient speleothems formed during previous sea level low-stands. The presence of speleothems is a notable aspect of this cave. In particular, some drowned chambers and galleries show impressive precipitation morphologies forming bands of crystal coatings on the cave walls as well as on previous vadose speleothems.

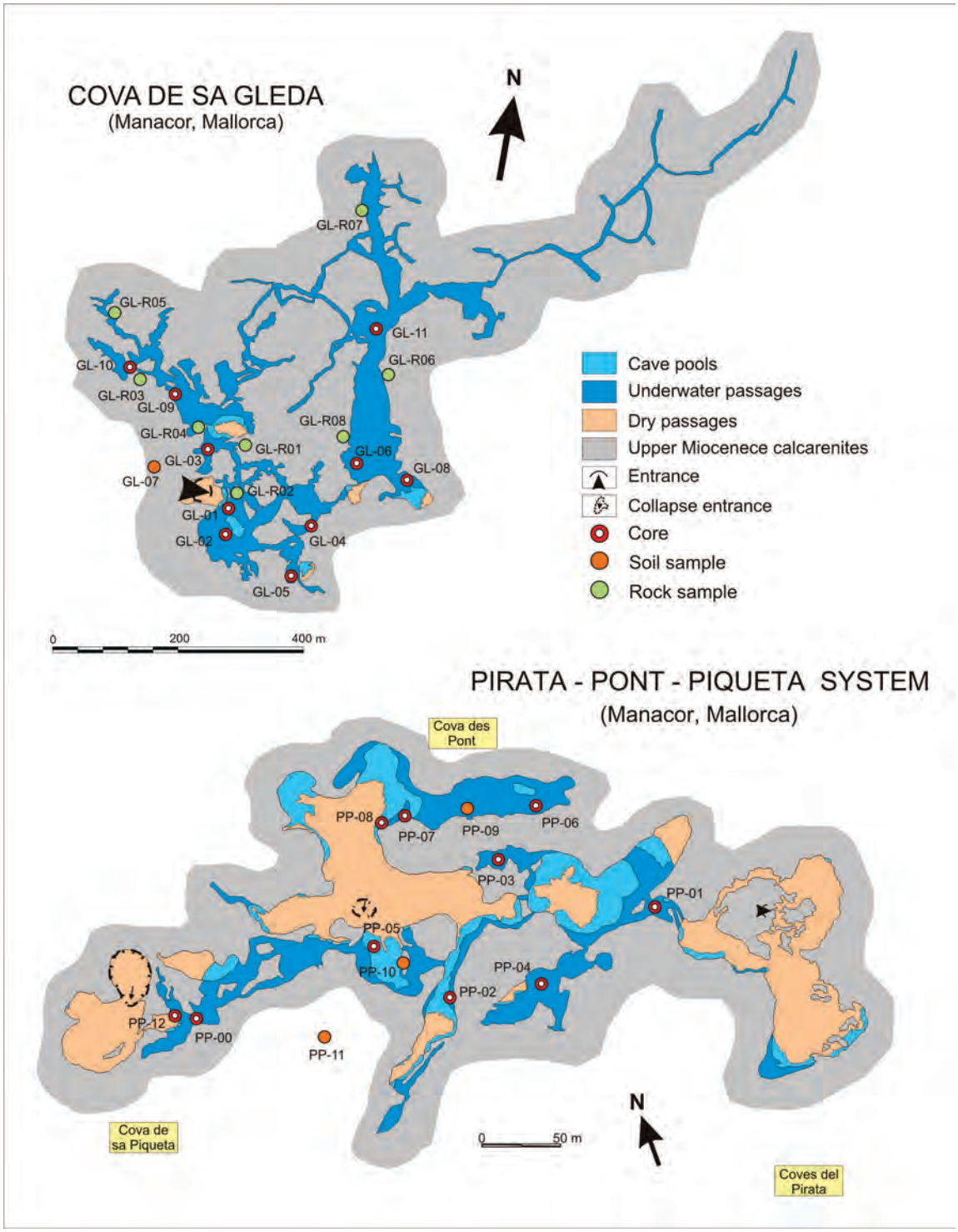


**Figure 2. Cave maps of the Pirata-Pont-Piqueta system and Cova de sa Gleda (Manacor, Mallorca) showing the location of collected cores and samples. Notice that scales are different in both maps. See caves location on Fig. 1.**

These bands are generated by noticeable epiaquatic carbonate precipitation, being related to previous stability levels of the water table which were in turn controlled by Quaternary sea-level oscillations (Tuccimei et al., 2006).

Both the Pirata-Pont-Piqueta cave system and the Cova de sa Gleda have important accumulations of sediments in their chambers and passages, that are today drowned after the Holocene sea-level rise. Most of the cave floors are covered by muddy and/or sandy sediments, which in a wide sense, are marked by two well differentiated characteristics. On the one hand, we have red mud sediments (mainly siliciclastic) and on the other hand, a yellowish carbonate

mud or sand. The mixing of both materials is also frequent, as is the accumulation of large blocks and debris due to the collapse and breakdown of roof and cave walls.

## METHODS

Although practically all the caves known in the eastern and southern coasts of Mallorca island show sediments in their flooded passages (Cova Genovesa [Gràcia et al., 2003]; Cova des Coll [Gràcia et al., 2005]; Cova de s'Ònix [Ginés et al., 2007]; among others), we have focused our work in only two coastal caves that are today the most representative and well known.

### Field Sample Collection

A series of 20 manual cores (Fig. 2) was obtained by scuba-divers in the underwater passages of both caves (10 at Pirata-Pont-Piqueta system and 10 in Cova de sa Gleda) by introducing in the floor sediments a PVC pipe, 5.1 cm in diameter and 50-cm-long, until the full thickness of loose sedimentary fill was attained (Fig. 3). Soil samples at the entrance of the caves as well as rock samples from the walls of both caves were also obtained for subsequent comparison.

Cores obtained were bagged, sealed, numbered, and brought back to the Earth Sciences Department of the Universitat de les Illes Balears, where they were opened, longitudinally sectioned, photographed, and sampled in stratigraphic order according to the different observed levels. Samples were not taken at regular or fixed intervals due to the fact that the scope of the study was an approach to determine the different sedimentary facies existing in these littoral karst caves. Presence of sedimentary structures such as laminations and other general observations were annotated.

### Laboratory Analyses

A total of 136 samples (50 from Pirata-Pont-Piqueta system and 86 from Cova de sa Gleda) were sent to the laboratory where each sediment sample was air-dried for 24 hours prior to analysis. After a color description (dry and humid) using the MUNSELL soil color chart, grain-size, mineralogy, and organic matter were analyzed. Organic matter (lost on ignition [LOI]) was determined by weight loss after placing the samples in a furnace at 550 °C for three hours. Particle size distribution was determined using a Beckman Coulter-LS particle size analyzer. Cumulative curves, frequency histograms, and summary statistics were calculated.

Mineralogy was determined with a Siemens D-5000 X-ray diffractometer, using randomly oriented powders of the bulk samples. Samples were pre-treated with $H_2O_2$ to remove organic matter. Replicates were heated to 375 or 600 °C for 1 hour or treated with ethylene glycol at 60 °C to differentiate between clay minerals. Selected samples were analyzed by EDX (Bruker X-Falsh Detector 4020) or observed by SEM (Hitachi© S-3400N). Semi-quantitative mineral analyses were based on the peak areas obtained using EVA ver. 7.0 software.

Radiocarbon dates were obtained from two organic debris (seeds) in order to establish a chronological frame for the studied cave sediment accumulation. The dating was performed at the Laboratoire IRPA KIK (Institut Royal du Patrimoine Artistique) of Brussels. Analyses of sampled sediments may be found on the NSS web site.

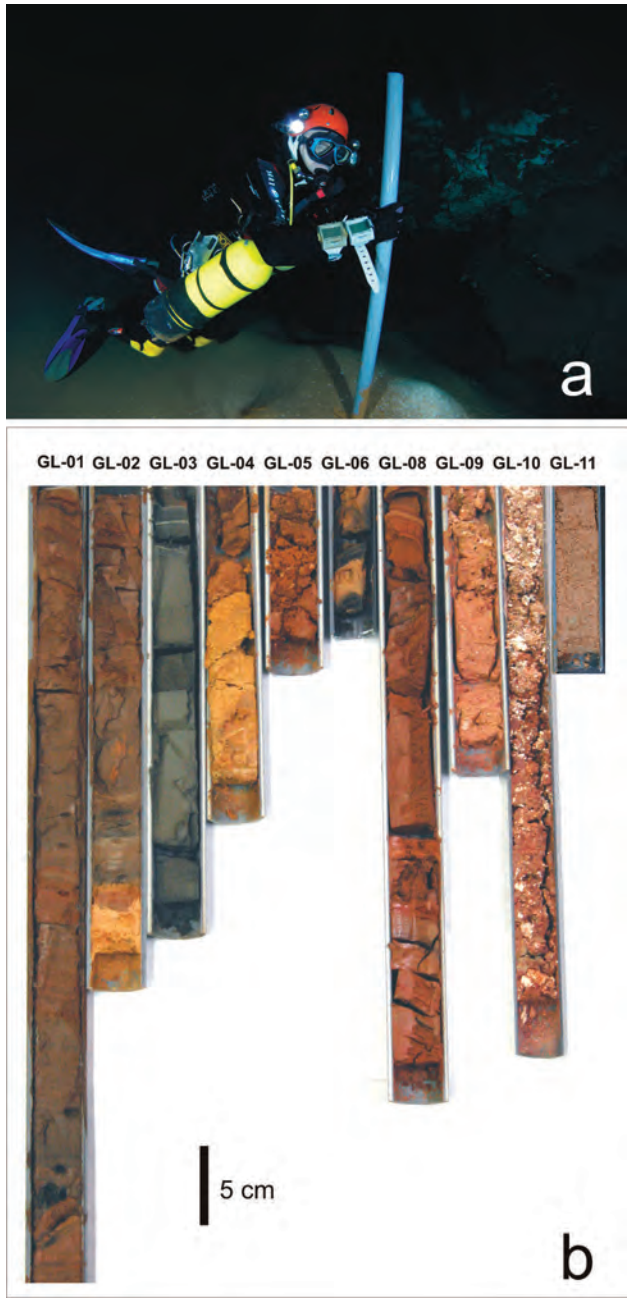


**Figure 3. a) Sampling through manual coring inside the underwater passages of the caves; b) cores of sedimentary infilling from Cova de sa Gleda. See core location on Fig. 2.**

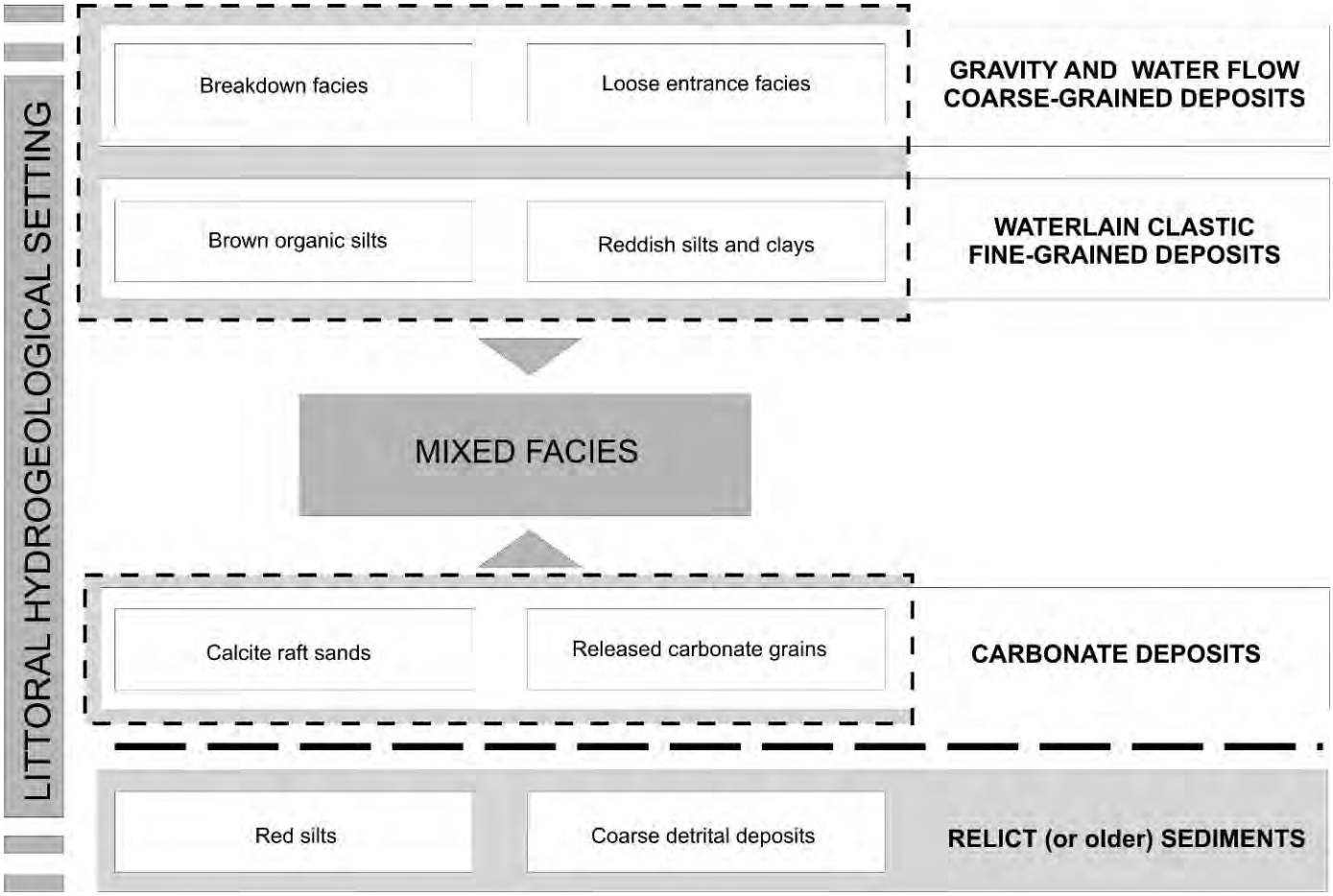


**Figure 4. Sketch showing the sedimentary facies observed in the studied littoral caves.**

## Results

Present-day sediments in the sampled caves of the Mallorcan coastal zone show accumulation thicknesses ranging between 0.5 and 1.5 m, deposited on the floors of underwater solutional galleries, small to medium in size, as well as in submerged breakdown chambers of notable dimensions. The sediments show a very irregular distribution mainly related to present or relatively recent entrances to the caves, where a light thinning trend towards the inner part of the passages can be observed. The irregular morphology of the cavities, together with the breakdown processes that affect most of the chambers, controls the thickness of the sediments.

### Sedimentary Facies

In a general way we can describe the presence of red to brown siliciclastic silty and clayey sediments, pink to yellow carbonate sands, and coarse lithoclastic gravels and breccia deposits. All these deposits can be gathered into four different categories of sediments according to their textural, organic and mineralogical composition as well as their genesis: (1) Gravity and water flow coarse-grained deposits, (2) Waterlain clastic fine-grained deposits, (3) Carbonate deposits, and (4) Relict or older deposits (Fig. 4) most of which are composed of several sedimentary facies that are forthwith described.

#### *Gravity and Water Flow Coarse-Grained Deposits*

**Breakdown Facies.** This facies includes unsorted boulders (ranging in size from several centimeters to near 15 m) and cobble piles with no cement binding the clasts (Fig. 5). Their composition corresponds entirely to calcarenites and, in small amount, calcisiltites coming from the Upper Miocene rocks in which the cave is located. Grain size is related to the bedding thickness of the source limestones, being usually from medium to thick (decimetric to metric) or even massive. Surface textures of the clasts are slightly weathered depending on their depth in the cave waters and the diverse geochemical behavior found there. Clasts range from subangular to sub-rounded depending on the textural characteristics of the original rock. Although they show a chaotic mixture regarding size and disposition, some preferred clast orientation can be observed. They are flattened in shape, according to the rock bedding, and the largest clasts show their flat sides facing parallel to the surface accumulation of

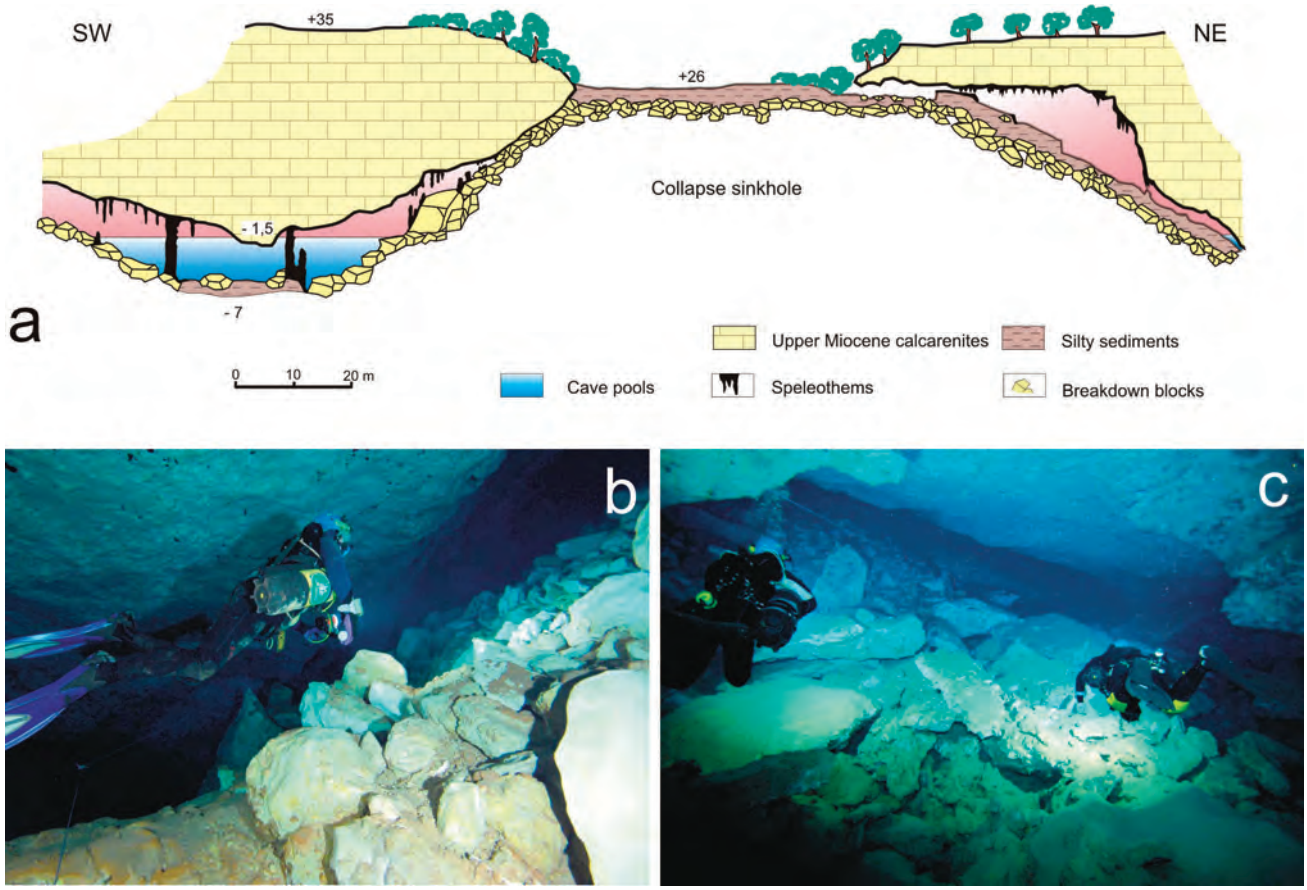


**Figure 5. Pirata-Pont-Piqueta cave system, a) geomorphological section of one of the entrances with related breakdown processes; b) entrance talus deposits; c) breakdown piles due to collapse are present all around the caves.**

the debris cone. The clasts don't show any imbricated structure, or any other sign of transport.

This facies corresponds to the accumulation of debris from roof as well as wall collapse, altered by solutional processes that take place in relationship to the halocline. Chip, slab or even block breakdown can be found.

**Loose Entrance Facies.** These deposits have some similarities to the breakdown materials previously described. Located near the current entrances or choked openings, this facies is a breccia accumulation with clasts, blocks and boulders very irregular in size and shape, mostly showing a sub-rounded morphology and having a slight inverse grading. Matrix content can be abundant and is mainly formed by silts and very fine sand coming from outside, but with a very irregular distribution. They form prograding fans usually with a high degree of slope (Fig. 5).

This facies consists of a mixing between mainly fine-grained particulate material, carried by external currents that drain to the entrance pools of the caves, and fallen fragments of rock from the cave walls. It is one of the coarsest facies present in these coastal caves, containing no well rounded sediments due to the absence of currents of sufficient strength flowing into the littoral aquifer and the lack of allogenic currents draining to the caves. We have not observed debris flow deposits. These deposits correspond to the entrance talus of White (2007).

### *Waterlain Clastic Fine-Grained Deposits*

**Brown Organic Silts.** The brown organic silts facies is one of the most extensive found in the caves, and it presents variable thicknesses ranging from 0.2 m to nearly 1 m. This facies is especially represented in the chambers and galleries with openings to the surface. They correspond to silt with low proportions of clay (around 10%) and fine sands (less than 5%). With a moderate sorting, they have a mean grain size corresponding to coarse silt and a median (D50) of fine silt (Fig. 6). Samples taken in the sediment cores show a dark reddish brown color (5YR3/4) when moist and reddish yellow (7.5YR6/6) when dried in the laboratory. The most conspicuous feature of these sediments is the presence of very fine laminations clearly defined by the alternation of reddish-brown and black laminae (Fig. 7). These millimeter-scale black laminae show a notable accumulation of vegetal fibers and seeds. The median organic content of the facies is slightly higher than 5% (LOI). From the point of view of their mineralogy it can be considered basically siliceous, with a high proportion of

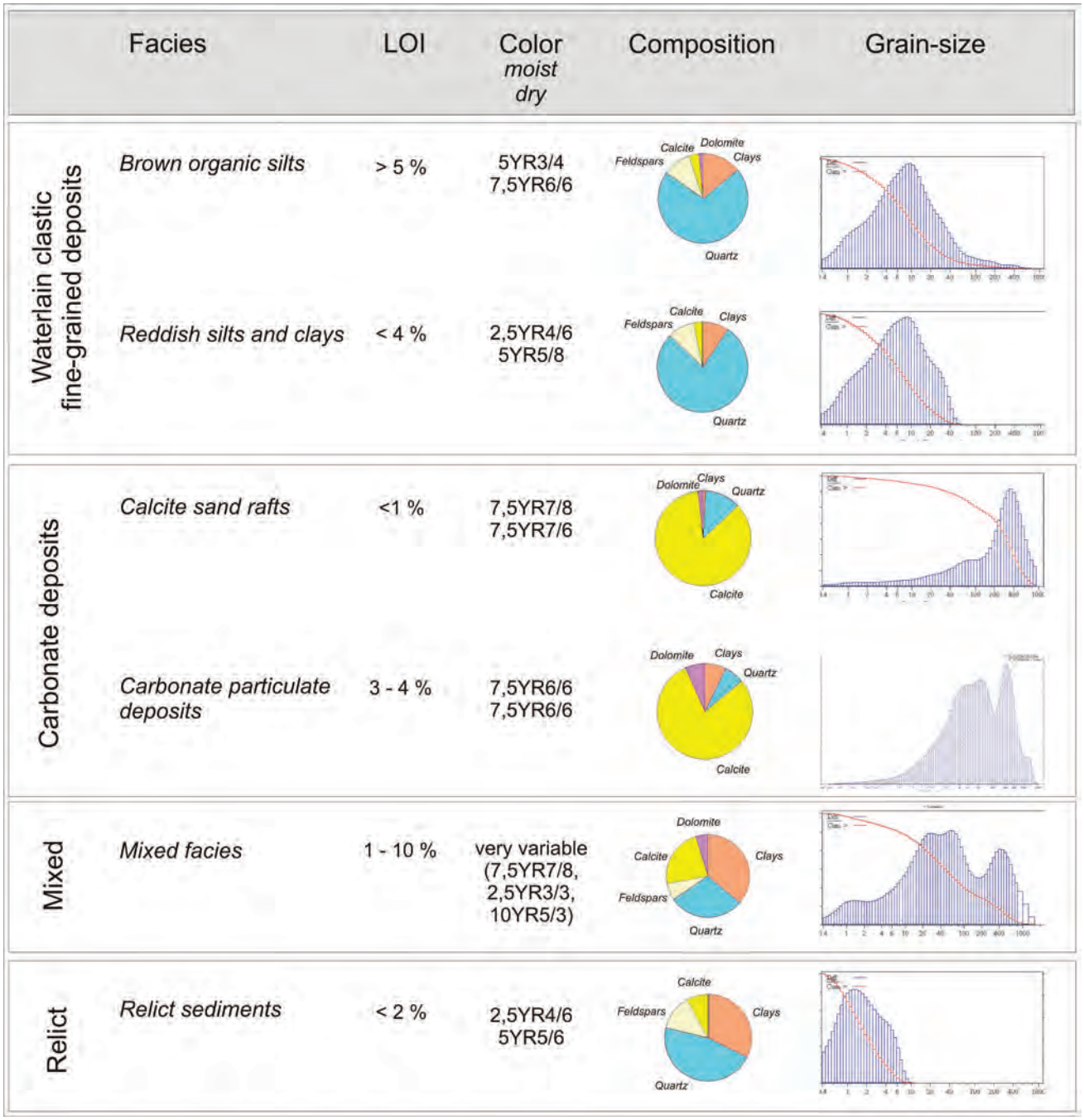


**Figure 6. LOI (lost on ignition) percentage, color, mineralogical composition, and texture of the sedimentary facies described.**

quartz (more than 65%), clay minerals (around 20%) and feldspars (near 10%). Carbonates (mainly calcite) are present in very low proportions (less than 5%).

The sediments that correspond to this facies are accumulated mainly in those pools and underwater passages that are located nearest the great collapse entrances to the caves. Sediment composition corresponds to soil materials transported inside the caves by flowing rain water, especially during storm events. Their composition has been traditionally related to allochthonous siliciclastic components supplied by rains carrying down dust particles of Saharan origin (Fiol et al., 2005, Goudie and Middleton, 2001). The clear laminations due to the periodic accumulation of organic matter, including abundant vegetal fibers and seeds, are related to each one of the successive storm events entering the cave, and may not in fact have any seasonal significance. They also do not have any relation with the varve deposits so classical in glaciated regions. Carbon-14 dating of some organic components (seeds and vegetal fibers) from cores PP-08 and GL-01

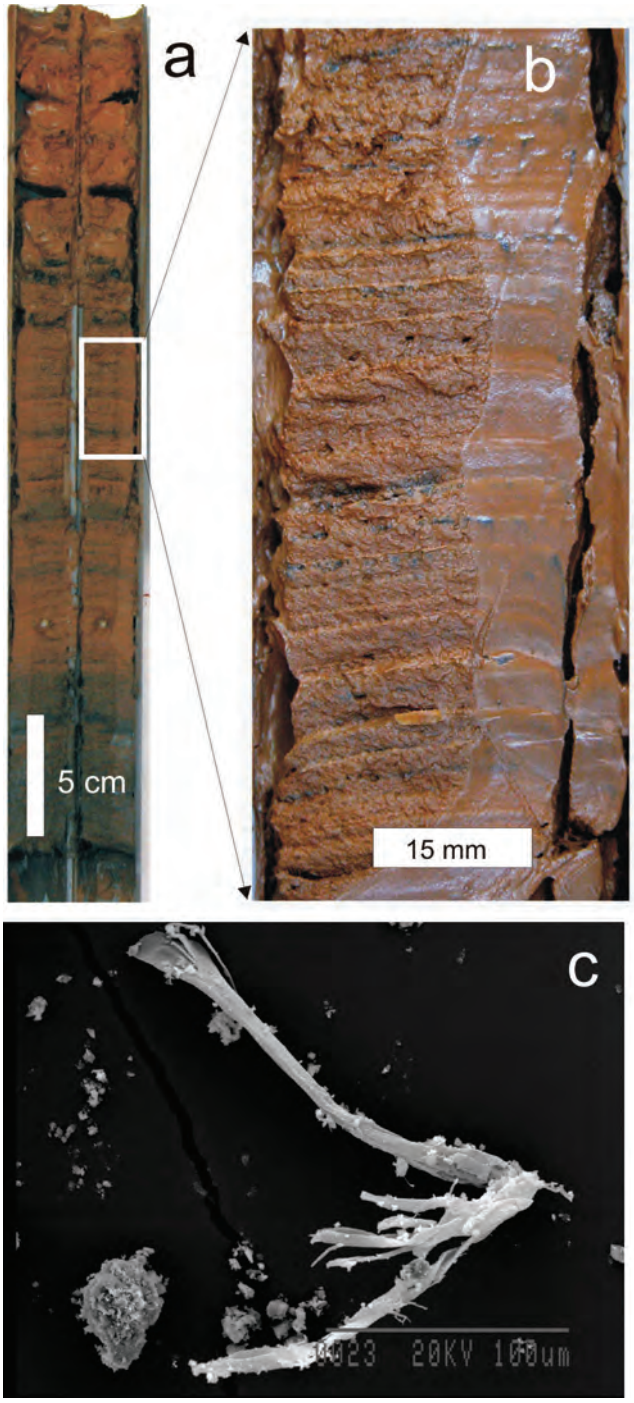


**Figure 7. Brown organic silts; a) General aspect of core PP07 collected at Galeria del Llac Ras in Pirata-Pont-Piqueta cave system; b) conspicuous thin-laminations due to grain-size sorting and organic accumulation; c) vegetal fibers are the main constituents of the black laminae.**

yielded ages of 220 and 330 yr BP, respectively (Fornós and Gràcia, 2007).

**Reddish Silts and Clays.** This facies is the least common in the studied caves, in extension as well as in thickness.

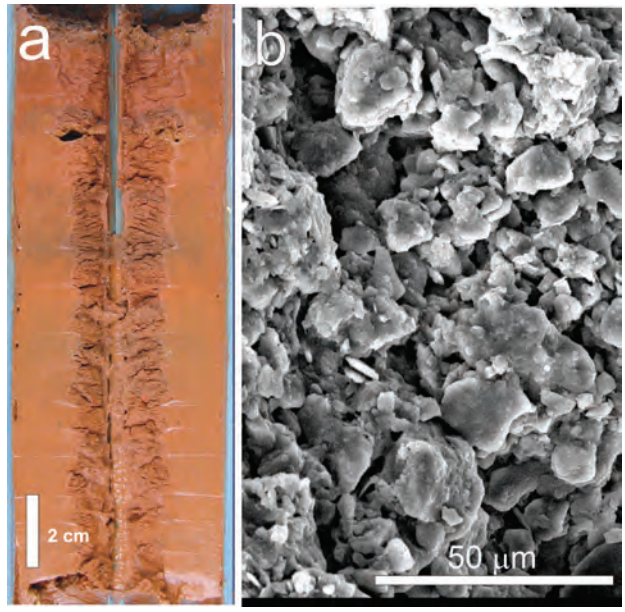


**Figure 8. Reddish mud; a) core PP06 collected at the end of Galeria del Llac Ras in the Pirata-Pont-Piqueta cave system showing a massive aspect with faint lamination; b) detailed SEM image of the sediments mainly composed of quartz grains and clays.**

Localized in the cores collected in the inner passages, it shows a thickness that scarcely reaches 20 cm, showing a dark red color (2.5YR4/6) when moist that transforms to yellowish red (5YR5/8) when dried in the laboratory (Fig. 8). The presence of organic matter is reduced (LOI less than 4%). Texturally (Fig. 6) the facies corresponds to silt (81%) with a small proportion of clay fraction (19%). The sand fraction is absent. It shows good sorting. Their mineralogical composition is formed of siliceous minerals with quartz representing more than 75%, feldspars with more than 10%, and clay minerals that practically never reach 10%. Presence of carbonate minerals is very low (mainly calcite with less than 3%).

Being restricted to the inner part of the caves, far away from the main entrances as well as in places with limited connections with the surface, this facies represents the fine-grained sediments that can be transported as suspended load deep into the cave system. As in the case of the organic brown silts facies, the muddy reddish silts are integrated by abundant allochthonous silicic sediments related to dust rains coming from Africa, which were progressively accumulated into the soil mantle.

### *Carbonate Deposits*

**Calcite Raft Sands.** The thickness of this facies varies from a few centimeters to more than 40 cm in the sampled chambers. The sand deposits show a reddish yellow color (7.5YR7/8 moist to 7.5YR7/6 dry). Bedding is poorly defined by the existence of sub-millimeter scale horizontal

lamination resulting from the subtle presence of red muddy particles. Texture is moderately sorted and clearly dominated by the sands (> 78%) with small amounts of silts representing slightly more than 18%, and some clay (less than 3%). Thin limestone angular particles are scarce. Mean grain-size as well as the median value correspond to the transition from fine to medium sand size (Fig. 6). The organic content is very low (LOI less than 1%). Grain mineralogy is dominated by a carbonate composition with calcite (> 85%) and some dolomite (< 2%); the rest corresponds to quartz (12%) and scarce clay minerals (< 1%).

Sand grains are constituted of composite rhombohedral calcite crystals showing a clear differential geometric growth that starts with microsparite crystals, forming a planar surface that coincides with the surface of the water, and evolves to sparite crystals inside the water pool. Most of the composite crystals sand grains when found on the bottom of the pools present clear corrosion morphologies related to the geochemical processes (aggressiveness linked to the haloclines) occurring through the water column (Fig. 9).

This kind of sediment is especially abundant in the bottom of those cave pools having a free water surface that allows for $CO_2$ degassing. This process controls the precipitation of calcite rafts at the surface of the pools where they are maintained floating by means of surface tension, until some external process or their own growth triggers their sinking and a final accumulation at the bottom of the pool.

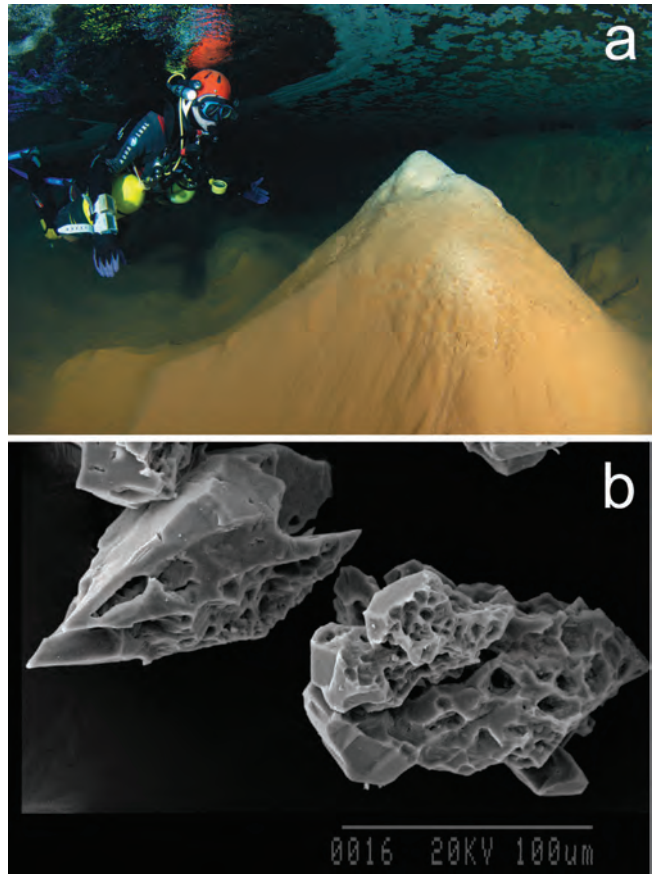


**Figure 9. a) Conical structure due to the accumulation of sunken calcite rafts; b) calcite crystals corresponding to calcite rafts affected by corrosion in the mixed zone once they are sunk to the bottom of the pools.**

**Carbonate Grains Released by Physico-Chemical Weathering of Limestone Walls.** Thickness of this sediment facies is very variable, ranging from a few centimeters to nearly 20 cm, with distribution mainly related to the proximity to the base of cave walls or rock protuberances in general. Color is consistently reddish yellow (7.5YR6/6). Their organic matter composition is variable with mean values of different cores ranging between 3 and 4% (LOI). The textural characteristics are also quite variable, usually giving bimodal curves and showing very poor sorting (Fig. 6). The mean grain size corresponds to the fine sand fraction and the median (D50) to very fine sand. The sand fraction represents nearly 60% of the total composition, while the silt fraction is greater than 35%; the clay fraction show values around 5%. From a mineralogical point of view, their composition is mainly carbonate. Calcite represents up to 80% and dolomite around 8%. Siliceous components are formed by quartz reaching near 7% of mean values and low percentages of clay minerals (less than 4%).

These carbonate particulate deposits are the coarsest fraction in the cave systems apart from those produced by the gravity and breakdown processes. They are mainly composed of carbonate rock particles detached from the cave walls (Fig. 10), due to the differential response to weathering and corrosion of the variegated bioclastic grains (differing both in mineralogy and texture) that compose the enveloping calcarenite rock. This facies is particularly abundant where the current haloclines are present and carbonate grains are released by mixing corrosion.

### *Mixed Facies*

Mixed facies are present all along the entire cave systems. They constitute a mixture of the above described facies, including both siliciclastic and carbonate sediments in different proportions (Fig. 11). The quantitative characteristics of the mixture are related to the location in the cave, presence of surface openings, depth of the drowned areas, distance to the sea, presence of pools with free air surface, etc. The resulting texture and composition differ from the end members corresponding to the different facies which have been characterized in the previous paragraphs (Fig. 6). From the mineralogical point of view, these facies also correspond to a very variable mixture of siliceous components and carbonate grains, including both crystal aggregates as well as particulate material.

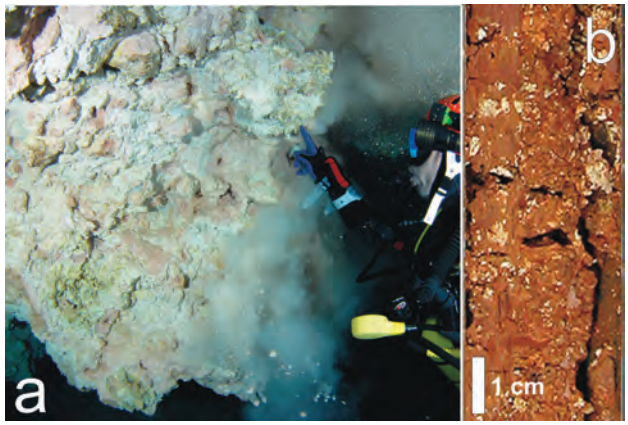


**Figure 10. Incongruent corrosion of the Miocene calcarenites related to the mixing zone gives way to a granular disintegration producing abundant carbonate sediment; a) sandy grain size rain of sediment; b) core GL10 from Galeria dels Degotissos in Cova de sa Gleda showing the coarsest sediments in the cave systems, being mainly composed of heterometric carbonate rock particles.**

Color is very variable embracing shades of reddish yellow (7.5YR7/8) to dusky red (2.5Y3/3) or even brown (10YR5/3). Organic matter also has a great variability, ranging from 1% to more than 10%. Usually the textural curves show bimodality and poor to very poor degrees of sorting. Mean grain size ranges from fine sand to coarse silt, while the median varies between very coarse silt to medium silt. Textural fractions show figures between 14% and 40% for sand, between 50% and 60% for silt and between 7% and 25% for the clay fraction. The mineral composition also has a great variability. Calcite ranges between more than 90% to less than 30%, dolomite from 3% to 6%, quartz from more than 40% to less than 3%; feldspars have a maximum of 10%, but can be also absent in some samples and, finally, the clay minerals range from 1% to slightly more than 10%.

### *Relict or Older Deposits*

**Red Silts.** Ancient deposits composed of red silts are up to 15 cm thick in some sampled chambers. The color is dark red (2.5YR4/6) when moist and yellowish red (5YR5/6) when dry. Bedding is very poorly defined but locally there is a millimeter-scale black lamination, resulting from organic-matter concentration. On the surface of these sediments decimeter-scale mud desiccation cracks (up to 4 cm deep) are clearly visible (Fig. 12). The mean organic content (LOI) is around 2%. Texturally this facies represents a mixing of silts (52%) and clays (47%) with a very low presence of sand material (less than 1%); it shows a very good sorting. The mean grain-size corresponds to very fine silt and the median (D50) lies between silt and clay fractions. Mineralogical content is dominated by quartz (> 43%) and clays (mainly illite and kaolinite with some montmorillonite) with values above 33%. Feldspar minerals represent slightly less than 13%, calcite near 9% and dolomite 2%.

**Figure 11. Carbonate, silicic or mixed sediments presently extensively covering the floor of the caves (Galeria de les Còniques, Cova de sa Gleda).**

This sedimentary facies is composed of clay and silt particles that accumulate in ponded areas of passages receiving episodic slow-moving storm water input from the collapse entrances. The presence of abundant mud cracks splitting the sedimentation into polygonal blocks on the top of these red silty materials indicates a drying period occurred after the deposition of such mud by slow-moving water. The existence of mud cracks on the surface of these sediments (today located in underwater passages extending well below the sea level) clearly reflects the fact that they correspond to an early infilling of the cave linked to some Pleistocene sea-level fall, probably corresponding to the last glacial event.

**Figure 12. Sediments very similar to present-day reddish mud, but presenting desiccation cracks are present in some places (−4 m, Galeria del Llac Ras, Pirata-Pont-Piqueta cave system). Their deposition must correspond to some sea-level fall event, probably to the last glaciation.**

**Coarse Detrital and Gravity Fallen Deposits.** These materials are analogous to the coarse-grained deposits previously described (mainly gravity emplaced) but with a genesis related to previous episodes of breakdown in the cave. They are the result of autogenic breakdown processes favored by the repetitive loss of hydraulic buoyancy during Pleistocene glacial periods and the subsequent sea-level falls. Usually they are covered with a thin veil of more recent sediments, which can be found also as matrix infiltrates between the breccia clasts.

## Discussion

Sedimentation inside the coastal karst caves of Mallorca comprises both autochthonous and allochthonous components provided by a relatively wide diversity of geomorphic mechanisms acting in the different aquatic environments existing along the cave systems. The processes involved vary from rock collapse to fine-grained waterlain clastic sediments, including diverse mechanisms such as underwater weathering of rock surfaces, precipitation of calcite crystals, and infiltration of soil materials (Fig. 13). Investigations carried out on two of the most important coastal caves of the island have allowed the characterization of several differentiated sediment facies, which clearly correspond to specific locations within the whole cave system. The proximity to the cave entrances or blocked openings to the surface, as well as the geochemical behavior of the phreatic waters (dissolution, precipitation, etc.), is crucial in order to explain the cave sediments distribution together with the particular topography of the underwater galleries and chambers.

### Interpretation of the Cave Sedimentary Record

Breakdown or collapse has been one of the most invoked processes of later evolution in the development of the coastal caves of Mallorca (Gràcia et al. 2006, 2007a, 2007b). The repeated flooding and emptying of the original phreatic passages, during the Pleistocene glacio-eustatic oscillations, caused the passages to be altered in shape and dimensions by breakdown processes, especially when the caves were drained during sea-level falls, and favoring the failure of roofs and walls particularly along the bedding planes and joints (Gillieson, 1996; Ginés and Ginés, 2007). The maximum sea-level fall during the last glacial period was around 135 m below present-day datum (Lambeck and Chappell, 2001; Lambeck and Purcell, 2005); this figure, together with the rather modest depth attained by the caves (maximum 25 m below the current sea level) due to the presence of impervious facies at the base of the Miocene sequence, suggests that all the known chambers and passages had been emptied several times during the Pleistocene cold periods, favoring in that way the actuation of collapse processes.

Most of the entrances to the caves correspond to collapsed roofs that today act as collectors of some surface

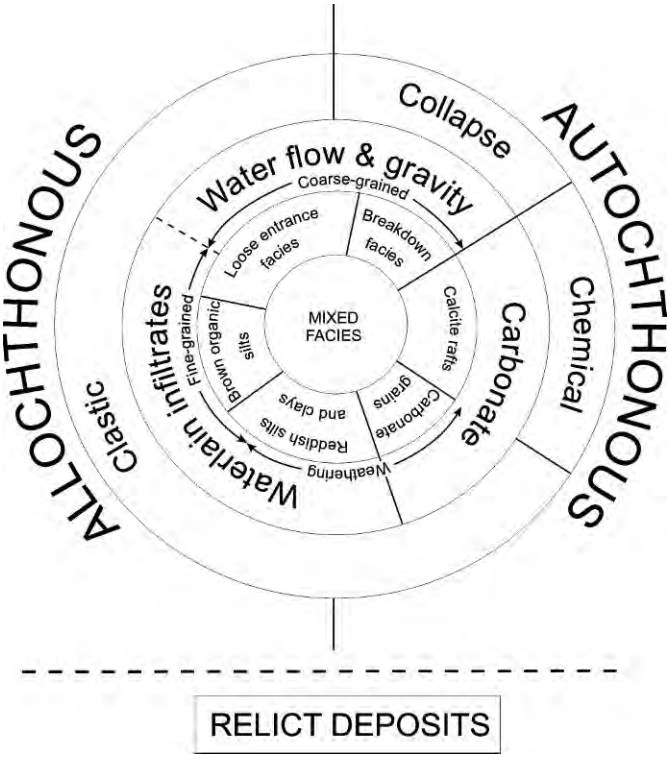


**Figure 13. Sedimentary facies and involved processes in the coastal karst caves of Mallorca island.**

runoff, and represent preferential sinking points that quickly drain precipitation towards the water table. Depending on the strength of the storm events and the resulting runoff, many types of sedimentary material can be transported down slope by episodic water flows. Furthermore, the processes related to the breakdown facies are also present in the cave openings, where intensive weathering of the rock walls also takes place. All these materials, as well as particles eroded from the soil, are incorporated in the loose entrance facies, and after a more or less prolonged sheet flow transport may be deposited at some cave pools near the entrances forming a delta-like architecture. Thus, loose materials can accumulate in the entrance chambers simply by gravity or by being carried in flowing water. The result is a mixing of gravels, sands, and silty material deposited in the caves by the runoff from the land surface together with weathered elements from the cave walls or ceilings as well as soil particles. The Migjorn region, where the caves are found, is an autogenic karst mantled with only a discontinuous thin soil. The catchment area is relatively minor (some square kilometers) so the volume of external detrital sediment is rather small.

Episodic water flows that enter the caves through the existing collapse openings after intense periods of rainfall, which characterize the Mediterranean weather particularly in autumn (Guijarro, 1986), transport heterometric materials until reaching the water table at the ponds inside the caves. The coarsest elements accumulate at the entrance

pools forming pseudo deltas, as have been mentioned above, while the muddy finest material is introduced inside the submerged galleries of the cave where the sedimentary accumulation takes place mostly by decantation according to the hydraulic characteristics of the water body and the grain size properties of the transported particles. Clay and silt accumulate thus in drowned inner passages where there is a slow-moving floodwater transport. The distance inside the cave that sediment can reach will depend on the geometry and morphology of the cave system and the initial impulse of the water flooding after heavy storms, as well as the interaction with the slow water movement inside the aquifer induced by the tidal (and/or barometric) sea-level oscillations. In this manner, different facies are deposited varying mainly in grain-size and organic matter content. As a result, the inner fine sedimentation is clayey and with very low organic-matter content (reddish mud facies), whereas sediments emplaced nearest the collapse openings are silty and usually show very clear black laminations of organic matter, and are related to the successive storm events that supply materials to the entrance pools (brown organic silts). Carbon-14 datings of organic components (220 and 330 yr) confirm the subactual character of these deposits.

Mineralogy of the fine-grained sediments (both brown organic silts and reddish mud) is mainly siliceous, including quartz, feldspar and clay minerals. This fact points to an allochthonous origin related to rains, coming from the south or south-east, that supply silicic dust of Saharan source; these atmospheric situations are relatively common in the western Mediterranean when a center of low pressure remains situated over the Iberian peninsula (Fiol et al., 2005). Although some of the insoluble residue from the dissolution of bedrock can contribute to the detrital sedimentation in the caves, the analysis done on the surrounding rocks shows that their non-carbonate impurities are less than 1%. Nevertheless there is a great amount of carbonate granular (sand sized) material that has been produced by the weathering and disaggregation of the bedrock, producing detached particles that are eventually accumulated simply by falling into the submerged passages and chambers. These carbonate grains are released by the differential physico-chemical weathering of limestone or dolomite from the bedrock, as well as by the different solubility of bioclastic grains according to their mineralogy and in relation to their biological composition. In that way, the production of released carbonate grains is favored owing to the incorporation of these particulate materials into the sedimentary record of the cave system. Although these processes are most typical of caves that contain little or no running water, being exposed to long-term weathering in air (Palmer, 2007), in littoral caves, as is our case, weathering in this phreatic environment can be enhanced by the geochemical activity of the coastal mixing zone.

Deposits constituted by calcite raft sands are linked to those cave pools with free water surface, that allows for $CO_2$ degassing and carbonate precipitation. When these calcite rafts are sunk by dripping water, or for whatever reason, they accumulate as coarse sands of loose crystal aggregates of calcite that can reach notable thickness. When submerged and deposited in the bottom of the pools, the calcite crystals may present dissolution traces related to the geochemical processes occurring in the haloclines. The so called mixed facies are the most abundant sediments in the studied caves, being a mixture of all the previously described materials in different proportions. Grain size is normally bimodal (sand and silt fractions are predominant) and mineralogy is very diverse, including both allochthonous siliceous grains together with carbonate particles released by dissolution and/or calcite raft crystals. Their distribution and importance are very variable and depend mainly on the relationship between main entrances to the caves, presence of pools with free-air surfaces, and depth of the haloclines in the submerged galleries.

In spite of the previously discussed specificity of the coastal karst environment, most of the observed sediment types correspond in broad terms to the backswamp facies of Bosch and White (2004) because they are constituted by a variety of infiltrated soil materials, weathering residues, and carbonate precipitates having experienced very limited lateral transport. On the other hand, the reddish mud deposits present in the inner parts of the cave systems show some analogies to the slackwater facies (Bosch and White, 2004), but framed in a low-energetic context linked to the coastal karst hydrological behavior quite different from conventional stream caves.

Relict or ancient sediments are also present in the studied caves, being very similar to present-day reddish mud deposits, but showing desiccation cracks that situate their deposition in some sea-level fall event (perhaps the Last Glaciation). Mineralogy predominantly includes allochthonous siliceous grains, supplied by dust rains of African origin. An adequate interpretation of these ancient sedimentation phases will strongly benefit from the investigation of the present-day deposits from the coastal caves of the island.

## CONCLUSIONS

Several main conclusions can be drawn in reference to the sedimentary processes occurring in this specific cave environment of the coastal karst system. Clastic sedimentation in the coastal caves of Mallorca island is fully conditioned by the hydrogeological specificity of the littoral karstification affecting high permeability rocks (calcarenites Upper Miocene in age). No allogenic streams are present in the Migjorn karst region, and the coastal aquifers are characterized by a rather diffuse flow to the sea. Nevertheless, an important factor in the distribution of sediment is episodic influx of meteoric water during storm events.

Several facies can be found in the cave systems, which can be grouped into gravity and waterflow coarse-grained

deposits, waterlain clastic fine-grained deposits, carbonate deposits and mixed facies. Relict deposits are also present, being related to the morphological evolution of the cave during the Pleistocene.

The diversity of represented facies is related to the topographical and geomorphological position of sampled points within the cave system. Breakdown processes of underground passages, triggered by Pleistocene sea-level oscillations, give place to collapse entrances and choked openings favoring the presence of entrance facies, and the penetration of sediments carried by runoff waters. Brown organic silt facies are particularly widespread near present-day entrances to the caves. The abundance of siliceous sediments in the fine-grained deposits must be related to dust rains of Saharan origin, which are frequent in the Western Mediterranean. Particles of carbonate material are important constituents of some deposits, in the form of rock grains released by differential dissolution weathering or sunken calcite rafts. It is very common to have the presence of mixed facies that include allochthonous siliciclastic silts and mud together with autochthonous carbonate particles. Coastal karst caves host a very specific sediment assemblage that requires increasing attention.

## Acknowledgements

This work was partially supported by the research fund of Ministerio de Educación y Ciencia – FEDER, CGL2006-11242-C03-01/BTE. We thank to F. Hierro (SEM), J. Cifre (X-ray analysis), and M. Guart (grain-size analysis) for helping in lab analysis. The authors are grateful to B. Clamor, M. Febrer and P. Gamundí for their help during the field sampling and A. Ginés for their constructive comments and help in writing the manuscript.

## References

Bosch, R.F., and White, W.B., 2004, Lithofacies and transport of clastic sediments in karstic aquifers, *in* Sasowsky, I.D., and Mylroie, J., eds., Studies of cave sediments: Physical and chemical records of paleoclimate: New York, Kluwer Academic/Plenum Publishers, p. 1–22.

Fiol, L., Fornós, J.J., Gelabert, B., and Guijarro, J.A., 2005, Dust rains in Mallorca (Western Mediterranean): Their occurrence and role in some recent geological processes: Catena, v. 63, p. 64–84.

Ford, D.C., and Williams, P.W., 2007, Karst hydrogeology and geomorphology: Chichester, Wiley, 561 p.

Ford, T.D., 2001, Sediments in caves: Somerset, U.K., BCRA Cave Studies Series, no. 9, 32 p.

Fornós, J.J., and Gràcia, F., 2007, Datació dels sediments recents que rebleixen les cavitats de sa Gleda i del sistema Pirata-Pont-Piqueta: Primeres dades: Endins, v. 31, p. 97–100.

Gillieson, D., 1996, Caves. Processes, Development, Management: Camridge, Blackwell Publishers, 324 p.

Ginés, A., and Ginés, J., 2007, Eogenetic karst, glacioeustatic cave pools and anchialine environments on Mallorca Island: A discussion of coastal speleogenesis: International Journal of Speleology, v. 36, no. 2, p. 57–67.

Ginés, J., Fornós, J.J., Trias, M., Ginés, A., and Santandreu, G., 2007, Els fenòmens endocàrstics de la zona de ca n'Olesa: la cova de s'Ònix i altres cavitats veïnes (Manacor, Mallorca): Endins, v. 31, p. 5–30.

Goudie, A.S., and Middleton, N.J., 2001, Saharan dust storms: Nature and consequences: Earth-Science Reviews, v. 56, no. 1–4, p. 179–204.

Gràcia, F., Clamor, B., Fornós, J.J., Jaume, D., and Febrer, M., 2006, El sistema Pirata-Pont-Piqueta (Manacor, Mallorca): Geomorfologia, espeleogènesi, hidrologia, sedimentologia i fauna: Endins, v. 29, p. 25–64.

Gràcia, F., Clamor, B., Jaume, D., Fornós, J.J., Uriz, M.J., Martín, D., Gil, J., Gracia, P., Febrer, M., and Pons, G., 2005, La cova des Coll (Felanitx, Mallorca): Espeleogènesi, geomorfologia, hidrologia, sedimentologia, fauna i conservació: Endins, v. 27, p. 141–186.

Gràcia, F., Fornós, J.J., and Clamor, B., 2007a, Cavitats costaneres de les Balears generades a la zona de mescla, amb importants continuacions subaquàtiques, *in* Pons, G.X., and Vicens, D., eds., Geomorfología Litoral i Quaternari. Homenatge a Joan Cuerda Barceló. Mon. Soc. Hist. Nat. Balears, v. 14, p. 299–352.

Gràcia, F., Fornós, J.J., Clamor, B., Febrer, M., and Gamundí, P., 2007b, La cova de sa Gleda I. Sector Clàssic, Sector de Ponent i Sector Cinccents. (Manacor, Mallorca): Geomorfologia, espeleogènesi, sedimentologia i hidrologia: Endins, v. 31, p. 43–96.

Gràcia, F., Jaume, D., Ramis, D., Fornós, J.J., Bover, P., Clamor, B., Gual, M.A., and Vadell, M., 2003, Les coves de Cala Anguila (Manacor, Mallorca). II: La Cova Genovesa o Cova d'en Bessó. Espeleogènesi, geomorfologia, hidrologia, sedimentologia, fauna, paleontologia, arqueologia i conservació: Endins, v. 25, p. 43–86.

Guijarro, A., 1986, Contribución a la bioclimatología de las Baleares [Ph.D. thesis]: Palma de Mallorca, Universitat de les Illes Balears, 232 p.

Lambeck, K., and Chappell, J., 2001, Sea level change through the Last Glacial Cycle: Science, v. 292, no. 5517, p. 679–686.

Lambeck, K., and Purcell, A., 2005, Sea-level change in the Mediterranean Sea since the LGM-. Model predictions for tectonically stable areas: Quaternary Science Reviews, v. 24, p. 1969–1988.

Mylroie, J.E., and Carew, J.L., 1990, The flank margin model for dissolution cave development in carbonate platforms: Earth Surface Processes and Landforms, v. 15, p. 413–424.

Mylroie, J.R., and Mylroie, J.E., 2007, Development of the carbonate island karst model: Journal of Cave and Karst Studies, v. 69, no. 1, p. 59–75.

Palmer, A.N., 2007, Cave Geology: Dayton, Cave Books, 454 p.

Pomar, L., 1991, Reef geometries, erosion surfaces and high-frequency sea-level changes, Upper Miocene Reef Complex, Mallorca, Spain: Sedimentology, v. 38, p. 243–269.

Sasowsky, I.D., and Mylroie, J., eds., 2004, Studies of cave sediments. Physical and Chemical Records of Paleoclimate: New York, Kluwer Academic/Plenum Publishers, 329 p.

Tuccimei, P., Ginés, J., Delitala, M.C., Ginés, A., Gràcia, F., Fornós, J.J., and Taddeucci, A., 2006, Last interglacial sea level changes in Mallorca island (western Mediterranean). High precision U-series data from phreatic overgrowths on speleothems: Zeitschrift für Geomorphologie N.F., v. 50, no. 1, p. 1–21.

White, W.B., 2007, Cave sediments and paleoclimate: Journal of Cave and Karst Studies, v. 69, no. 1, p. 76–93.

## APPENDIX I

**Table 1. Sample color, in dry and wet conditions, and LOI of sediments present at Pirata-Pont-Piqueta System.**

| Core | Sample Number | Depth (cm) | Color | | LOI (%) |
|---|---|---|---|---|---|
| | | | moist | dry | |
| PP-00 | | | | | |
| | 01 | 0–2.5 | 5YR4/6 | – | – |
| | 02 | 2.5–4 | 7.5YR6/8 | – | – |
| PP-01 | | | | | |
| | 01 | 0–3 | 2.5YR5/8 | 7.5YR6/6 | 6.27 |
| | 02 | 3–9 | 7.5YR5/8 | 7.5YR7/6 | 5.08 |
| | 03 | 9–15 | 7.5YR5/8 | 7.5YR7/6 | 6.60 |
| | 04 | 15–20 | 2.5YR3/6 | 7.5YR5/8 | 3.11 |
| | 05 | 20–26 | 2.5YR3/6 | 7.5YR5/8 | 2.37 |
| PP-02 | | | | | |
| | 01 | 0–3 | 7.5YR5/8 | 7.5YR7/6 | 7.63 |
| | 02 | 3–3.5 | 5YR4/6 | 7.5YR6/6 | 2.86 |
| | 03 | 3.5–7 | 7.5YR5/8 | 7.5YR7/6 | 3.89 |
| | 04 | 7–13.5 | 7.5YR6/8 | 7.5YR8/4 | 3.34 |
| | 05 | 13.5–21 | 7.5YR6/6 | 10YR7/6 | 2.52 |
| | 06 | 21–23 | 7.5YR7/6 | 7.5YR8/4 | 2.77 |
| | 07 | 23–25 | 7.5YR6/6 | – | |
| PP-03 | | | | | |
| | 01 | 0–3 | 2.5YR3/3 | 7.5YR5/6 | 4.34 |
| PP-04 | | | | | |
| | 01 | 0–4 | 5YR4/6 | 7.5YR6/6 | 1.76 |
| | 02 | 4–9 | 5YR4/6 | 7.5YR6/6 | 1.90 |
| PP05 | | | | | |
| | 01 | 0–7 | 2.5YR4/6 | 7.5YR5/6 | 4.07 |
| | 02 | 7–13 | 2.5YR4/6 | 7.5YR5/6 | 3.39 |
| | 03 | 13–16 | 2.5YR4/6 | 7.5YR6/6 | 3.07 |
| | 04 | 16–21 | 2.5YR4/6 | 7.5YR6/6 | 3.41 |
| PP-06 | | | | | |
| | 01 | 0–3 | 2.5YR4/6 | 5YR5/8 | 2.24 |
| | 02 | 3–5 | 2.5YR4/8 | 5YR5/8 | 2.44 |
| | 03 | 5–7.5 | 2.5YR4/6 | 5YR5/6 | 3.49 |
| | 04 | 7.5–11 | 2.5YR4/8 | 5YR5/6 | 3.07 |
| | 05 | 11–16 | 2.5YR4/8 | 5YR5/6 | 2.07 |
| PP-07 | | | | | |
| | 01 | 0–3 | 2.5YR3/6 | 7.5YR5/6 | 3.97 |
| | 02 | 3–7 | 2.5YR3/6 | 7.5YR5/6 | 3.31 |
| | 03 | 7–9.5 | 2.5YR3/4 | 7.5YR6/6 | 2.80 |
| | 04 | 9.5–12.5 | 5YR3/3 | 7.5YR6/6 | 4.60 |
| | 05 | 12.5–16.5 | 5YR3/4 | 7.5YR6/6 | 4.69 |
| | 06 | 16.5–19.5 | 5YR3/4 | 7.5YR6/6 | 4.66 |
| | 07 | 19.5–20.5 | 5YR3/4 | 7.5YR6/6 | 5.17 |
| | 08 | 20.5–22.5 | 5YR3/3 | 7.5YR5/4 | 4.43 |
| | 09 | 22.5–26 | 5YR2.5/2 | 7.5YR5/4 | 3.91 |
| | 10 | 26–34 | 5YR2.5/1 | 7.5YR6/4 | 4.09 |
| PP-08 | | | | | |
| | 01 | 0–3.5 | 2.5YR4/4 | 5YR5/6 | 5.26 |
| | 02 | 3.5–6 | 2.5YR4/6 | 7.5YR5/6 | 5.15 |
| | 03 | 6–12.5 | 2.5YR4/6 | 5YR5/8 | 4.65 |

**Table 1. Continued.**

| Core | Sample Number | Depth (cm) | Color | | LOI (%) |
|---|---|---|---|---|---|
| | | | moist | dry | |
| | 04 | 12.5–17.5 | 5YR3/4 | 7.5YR5/6 | 4.55 |
| | 05 | 17.5–25.5 | 5YR3/4 | 7.5YR5/6 | 4.74 |
| | 06 | 25.5–27.5 | 5YR3/4 | 7.5YR5/6 | 4.20 |
| | 07 | 27.5–32 | 5YR3/4 | 7.5YR5/6 | 5.22 |
| | 08 | 32–37 | 5YR3/3 | 7.5YR5/6 | 4.77 |
| PP-08bis | | | | | |
| | 09 | 37–45 | 7.5YR3/2 | 7.5YR5/6 | 7.06 |
| | 10 | 45–53 | 10YR3/3 | 7.5YR5/4 | 7.59 |
| | 11 | 53–62 | 10YR3/3 | 7.5YR6/4 | 6.81 |
| PP-09 | | | | | |
| | 01 | 0–10 | 2.5YR4/8 | 5YR5/6 | 4.45 |
| PP-11 | | | | | |
| | 01 | surface | 7.5YR4/6 | 5YR4/6 | 12.50 |
| PP-12 | | | | | |
| | 01 | 0–10 | 7.5YR7/8 | 7.5YR7/6 | 1.09 |
| | 02 | 10–20 | 7.5YR7/8 | 7.5YR7/4 | 1.36 |
| | 03 | 20–30 | 7.5YR7/8 | 7.5YR7/6 | 1.18 |
| | 04 | 30–40 | 7.5YR7/8 | 7.5YR8/4 | 1.53 |

**Table 2. Sample color, in dry and wet conditions, and LOI of sediments present at Cova de sa Gleda passages.**

| Core | Sample Number | Depth (cm) | Color | | LOI (%) |
|---|---|---|---|---|---|
| | | | moist | dry | |
| GL-01 | | | | | |
| | 01 | 0–5.5 | 2.5YR4/8 | 7.5YR6/4 | 9.43 |
| | 02 | 5.5–13 | 5YR4/6 | 7.5YR6/4 | 9.39 |
| | 03 | 13–17 | 5YR4/3 | 7.5YR6/6 | 9.80 |
| | 04 | 17–21 | 7.5YR3/3 | 10YR5/4 | 9.59 |
| | 05 | 21–26.5 | 7.5YR3/4 | 7.5YR6/3 | 11.03 |
| | 06 | 26.5–30 | 10R4/8 | 7.5YR5/6 | 9.34 |
| | 07 | 30–36 | 2.5R4/4 | 7.5YR6/4 | 9.85 |
| | 08 | 36–39 | 5YR3/3 | 10YR5/4 | 9.68 |
| | 09 | 39–43.5 | 5YR3/3 | 7.5YR5/4 | 9.86 |
| | 10 | 43.5–46 | 5YR3/2 | 7.5YR5/4 | 10.91 |
| | 11 | 46–50 | 5YR3/3 | 10YR4/4 | 10.99 |
| | 12 | 50–51.8 | 2.5YR4/6 | – | – |
| | 13 | 51.8–52.5 | 2.5YR5/8 | 7.5YR5/6 | 10.03 |
| | 14 | 52.5–56.5 | 2.5YR4/6 | 7.5YR5/4 | 9.55 |
| | 15 | 56.5–60 | 7.5YR3/4 | 7.5YR5/6 | 9.35 |
| GL-02 | | | | | |
| | 01 | 0–4 | 2.5YR4/6 | 7.5YR5/6 | 9.66 |
| | 02 | 4–10 | 7.5YR4/4 | 10YR6/6 | 9.67 |
| | 03 | 10–14.5 | 7.5YR4/4 | 10YR6/6 | 8.78 |
| | 04 | 14.5–17 | 7.5YR4/3 | 10YR5/4 | 9.09 |
| | 05 | 17–20.5 | 7.5YR2.5/2 | 10YR5/4 | 9.49 |
| | 06 | 20.5–23 | 2.5Y3/3 | 10YR5/3 | 11.17 |
| | 07 | 23–24.5 | 2.5Y2.5/1 | 2.5Y5/3 | 8.72 |
| | 08 | 24.5–28 | 2.5YR4/3 | 2.5Y6/4 | 7.39 |
| | 09 | 28–29.5 | 5YR4/6 | 5YR6/8 | 4.54 |
| | 10F | 29.5–32 | 10YR8/6 | 10YR8/4 | 11.36 |
| | 11A | 32–34? | 7.5YR5/6 | 10YR7/4 | 11.54 |
| | 11F | – | – | – | – |
| GL-03 | | | | | |
| | 01 | 0–3 | 10YR3/2 | 10YR4/4 | 11.72 |
| | 02 | 3.5–5 | 5Y4/1 | 10YR5/1 | 15.38 |
| | 03 | 5–5.5 | 5Y7/1 | 10YR6/1 | – |
| | 04 | 5.5–6 | 5Y6/1 | 10YR6/1 | 18.57 |
| | 05 | 6–7 | 5Y5/1 | 2.5YR5/1 | 20.62 |
| | 06 | 7–10.5 | 5Y4/1 | 2.5YR6/1 | 14.81 |
| | 07 | 10.5–14 | 5Y3/1 | 2.5YR5/1 | 17.59 |
| | 08 | 14–17 | 5Y2.5/1 | 2.5YR5/1 | 21.50 |
| | 09 | 17–21 | 5Y4/1 | 2.5YR6/1 | 14.99 |
| | 10 | 21–24 | 5Y4/1 | 2.5YR6/1 | 15.88 |
| | 11 | 24–27 | 5Y4/1 | 2.5YR6/1 | 1.29 |
| | 12 | 27–31 | 5Y3/1 | 2.5YR5/1 | 13.93 |
| GL-04 | | | | | |
| | 01 | 0–2 | 7.5YR3/4 | 7.5YR5/6 | 14.47 |
| | 02 | 2–6 | 7.5YR4/6 | 7.5YR6/6 | 15.52 |
| | 03 | 6–7.5 | 7.5YR5/6 | 7.5YR6/6 | – |
| | 04 | 7.5–9.5 | 7.5YR6/6 | 7.5YR6/6 | 4.19 |
| | 05 | 9.5–13 | 10YR7/6 | 10YR7/6 | 3.40 |
| | 06 | 13–17.5 | 10YR7/6 | 10YR7/6 | 2.15 |
| | 07 | 17.5–20 | 10YR6/6 | 10YR5/6 | 9.28 |
| | 08 | 20–22.5 | 10YR5/6 | 10YR6/6 | 5.15 |

**Table 2. Continued.**

| Core | Sample Number | Depth (cm) | Color | | LOI (%) |
|---|---|---|---|---|---|
| | | | moist | dry | |
| GL-05 | | | | | |
| | 01 | 0–3 | 7.5YR4/6 | 5YR6/6 | – |
| | 02 | 3–4.5 | 5YR4/6 | 5YR6/6 | 15.32 |
| | 03 | 4.5–6.5 | 7.5YR5/6 | 7.5YR5/6 | 6.92 |
| | 04 | 6.5–9.5 | 2.5YR4/6 | 5YR5/8 | 7.90 |
| | 05 | 9.5–12 | 2.5YR4/6 | 5YR5/8 | 6.12 |
| GL-06 | | | | | |
| | 01 | 0–3.5 | 7.5YR6/6 | 10YR6/4 | 19.15 |
| | 02 | 3.5–6.5 | 5Y2.5/1 | 10YR4/1 | 20.63 |
| | 03 | 6.5–8.5 | 10YR5/4 | 10YR7/4 | 19.53 |
| | 04 | 8.5–10 | 5Y3/2 | 10YR5/2 | 21.43 |
| GL-07 | | | | | |
| | 01 | surface | 7.5YR4/4 | 7.5YR4/4 | 16.20 |
| GL-08 | | | | | |
| | 01 | 0–3.5 | 5YR5/6 | 7.5YR5/6 | 10.18 |
| | 02 | 3.5–9 | 5YR5/6 | 5YR6/6 | 6.65 |
| | 03 | 9–10.5 | 5YR4/6 | 7.5YR5/6 | 7.75 |
| | 03a | 10.5–11 | 5YR5/4 | 7.5YR5/4 | 5.13 |
| | 04 | 11–17 | 2.5YR4/6 | 7.5YR5/6 | 8.27 |
| | 05 | 17–20 | 2.5YR4/6 | 7.5YR6/6 | 7.57 |
| | 06 | 20–23 | 5YR4/6 | 7.5YR6/6 | 7.38 |
| | 07 | 23–27 | 5YR4/6 | 7.5YR6/6 | 7.63 |
| | 08 | 27–29 | 2.5YR4/6 | 7.5YR6/6 | 7.81 |
| | 09 | 29–31 | 2.5YR4/6 | 7.5YR5/6 | 7.47 |
| | 10 | 31–34 | 5YR4/6 | 7.5YR5/4 | 8.49 |
| | 11 | 34–36 | 5YR4/6 | 7.5YR6/6 | 8.06 |
| | 12 | 36–39 | 5YR4/6 | 7.5YR6/6 | 7.17 |
| | 13 | 39–42.5 | 2.5YR4/6 | 7.5YR6/6 | 7.07 |
| GL-09 | | | | | |
| | 01 | 0–5 | 7.5YR7/4 | 7.5YR8/2 | 20.77 |
| | 02 | 5–9 | 2.5YR6/6 | 5YR8/3 | 22.63 |
| | 03 | 9–12 | 10R6/6 | 5YR7/4 | 23.81 |
| | 04 | 12–16.5 | 10R6/6 | 5YR6/4 | 23.40 |
| | 05 | 16.5–20 | 10R6/4 | 5YR8/3 | 23.29 |
| GL-10 | | | | | |
| | 01 | 0–5 | 5YR8/3 | 5YR7/3 | 12.64 |
| | 01a | – | – | – | – |
| | 02 | 5–10 | 5YR8/3 | 5YR8/3 | 3.07 |
| | 03 | 10–15.5 | 5YR6/3 | 5YR7/3 | 9.72 |
| | 03a | – | – | – | – |
| | 04 | 15.5–21 | 5YR5/4 | 5YR7/3 | 12.13 |
| | 05 | 21–27 | 5YR4/4 | 5YR6/3 | 12.17 |
| | 06 | 27–31 | 2.5YR4/6 | 5YR6/3 | 12.74 |
| | 07 | 31–35 | 2.5YR4/4 | 2.5YR6/4 | 7.58 |
| | 07a | | N9 | N9 | – |
| | 08 | 35–36 | 5Y5/3 | 10R6/4 | 10.75 |
| | 09 | 36–40 | 2.5YR4/3 | 5YR7/3 | 5.17 |
| GL-11 | | | | | |
| | 01 | 0–6 | 2.5YR6/8 | 5YR7/4 | 4.02 |
| | 02 | 6–12 | 2.5YR6/8 | 5YR7/4 | 4.84 |

**Table. 3. Percentage values of the different textural parameters of sediments from Pirata-Pont-Piqueta system.**

| Core | Sample Number | Gravel (%) | Sand | | | | | Silt (%) | Clay (%) |
|---|---|---|---|---|---|---|---|---|---|
| | | | VCS (%) | CS (%) | MS (%) | FS (%) | VFS (%) | | |
| PP-00 | | | | | | | | | |
| | 01 | 85.00 | | | | | | 5.00 | ? |
| | 02 | 60.00 | | | | | | 25.00 | ? |
| PP-01 | | | | | | | | | |
| | 01 | 0.00 | 0.40 | 5.50 | 17.10 | 18.30 | 18.90 | 32.68 | 7.12 |
| | 02 | 0.00 | 0.68 | 7.20 | 17.80 | 13.00 | 14.80 | 35.10 | 11.40 |
| | 03 | 0.00 | 0.94 | 6.10 | 14.40 | 10.20 | 5.00 | 39.60 | 23.30 |
| | 04 | 0.00 | 0.00 | 0.00 | 0.06 | 0.40 | 1.50 | 81.40 | 16.60 |
| | 05 | 0.00 | 0.00 | 0.00 | 0.24 | 2.60 | 7.90 | 78.30 | 11.00 |
| PP-02 | | | | | | | | | |
| | 01 | 0.00 | 0.00 | 0.00 | 0.00 | 2.11 | 13.90 | 69.30 | 14.70 |
| | 02 | 0.00 | 0.20 | 3.00 | 10.40 | 11.70 | 13.50 | 50.80 | 10.40 |
| | 03 | 0.00 | 3.98 | 18.40 | 16.40 | 6.60 | 9.30 | 35.20 | 10.10 |
| | 04 | 0.00 | 0.00 | 0.11 | 8.10 | 19.50 | 21.70 | 43.52 | 7.08 |
| | 05 | 0.00 | 2.90 | 11.80 | 22.70 | 13.70 | 12.10 | 32.87 | 4.34 |
| | 06 | 0.00 | 0.00 | 0.35 | 14.10 | 27.00 | 18.90 | 35.77 | 3.93 |
| PP-03 | | | | | | | | | |
| | 01 | 0.00 | 0.00 | 0.00 | 0.00 | 0.00 | 0.00 | 80.21 | 19.80 |
| PP-04 | | | | | | | | | |
| | 01 | 0.00 | 0.00 | 0.00 | 0.19 | 2.70 | 6.00 | 83.85 | 7.25 |
| | 02 | 0.00 | 0.00 | 0.00 | 0.12 | 2.60 | 7.40 | 81.17 | 8.73 |
| PP-05 | | | | | | | | | |
| | 01 | 0.00 | 0.00 | 0.38 | 1.60 | 3.20 | 2.90 | 74.30 | 17.60 |
| | 02 | 0.00 | 0.00 | 0.00 | 0.46 | 5.40 | 3.30 | 72.80 | 18.00 |
| | 03 | 0.00 | 0.00 | 0.00 | 0.06 | 4.70 | 2.50 | 73.40 | 19.30 |
| | 04 | 0.00 | 0.00 | 0.00 | 0.01 | 0.50 | 2.00 | 78.20 | 19.30 |
| PP-06 | | | | | | | | | |
| | 01 | 0.00 | 0.00 | 0.00 | 0.01 | 1.28 | 3.20 | 66.50 | 29.00 |
| | 02 | 0.00 | 0.00 | 0.00 | 0.00 | 0.00 | 0.04 | 52.80 | 47.20 |
| | 03 | 0.00 | 0.00 | 0.00 | 0.00 | 0.00 | 0.00 | 50.51 | 49.50 |
| | 04 | 0.00 | 0.00 | 0.00 | 0.00 | 0.00 | 0.00 | 50.41 | 49.60 |
| | 05 | 0.00 | 0.00 | 0.00 | 0.00 | 0.00 | 0.00 | 39.87 | 60.10 |
| PP-07 | | | | | | | | | |
| | 01 | 0.00 | 0.00 | 0.00 | 0.00 | 0.00 | 0.04 | 84.16 | 15.80 |
| | 02 | 0.00 | 0.00 | 0.00 | 0.00 | 0.00 | 0.67 | 87.20 | 12.10 |
| | 03 | 0.00 | 0.00 | 0.27 | 0.70 | 1.10 | 4.30 | 81.90 | 11.70 |
| | 04 | 0.00 | 0.00 | 0.00 | 0.00 | 0.00 | 0.14 | 85.00 | 14.90 |
| | 05 | 0.00 | 0.00 | 0.07 | 0.75 | 1.40 | 2.80 | 79.40 | 15.60 |
| | 06 | 0.00 | 0.00 | 0.00 | 0.93 | 2.30 | 3.30 | 76.90 | 16.60 |
| | 07 | 0.00 | 0.00 | 0.00 | 0.28 | 2.00 | 3.00 | 80.30 | 14.40 |
| | 08 | 0.00 | 0.00 | 0.00 | 0.01 | 0.61 | 1.60 | 81.60 | 16.20 |
| | 09 | 0.00 | 0.00 | 0.08 | 0.16 | 2.30 | 3.80 | 78.40 | 15.20 |
| | 10 | 0.00 | 0.00 | 0.00 | 0.06 | 1.80 | 2.60 | 77.60 | 17.90 |
| PP-08 | | | | | | | | | |
| | 01 | 0.00 | 0.00 | 0.16 | 0.90 | 3.20 | 7.20 | 75.60 | 12.90 |
| | 02 | 0.00 | 0.00 | 0.00 | 0.05 | 2.75 | 5.20 | 73.60 | 18.40 |
| | 03 | 0.00 | 0.00 | 0.00 | 0.00 | 0.00 | 0.00 | 80.75 | 19.20 |
| | 04 | 0.00 | 0.00 | 0.00 | 0.01 | 0.61 | 2.30 | 79.30 | 17.80 |
| | 05 | 0.00 | 0.00 | 0.00 | 0.42 | 1.80 | 3.70 | 76.00 | 18.10 |
| | 06 | 0.00 | 0.00 | 0.00 | 0.04 | 1.63 | 2.70 | 77.10 | 18.50 |
| | 07 | 0.00 | 0.00 | 0.00 | 0.00 | 0.00 | 0.00 | 80.30 | 19.70 |

**Table 3. Continued.**

| Core | Sample Number | Gravel (%) | Sand | | | | | Silt (%) | Clay (%) |
|---|---|---|---|---|---|---|---|---|---|
| | | | VCS (%) | CS (%) | MS (%) | FS (%) | VFS (%) | | |
| | 08 | 0.00 | 0.00 | 0.00 | 0.43 | 2.80 | 2.50 | 77.10 | 17.20 |
| PP-08bis | | | | | | | | | |
| | 09 | 0.00 | 0.00 | 0.00 | 0.11 | 2.05 | 3.50 | 78.00 | 16.30 |
| | 10 | 0.00 | 0.00 | 0.01 | 2.23 | 7.60 | 5.50 | 70.90 | 14.00 |
| | 11 | 0.00 | 0.00 | 0.00 | 0.00 | 0.00 | 0.00 | 81.27 | 18.70 |
| PP-09 | | | | | | | | | |
| | 01 | 0.00 | 0.00 | 0.00 | 0.00 | 0.00 | 0.00 | 61.18 | 38.80 |
| PP-11 | | | | | | | | | |
| | 01 | 0.00 | 0.00 | 0.00 | 0.44 | 8.90 | 17.80 | 67.44 | 5.46 |
| PP-12 | | | | | | | | | |
| | 01 | 0.00 | 0.00 | 11.80 | 38.50 | 16.90 | 11.60 | 18.57 | 2.63 |
| | 02 | 0.00 | 0.00 | 3.60 | 15.60 | 17.10 | 20.50 | 36.73 | 6.47 |
| | 03 | 0.00 | 0.77 | 6.80 | 12.90 | 7.80 | 14.30 | 50.40 | 7.31 |
| | 04 | 0.00 | 0.55 | 5.08 | 8.90 | 4.80 | 19.60 | 56.71 | 4.39 |

**Table. 4. Percentage values of the different textural parameters of sediments from Cova de sa Gleda.**

| Core | Sample Number | Gravel (%) | Sand | | | | | Silt (%) | Clay (%) |
|---|---|---|---|---|---|---|---|---|---|
| | | | VCS (%) | CS (%) | MS (%) | FS (%) | VFS (%) | | |
| GL-01 | | | | | | | | | |
| | 01 | 0.00 | 0.00 | 0.00 | 0.00 | 0.00 | 0.01 | 53.29 | 46.70 |
| | 02 | 0.00 | 0.00 | 0.00 | 0.00 | 1.20 | 5.80 | 53.50 | 39.50 |
| | 03 | 0.00 | 0.00 | 0.00 | 0.00 | 0.00 | 0.00 | 50.30 | 49.70 |
| | 04 | 0.00 | 0.00 | 0.00 | 0.00 | 1.00 | 1.90 | 46.80 | 50.30 |
| | 05 | 0.00 | 0.00 | 0.00 | 0.00 | 1.00 | 2.20 | 55.20 | 41.60 |
| | 06 | 0.00 | 0.00 | 0.00 | 0.00 | 1.10 | 6.30 | 53.80 | 38.80 |
| | 07 | 0.00 | 0.00 | 0.00 | 0.00 | 0.60 | 6.60 | 56.80 | 36.00 |
| | 08 | 0.00 | 0.00 | 0.00 | 0.00 | 0.20 | 1.80 | 49.50 | 48.50 |
| | 09 | 0.00 | 0.00 | 0.00 | 0.00 | 0.00 | 1.50 | 54.60 | 43.90 |
| | 10 | 0.00 | 0.00 | 0.00 | 0.00 | 2.00 | 6.80 | 64.60 | 26.60 |
| | 11 | 0.00 | 0.00 | 0.00 | 0.00 | 0.00 | 2.00 | 52.80 | 45.20 |
| | 12 | – | – | – | – | – | – | – | – |
| | 13 | 0.00 | 0.00 | 0.00 | 0.80 | 3.90 | 7.50 | 53.60 | 34.20 |
| | 14 | 0.00 | 0.00 | 0.00 | 0.00 | 0.30 | 2.10 | 55.10 | 42.50 |
| | 15 | 0.00 | 0.00 | 0.00 | 0.00 | 0.10 | 1.80 | 47.50 | 50.60 |
| GL-02 | | | | | | | | | |
| | 01 | 0.00 | 0.00 | 0.00 | 0.00 | 0.30 | 5.90 | 51.80 | 42.00 |
| | 02 | 0.00 | 0.00 | 0.00 | 0.00 | 0.20 | 3.10 | 57.00 | 39.70 |
| | 03 | 0.00 | 0.00 | 0.00 | 0.00 | 0.00 | 3.30 | 51.30 | 45.40 |
| | 04 | 0.00 | 0.00 | 0.00 | 0.00 | 1.10 | 2.00 | 50.60 | 46.30 |
| | 05 | 0.00 | 0.00 | 0.00 | 0.00 | 0.70 | 3.40 | 55.40 | 40.50 |
| | 06 | 0.00 | 0.00 | 0.00 | 0.00 | 2.20 | 11.80 | 59.70 | 26.30 |
| | 07 | 0.00 | 0.00 | 0.00 | 0.00 | 2.00 | 9.20 | 64.30 | 24.50 |
| | 08 | 0.00 | 0.00 | 0.00 | 0.00 | 0.30 | 5.60 | 56.20 | 37.90 |
| | 09 | 0.00 | 0.00 | 0.00 | 0.00 | 0.10 | 1.60 | 52.10 | 46.20 |
| | 10F | 0.00 | 0.00 | 0.00 | 0.00 | 0.20 | 1.00 | 67.20 | 31.60 |
| | 11A | – | – | – | – | – | – | – | – |
| | 11F | 0.00 | 0.00 | 0.00 | 0.00 | 0.00 | 1.00 | 69.90 | 29.10 |
| GL-03 | | | | | | | | | |
| | 01 | 0.00 | 0.00 | 0.00 | 0.00 | 2.50 | 17.30 | 70.90 | 9.30 |
| | 02 | 0.00 | 0.00 | 0.00 | 0.00 | 2.70 | 19.00 | 69.20 | 9.10 |
| | 03 | 0.00 | 0.00 | 0.00 | 0.00 | 6.00 | 25.40 | 60.50 | 8.10 |
| | 04 | 0.00 | 1.70 | 4.50 | 9.90 | 14.80 | 26.00 | 39.37 | 3.73 |
| | 05 | 0.00 | 0.00 | 0.00 | 0.00 | 6.40 | 28.20 | 57.60 | 7.80 |
| | 06 | 0.00 | 0.00 | 0.00 | 0.10 | 8.00 | 30.30 | 53.19 | 8.41 |
| | 07 | 0.00 | 0.00 | 1.10 | 9.10 | 20.00 | 22.70 | 40.25 | 6.85 |
| | 08 | 0.00 | 3.60 | 14.80 | 22.90 | 15.20 | 14.00 | 25.59 | 3.91 |
| | 09 | 0.00 | 0.00 | 0.00 | 0.10 | 10.60 | 31.10 | 50.29 | 7.91 |
| | 10 | 0.00 | 0.00 | 0.10 | 3.60 | 15.30 | 26.60 | 46.83 | 7.57 |
| | 11 | 0.00 | 0.00 | 0.40 | 7.60 | 19.80 | 23.40 | 42.52 | 6.28 |
| | 12 | 0.00 | 0.00 | 0.40 | 8.80 | 19.80 | 23.50 | 41.61 | 5.89 |
| GL-04 | | | | | | | | | |
| | 01 | 0.00 | 0.00 | 0.30 | 4.20 | 14.50 | 27.10 | 46.72 | 7.18 |
| | 02 | 0.00 | 0.00 | 0.00 | 0.00 | 5.90 | 24.50 | 61.13 | 8.47 |
| | 03 | 0.00 | 0.00 | 0.00 | 0.10 | 7.40 | 24.00 | 61.27 | 7.23 |
| | 04 | 0.00 | 3.60 | 9.70 | 16.70 | 12.90 | 16.40 | 36.22 | 4.48 |
| | 05 | 0.00 | 1.10 | 9.60 | 16.60 | 17.50 | 18.50 | 34.68 | 2.02 |
| | 06 | 0.00 | 0.00 | 3.20 | 14.80 | 24.80 | 23.10 | 31.87 | 2.23 |
| | 07 | 0.00 | 0.20 | 1.30 | 6.30 | 11.00 | 25.60 | 50.75 | 4.85 |
| | 08 | 0.00 | 1.60 | 5.00 | 7.00 | 11.90 | 25.40 | 44.44 | 4.66 |

**Table 4. Continued.**

| Core | Sample Number | Gravel (%) | Sand | | | | | Silt (%) | Clay (%) |
|---|---|---|---|---|---|---|---|---|---|
| | | | VCS (%) | CS (%) | MS (%) | FS (%) | VFS (%) | | |
| GL-05 | | | | | | | | | |
| | 01 | – | – | – | – | – | – | – | – |
| | 02 | 0.00 | 0.00 | 0.00 | 0.00 | 4.90 | 17.50 | 67.00 | 10.60 |
| | 03 | 19.13 | 21.44 | 21.47 | 16.88 | 9.94 | 1.48 | 3.48 | 0.32 |
| | 04 | 0.00 | 0.00 | 0.00 | 0.00 | 4.50 | 19.40 | 67.95 | 8.15 |
| | 05 | 0.00 | 0.00 | 0.00 | 0.00 | 2.60 | 15.60 | 73.15 | 8.65 |
| GL-06 | | | | | | | | | |
| | 01 | 0.00 | 0.90 | 4.80 | 10.10 | 15.00 | 22.00 | 41.31 | 5.89 |
| | 02 | 0.30 | 11.00 | 23.00 | 18.10 | 10.40 | 10.90 | 23.36 | 2.94 |
| | 03 | 0.00 | 0.00 | 1.30 | 10.10 | 18.80 | 24.10 | 39.70 | 6.00 |
| | 04 | 0.00 | 3.50 | 13.00 | 18.10 | 14.80 | 14.90 | 31.41 | 4.29 |
| GL-07 | | | | | | | | | |
| | 01 | 0.00 | 0.00 | 0.00 | 1.80 | 5.10 | 7.40 | 49.30 | 36.40 |
| GL-08 | | | | | | | | | |
| | 01 | 0.00 | 0.00 | 0.00 | 0.00 | 2.60 | 19.80 | 69.24 | 8.36 |
| | 02 | 0.00 | 0.00 | 0.00 | 0.00 | 5.50 | 26.80 | 60.30 | 7.40 |
| | 03 | 0.00 | 0.00 | 0.00 | 0.00 | 2.10 | 19.20 | 69.45 | 9.25 |
| | 03a | 0.00 | 0.00 | 0.00 | 0.00 | 1.90 | 22.90 | 67.80 | 7.40 |
| | 04 | 0.00 | 0.00 | 0.00 | 0.00 | 5.10 | 25.90 | 61.36 | 7.64 |
| | 05 | 0.00 | 0.00 | 0.00 | 0.00 | 2.90 | 23.30 | 65.81 | 7.99 |
| | 06 | 0.00 | 0.00 | 0.00 | 0.00 | 4.10 | 23.90 | 63.63 | 8.37 |
| | 07 | 0.00 | 0.00 | 0.00 | 0.00 | 4.40 | 25.10 | 62.10 | 8.40 |
| | 08 | 0.00 | 0.00 | 0.00 | 0.00 | 1.60 | 17.90 | 70.60 | 9.90 |
| | 09 | 0.00 | 0.00 | 0.00 | 0.00 | 1.60 | 17.50 | 70.50 | 10.40 |
| | 10 | 0.00 | 0.00 | 0.10 | 3.10 | 9.60 | 22.10 | 56.18 | 8.92 |
| | 11 | 0.00 | 0.00 | 0.00 | 0.00 | 5.30 | 21.00 | 64.75 | 8.95 |
| | 12 | 0.00 | 0.00 | 0.00 | 0.00 | 1.30 | 16.80 | 71.97 | 9.93 |
| | 13 | 0.00 | 0.00 | 0.00 | 0.00 | 2.90 | 21.50 | 66.41 | 9.19 |
| GL-09 | | | | | | | | | |
| | 01 | 0.00 | 0.50 | 5.10 | 9.60 | 8.20 | 14.10 | 51.50 | 11.00 |
| | 02 | 0.00 | 1.90 | 8.90 | 11.10 | 7.60 | 14.20 | 47.32 | 8.98 |
| | 03 | 0.00 | 0.00 | 0.60 | 5.20 | 6.70 | 21.30 | 56.62 | 9.58 |
| | 04 | 0.00 | 0.00 | 0.50 | 3.70 | 7.90 | 23.30 | 55.73 | 8.87 |
| | 05 | 0.00 | 0.00 | 1.10 | 8.60 | 7.20 | 18.10 | 55.83 | 9.17 |
| GL-10 | | | | | | | | | |
| | 01 | – | – | – | – | – | – | – | – |
| | 01a | – | – | – | – | – | – | – | – |
| | 02 | – | – | – | – | – | – | – | – |
| | 03 | – | – | – | – | – | – | – | – |
| | 03a | – | – | – | – | – | – | – | – |
| | 04 | – | – | – | – | – | – | – | – |
| | 05 | 0.00 | 0.00 | 0.20 | 5.10 | 11.80 | 26.40 | 51.06 | 5.44 |
| | 06 | – | – | – | – | – | – | – | – |
| | 07 | – | – | – | – | – | – | – | – |
| | 07a | – | – | – | – | – | – | – | – |
| | 08 | 0.00 | 0.00 | 0.00 | 0.00 | 6.60 | 28.50 | 58.56 | 6.34 |
| | 09 | – | – | – | – | – | – | – | – |
| GL-11 | | | | | | | | | |
| | 01 | 0.00 | 14.16 | 37.30 | 18.60 | 7.80 | 3.40 | 10.48 | 8.26 |
| | 02 | 0.00 | 6.20 | 28.30 | 26.41 | 11.80 | 5.50 | 12.60 | 9.19 |

**Table. 5. Textural statistical parameters of sediments from Pirata-Pont-Piqueta system.**

| Core | Sample Number | Mean (μm) | Median (μm) | m/M | Mode (μm) | S.D. (μm) | Skewness |
|---|---|---|---|---|---|---|---|
| PP-00 | | | | | | | |
| | 01 | | | | | | |
| | 02 | | | | | | |
| PP-01 | | | | | | | |
| | 01 | 161.80 | 94.77 | 1.71 | 170.80 | 188.20 | 1.86 |
| | 02 | 168.00 | 74.32 | 2.26 | 361.80 | 216.00 | 1.88 |
| | 03 | 134.50 | 10.72 | 12.55 | 291.90 | 223.30 | 2.28 |
| | 04 | 12.44 | 7.78 | 1.61 | 10.52 | 18.67 | 5.25 |
| | 05 | 27.96 | 16.14 | 1.73 | 30.73 | 36.05 | 3.04 |
| PP-02 | | | | | | | |
| | 01 | 28.64 | 13.86 | 2.07 | 17.98 | 35.01 | 1.71 |
| | 02 | 102.90 | 29.64 | 3.47 | 137.80 | 159.60 | 2.55 |
| | 03 | 272.90 | 91.22 | 2.99 | 618.40 | 343.80 | 1.55 |
| | 04 | 92.35 | 60.43 | 1.53 | 170.80 | 94.05 | 1.29 |
| | 05 | 248.70 | 139.40 | 1.78 | 361.80 | 295.00 | 1.97 |
| | 06 | 124.60 | 95.25 | 1.31 | 211.60 | 111.80 | 1.26 |
| PP-03 | | | | | | | |
| | 01 | 7.69 | 5.51 | 1.40 | 8.49 | 6.84 | 1.37 |
| PP-04 | | | | | | | |
| | 01 | 29.66 | 20.90 | 1.42 | 27.61 | 34.58 | 3.28 |
| | 02 | 27.92 | 17.12 | 1.63 | 27.61 | 34.29 | 2.95 |
| PP-05 | | | | | | | |
| | 01 | 24.30 | 6.28 | 3.87 | 6.85 | 62.77 | 4.95 |
| | 02 | 21.66 | 5.99 | 3.62 | 6.85 | 46.13 | 3.29 |
| | 03 | 17.71 | 5.54 | 3.20 | 6.85 | 39.29 | 3.60 |
| | 04 | 10.23 | 5.49 | 1.86 | 7.63 | 17.70 | 5.27 |
| PP-06 | | | | | | | |
| | 01 | 11.40 | 4.29 | 2.65 | 5.53 | 24.46 | 4.53 |
| | 02 | 4.10 | 2.18 | 1.88 | 1.11 | 5.79 | 4.33 |
| | 03 | 2.90 | 2.02 | 1.43 | 1.53 | 2.41 | 1.52 |
| | 04 | 2.76 | 2.02 | 1.37 | 1.37 | 2.14 | 1.18 |
| | 05 | 2.16 | 1.60 | 1.35 | 1.23 | 1.62 | 1.34 |
| PP-07 | | | | | | | |
| | 01 | 11.16 | 7.73 | 1.44 | 10.52 | 10.73 | 1.59 |
| | 02 | 15.53 | 10.52 | 1.48 | 11.71 | 14.58 | 1.28 |
| | 03 | 23.71 | 11.10 | 2.14 | 10.52 | 47.69 | 6.76 |
| | 04 | 12.13 | 7.84 | 1.55 | 9.45 | 12.14 | 1.58 |
| | 05 | 18.85 | 7.60 | 2.38 | 9.45 | 40.20 | 6.55 |
| | 06 | 20.07 | 7.58 | 2.65 | 9.45 | 41.58 | 4.66 |
| | 07 | 17.39 | 7.93 | 2.19 | 9.45 | 32.63 | 4.78 |
| | 08 | 11.48 | 6.40 | 1.79 | 8.49 | 19.20 | 5.98 |
| | 09 | 17.89 | 7.15 | 2.50 | 8.49 | 37.98 | 5.92 |
| | 10 | 13.60 | 5.88 | 2.31 | 7.63 | 26.53 | 4.71 |
| PP-08 | | | | | | | |
| | 01 | 28.06 | 10.19 | 2.75 | 9.45 | 51.58 | 4.61 |
| | 02 | 18.97 | 6.98 | 2.72 | 8.49 | 33.75 | 3.39 |
| | 03 | 9.09 | 6.02 | 1.51 | 8.49 | 8.96 | 1.64 |
| | 04 | 12.76 | 6.39 | 2.00 | 8.49 | 20.33 | 5.00 |
| | 05 | 17.26 | 6.45 | 2.68 | 7.63 | 34.49 | 4.80 |
| | 06 | 14.14 | 6.01 | 2.35 | 7.63 | 27.15 | 4.66 |
| | 07 | 8.13 | 5.49 | 1.48 | 7.63 | 8.09 | 1.91 |
| | 08 | 17.85 | 6.86 | 2.60 | 8.49 | 35.77 | 4.51 |

**Table 5. Continued.**

| Core | Sample Number | Mean (μm) | Median (μm) | m/M | Mode (μm) | S.D. (μm) | Skewness |
|---|---|---|---|---|---|---|---|
| PP-08bis | | | | | | | |
| | 09 | 17.35 | 6.97 | 2.49 | 8.49 | 31.02 | 4.11 |
| | 10 | 34.55 | 7.94 | 4.35 | 7.63 | 64.49 | 2.73 |
| | 11 | 7.08 | 5.13 | 1.38 | 6.16 | 6.11 | 1.42 |
| PP-09 | | | | | | | |
| | 01 | 4.00 | 2.83 | 1.41 | 4.97 | 3.42 | 1.35 |
| PP-11 | | | | | | | |
| | 01 | 48.21 | 29.12 | 1.66 | 38.08 | 52.59 | 1.68 |
| PP-12 | | | | | | | |
| | 01 | 267.60 | 250.60 | 1.07 | 361.80 | 206.30 | 0.64 |
| | 02 | 138.70 | 77.98 | 1.78 | 72.46 | 158.20 | 1.75 |
| | 03 | 142.90 | 44.82 | 3.19 | 58.48 | 215.00 | 2.25 |
| | 04 | 116.00 | 44.23 | 2.62 | 65.10 | 189.80 | 2.88 |

**Table. 6. Textural statistical parameters of sediments from Cova de sa Gleda.**

| Core | Sample Number | Mean (μm) | Median (μm) | m/M | Mode (μm) | S.D. (μm) | Skewness |
|---|---|---|---|---|---|---|---|
| GL-01 | | | | | | | |
| | 01 | 7.56 | 4.36 | 1.74 | 4.44 | 8.98 | 2.46 |
| | 02 | 15.14 | 5.65 | 2.68 | 4.44 | 22.57 | 2.45 |
| | 03 | 6.35 | 4.03 | 1.58 | 4.44 | 6.81 | 2.20 |
| | 04 | 8.41 | 3.87 | 2.18 | 4.05 | 14.29 | 4.12 |
| | 05 | 14.60 | 5.42 | 2.69 | 4.88 | 26.76 | 3.71 |
| | 06 | 17.23 | 5.76 | 2.99 | 4.05 | 26.37 | 2.49 |
| | 07 | 17.30 | 6.64 | 2.61 | 4.88 | 25.08 | 2.38 |
| | 08 | 8.94 | 4.16 | 2.15 | 4.05 | 15.43 | 4.38 |
| | 09 | 9.37 | 4.70 | 1.99 | 4.44 | 13.49 | 3.35 |
| | 10 | 22.21 | 10.48 | 2.12 | 12.40 | 30.10 | 2.51 |
| | 11 | 9.99 | 4.56 | 2.19 | 4.44 | 14.39 | 2.68 |
| | 12 | – | – | – | – | – | – |
| | 13 | 26.00 | 6.90 | 3.77 | 4.44 | 46.65 | 3.16 |
| | 14 | 10.90 | 4.93 | 2.21 | 4.44 | 17.41 | 3.74 |
| | 15 | 8.59 | 3.94 | 2.18 | 4.05 | 15.66 | 4.63 |
| GL-02 | | | | | | | |
| | 01 | 14.96 | 5.13 | 2.92 | 4.05 | 23.43 | 2.55 |
| | 02 | 12.29 | 5.51 | 2.23 | 5.36 | 18.74 | 3.24 |
| | 03 | 11.38 | 4.56 | 2.50 | 4.05 | 17.51 | 2.89 |
| | 04 | 10.90 | 4.40 | 2.48 | 4.05 | 22.22 | 4.76 |
| | 05 | 13.35 | 5.31 | 2.52 | 4.44 | 21.58 | 3.32 |
| | 06 | 26.92 | 11.13 | 2.42 | 9.37 | 34.26 | 1.83 |
| | 07 | 24.78 | 11.20 | 2.21 | 10.29 | 32.40 | 2.18 |
| | 08 | 16.77 | 5.97 | 2.81 | 4.44 | 26.27 | 2.70 |
| | 09 | 9.88 | 4.49 | 2.20 | 4.05 | 14.96 | 3.48 |
| | 10F | 10.56 | 7.02 | 1.50 | 10.29 | 13.39 | 4.26 |
| | 11A | – | – | – | – | – | – |
| | 11F | 11.48 | 7.32 | 1.57 | 9.37 | 12.73 | 2.42 |
| GL-03 | | | | | | | |
| | 01 | 39.16 | 31.71 | 1.24 | 41.68 | 33.01 | 1.21 |
| | 02 | 40.03 | 31.93 | 1.25 | 50.22 | 33.93 | 1.13 |
| | 03 | 49.00 | 39.67 | 1.24 | 66.44 | 40.84 | 0.97 |
| | 04 | 149.10 | 75.47 | 1.98 | 80.07 | 216.30 | 3.26 |
| | 05 | 51.41 | 42.98 | 1.20 | 72.94 | 41.32 | 0.80 |
| | 06 | 54.59 | 46.26 | 1.18 | 87.90 | 44.12 | 0.75 |
| | 07 | 104.60 | 70.34 | 1.49 | 116.30 | 113.00 | 1.79 |
| | 08 | 274.90 | 166.20 | 1.65 | 429.20 | 294.90 | 1.63 |
| | 09 | 58.76 | 49.65 | 1.18 | 96.49 | 46.90 | 0.66 |
| | 10 | 75.77 | 54.88 | 1.38 | 105.90 | 78.89 | 2.19 |
| | 11 | 96.35 | 65.65 | 1.47 | 127.60 | 99.33 | 1.68 |
| | 12 | 100.80 | 68.11 | 1.48 | 127.60 | 103.30 | 1.71 |
| GL-04 | | | | | | | |
| | 01 | 78.95 | 56.49 | 1.40 | 96.49 | 84.13 | 2.34 |
| | 02 | 48.55 | 39.28 | 1.24 | 60.52 | 40.36 | 1.00 |
| | 03 | 50.82 | 39.66 | 1.28 | 55.13 | 42.91 | 1.09 |
| | 04 | 208.30 | 93.59 | 2.23 | 429.20 | 268.50 | 2.16 |
| | 05 | 195.80 | 104.90 | 0.87 | 127.60 | 227.20 | 1.95 |
| | 06 | 145.90 | 105.10 | 1.39 | 140.10 | 139.40 | 1.51 |
| | 07 | 90.47 | 54.91 | 1.65 | 66.44 | 121.10 | 3.75 |
| | 08 | 135.80 | 64.57 | 2.10 | 87.90 | 214.80 | 3.25 |
| GL-05 | | | | | | | |
| | 01 | – | – | – | – | – | – |

**Table 6. Continued.**

| Core | Sample Number | Mean (μm) | Median (μm) | m/M | Mode (μm) | S.D. (μm) | Skewness |
|---|---|---|---|---|---|---|---|
| | 02 | 41.38 | 3.78 | 1.35 | 41.68 | 38.44 | 1.31 |
| | 03 | 79.68 | 46.85 | 1.70 | 37.97 | 95.48 | 2.45 |
| | 04 | 43.30 | 33.47 | 1.29 | 41.68 | 37.45 | 1.26 |
| | 05 | 37.94 | 29.58 | 1.28 | 34.58 | 32.74 | 1.37 |
| GL-06 | | | | | | | |
| | 01 | 136.70 | 69.29 | 1.97 | 105.90 | 190.60 | 2.84 |
| | 02 | 438.50 | 297.30 | 1.48 | 567.70 | 463.00 | 1.30 |
| | 03 | 108.70 | 72.35 | 1.50 | 116.30 | 116.20 | 1.80 |
| | 04 | 246.80 | 121.70 | 2.03 | 471.10 | 294.90 | 1.81 |
| GL-07 | | | | | | | |
| | 01 | 31.82 | 8.40 | 3.79 | 31.50 | 55.56 | 2.93 |
| GL-08 | | | | | | | |
| | 01 | 41.30 | 33.59 | 1.23 | 45.75 | 33.55 | 1.07 |
| | 02 | 50.20 | 41.91 | 1.20 | 60.52 | 39.28 | 0.87 |
| | 03 | 39.80 | 32.34 | 1.23 | 45.75 | 32.80 | 1.07 |
| | 03a | 43.67 | 38.74 | 1.13 | 50.22 | 32.15 | 0.81 |
| | 04 | 49.04 | 40.78 | 1.20 | 60.52 | 38.73 | 0.89 |
| | 05 | 44.35 | 37.05 | 1.20 | 55.13 | 34.84 | 0.91 |
| | 06 | 46.15 | 38.00 | 1.21 | 55.13 | 37.10 | 0.95 |
| | 07 | 47.17 | 38.97 | 1.21 | 60.52 | 37.69 | 0.89 |
| | 08 | 38.19 | 31.35 | 1.22 | 45.75 | 31.52 | 1.06 |
| | 09 | 37.51 | 30.28 | 1.24 | 41.68 | 31.50 | 1.09 |
| | 10 | 62.82 | 40.28 | 1.56 | 55.13 | 73.95 | 2.73 |
| | 11 | 45.42 | 35.73 | 1.27 | 45.75 | 39.16 | 1.19 |
| | 12 | 37.28 | 31.28 | 1.19 | 45.75 | 30.24 | 1.05 |
| | 13 | 42.64 | 35.22 | 1.21 | 50.22 | 34.68 | 0.99 |
| GL-09 | | | | | | | |
| | 01 | 115.10 | 37.22 | 3.09 | 34.58 | 186.60 | 2.59 |
| | 02 | 163.30 | 49.27 | 3.31 | 50.22 | 250.70 | 2.17 |
| | 03 | 68.63 | 40.13 | 1.71 | 55.13 | 93.58 | 2.88 |
| | 04 | 65.26 | 42.55 | 1.53 | 60.52 | 80.39 | 2.96 |
| | 05 | 81.10 | 39.79 | 2.04 | 45.75 | 113.00 | 2.34 |
| GL-10 | | | | | | | |
| | 01 | – | – | – | – | – | – |
| | 01a | – | – | – | – | – | – |
| | 02 | – | – | – | – | – | – |
| | 03 | – | – | – | – | – | – |
| | 03a | – | – | – | – | – | – |
| | 04 | – | – | – | – | – | – |
| | 05 | 77.20 | 52.68 | 1.47 | 87.90 | 86.21 | 2.40 |
| | 06 | – | – | – | – | – | – |
| | 07 | – | – | – | – | – | – |
| | 07a | – | – | – | – | – | – |
| | 08 | 52.28 | 44.07 | 1.19 | 72.94 | 41.43 | 0.84 |
| | 09 | – | – | – | – | – | – |
| GL-11 | | | | | | | |
| | 01 | 557.61 | 528.94 | 1.05 | 684.16 | 435.23 | 0.61 |
| | 02 | 410.23 | 360.78 | 1.14 | 517.18 | 348.29 | 0.73 |

**Table. 7. Semi-quantitative percentages of the mineralogical composition of samples from Pirata-Pont-Piqueta system.**

| Core | Sample Number | montmorillonita | clh/mont | illite | kaolinite | quartz | feldspars | dolomite | calcite |
|---|---|---|---|---|---|---|---|---|---|
| PP-00 | | | | | | | | | |
| | 01 | 0.00 | 1.77 | 4.29 | 2.46 | 40.81 | 6.64 | i | 44.04 |
| | 02 | | | | | | | | |
| PP-01 | | | | | | | | | |
| | 01 | 3.98 | 0.00 | 3.04 | 0.91 | 14.13 | 2.17 | 3.98 | 71.77 |
| | 02 | 0.00 | 0.00 | 1.88 | 0.00 | 13.66 | 0.00 | 4.71 | 75.29 |
| | 03 | 0.00 | 3.19 | 3.65 | 3.68 | 28.99 | 3.50 | 11.57 | 45.41 |
| | 04 | 2.45 | 0.00 | 8.55 | 5.59 | 70.62 | 6.02 | 0.00 | 6.78 |
| | 05 | 0.00 | 0.00 | 5.58 | 3.67 | 68.43 | 13.31 | 3.87 | 5.44 |
| PP-02 | | | | | | | | | |
| | 01 | 0.00 | 1.74 | 3.37 | 1.09 | 10.50 | 0.00 | 2.47 | 83.84 |
| | 02 | 0.00 | 0.00 | 2.10 | 2.16 | 19.89 | 5.78 | 1.39 | 68.78 |
| | 03 | 0.00 | 0.00 | 6.73 | 2.25 | 13.60 | 1.26 | 2.36 | 73.82 |
| | 04 | 0.00 | 0.00 | 6.29 | 2.34 | 13.33 | 1.60 | 2.68 | 73.76 |
| | 05 | 0.00 | 0.00 | 1.53 | 0.00 | 5.10 | 1.10 | 0.59 | 91.69 |
| | 06 | 0.00 | 0.00 | 1.43 | 0.00 | 3.14 | 3.49 | 0.79 | 91.14 |
| PP-03 | | | | | | | | | |
| | 01 | 0.00 | 0.00 | 11.98 | 4.07 | 66.88 | 12.71 | 0.00 | 4.36 |
| PP-04 | | | | | | | | | |
| | 01 | 0.00 | 3.30 | 5.99 | 2.71 | 64.44 | 11.60 | 5.87 | 6.10 |
| | 02 | 0.00 | 0.00 | 4.98 | 3.16 | 73.51 | 13.24 | 0.00 | 5.10 |
| PP-05 | | | | | | | | | |
| | 01 | 0.00 | 0.00 | 10.76 | 3.86 | 67.25 | 10.72 | 1.76 | 5.66 |
| | 02 | 0.00 | 0.00 | 14.39 | 6.02 | 63.12 | 11.27 | 0.00 | 5.19 |
| | 03 | 0.00 | 0.00 | 17.91 | 5.36 | 59.44 | 10.71 | 1.96 | 4.61 |
| | 04 | 4.24 | 0.00 | 13.76 | 5.51 | 56.82 | 12.76 | 0.00 | 6.91 |
| PP-06 | | | | | | | | | |
| | 01 | 0.00 | 5.28 | 14.56 | 7.74 | 44.16 | 10.10 | 3.43 | 14.74 |
| | 02 | 0.00 | 0.00 | 26.90 | 10.01 | 37.35 | 13.45 | 5.53 | 6.77 |
| | 03 | 0.00 | 4.82 | 22.43 | 9.79 | 39.99 | 14.40 | 0.00 | 8.59 |
| | 04 | 0.00 | 9.27 | 22.67 | 10.30 | 40.66 | 12.34 | 0.00 | 4.75 |
| | 05 | 0.00 | 3.08 | 18.25 | 11.03 | 46.38 | 13.29 | 0.00 | 7.96 |
| PP-07 | | | | | | | | | |
| | 01 | 0.00 | 0.00 | 7.97 | 5.33 | 69.70 | 11.01 | 0.00 | 5.98 |
| | 02 | 0.00 | 0.00 | 4.34 | 1.95 | 75.30 | 15.91 | 0.00 | 2.50 |
| | 03 | 0.00 | 0.00 | 7.17 | 2.41 | 78.73 | 8.51 | 0.00 | 3.18 |
| | 04 | 0.00 | 5.15 | 8.83 | 2.83 | 65.89 | 12.93 | 0.00 | 4.36 |
| | 05 | 0.00 | 2.36 | 8.44 | 3.22 | 70.60 | 10.34 | 1.31 | 3.63 |
| | 06 | 0.00 | 3.82 | 8.61 | 4.14 | 67.86 | 10.24 | 0.00 | 5.33 |
| | 07 | 0.00 | 5.21 | 9.63 | 4.26 | 66.27 | 9.71 | 0.00 | 4.92 |

**Table 7. Continued.**

| Core | Sample Number | montmorillonita | clh/mont | illite | kaolinite | quartz | feldspars | dolomite | calcite |
|---|---|---|---|---|---|---|---|---|---|
| | 08 | 1.97 | 0.00 | 7.23 | 2.32 | 68.82 | 14.73 | 0.00 | 5.67 |
| | 09 | 0.00 | 0.00 | 10.27 | 4.86 | 67.82 | 10.54 | 0.00 | 6.45 |
| | 10 | 0.00 | 0.00 | 9.32 | 4.31 | 70.47 | 11.42 | 0.00 | 4.38 |
| PP-08 | | | | | | | | | |
| | 01 | 0.00 | 0.00 | 7.09 | 2.26 | 76.11 | 9.86 | 0.00 | 4.69 |
| | 02 | 0.00 | 0.00 | 13.93 | 5.59 | 64.85 | 12.04 | 0.00 | 3.59 |
| | 03 | 0.00 | 0.00 | 6.39 | 2.94 | 77.98 | 9.54 | 0.00 | 3.15 |
| | 04 | 0.00 | 0.00 | 5.21 | 3.23 | 72.14 | 11.81 | 2.54 | 5.07 |
| | 05 | 0.00 | 0.00 | 8.78 | 4.63 | 68.81 | 13.75 | 0.00 | 4.03 |
| | 06 | 0.00 | 0.00 | 13.64 | 4.38 | 67.16 | 11.28 | 0.00 | 3.53 |
| | 07 | 0.00 | 0.00 | 16.86 | 4.72 | 66.55 | 11.88 | 0.00 | 0.00 |
| | 08 | 0.00 | 3.23 | 10.00 | 4.92 | 68.06 | 10.96 | 2.82 | 0.00 |
| PP-08bis | | | | | | | | | |
| | 09 | 0.00 | 0.47 | 10.66 | 4.98 | 72.49 | 11.40 | 0.00 | 0.00 |
| | 10 | 0.00 | 0.00 | 12.00 | 5.12 | 73.17 | 9.72 | 0.00 | 0.00 |
| | 11 | 0.00 | 0.00 | 15.26 | 4.55 | 65.37 | 11.15 | 0.00 | 3.68 |
| PP-09 | | | | | | | | | |
| | 01 | 0.00 | 1.37 | 21.24 | 9.01 | 55.19 | 8.14 | 0.00 | 5.06 |
| PP-10 | | | | | | | | | |
| | rock | 0.00 | 0.00 | 0.00 | 0.00 | 1.40 | 0.00 | 0.00 | 98.60 |
| | rock impurities | 0.00 | 0.00 | 0.65 | 0.00 | 99.34 | 0.00 | 0.00 | 0.00 |
| PP-11 | | | | | | | | | |
| | 01 | 0.00 | 0.00 | 6.76 | 1.82 | 76.69 | 10.26 | 1.22 | 3.24 |
| PP-12 | | | | | | | | | |
| | 01 | i | 0.00 | 0.91 | 0.00 | 12.27 | 0.00 | 1.55 | 85.27 |
| | 02 | 0.00 | 0.00 | 0.00 | 1.68 | 8.09 | 0.00 | 3.78 | 86.45 |
| | 03 | 0.00 | 0.00 | 1.08 | 0.00 | 2.85 | 0.00 | 2.67 | 93.41 |
| | 04 | 0.00 | 0.00 | 0.00 | 0.00 | 2.28 | 0.00 | 0.00 | 97.72 |

**Table. 8. Semi-quantitative percentages of the mineralogical composition of samples from Cova de sa Gleda.**

| Core | Sample Number | smectite | illite | gypsum | kaolinite | anhydrite | aragonite | quartz | feldspars | calcite | dolomite |
|---|---|---|---|---|---|---|---|---|---|---|---|
| GL-01 | | | | | | | | | | | |
| | 01 | 0.00 | 16.13 | 0.00 | 6.42 | 0.00 | 0.00 | 57.84 | 3.96 | 9.99 | 5.66 |
| | 02 | 0.00 | 14.76 | 0.00 | 5.71 | 11.98 | 0.00 | 49.00 | 7.43 | 11.12 | 0.00 |
| | 03 | 2.35 | 8.72 | 0.00 | 2.89 | 0.00 | 0.00 | 63.65 | 7.49 | 14.90 | 0.00 |
| | 04 | 0.00 | 11.47 | 0.00 | 6.25 | 9.48 | 0.00 | 53.45 | 11.04 | 8.30 | 0.00 |
| | 05 | 0.00 | 9.43 | 0.00 | 5.79 | 6.72 | 0.00 | 53.28 | 7.77 | 10.88 | 6.13 |
| | 06 | 0.00 | 12.03 | 0.00 | 7.81 | 0.00 | 0.00 | 58.37 | 8.86 | 7.02 | 5.92 |
| | 07 | 0.00 | 9.14 | 0.00 | 6.08 | 0.00 | 0.00 | 65.34 | 8.85 | 6.32 | 4.27 |
| | 08 | 0.00 | 12.48 | 0.00 | 9.29 | 0.01 | 0.00 | 60.10 | 8.29 | 9.82 | 0.00 |
| | 09 | 0.00 | 13.91 | 0.00 | 7.37 | 0.00 | 0.00 | 60.76 | 6.39 | 7.09 | 4.49 |
| | 10 | 6.47 | 8.59 | 0.00 | 5.41 | 0.00 | 0.00 | 56.74 | 5.65 | 8.22 | 8.91 |
| | 11 | 0.00 | 17.21 | 0.00 | 8.93 | 6.18 | 0.00 | 45.53 | 7.39 | 12.33 | 2.43 |
| | 12 | 0.00 | 12.03 | 0.00 | 5.98 | 0.00 | 0.00 | 54.50 | 5.98 | 14.12 | 7.40 |
| | 14 | 0.00 | 11.27 | 0.00 | 6.25 | 0.00 | 0.00 | 59.83 | 3.88 | 12.58 | 6.19 |
| | 15 | 12.45 | 12.60 | 0.00 | 6.58 | 4.05 | 0.00 | 46.13 | 4.77 | 7.98 | 5.45 |
| GL-02 | | | | | | | | | | | |
| | 01 | 0.00 | 17.46 | 0.00 | 7.03 | 0.00 | 0.00 | 69.67 | 0.00 | 0.00 | 5.85 |
| | 02 | 0.00 | 12.73 | 0.00 | 5.27 | 0.00 | 0.00 | 60.27 | 8.14 | 6.50 | 7.08 |
| | 03 | 0.00 | 15.18 | 0.00 | 6.07 | 0.00 | 0.00 | 64.40 | 7.86 | 6.49 | 0.00 |
| | 04 | 0.00 | 12.69 | 0.00 | 9.05 | 0.00 | 0.00 | 60.88 | 9.91 | 7.47 | 0.00 |
| | 05 | 0.00 | 14.14 | 2.93 | 5.77 | 0.00 | 0.00 | 68.41 | 0.00 | 8.75 | 0.00 |
| | 06 | 0.00 | 6.98 | 0.00 | 4.32 | 0.00 | 0.00 | 40.40 | 9.46 | 32.16 | 6.68 |
| | 07 | 0.00 | 7.91 | 0.00 | 3.67 | 0.00 | 0.00 | 55.10 | 7.44 | 12.99 | 12.89 |
| | 08 | 0.00 | 7.90 | 0.00 | 5.48 | 0.00 | 0.00 | 56.72 | 4.81 | 15.75 | 9.34 |
| | 09 | 0.00 | 9.41 | 0.00 | 5.75 | 0.00 | 0.00 | 60.75 | 7.18 | 9.70 | 7.21 |
| | 10F | 0.00 | 5.56 | 0.00 | 1.90 | 0.00 | 0.00 | 9.94 | 4.20 | 7.94 | 70.46 |
| | 11A | 0.00 | 0.00 | 0.00 | 0.02 | 0.00 | 0.00 | 0.00 | 0.00 | 92.47 | 7.51 |
| | 11F | 0.00 | 0.00 | 0.00 | 0.00 | 0.00 | 0.00 | 15.58 | 0.00 | 30.24 | 54.18 |
| GL-03 | | | | | | | | | | | |
| | 01 | 0.00 | 9.50 | 4.78 | 5.63 | 0.00 | 0.00 | 56.86 | 5.28 | 17.95 | 0.00 |
| | 02 | 0.00 | 3.55 | 0.00 | 0.01 | 0.01 | 0.00 | 34.08 | 4.01 | 47.84 | 10.50 |
| | 03 | 0.00 | 0.00 | 0.00 | 0.00 | 0.00 | 0.00 | 16.90 | 2.11 | 44.87 | 36.12 |
| | 04 | 0.00 | 0.01 | 0.00 | 0.00 | 0.00 | 0.00 | 34.83 | 2.52 | 41.99 | 20.65 |
| | 05 | 0.00 | 7.82 | 0.00 | 2.65 | 0.00 | 2.90 | 22.32 | 3.97 | 44.12 | 16.22 |
| | 06 | 0.00 | 7.79 | 0.00 | 2.46 | 0.00 | 0.00 | 24.17 | 3.48 | 58.21 | 3.89 |
| | 07 | 0.00 | 7.03 | 0.00 | 1.65 | 0.00 | 0.00 | 26.88 | 3.96 | 57.49 | 3.00 |
| | 08 | 0.00 | 6.26 | 0.00 | 3.15 | 3.64 | 0.00 | 25.76 | 9.35 | 49.90 | 1.94 |
| | 09 | 0.00 | 0.01 | 0.00 | 0.01 | 0.00 | 0.00 | 24.45 | 3.91 | 68.53 | 3.09 |
| | 10 | 0.00 | 0.00 | 0.00 | 0.00 | 0.00 | 0.00 | 24.85 | 2.47 | 69.12 | 3.55 |
| | 11 | 0.00 | 3.91 | 0.00 | 1.75 | 0.00 | 0.00 | 34.47 | 2.84 | 53.43 | 3.61 |
| | 12 | 0.00 | 5.10 | 0.00 | 0.00 | 0.00 | 0.00 | 31.26 | 0.00 | 60.89 | 2.74 |
| GL-04 | | | | | | | | | | | |
| | 01 | 0.00 | 9.87 | 0.00 | 6.87 | 4.65 | 0.00 | 49.83 | 6.06 | 4.55 | 18.17 |
| | 02 | 0.00 | 7.73 | 0.00 | 4.46 | 0.01 | 0.00 | 30.58 | 4.30 | 3.56 | 49.36 |
| | 03 | 0.00 | 8.91 | 0.00 | 0.02 | 4.42 | 0.00 | 31.42 | 0.00 | 17.30 | 37.94 |
| | 04 | 0.00 | 1.81 | 0.00 | 1.45 | 0.00 | 0.00 | 7.40 | 0.00 | 82.35 | 6.98 |
| | 05 | 0.00 | 1.58 | 0.00 | 0.00 | 0.00 | 0.00 | 3.25 | 0.00 | 95.17 | 0.00 |
| | 06 | 0.00 | 0.00 | 0.00 | 0.00 | 0.00 | 0.00 | 4.32 | 0.00 | 95.68 | 0.00 |
| | 07 | 0.00 | 17.19 | 0.00 | 8.01 | 0.00 | 0.00 | 35.59 | 5.54 | 33.67 | 0.00 |
| | 08 | 0.00 | 4.86 | 0.00 | 2.60 | 0.00 | 0.00 | 8.32 | 0.00 | 84.22 | 0.00 |
| GL-05 | | | | | | | | | | | |
| | 01 | 0.00 | 1.10 | 0.00 | 0.01 | 0.00 | 0.00 | 5.33 | 0.00 | 91.31 | 2.26 |

**Table 8. Continued.**

| Core | Sample Number | smectite | illite | gypsum | kaolinite | anhydrite | aragonite | quartz | feldspars | calcite | dolomite |
|---|---|---|---|---|---|---|---|---|---|---|---|
| | 02 | 0.00 | 5.33 | 0.00 | 3.61 | 0.00 | 0.00 | 41.49 | 6.96 | 9.07 | 33.54 |
| | 03 | 0.00 | 1.32 | 0.00 | 0.00 | 0.00 | 0.00 | 7.88 | 0.00 | 89.48 | 1.32 |
| | 04 | 0.00 | 6.97 | 0.00 | 3.19 | 3.23 | 0.00 | 72.51 | 5.66 | 2.00 | 6.45 |
| | 05 | 0.00 | 9.46 | 0.00 | 5.11 | 4.31 | 0.00 | 68.62 | 5.45 | 7.04 | 0.00 |
| GL-06 | | | | | | | | | | | |
| | 01 | 0.00 | 5.16 | 0.00 | 3.07 | 0.00 | 0.00 | 61.90 | 2.24 | 3.06 | 24.57 |
| | 02 | 0.00 | 7.69 | 0.00 | 2.34 | 0.00 | 0.00 | 72.85 | 5.62 | 6.10 | 5.40 |
| | 03 | 0.00 | 6.39 | 0.00 | 2.51 | 0.00 | 0.00 | 34.68 | 5.31 | 17.41 | 33.71 |
| | 04 | 0.00 | 3.74 | 0.00 | 3.19 | 14.68 | 0.00 | 51.65 | 5.67 | 11.20 | 9.87 |
| GL-07 | | | | | | | | | | | |
| | 01 | 1.11 | 3.51 | 0.00 | 2.24 | 0.00 | 0.00 | 74.24 | 7.31 | 11.59 | 0.00 |
| GL-08 | | | | | | | | | | | |
| | 01 | 0.00 | 6.90 | 0.00 | 4.19 | 0.00 | 0.00 | 64.64 | 5.97 | 18.29 | 0.00 |
| | 02 | 0.00 | 16.04 | 0.00 | 25.07 | 0.00 | 0.00 | 6.76 | 18.32 | 27.10 | 6.70 |
| | 03 | 0.00 | 7.33 | 0.00 | 3.72 | 0.00 | 0.00 | 58.15 | 8.88 | 19.00 | 2.92 |
| | 03a | 0.00 | 5.40 | 0.00 | 2.37 | 0.00 | 0.00 | 63.08 | 2.63 | 26.52 | 0.00 |
| | 04 | 0.00 | 6.98 | 0.00 | 4.16 | 0.00 | 0.00 | 67.05 | 7.01 | 14.80 | 0.00 |
| | 05 | 0.00 | 9.20 | 0.00 | 4.78 | 0.00 | 0.00 | 63.77 | 8.05 | 14.20 | 0.00 |
| | 06 | 0.00 | 11.44 | 0.00 | 4.46 | 0.00 | 0.00 | 55.30 | 9.11 | 19.69 | 0.00 |
| | 07 | 0.00 | 9.62 | 0.00 | 4.23 | 0.00 | 0.00 | 56.69 | 7.44 | 22.02 | 0.00 |
| | 08 | 0.00 | 7.10 | 0.00 | 3.55 | 0.00 | 0.00 | 49.26 | 4.66 | 29.58 | 5.86 |
| | 09 | 0.00 | 9.79 | 0.00 | 5.88 | 0.00 | 0.00 | 63.80 | 7.78 | 12.74 | 0.01 |
| | 10 | 0.00 | 8.64 | 0.00 | 4.47 | 0.00 | 0.00 | 61.27 | 6.25 | 19.37 | 0.01 |
| | 11 | 0.00 | 7.92 | 0.00 | 4.75 | 0.00 | 0.00 | 57.66 | 4.49 | 25.17 | 0.01 |
| | 12 | 0.01 | 7.17 | 0.00 | 4.20 | 0.00 | 0.00 | 61.75 | 4.44 | 22.44 | 0.00 |
| | 13 | 0.00 | 8.18 | 0.00 | 3.36 | 0.00 | 0.00 | 63.52 | 4.73 | 18.27 | 1.95 |
| GL-09 | | | | | | | | | | | |
| | 01 | 0.00 | 0.00 | 0.00 | 0.01 | 0.00 | 0.00 | 0.00 | 0.00 | 47.90 | 52.10 |
| | 02 | 0.00 | 0.01 | 0.00 | 0.00 | 0.00 | 0.00 | 5.98 | 0.00 | 0.00 | 94.01 |
| | 03 | 0.00 | 5.91 | 0.00 | 2.54 | 0.00 | 0.00 | 16.07 | 2.81 | 0.00 | 72.66 |
| | 04 | 0.00 | 5.41 | 0.00 | 3.07 | 0.00 | 0.00 | 15.03 | 0.00 | 6.08 | 70.41 |
| | 05 | 0.00 | 0.01 | 0.00 | 0.00 | 0.00 | 0.00 | 12.84 | 0.00 | 1.69 | 85.45 |
| GL-10 | | | | | | | | | | | |
| | 01 | 0.00 | 4.26 | 0.00 | 1.87 | 0.00 | 0.00 | 3.37 | 0.00 | 28.36 | 62.14 |
| | 01a | 0.00 | 0.01 | 0.00 | 0.00 | 0.00 | 0.00 | 0.00 | 0.00 | 4.57 | 95.42 |
| | 02 | 0.00 | 0.01 | 0.00 | 0.00 | 0.00 | 0.00 | 5.03 | 0.00 | 59.42 | 35.55 |
| | 03 | 0.00 | 0.01 | 0.00 | 0.00 | 0.00 | 0.00 | 4.09 | 0.00 | 60.38 | 35.52 |
| | 03a | 0.00 | 0.00 | 0.00 | 0.01 | 0.00 | 0.00 | 2.37 | 0.00 | 37.49 | 60.13 |
| | 04 | 0.00 | 0.01 | 0.00 | 0.01 | 0.00 | 0.00 | 4.61 | 0.00 | 41.19 | 54.17 |
| | 05 | 0.00 | 5.77 | 0.00 | 2.67 | 0.00 | 0.00 | 8.14 | 2.28 | 17.77 | 63.37 |
| | 06 | 0.00 | 8.87 | 0.00 | 3.28 | 0.00 | 0.00 | 10.74 | 0.00 | 28.62 | 48.49 |
| | 07 | 0.00 | 3.58 | 0.00 | 2.22 | 0.00 | 0.00 | 9.24 | 0.00 | 13.98 | 70.99 |
| | 07a | 0.00 | 0.00 | 0.00 | 0.00 | 0.00 | 0.00 | 0.00 | 0.00 | 0.00 | 100.00 |
| | 08 | 0.00 | 0.01 | 0.00 | 3.84 | 0.00 | 0.00 | 10.37 | 0.00 | 62.67 | 23.10 |
| | 09 | 0.00 | 3.15 | 0.00 | 0.00 | 0.00 | 0.00 | 4.31 | 0.00 | 49.72 | 42.82 |
| GL-11 | | | | | | | | | | | |
| | 01 | 0.00 | 0.00 | 0.00 | 0.00 | 0.00 | 0.00 | 0.47 | 0.00 | 85.61 | 13.92 |
| | 02 | 0.00 | 0.00 | 0.00 | 0.00 | 0.00 | 0.00 | 1.09 | 0.00 | 85.52 | 13.39 |

# THE LEGEND OF CARBON DIOXIDE HEAVINESS

GIOVANNI BADINO
*Dip. Fisica Generale, Università di Torino, Via Giuria, 1, Torino, Italy, badino@to.infn.it*

**Abstract:** The false legend of carbon dioxide traps resulting from the weight of carbon dioxide gas is disproved. In spite of water-vapor lightness in comparison with air, no water-vapor trap exists on cave ceilings. In fact, underground atmospheres with specific compositions are not related to gravity, but to the absence of any air movement around the gas sources. The process of double diffusion of oxygen and carbon dioxide during organic compound decomposition in still air is shown to be significant. This phenomenon can form atmospheres that are deadly due to oxygen deficiencies and poisonous because of excess carbon dioxide. Carbon dioxide storage behaves like a liquid and can flow or can be poured, as cold air can, but these are typical transient processes with no relation to a cave's foul air formation.

## INTRODUCTION

A very common opinion among cavers (and not only cavers, see (Al-Azmi, 2008)) is that dense gases tend to accumulate in depressions, and especially, at the bottom of caves. It is widely accepted that $CO_2$ accumulates at the bottom of shafts; this concept has been infrequently discussed, but often repeated from paper to paper. In this paper we show that this concept is in fact false and may be regarded as an underground legend (James, 2003; Cigna, 2008). The aim of this paper is to provide a quantitative assessment and details of gas entrapment processes.

## GAS DENSITIES

A first indication that those who use the concept of gas density for gas entrapment are simply repeating it, without any understanding of the processes, is the typical statement "the heavier gas accumulates…." Obviously 10 kg of nitrogen are heavier than 2 kg of carbon dioxide, or even of 1 kg of radon. Carbon dioxide is not heavier than oxygen or water vapor, but it is denser than those gases.

Even in papers where the term density is used, the downward increase of carbon dioxide concentration is qualified as normal. Renault (1972) wrote that this phenomenon is predictable from the laws of physics and then noticed that inverse gradients are not so easily explained. In fact, the phenomena are much more complex. In addition, the normal $CO_2$ gradient that could be attributed to density differences is undetectable on the scale of typical cave dimensions (see Equation (A3) in Appendix A).

Air is composed of many different gases, each one with a different molar mass. Considering an isothermal mass of a gas (temperature $T_0$, molar mass $M_{mol}$, density $\rho_g$), its density really depends on $M_{mol}$

$$\rho_g = \frac{M_{mol} P}{R T_0} \tag{1}$$

where $R = 8.3142$ J mol$^{-1}$ K$^{-1}$ is the gas constant.

Table 1 shows that, depending on molar mass, gas density changes significantly with water vapor, with methane and hydrogen being less dense than air, while carbon dioxide and radon are much denser. If stratification really does occur, according to the meaning adopted by those who state that heavier gases accumulate in depressions, then we would live in a carbon dioxide atmosphere just a few meters above sea level, in oxygen at the top of mountains, in nitrogen above the mountains, and finally, in water vapor (and rain) in the stratosphere. The Dead Sea and the Caspian Sea would exist in pure radon atmospheres whereas hydrogen would be concentrated in the ionosphere (incidentally, where it actually is, but due to reasons other than stratification). This is an unrealistic scenario.

So do denser fluids sink into less dense fluids? In the case of liquids the answer is complex. It is necessary to take into account many effects connected with the interactions of the molecules involved. For gases, the behavior is much simpler if it is assumed that the gas molecules do not interact with each other (i.e. that the gas molecules behave in an ideal way). Each air molecule is free to diffuse in every direction and it is easy to calculate the atmospheric structure at equilibrium.

## GRAVITATIONAL STRATIFICATION

Let us calculate the pressure and density of a gas at constant temperature $T_0$ stratified in the gravitational field ($g = 9.8$ m s$^{-2}$) on a flat surface at $z = 0$. The hydrostatic equilibrium imposes a pressure $P(z)$ variation with altitude $z$ (positive upward) as

$$\frac{dP}{P} = -\frac{M_{mol} g}{R T_0} dz \tag{2}$$

Integrating between the surface (z=0, $P=P_0$) and (z, $P$(z)) yields

$$P = P_0 \exp\left(-\frac{M_{mol} g}{R T_0} z\right) \tag{3}$$

**Table 1. Molar mass and density of common gases.**

| Gas | $M_{mol}$ ($10^{-3}$ kg mol$^{-1}$) | $\rho_g$ at $SP$, $T = 288$ K (kg m$^{-3}$) |
|---|---|---|
| Nitrogen | 28 | 1.19 |
| Oxygen | 32 | 1.36 |
| Air | 28.9 | 1.22 |
| Hydrogen | 2 | 0.08 |
| Methane | 10 | 0.42 |
| Water Vapour | 18 | 0.76 |
| Carbon Dioxide | 38 | 1.61 |
| Radon | 222 | 9.40 |

The result is an exponential pressure decrease with altitude. Our atmosphere is not isothermal, obviously, but this equation can be used to describe the upper parts of the Earth's atmosphere, from 10 to 80 km where the air temperature is quite constant (≈220 K). It is not correct to use this formula for the lowest portion of the Earth's atmosphere where we live, but the equation still describes the possibility of chemical gas stratification in caves very well because underground the temperature is locally constant. There are some details about the equilibrium of such an atmosphere which are interesting because they touch on the thermal stratification of a cave's atmosphere, but the equilibrium details are not important for our discussion.

The term in brackets in Equation (3) must be dimensionless, which introduces the length scale $L_z$ for gas stratification in a gravitational field

$$L_z = \frac{RT_0}{M_{mol}g} \tag{4}$$

and allows calculation of the length scale $L_z$ at $T_0 = 288$ K. Atmospheres of pure gases in equilibrium stratify exponentially; meaning that each altitude rise of $L_z$ causes a relative reduction by a factor $e^{-1} = 0.36$ of pressure. For instance, in pure oxygen, we would have to rise 7.6 km to reduce the pressure by 63%. In pure hydrogen, the rise would have to be 120 km, in radon 1.1 km, and so on.

It is then possible to calculate the natural $CO_2$ gradient enrichment with depth (see Appendix A). The real atmosphere is a gas mixture, but gases are independent of each other. Gases collaborate to create a final total pressure, but the partial pressure of each gas behaves as if the others did not exist.

Hence, the atmosphere can be considered not only a mixture of different gases, but also a mixture of different atmospheres, with each atmosphere composed of pure gas. Table 2 shows that gases have a tendency to separate from each other according to altitude differences of many kilometers. At higher altitudes, the air would be enriched by gases with small molar masses and depleted of those with greater molar masses. As a matter of fact, however, this stratification does not exist because in the real atmosphere the strong vertical mixing in its lower part (called the homosphere, up to 100 km) prevents such separation, and creates a quite uniform chemical composition.

**Table 2. Comparison of pure gas atmosphere in neutral equilibrium.**

| Gas | Molar Mass, $M_{mol}$ ($10^{-3}$ kg mol$^{-1}$) | Scale Length, $L_z$ (km) | Pressure at $z = 1$ km $P(z)/P_0$ | Pressure at $z = 10$ km $P(z)/P_0$ |
|---|---|---|---|---|
| Nitrogen | 28 | 87 | 0.89 | 0.32 |
| Oxygen | 32 | 76 | 0.88 | 0.27 |
| Air | 289 | 85 | 0.89 | 0.31 |
| Hydrogen | 2 | 120 | 0.99 | 0.92 |
| Methane | 10 | 24 | 0.96 | 0.66 |
| Water Vapor | 18 | 136 | 0.93 | 0.48 |
| Carbon Dioxide | 38 | 64 | 0.86 | 0.21 |
| Radon | 222 | 11 | 0.40 | 0.000113 |

Chemical stratification appears only in the extreme upper layers (heterosphere), where the Earth's atmosphere is arranged into four shells, the lower dominated by molecular nitrogen, the second by atomic oxygen, the third by helium, and finally by hydrogen atoms (Lutgens, 1998). If we cancel the vertical mixing and consider an ideal perfectly calm atmosphere, we could develop differences in chemical composition, but only with large altitude differences because the gases' length scales are around ten kilometers. Table 2 shows that 1 km above sea level, the different gases have essentially the same partial pressure, but in this imaginary situation it would be difficult to detect the different molar weights of the pressures. The chemical stratification would be noticeable only at $z =$ 10 km (Table 2).

Stratification could exist, but only in a non-mixing atmosphere with kilometers of drop, whereas on the scale of a few meters, it is impossible to detect any chemical variation, even by measuring radon concentrations. So, water vapor and methane do not concentrate on cave ceilings, but neither does carbon dioxide or radon concentrate on cave floors unless vertical cave dimensions are on the order of many kilometers. The stratification idea, repeated thousands of times from one caving book to another, is absolutely false.

## The Carbon Dioxide Traps

There is a problem with the supposed nonstratification of carbon dioxide, however, because the stratification effect does actually appear to exist. Our work in the Tropics finding caves filled with carbon dioxide resulted in the development of specialized shaft equipment for descending into holes where encountering deadly atmospheres was likely (Antonini, 1998).

Carbon dioxide traps do exist, but their classical interpretation is false. The shafts were filled with carbon dioxide not because it is a dense gas, but because carbon dioxide is produced at the bottom of the shaft in an absolutely calm atmosphere. The reason for stratification is not gravitation, but diffusion of gas in gas. Gas traps could also exist in the absence of gravity.

It is worth noting that the false concept of gas stratification depends on the fact that the gas is potentially deadly. If at the shaft bottom there is a lake, the surrounding air is filled with water vapor, which means that the relative humidity is 100%. This high humidity is not a result of the heaviness of water vapor (which is actually less dense than air), but is merely due to the presence of water. The water vapor is concentrated at the water surface.

In exactly the same way, carbon dioxide is concentrated at the carbon dioxide sources and in the same way the gases of upper atmosphere are concentrated at their source. In the ionosphere, the X and UV solar radiations produce atomic oxygen and hydrogen and they accumulate there. This is the reason why radon accumulates in cellars and in lower floors and why methane traps are set at mine conduit ceilings where thermal stratification (hot air) creates relatively quiet bubbles for methane concentration.

Carbon dioxide is generated essentially from the oxidation of organic substances, is much denser than the surrounding air, and tends to accumulate at the lowest cave levels as water often does (although water can potentially flow away whereas dead organic substances cannot). So, carbon dioxide and water vapor tend to accumulate in the depressions that are often humid and sometimes enriched to deadly levels with carbon dioxide.

Worse, but often neglected, are hypoxic conditions. Carbon dioxide is dangerous at high concentrations, but oxygen-poor atmospheres, independent of the presence of other gases, are also deadly. Each carbon dioxide molecule is derived from the reaction of a carbon atom with an oxygen molecule. Therefore, in general, near a carbon dioxide source we can find a deadly presence of carbon dioxide as well as a deadly absence of oxygen.

A $CO_2$ trap thus represents a two-fold phenomenon. For organic compounds on the left, we have to calculate the oxygen flux from right to left and the carbon dioxide flux from left to right.

## GAS DIFFUSION IN GASES

It is quite easy to model carbon dioxide trap formation, but it is necessary to first discuss why and how a gas diffuses in a certain direction. Gas molecules are quite free to move and they do so continuously. For a surface in space, the molecules flow through it in the two possible directions. If the concentration $c_1$ of a molecule per volume unit near one surface side is the same as $c_2$ near the other surface side, the net flux is the same and no net gas transfer through the surface occurs. In this instance, it is commonly stated, incorrectly, that no diffusion occurs when in fact the two diffusions cancel each other. However, if $c_1$ is greater than $c_2$, then more molecules will flow from side one than will flow from side two as a result of concentration gradients (Fig. 1). This process is usually described as the gas diffusing through the surface with an intensity proportional to the concentration difference and is known as Fick's law.

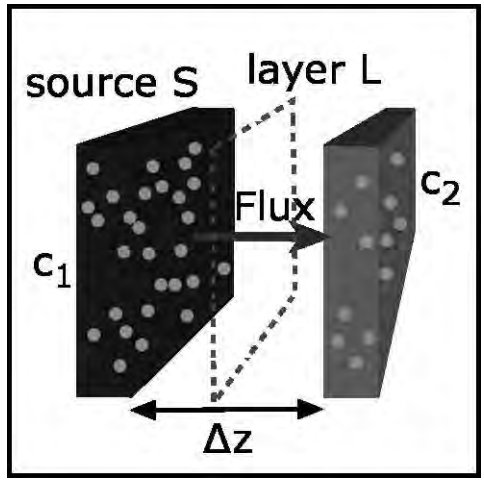


**Figure 1.**

In order to quantify the gas diffusion process, it is necessary to state that the total flux $F$ (kilograms per second per square meter) over some distance $\Delta z$ that separates two gas volumes with $c_1$ and $c_2$ gas concentrations (kilograms per cubic meter) is given by

$$F = D_g \frac{c_1 - c_2}{\Delta z} \tag{5}$$

where $D_g$ is the gas coefficient of diffusion, which generally depends on the gas viscosity $\eta_g$ and density $\rho_g$ as

$$D_g = f \frac{\eta_g}{\rho_g} \tag{6}$$

where $f$ is a factor of order unity. From Equation (6) we can easily obtain the $D_g$ dependence on pressure $P$ and temperature $T$ because

$$D_g \propto \frac{1}{P}$$
$$D_g \propto T^{3/2} \tag{7}$$

Diffusion processes are, in general, very complex, and only self-diffusion (molecule diffusivity in a gas of identical molecules) is usually described. The real case, in which one gas diffuses inside another, requires consideration of different molecule sizes, asymmetries, masses, and repulsive forces between molecules. A detailed review of the processes may be found in Jost (1952).

Changes in the diffusion coefficient $D_g$ are quite small. Table 3, adapted from Jost (1952), lists this parameter at

**Table 3. Diffusion coefficients of common gases.**

| Gas in Gas | $D_g$ ( $m^2\ s^{-1}$) |
|---|---|
| $O_2$ in $O_2$ | $1.89 \times 10^{-5}$ |
| $N_2$ in $N_2$ | $1.98 \times 10^{-5}$ |
| $CO_2$ in $CO_2$ | $1.04 \times 10^{-5}$ |
| $O_2$ in Air | $1.78 \times 10^{-5}$ |
| $CO_2$ in Air | $1.38 \times 10^{-5}$ |
| $H_2O$ in Air | $2.36 \times 10^{-5}$ |

standard temperature and pressure (STP). It should be noted that Equation (5) states that diffusion does not depend, at first order, on gravity. The upward or downward diffusion of a gas in another, heavier or lighter gas, has the same intensity because the buoyancy term is negligible.

The equations describing diffusion processes are the same as those that describe conductive thermal transfer, transient time-dependent processes (Fourier equation), and stationary processes (Laplace equation). Thermal-transfer processes also describe a diffusion process known as thermal-energy diffusion (Badino, 2005). These equations are not easily solved exactly, especially for transient conditions (Nashchokin, 1979), because even apparently simple boundary conditions can cause significant difficulties.

Nevertheless, it is possible to demonstrate that minimal carbon dioxide production in a non-mixing atmosphere can create deadly concentrations close to the source. Consider a reservoir $S$ connected to a free atmosphere by a layer $L$ of $\Delta z$ thickness of non-mixing air with a continuous carbon dioxide production in $S$. Assuming in Equation (5) $c_1 = 1.61\ kg\ m^{-3}$ and $c_2 = 0$ that is a pure gas in $S$ and nothing at the other side of $L$, we obtain the maximum gas flux which can be evacuated by diffusion through $L$

$$F_{\max} = D_{CO_2} \frac{1.61}{\Delta z} = \frac{2.2 \times 10^{-5}}{\Delta z} \tag{8}$$

If the produced flux is greater than $F_{max}$, the carbon dioxide concentration in $S$ tends asymptotically to saturation and also accumulates $L$ where the concentration is not linearly decreasing and is time independent. A perfectly toxic atmosphere of almost pure carbon dioxide is obtained because of a very small flux and very calm conditions at the bottom (or at the top) of the cave.

For example, consider a $CO_2$ source $S$ extended on a flat surface which can be either horizontal or vertical. Suppose that the source is able to release 0.01 kg of $CO_2$ per day per square meter ($F = 10^{-7}\ kg\ m^{-2}\ s^{-1}$) that is evacuated by diffusion in a quiet atmosphere $L$ in front of $S$ over a distance of $\Delta z = 10$ m where the gas meets the free atmosphere. Assuming a $CO_2$ concentration $c_2 = 0$ (actually the average concentration is 383 ppmv and quickly increasing) yields

$$c_1 = \frac{F \Delta z}{D_g} = \frac{10^{-7} \times 10}{1.4 \times 10^{-5}} \approx 0.07 \tag{9}$$

In this case, given such a minimal flux, the carbon dioxide concentration at equilibrium and near the source reaches roughly 5% in volume, a value that is already dangerous. The $F_{max}$ is now $2.2 \times 10^{-6}$.

Increasing the flux $F = 10^{-5}\ kg\ m^{-2}\ s^{-1}$ one hundred times stronger than in the previous example, the equation would yield a meaningless value of 7 kg $m^{-3}$. The reason for this is that the assumption of a linear decrease in $z$ of concentration at equilibrium cannot be satisfied for transfer of such high fluxes over such long paths and $F > F_{max}$. For these conditions, at the first few meters in front of $S$, the $CO_2$ concentration would be extremely high, and only near the free atmosphere would the concentration decrease almost linearly to zero.

The weight (density) of carbon dioxide does not matter. Exactly the same approach can be used for oxygen or nitrogen (or methane, in coal mines) sources to obtain almost pure gas atmospheres near the source. The same could be said for a water-vapor source, but this gas is far from perfect at room temperature (i.e., its behavior is highly complicated by processes like saturation, condensation, enthalpy releases, eddies, etc.). The problem of water-vapor diffusion in stable atmospheres is very complex.

The key point in creating a $CO_2$ trap underground is the thermal uniformity of cave atmospheres that hampers air movements and which can create traps of quiet cold air. No heavy gas stratifiation occurs, but thermal stratifiation does. Ek and Gewelt (1985) includes several incorrect comments on the role of gravity and normal gradient increasing downward, but the importance of thermal stratifiation is correctly noted. Ek and Gewelt also note the apparently surprising fact that "…in a single room or gallery the $pCO_2$ is frequently higher near the roof than near the ground."

## DOUBLE DIFFUSION

There are many studies explaining carbon dioxide enrichment in caves (see, for example James, 2003 and references therein). The main, and most dangerous, reason for carbon dioxide enrichment in caves is the oxidation of organic compounds in motionless atmospheres (Ek and Gewelt, 1985). This leads to another underground legend: that carbon dioxide is able to extinguish flames.

Oxidation and degradation of any long organic molecule causes an entropy increase in one direction. Each carbon atom and each hydrogen atom in an organic waste will bind to oxygen to flow away and return as wood, skin, milk, etc. In open-air, the process is generally very fast and is helped by countless types of creatures (fungi, bacteria, birds, jackals, human beings, etc.) that live off the degradation of these dead structures, and are able to quickly distribute it to

surrounding life. However, when the organic compounds stay in a very stable situation, far from the degradation workers, as in a cave, only the Second Law of Thermodynamics can work, and it works slowly by diffusion, by slow air draughts, and by minimal temperature differences.

In general, a carbon dioxide source does not exist, but some organic residues (i.e., vegetable matter) are in contact with air. It is possible to see that if (1) the oxygen and carbon dioxide just diffuse in the same surrounding atmosphere without any draught and (2) the oxidation rate is proportional to the oxygen concentration (see Appendix B). There is then a correspondence between the oxygen and carbon dioxide concentrations around the organic storage as shown by

$$c_{CO_2,0} = 1.17(0.28 - c_{O_2,0}) \tag{10}$$

Calling $F_{id}$ the oxidation rate of $S$ in free atmosphere when the oxygen concentration is $c_{O,1} = 0.28$ kg m$^{-3}$, the actual oxidation rate is slower due to the lower oxygen concentration

$$F = F_{id}\frac{1}{\left(1+\dfrac{F_{id}\Delta z}{0.28D_{O_2}}\right)} = \varepsilon F_{id} \tag{11}$$

The reduction factor ε depends on the geometry of diffusing atmosphere. It is directly connected with the oxygen concentration near the deposit, given by

$$c_{O,0} = 0.28\varepsilon \tag{12}$$

Returning to the previous example and assuming that the flux used, $10^{-7}$, is $F_{id}$, it is possible to calculate new values that result from the effect of double diffusion to give

$$\begin{aligned} F &= 0.85F_{id} \\ c_{O_2,0} &= 0.85c_{O_2,1} \\ c_{CO_2,0} &= 0.06 \end{aligned} \tag{13}$$

The oxidation flux is reduced in comparison to free atmosphere, and correspondingly, the concentrations of oxygen and carbon dioxide are reduced. For extreme conditions and if $F_{id}$ is very high, $F$ cannot increase over the maximum value given by:

$$F \approx \frac{5.0\times10^{-6}}{\Delta z} \tag{14}$$

with concentrations:

$$c_{O_2,0} \approx 0 \tag{15}$$

$$c_{CO_2,0} \approx 0.35 \tag{16}$$

This means that in the case of oxidative processes, the maximum carbon dioxide concentration around the source is approximately 21% in volume as oxygen in free air.

These are typical conditions in which a flame will extinguish, not because of the high carbon dioxide concentration (which does not take part in combustion, as does not nitrogen), but because of low oxygen partial pressure. Flames burn only if there is a sufficient oxygen concentration. In fact, if carbon dioxide does not come from oxidation, as it usually does, but from other sources like reaction of sulphuric acid with carbonates or volcanic gases, the atmospheres can be very dangerous and the flames burn very well (Mucedda, 1998).

## Enthalpy Release and Trap Stability

The logic of a very stable atmosphere around $S$ is an issue. Oxidation always involves enthalpy releases and temperature increases causing convective processes that transfer air much more efficiently than does diffusion.

The reaction of organic substances with oxygen produces typically $3 \times 10^7$ J kg$^{-1}$. As previously demonstrated, the reaction of 1 kg of matter releases 3.1 kg of carbon dioxide, with a consequent energy release of 10 MJ kg$^{-1}$ of carbon dioxide. For a flux $F$ (kilograms of carbon dioxide per square meter per second) we then have

$$I_{O_2} \approx 10^7 F; \quad \left[\mathrm{Wm^{-2}}\right] \tag{17}$$

Water molecules that are produced during the reaction form a gas, and in general, have to release the vaporization enthalpy $L_w$ where it condenses on $S$ or on farther walls to obtain:

$$I_w = \frac{1.3}{3.1}FL_w = 10^{-6}F; \quad \left[\mathrm{Wm^{-2}}\right] \tag{18}$$

where $I_w$ is significantly smaller than $I_{O_2}$.

The flux assumed in the previous examples ($F = 10^{-7}$ kg m$^{-2}$ s$^{-1}$) releases an energy flux approximately 1 W m$^{-2}$. This energy flux can increase the temperature of air and then force gas migration more efficiently than diffusion to transfer carbon dioxide and oxygen, but the rate of temperature increase and gas evacuation depends on the shape of the system. For example, a similar energy release is able to increase in a day 100 kg of air by 1 K, or 100 kg of moist vegetables of about 0.2 K, but it can only evaporate 0.04 kg of water. In general, this is a very small energy release and its effect is dependent on the system shape, such as organic deposit orientation, reactivity and depth, water presence in the deposit, and heat exchanges. If the temperature differences between the organic deposit and the cave are around 0.1–0.5 K, they force air convections of a few centimeters per second, which are much more efficient than diffusion to evacuate such small fluxes of carbon dioxide.

The situation that appears most favorable to use this energy to trigger convective movements is when $S$ is on a vertical wall. The heated air form eddies in front of $S$, and

at the same time, the water flows away from it to reduce its cooling role.

The least favorable situation use of this energy occurs when *S* is on the ceiling (or, more reasonably, in a closed ascending cave branch). The energy released creates a thermal sedimentation that traps air in the hot bubble and only diffusion can evacuate gases from there, even if the entrance is quite large. The escape route from a similar trap is downward and it is then quite easy to get away from it with little effort and without the need for intense breathing. The presence of water thus allows for a relatively isothermal reaction and contributes to system closure, because the temperature differences are not sufficient to create eddies. In any case, it appears that extremely low air fluxes are sufficient to prevent the formation of carbon dioxide-rich or oxygen-poor atmosphere inside caves. In actuality, these conditions are quite rare.

## Transient Conditions

The preceding discussion covered steady-state situations in which the parameters do not depend on time and quiet conditions. For those systems, it was shown that even when essentially at equilibrium, it is possible to create exotic micro-atmospheres.

A sudden gas emission of one cubic kilometer of carbon dioxide from Nyos Lake is not a process at equilibrium (Sigvaldason, 1989; Tazieff, 1989; Evans et al., 1993), and it is very similar to the cold air bubble that falls on our legs when we open a refrigerator. These are typical transient situations. A carbon dioxide-filled cup is very similar to a hot stone, which is going to cool, slowly, according to a similar diffusion law.

A hot stone is not stable in the long term because it is in a state of disequilibrium and will eventually reach a final stable state over a relatively long period of time. A carbon dioxide reservoir behaves in a similar way. Over a long time scale, it is unstable and tends to diffuse into the atmosphere within an altitude of a dozen kilometers. On a much shorter time scale than the time scale of equilibrium drift, the general behavior changes. The Fourier (not the Laplace) equation has to be used and our approach to study the asymptotic state does not describe the process. This means that if we produce, in some way, the filled cup, its gas will remain there for some period of time, like the cold air in a supermarket freezer, but the situation is unstable. Just like the freezer situation is usually stabilized by continuous air-cooling, the carbon dioxide trap can be stabilized by a gas source resulting in a return to stationary physics. However, if these sources are absent, the systems evolve to the maximum entropy state, with one progressing to uniform temperature, and the other progressing to complete gas mixing. In this case, gas will then diffuse away to fill the Earth's atmosphere very slowly, but it can be poured like a liquid or flow along a gallery floor.

## Conclusions

Confusion between stationary and transient conditions has created a false underground legend of gas entrapment, which obscures recognition of the true processes that produce carbon dioxide, methane, and radon traps in caves and mines. The basic concepts have been further confused by the fact that if carbon dioxide is produced by oxidation near its source, there is not only high carbon dioxide concentration, but also a very low oxygen concentration, which leads to the occurrence of flame extinctions and similar evidences of poor atmospheres.

The traps are essentially due to accumulation near a source (whatever the origin) in motionless atmospheres. The up-down gradients are generally due to (1) preferred point of organic accumulation and (2) air thermal stratifiation that creates a motionless trap of cold or warm air.

Structure, periodicity, and intensity of traps depend on organic matter inflow, thermal stratifiation, and shape of the cavity.

## References


Al-Azmi, D., Abu-Shady, A.I., Sayed, A.M., and Al-Zayed, Y., 2008, Indoor Radon in Kuwait: Health Physics, v. 94, p. 49–56.

Antonini, G., and Badino, G., 1998, Tecniche Speciali e di Autosoccorso: Erga, Genova, 288 p.

Badino, G., 2005, Underground Drainage Systems and Geothermal Flux: Acta Carsologica, v. 34, no. 2, p. 277–316.

Cigna, A., and Badino, G., 2008, Indoor Radon in Kuwait: Comment: Health Physics, v. 95, no. 2, p. 255–256.

Ek, C., and Gewelt, M., 1985, Carbon-dioxide in cave atmospheres: Earth Surface Processes and Landforms, v. 10, no. 2, p. 173–187.

Evans, W.C., Kling, G.W., Tuttle, M.L., Tanyileke, G., and White, L.D., 1993, Gas Buildup in Lake Nyos, Cameroon: The Recharge Process and its Consequences: Applied Geochemistry, v. 8, p. 207–221.

James, J., 2003, Carbon Dioxide-Enriched Caves, *in* Guun, J., ed., Encyclopedia of Cave and Karst Science, London, Fitzroy Dearbon, p. 183–184.

Jost, W., 1952, Diffusion in Solids, Liquids, Gases, New York, Academic Press, 558 p.

Lutgens, F., and Tarbuck, E., 1998, The Atmosphere, 7th Edition: N.J., Prentice-Hall, 544 p.

Mucedda, M., 1998, Grotte e pozzi della Nurra di Sassari: Bollettino Gruppo Speleologico Sassarese, v. 17, p. 10–26.

Nashchokin, V., 1979, Engineering Thermodynamics and Heat Transfer, Moscow, MIR Publisher, 572 p.

Renault, P., 1972, Le gaz des cavernes: Decouverte, v. 2443, p. 12–18.

Sigvaldason, G.E., 1989, Conclusions and recommendations of International conference on Lake Nyos disaster: Journal of Volcanology and Geothermal Research, v. 39, p. 97–109.

Tazieff, H., 1989, Mechanisms of the Nyos Carbon Dioxide Disaster: Journal of Volcanology and Geothermal Research, v. 39, p. 109–116.


## Appendix A

### The Natural Carbon Dioxide Gradient

The air pressure in an isothermal atmosphere, in neutral equilibrium, at height *h* [km] as given by Equation (5) and Table 2, leads to

$$P_{\text{air}} = P_0 \exp\left(-\frac{h}{8.5}\right) \qquad \text{(A1)}$$

Similarly, in a pure $CO_2$ atmosphere the pressure behaves according to

$$P_{CO_2} = P_0 \exp\left(-\frac{h}{6.4}\right) \quad \text{(A2)}$$

The ratio between $P_{CO_2}$ and $P_{air}$ in the previous equations gives the ideal carbon dioxide impoverishment with altitude so that we can then obtain:

$$\frac{P_{CO_2}}{P_{air}} = \exp\left(\frac{h}{8.5} - \frac{h}{6.4}\right) = \exp\left(-\frac{h}{26}\right) \quad \text{(A3)}$$

The scale length of reduction of carbon dioxide concentration due to buoyancy is then around 26 km. For these conditions and with a carbon dioxide concentration of 3% at the floor, it is necessary that the ceiling be located at 10.4 km of altitude to reach 2% concentration. This is in fact the true natural $CO_2$ gradient under ideal conditions.

## APPENDIX B

### DOUBLE DIFFUSION

Using an organic deposit $S$ and some mass $M$ per square meter, the chemical composition of organic matter is very roughly $C_nH_{2n}$. Putrefaction (oxidation) of these molecules eventually is

$$\frac{3}{2}O_2 + CH_2 \Rightarrow CO_2 + H_2O \quad \text{(B1)}$$

which in term of reacting masses gives

$$(3.4M)_{O_2} + M \Rightarrow (3.1M)_{CO_2} + (1.3M)_{H_2O} \quad \text{(B2)}$$

Volumetrically, this means that putrefaction of one kilogram of vegetable mass needs the oxygen in about 12 cubic meters of air and emits two cubic meters of carbon dioxide. Most importantly, it needs an oxygen supply.

It is reasonable to assume that the oxidation rate of a compound is proportional to the local oxygen concentration in $S$. Therefore the produced flux of $CO_2$ is given by:

$$F = K_{O_2} c_{O_2,0} \quad \text{(B3)}$$

where $c_{O_2,0}$ is the oxygen concentration near the compounds.

The proportionality depends on exposed surface, compound type, reactivity, temperature, presence of bacteria, total mass of $S$, etc. Calculation of $K_O$ is basically impossible, but some $K_O$ does exist. We can assume that the free atmosphere that feeds oxygen to $S$ is also the same atmosphere that evacuates carbon dioxide (it is not an obvious assumption, but in general, it is true), so we can also assume that the free atmosphere is at a distance $\Delta z$ from $S$. At equilibrium, system parameters do not depend on time (the system is stationary) and the rate of $CO_2$ molecules evacuation must equal exactly the incoming oxygen molecules, as well as the carbon dioxide production.

The concentrations $c_{CO_2,0}$ and $c_{O_2,0}$ are the gas concentrations in $S$, and the concentrations $c_{CO_2,1}$ and $c_{O_2,1}$ are those in the free atmosphere. We must also account the for the different masses involved, and assuming that the flux is not so strong as to destroy the linear distribution, we have

$$F_{CO_2} = D_{CO_2} \frac{c_{CO_2,0} - c_{CO_2,1}}{\Delta z} \quad \text{(B4)}$$

for the diffused carbon dioxide flux from $S$ to $z > 0$, and

$$F_{O_2} = D_{O_2} \frac{c_{O_2,0} - c_{O_2,1}}{\Delta z} \quad \text{(B5)}$$

for the flux of diffused oxygen to $S$. The mass balance shown in Equation (B2) gives

$$F_{O_2} = \frac{3.4}{3.1} F_{CO_2} \quad \text{(B6)}$$

At sea level we can assume that

$$\begin{aligned} c_{O_2,1} &= 0.28 \text{kgm}^{-3} \\ c_{CO_2,1} &= 0 \text{kgm}^{-3} \end{aligned} \quad \text{(B7)}$$

so that we can then obtain a relation between the carbon dioxide and oxygen in $S$

$$D_{O_2} \frac{0.28 - c_{O_2,0}}{\Delta z} = \left(\frac{3.4}{3.1}\right) D_{CO_2} \frac{c_{CO_2,0}}{\Delta z} \quad \text{(B8)}$$

Then, with numerical values

$$c_{CO_2,0} = 1.17(0.28 - c_{O_2,0}) \quad \text{(B9)}$$

setting $F_{id}$ the oxidation rate of $S$ in free atmosphere (i.e., when the oxygen concentration is $c_{O_2,1} = 0.28$ kg m$^{-3}$). We expect that the real oxidation rate to be slower due to the lower oxygen concentration which is proportional to $K_{O_2}$

$$F_{O_2} = K_{O_2} c_{O_2,0} = F_{id} \frac{c_{O_2,0}}{c_{O_2,1}} \quad \text{(B10)}$$

Combining and rearranging

$$F = F_{id} \frac{1}{\left(1 + \frac{F_{id}\Delta z}{0.28 D_{O_2}}\right)} = \varepsilon F_{id} \quad \text{(B11)}$$

$$c_{O_2,0} = c_{O_2,1} \frac{F}{F_{id}} = 0.28\varepsilon \quad \text{(B12)}$$

The carbon dioxide concentration in $S$ is simply

$$c_{CO_2,0} = \frac{F\Delta z}{D_{CO_2}} = \varepsilon \frac{F_{id}\Delta z}{D_{CO_2}} \quad \text{(B13)}$$

That is, carbon dioxide concentration is also reduced by a factor ε when compared with the concentration that we would obtain in the case of single diffusion.

We found a reduction factor ε that takes into account the limited transfer possibilities due to the double diffusion which showed that the actual flux ratio $F/F_{id}$ only depends on the oxygen transfer capacity of local atmosphere. If $D_{O_2}/\Delta z$ is very large (that is, the gases diffuse very easily) in comparison with $F_{id}$, then $\varepsilon = 1$ and $F$ is near $F_{id}$ as it must be. The equations then reduce to the conditions for single diffusion. So, the limiting behavior of double diffusion need only be considered when dealing with high reactivity and, correspondingly, with high $CO_2$ concentrations.

It is easy to show that for these conditions, oxidation rate tends to zero, there is no oxygen near the source (hypoxic atmosphere), and flames smother.

Equation (B11) can be rewritten as

$$F = \frac{1}{\left(\frac{1}{F_{id}} + \frac{\Delta z}{0.28 D_{O_2}}\right)} \tag{B14}$$

and if $F_{id}$ is high, $F$ reaches its maximum value according to

$$F \approx \frac{5.0 \times 10^{-6}}{\Delta z} \tag{B15}$$

$$c_{O_2,0} \approx 0 \tag{B16}$$

$$c_{CO_2,0} \approx 0.35 \tag{B17}$$

which means that in the case of oxidative processes, the maximum carbon dioxide concentration around the source is approximately 21% in volume.